

ANALYSIS OF THE PERFORMANCE OF DROOP CONTROLLED  
INVERTERS IN MINI-GRIDS

Abderrahmane El Boubakri

A Thesis

in

The Department

of

Electrical and Computer Engineering

Presented in Partial Fulfillment of the Requirements

for the Degree of Master of Applied Science at

Concordia University

Montreal, Quebec, Canada

April 2013

© Abderrahmane El Boubakri, 2013

**CONCORDIA UNIVERSITY**  
**SCHOOL OF GRADUATE STUDIES**

This is to certify that the thesis prepared

By: Mr. Abderrahmane El Boubakri

Entitled: "ANALYSIS OF THE PERFORMANCE OF DROOP CONTROLLED INVERTERS IN MINI-GRIDS"

and submitted in partial fulfillment of the requirements for the degree of

**Master of Applied Science**

Complies with the regulations of this University and meets the accepted standards with respect to originality and quality.

Signed by the final examining committee:

\_\_\_\_\_ Chair  
Dr. Luis Rodrigues

\_\_\_\_\_ Examiner, External to the Program  
Dr. Wen-Fang Xie (MIE)

\_\_\_\_\_ Examiner  
Dr. Pragasen Pillay

\_\_\_\_\_ Supervisor  
Dr. Luiz A. C. Lopes

Approved by:

\_\_\_\_\_  
William E. Lynch, Chair  
Chair of Department of Electrical and Computer Engineering

April 15<sup>th</sup>, 2013

\_\_\_\_\_  
Dr. Robin A. L. Drew  
Dean, Faculty of Engineering

# Abstract

DC-AC Converters (inverters) are frequently employed as interfaces of distributed power sources and energy storage units to ac distribution grids. The approach of operating them as a voltage source with droop based control loops and using locally measured quantities offers an effective way to control the amount of active and reactive power they provide/absorb. In this way, fluctuating renewable energy sources, such as photovoltaic (PV) and wind, can help with power balancing, while grid forming units can better share load variations without dedicated communication channels. Besides, it can allow a smooth transition of a micro-grid from the grid-tie to the autonomous mode in case of a grid fault. However, the dynamic response and steady state operation of a system with droop controlled inverters depends quite a bit on systems parameters, such as feeder impedances, as well as on the droop characteristics of the other units, what is not usually known.

This work focuses on the analysis of the performance of droop controlled inverters operating in various conditions. First, a 10 kVA three-phase inverter with a dq (vector) voltage control loop and active power (P) vs. frequency (f) and reactive power (Q) vs. grid voltage magnitude (V) droop characteristics is designed. Then, its behavior when operating connected to a stiff grid is investigated. Time domain simulations with SIMULINK and the technique of root locus, for which a small signal model is derived, are used to observe how the droop factors, frequency of the low pass filters used in the power measurements and feeder impedance affect the dynamic response. Next, the operation of two grid forming inverters in an autonomous micro-grid is considered. Again, the performance of the system is investigated with time domain simulations and root locus. The need for a virtual impedance loop as a means for allowing large droop factors to be used along with feeders with small inductances is observed and the effectiveness of this technique is demonstrated. The adverse impact of the conventional virtual

impedance loop on the load voltage regulation is observed and an alternative implementation that minimizes this problem is proposed and its effectiveness is demonstrated. Finally, an autonomous micro-grid consisting of an inverter and a diesel engine generator set (genset) is studied. Time domain simulations are used to show that when the speed of response, in terms of power, of two grid forming units is very different, the smallest one can be overloaded. An approach for slowing down the fastest unit is proposed to minimize this issue.

**Keywords:** Three-Phase Inverter, Voltage Regulation, Distributed generation, Micro-grid, Islanded Mode, Grid-Connected Mode, Droop Control, Virtual Impedance, Genset.

# Dedication

To my father Abdellah El Boubakri, my mother Houria Belfaqir, my brother Mohamed Amine El Boubakri and my lovely wife Firdaousse Oussarghin.

# Acknowledgements

I would like to express my sincere gratitude to Professor Luiz A. C. Lopes for his invaluable supervision, ideas, and encouragement through the research.

I would like to thank the Government of Canada, through the Program on Energy Research and Development (PERD) for the financial support that they provided for my studies.

Last, but not least, I would like to thank my colleagues in the Power Electronics and Energy Research (PEER) group for their support and encouragement.

# Contents

Abstract.....	iii
Dedication.....	v
Acknowledgements.....	vi
List of Figures .....	xi
List of Tables .....	xix
Abbreviations.....	xxi
Nomenclature .....	xxii
Chapter 1 - Introduction .....	1
1.1 Introduction .....	1
1.2 Droop control theory .....	4
1.3 Thesis objectives .....	11
1.4 Outline of the Thesis .....	12
Chapter 2 - Three-phase voltage source inverter design.....	15
2.1 Introduction .....	15
2.2 Design of the power stage of the inverter .....	15
2.2.1 The 2 <sup>nd</sup> order low pass harmonic filter .....	15
2.2.2 Selection of the DC bus voltage magnitude.....	17

2.2.3 Design of the power switches .....	17
2.3 Three-phase Voltage Source Inverter modeling in dqo coordinates for balanced linear load.....	18
2.4 Voltage controller design .....	22
2.5 Performance verification .....	27
2.5.1 Performance of the inverter in steady-state .....	27
2.5.2 Transient response of the inverter .....	29
2.6 Conclusion .....	35
Chapter 3 - Parallel operation of a droop controlled three-phase voltage source inverter with a stiff grid .....	36
3.1 Introduction .....	36
3.2 P vs. f and Q vs. V droop loops implementation .....	36
3.3 Small-signal model .....	39
3.4 Schematics of the simulation file .....	53
3.5 Root locus of the system to various parameters .....	59
3.6 Performance verification .....	68
3.6.1 Response of the system due to reference signal variations .....	68
3.6.2 Response of the system during a grid disconnection .....	78
3.7 Conclusions .....	80
Chapter 4 - Parallel operation of two droop controlled three-phase voltage source inverters.....	82
4.1 Introduction .....	82
4.2 Small-signal model .....	82



4.3 Schematics of the simulation file .....	96
4.4 Root locus of the system to various parameters .....	100
4.5 Performance verification .....	107
4.5.1 Response of the system to load variations .....	108
4.5.2 Response of the system due to reference (power) signal variations .....	114
4.6 Virtual impedance loop.....	117
4.6.1 Virtual impedance loop implementation.....	117
4.6.2 The system small-signal model including the virtual impedance loop .....	120
4.6.3 Performance verification of the system including the virtual impedance loop .....	126
4.7 Proposed virtual impedance loop .....	133
4.7.1 Proposed virtual impedance implementation .....	135
4.7.2 Small-signal model including the proposed virtual impedance.....	136
4.7.3 Performance verification of the system including the proposed virtual impedance loop ....	138
4.8 Conclusions .....	148
Chapter 5 - Parallel operation of three-phase voltage source inverter with Genset .....	151
5.1 Introduction .....	151
5.2 Problematic description .....	151
5.3 Proposed solution: Settling time variation .....	155
5.4 The proposed settling time control loop implementation in the three-phase inverter.....	161
5.5 Performance verification of the system including the proposed control loop.....	164

5.5.1 Load variation test .....	165
5.5.2 Power signal variation test.....	167
5.6 Conclusion.....	168
Chapter 6 - Conclusions and future work .....	170
6.1 Conclusions .....	170
6.2 Future work.....	170
Appendix A.....	173
Appendix B .....	176
Appendix C .....	178
Appendix D.....	182
Appendix E .....	184
Appendix F .....	188
Appendix G.....	190
Bibliography .....	195

# List of Figures

Figure 1.1: AC-Coupled Diesel Hybrid Mini-Grid..... 2

Figure 1.2: Two AC voltage sources connected in parallel through line impedance..... 4

Figure 1.3: Phase angle generation curve..... 6

Figure 1.4: Droop curves..... 7

Figure 1.5: Droop curves of G1 and G2..... 9

Figure 2.1: The power stage of the three-phase voltage source inverter with the output LC filter and load  
..... 16

Figure 2.2: dqo equivalent circuit of a three-phase voltage source inverter ..... 21

Figure 2.3: dqo block diagrams of a three-phase voltage source inverter ..... 21

Figure 2.4: Voq/Eq Bode diagram with different load values..... 22

Figure 2.5: Bode diagram of the system under light load condition ..... 23

Figure 2.6: Voltage control loop scheme ..... 24

Figure 2.7: Bode diagram of the voltage controller..... 25

Figure 2.8: Bode diagram of the loop transfer function under light load condition ..... 26

Figure 2.9: Bode diagram of the loop transfer function under heavy load condition..... 26

Figure 2.10: Inverter’s output voltage when PF=0.8 (lagging) (V) vs. Time (s)..... 28

Figure 2.11:  $V_{oq}$  and  $V_{od}$  when PF=0.8 (lagging) (V) vs. Time (s) ..... 28

Figure 2.12: Inverter's output active and reactive power (W & VAR) vs. Time (s)..... 29

Figure 2.13: FFT of the inverter's output voltage when PF=0.8 (lagging) (V) vs. Frequency (Hz)..... 29

Figure 2.14: Zoom on switching frequency harmonics (From Fig. 2.13) (V) vs. Frequency (Hz) ..... 30

Figure 2.15: Inverter's output voltage under various conditions (V) vs. Time (s).....	31
Figure 2.16: $V_{oq}$ and $V_{od}$ under various conditions (V) vs. Time (s).....	31
Figure 2.17: FFT of the inverter's output voltage under light load (V) vs. Frequency (Hz).....	32
Figure 2.18: Zoom on switching frequency harmonics under light load (From Fig. 2.17) (V) vs. Frequency (Hz) .....	32
Figure 2.19: FFT of the inverter's output voltage under heavy load (V) vs. Frequency (Hz) .....	32
Figure 2.20: Zoom on switching frequency harmonics under light load (From Fig. 2.19) (V) vs. Frequency (Hz) .....	33
Figure 2.21: Inverter's output current (A) vs. Time (s) .....	33
Figure 2.22: Inverter's operating frequency (Hz) vs. Time (s).....	34
Figure 2.23: Inverter's output voltage when the operating frequency varies (V) vs. Time (s).....	34
Figure 3.1: Parallel three-phase voltage source inverter and stiff grid .....	38
Figure 3.2: Bloc diagram of parallel grid and inverter in dq coordinates .....	40
Figure 3.3: Reference frames of the grid and the inverter .....	40
Figure 3.4: Inverter's bloc diagram .....	41
Figure 3.5: Inverter's voltage control loop.....	43
Figure 3.6: dq equivalent circuit of a three-phase LC filter including local load .....	44
Figure 3.7: dq equivalent circuit of an inductive load .....	45
Figure 3.8: dq equivalent circuit of the line impedance .....	46
Figure 3.9: The system's Simulink/Matlab simulation file scheme .....	55
Figure 3.10: The system's dq average model in Simulink/Matlab.....	56
Figure 3.11: Inverter and grid's output active power (W) vs. Time (s) .....	58
Figure 3.12: Inverter and grid's output reactive power (VAr) vs. Time (s) .....	58
Figure 3.13: Roots of the complete system small-signal model .....	62

Figure 3.14: Roots of the reduced system small-signal model .....	62
Figure 3.15: Low frequency poles of the detailed and reduced system's small-signal models.....	63
Figure 3.16: Dominant poles of the detailed and reduced system models when $m_p$ or $\Delta f$ is increasing ...	64
Figure 3.17: Roots of the reduced system model when $n_q$ or $\Delta V\%$ is increasing .....	65
Figure 3.18: Root locus of the reduced system model when $R_g$ is fixed and $X_g$ is increasing .....	66
Figure 3.19: Root locus of the reduced system model when $X_g$ is fixed and $R_g$ is increasing .....	66
Figure 3.20: Root locus of the reduced system model when $f_c$ is increasing .....	67
Figure 3.21: P vs. f droop control loop.....	67
Figure 3.22: Inverter and grid's output active power when $m_p$ varies (W) vs. Time (s) .....	69
Figure 3.23: Roots of the reduced system model with different values of $m_p$ .....	70
Figure 3.24: Inverter and grid's reactive power when $n_q$ varies (VAr) vs. Time (s).....	72
Figure 3.25: Roots of the reduced system model with different values of $n_q$ .....	72
Figure 3.26: Inverter and grid's reactive power damped with $m_p$ decreasing (VAr) vs. Time (s) .....	73
Figure 3.27: Root locus of the reduced system model when decreasing $m_p$ while $n_q$ is large .....	73
Figure 3.28: Inverter and grid's output active power when the ratio $X_g/R_g$ varies while $R_g$ is fixed (W) vs. Time (s) .....	74
Figure 3.29: Inverter and grid's output active power when $R_g$ varies while $X_g/R_g$ is fixed (W) vs. Time (s) .....	75
Figure 3.30: Root locus of the reduced system model when $R_g$ varies while $X_g/R_g$ is fixed.....	75
Figure 3.31: Inverter and grid's output active power when $f_c$ varies (W) vs. Time (s) .....	77
Figure 3.32: Root locus of the reduced system model when $f_c$ varies.....	77
Figure 3.33: Inverter and grid's reactive power damped when $f_c$ is increased (VAr) vs. Time (s) .....	78
Figure 3.34: Roots of the reduced system model when $f_c$ is increased while $n_q$ is large.....	78

Figure 3.35: Inverter and grid's active and reactive power during grid disconnection (W & VAr) vs. Time (s).....	79
Figure 4.1: Micro-grid composed by two droop controlled inverters, a feeder and local loads.....	83
Figure 4.2: The system bloc diagram on dq coordinates.....	86
Figure 4.3: Reference frames of the inverters.....	86
Figure 4.4: The system's Simulink/Matlab simulation file scheme.....	98
Figure 4.5: The system's dq model in Simulink/Matlab.....	99
Figure 4.6: Inverters' output active power (W) vs. Time (s).....	99
Figure 4.7: Inverters' output reactive power (VAr) vs. Time (s).....	100
Figure 4.8: Location of the roots of the complete system small-signal model.....	101
Figure 4.9: Location of the roots of the reduced system small-signal model.....	101
Figure 4.10: Low frequency poles of the complete and reduced system's small-signal models.....	103
Figure 4.11: Low frequency poles of the complete system model when increasing $L_f$ while $f_{LCF}$ is fixed at 2kHz.....	103
Figure 4.12: Roots of the reduced and the complete system models when $m_{p1}$ & $m_{p2}$ are increased.....	104
Figure 4.13: Roots of the reduced system model when $n_{q1}$ & $n_{q2}$ are increased.....	105
Figure 4.14: Roots of the reduced system model when $X_g/R_g$ is increased while $R_g$ is fixed at $0.23\Omega$ .....	106
Figure 4.15: Root locus of the reduced system model when $X_g/R_g$ is decreased while $X_g$ is fixed at $0.1\Omega$ .....	107
Figure 4.16: Root locus of the reduced system model when $f_c$ is increased.....	107
Figure 4.17: Inverters' output active power when large load step occurred (W) vs. Time (s).....	109
Figure 4.18: Dominant pole of the complete system model for large load variation condition.....	110
Figure 4.19: Inverters' output active power when large load step occurred when $\Delta f=2\text{Hz}$ (W) vs. Time (s).....	110

Figure 4.20: Dominant pole of the complete system model when $\Delta f$ is decreased (W) vs. time (s).....	111
Figure 4.21: Inverters' output active power when large load step occurred when $R_g=0.3\Omega$ (W) vs. Time (s) .....	111
Figure 4.22: Dominant pole of the complete system model when $R_g$ is increased (W) vs. time (s).....	112
Figure 4.23: Inverters' output active power when large load step occurred while $X_q/R_g=5$ and $R_g=0.3\Omega$ (W) vs. Time (s).....	113
Figure 4.24: Inverters' output active power when large load step occurred when $f_c=60\text{Hz}$ (W) vs. Time (s) .....	113
Figure 4.25: Dominant pole of the complete system model when $f_c$ is increased (W) vs. time (s).....	114
Figure 4.26: output active power when $f_{nL1}$ is varied (W) vs. Time (s) .....	115
Figure 4.27: Inverters' output active power when $f_{nL1}$ is varied while $X_q/R_g=5$ and $R_g=0.3\Omega$ (W) vs. Time (s) .....	116
Figure 4.28: virtual impedance in series with the real line impedance.....	117
Figure 4.29: Virtual impedance loop.....	118
Figure 4.30: Virtual impedance loop implementation.....	119
Figure 4.31: Bloc diagram of the dq model of the inverters including the virtual impedance loop.....	120
Figure 4.32: Dominant poles of the reduced and the complete system models when the virtual impedance is increased.....	123
Figure 4.33: The dominant pole of the reduced system model when the $X_{gT}/R_{gT}$ is increased by increasing $L_v$ .....	125
Figure 4.34: The dominant pole of the reduced system model when the $X_{gT}/R_{gT}$ is decreased by increasing $R_v$ .....	125
Figure 4.35: Inverters' output active power when $R_v$ is increased while $X_v$ is null (W) vs. Time (s) .....	127
Figure 4.36: Inverters' output reactive power when $R_v$ is increased while $X_v$ is null (VAr) vs. Time (s) ...	128

Figure 4.37: Inverters' output peak voltage amplitudes when $R_v$ is increased while $X_v$ is null (V) vs. Time (s).....	128
Figure 4.38: Dominant pole of the reduced system model when purely resistive VI is increased.....	129
Figure 4.39: Inverters' output active power when $X_v$ is increased while $R_v$ is null (W) vs. Time (s) .....	129
Figure 4.40: Inverters' output reactive power when $X_v$ is increased while $R_v$ is null (VAr) vs. Time (s) ...	130
Figure 4.41: Inverters' output peak voltage amplitudes when $X_{v1}$ is increased while $R_{v1}$ is null (V) vs. Time (s).....	130
Figure 4.42: Dominant pole of the reduced system model when purely inductive VI is increased .....	131
Figure 4.43: Inverters' output reactive power including VI and when $n_q$ is increased (VAr) vs. Time (s). 132	
Figure 4.44: Virtual angle .....	134
Figure 4.45: Phase angles between the inverters' output voltages when $R_v$ is increased (Degree) vs. Time (s).....	134
Figure 4.46: Proposed virtual impedance implementation .....	135
Figure 4.47: Voltage reference generator bloc.....	136
Figure 4.48: Dominant poles of the systems detailed model with conventional and proposed VI when $R_v$ is increased .....	138
Figure 4.49: Dominant poles of the systems detailed model with conventional and proposed VI when $L_v$ is increased .....	138
Figure 4.50: Inverters' output active power when $R_v$ in the proposed VI is increasing (W) vs. Time (s)..	139
Figure 4.51: Inverters' output reactive power when $R_v$ in the proposed VI is increasing (VAr) vs. Time (s) .....	140
Figure 4.52: Dominant pole of the detailed system including the proposed VI for different values of $R_v$ .....	140
Figure 4.53: Inverters' output peak voltage magnitudes for different values of $R_v$ (V) vs. Time (s).....	141



Figure 4.54: Inverters' output active power when $L_v$ in the proposed VI is increasing (W) vs. Time (s)..	141
Figure 4.55: Inverters' output reactive power when $L_v$ in the proposed VI is increasing (VAr) vs. Time (s) .....	142
Figure 4.56: Dominant pole of the detailed system including the proposed VI for different values of $L_v$	142
Figure 4.57: Inverters' output peak voltage magnitudes for different values of $L_v$ (V) vs. Time (s) .....	143
Figure 4.58: Inverters' output reactive power including proposed VI and when $n_q$ is increased (VAr) vs. Time (s) .....	144
Figure 4.59: Inverters' output active power while using purely resistive proposed VI when a step occurred in $f_{nL2}$ (W) vs. Time (s) .....	145
Figure 4.60: Inverters' output active power when $R_v$ in the proposed VI is very large (W) vs. Time (s) ..	146
Figure 4.61: Inverters' output active power when $R_v$ in the proposed VI is very large and $X_g/R_g$ is fixed (W) vs. Time (s).....	147
Figure 4.62: Inverters' output active power when $R_v$ in the proposed VI is very large and $X_g/R_g$ is variable (W) vs. Time (s).....	148
Figure 5.1: Three-phase Voltage Source Inverter connected in parallel with a Genset via a feeder .....	152
Figure 5.2: P vs. f droop curves .....	153
Figure 5.3: Frequency responses of the inverter and the Genset under heavy load variations (Hz) vs. Time (s) .....	154
Figure 5.4: Inverter and Genset's output active power (W) vs. Time (s).....	154
Figure 5.5: Parallel AC voltage sources via a purely inductive feeder .....	155
Figure 5.6: The closed loop bloc diagram of the large-signal of $P_1$ when conventional droop control is used .....	156
Figure 5.7: The closed loop bloc diagram of the small-signal of $P_1$ when conventional droop control is used .....	156

Figure 5.8: Large-signal representation of $P_1$ including the proposed control loop.....	159
Figure 5.9: Large-signal representation of $P_1$ including the simplified proposed control loop .....	159
Figure 5.10: Small-signal representation of $P_1$ including the simplified proposed control loop .....	159
Figure 5.11: Line active power when $K_d$ is increased (W) vs. Time (s).....	161
Figure 5.12: Matlab/Simulink simulation file of the inverter, Genset, local loads and the feeder .....	162
Figure 5.13: Voltage reference generator including the proposed control loop and the proposed VI loop .....	163
Figure 5.14: The Diesel Engine and the Terminal Voltage Exciter models of the Genset [23] .....	164
Figure 5.15: Diesel Engine Model .....	164
Figure 5.16: Inverter and Genset's output active power for different $K_d$ without the proposed VI (W) vs. Time (s).....	166
Figure 5.17: Inverter and Genset's output active power for different $K_d$ (W) vs. Time (s).....	167
Figure 5.18: Inverter and Genset's output active power when $K_d$ is increased and $R_v=2\Omega$ , (W) vs. Time (s) .....	167
Figure 5.19: and Genset's output active power when $K_d$ is increased and $R_v=2\Omega$ (W) vs. Time (s).....	168

# List of Tables

Table 1.1: Line parameters for different networks.....	10
Table 2.1: LC filter components .....	16
Table 2.2: The IGBT’s maximum ratings.....	18
Table 2.3: Damping ratios with various load values .....	22
Table 2.4: Voltage controller parameters.....	24
Table 2.5: The system parameters.....	27
Table 2.6: Simulation steps for transient response verification when voltage reference and load variations occur .....	30
Table 2.7: Simulation steps for transient response verification when voltage reference and load variations occur .....	33
Table 3.1: System parameters .....	54
Table 3.2: Simulation steps.....	54
Table 3.3: system parameters for $m_p$ increasing simulations .....	69
Table 3.4: The dominant pole with different $m_p$ .....	70
Table 3.5: System parameters for $n_q$ increasing simulations.....	71
Table 4.1: system parameters.....	102
Table 4.2: system parameters when $n_{q1}$ & $n_{q2}$ are increased .....	105
Table 4.3: system parameters for load variation condition.....	108
Table 4.4: Simulation steps for load variation test .....	108
Table 4.5: Simulation steps for $f_{nL}$ variation condition .....	114

Table 4.6: Simulation steps when VI loop is included.....	126
Table 4.7: Simulations' steps when $R_v$ is large .....	147
Table 5.1: Genset and Inverter ratings .....	152
Table 5.2: System parameters in Fig. 5.5 .....	160
Table 5.3: Step-info of the system when $K_d$ is increased .....	161
Table 5.4: System parameters .....	165
Table 5.5: Simulations steps for load variation test .....	166
Table 5.6: Simulations steps for power signal variation test.....	168

# Abbreviations

DES	Distributed Energy Source
DGs	Distributed Generators
ESR	Equivalent Series Resistance
HV	High-Voltage
IGBT	Insulated Gate Bipolar Transistor
LPF	Low-Pass Filter
LTF	Loop Transfer Function
LV	Low-Voltage
MPPT	Maximum Power-Point Tracking
MV	Medium-Voltage
PCC	Point of Common Coupling
PEIDG	Power Electronic Interfaced Distributed Generator
PF	Power Factor
PI	Proportional-Integral
PLL	Phase-Locked Loop
PM	Phase-Margin
RES	Renewable energy Source
SPWM	Sinusoidal Pulse-Width Modulation
THD <sub>v</sub>	Total Voltage Harmonics Distortion
VI	Virtual Impedance
VSI	Voltage Source Inverter

# Nomenclature

$\Delta f$	: frequency range of P vs. f droop curve
$\Delta V$	: Voltage range of Q vs. V droop curve
$\Delta V\%$	: Voltage range of Q vs. V droop curve in percentage
$C_f$	: The LC filter capacitor
$E_{abc}$	: Inverter's output switched voltage
$E_{abci}$	: Output switched voltage of the $i^{\text{th}}$ inverter
$E_i$	: RMS voltage magnitude of the $i^{\text{th}}$ ideal ac voltage source
$E_{io}$	: Initial RMS voltage magnitude of the $i^{\text{th}}$ ideal ac voltage source
$e_{qd}$	: Command signal to the inverter's gates in dq vector
$e_{qdi}$	: Command signal to the $i^{\text{th}}$ inverter's gates in dq vector
$E_{qdo}$	: Inverter's output switched voltage in dqo vector
$f_c$	: The LPF cut-off frequency
$f_{cd}$	: The LPF cut-off frequency for the new control loop
$f_{\text{Inv}}$	: Operating frequency of the inverter
$f_{\text{LCF}}$	: Cut-off frequency of the inverter's output LC filter
$f_{\text{nL}}$	: No-load frequency
$f_{\text{nL}_{\text{gs}}}$	: The no-load frequency of the genset
$f_{\text{nL}_{\text{inv}}}$	: The no-load frequency of the inverter
$f_{\text{nLi}}$	: No-load frequency of the $i^{\text{th}}$ inverter
$f_r$	: Rating frequency
$f_{\text{ref}}$	: frequency reference of the inverter
$f_{\text{sw}}$	: The inverter's switching frequency

$f_x$	: The cross-over frequency
$I_{Labc}$	: LCF inductors' current
$I_{Labc_i}$	: LCF inductor current of the $i^{\text{th}}$ inverter
$I_{Lineabc}$	: Tie-line current
$I_{Lineqd}$	: Tie-line current in dq vector
$I_{Lineqdo}$	: Initial tie-line current in dq vector
$I_{Loadabc}$	: Load currents
$I_{Loadabc_i}$	: Local load current of the $i^{\text{th}}$ inverter
$I_{loadqd}$	: Load current in dq vector
$I_{loadqdi}$	: Local load current of the $i^{\text{th}}$ inverter in dq vector
$I_{Loadqdio}$	: Initial local load current of the $i^{\text{th}}$ inverter in dq vector
$I_{Loadqdo}$	: Inverter's initial local load current in dq vector
$I_{Lqdi}$	: LCF inductor current of the $i^{\text{th}}$ inverter in dq vector
$I_{Lqdo}$	: LCF inductors' current in dqo vector
$I_{o,rms}$	: RMS current magnitude rating of the inverter
$I_{oabc}$	: Inverter's output currents
$I_{oabc_i}$	: Output current of the $i^{\text{th}}$ inverter
$I_{oqd}$	: Inverter's output current in dq vector
$I_{oqdi}$	: Output current of the $i^{\text{th}}$ inverter in dq vector
$I_T$	: Current magnitude rating of each IGBT of the inverter
$K_d$	: The coefficient of $\delta_d$
$K_{pi}$	: Voltage controller parameter
$L_f$	: The LC filter inductor
$L_g$	: Line impedance inductive component

$L_{Load}$	: Inductive load
$L_{Loadi}$	: Inductive local load of the $i^{th}$ inverter
$L_v$	: Inductive component of $Z_v$
$L_{vi}$	: Inductive virtual impedance of the $i^{th}$ inverter
$m_a$	: The modulation index
$m_p$	: P vs. f droop gain
$m_{pgs}$	: P vs. f droop gain of the Genset
$m_{pi}$	: Active power droop gain of the $i^{th}$ inverter
$m_{pInv}$	: P vs. f droop gain of the inverter
$n_q$	: Q vs. V droop gain
$n_{qi}$	: Reactive power droop gain of the $i^{th}$ inverter
$n_{qInv}$	: Q vs. V droop gain of the inverter
$P$	: Active Power
$P_g$	: Grid's output active power
$P_{Gi}$	: Output active power of the $i^{th}$ generator
$P_{Gi\_max}$	: Active power rating of the $i^{th}$ generator
$P_{gs}$	: Genset's output active power
$P_{Inv}$	: Inverter's output active power
$\tilde{p}_{Inv}$	: Inverter's output active power ripples
$P_{Invi}$	: Output active power of the $i^{th}$ inverter
$P_{Load}$	: Load active power
$P_{Load\_max}$	: Maximum load active power
$P_{Loadi}$	: Local load active power of the $i^{th}$ inverter
$Q$	: Reactive Power



$Q_g$	: Grid's output reactive power
$Q_{Inv}$	: Inverter's output reactive power
$\tilde{q}_{Inv}$	: Inverter's output reactive power ripples
$Q_{Invi}$	: Output reactive power of the $i^{th}$ inverter
$Q_{Load}$	: Load reactive power
$r_c$	: The ESR of $C_f$
$R_g$	: Line impedance resistive component
$R_{gT}$	: Total line impedance resistance ( $R_g+R_{vi}$ )
$r_L$	: The ESR of $L_f$
$R_{Load}$	: Resistive load
$R_{loadi}$	: Resistive local load of the $i^{th}$ inverter
$R_v$	: Resistive component of $Z_v$
$R_{vi}$	: Resistive virtual impedance of the $i^{th}$ inverter
$S_{maxi}$	: Apparent power rating of the $i^{th}$ inverter
$T_1$	: Park's transformation matrix
$T_p$	: Voltage controller parameter
$V_{DC}$	: DC bus voltage magnitude
$V_{dqNewref}$	: The new voltage reference in dq vector for the inverter
$V_{dqv}$	: Voltage drop across the virtual impedance in dq vector
$V_{gqd}$	: Grid's voltage magnitude in dq vector
$V_{Invi}$	: Peak voltage magnitude of the $i^{th}$ inverter
$V_{LL,rms}$	: RMS Phase to phase voltage magnitude at the inverter's terminal
$V_{nL}$	: No-load voltage magnitude
$V_{nLi}$	: No-load voltage magnitude of the $i^{th}$ inverter

$V_{oabc}$	: Inverter's terminal voltage
$V_{oabci}$	: Terminal voltage of the $i^{\text{th}}$ inverter
$V_{oqdi}$	: Terminal voltage of the $i^{\text{th}}$ inverter in dq vector
$V_{oqdio}$	: Initial terminal voltage of the $i^{\text{th}}$ inverter in dq vector
$V_{oqdo}$	: Inverter's initial output voltage in dq vector
$V_{oqdo}$	: Inverter's terminal voltage in dqo vector
$V_{qdNewref1}$	: The new voltage reference in dq vector for inverter #1
$V_{qdNewref2com}$	: The new voltage reference on the common dq reference frame for inverter #2
$V_{qdref}$	: Voltage reference magnitude in dq vector
$V_{qdrefcom}$	: Inverter's voltage reference on dq common reference frame
$V_{qdrefi}$	: Voltage reference magnitude of the $i^{\text{th}}$ inverter in dq vector
$V_{qdrefio}$	: Initial voltage reference magnitude of the $i^{\text{th}}$ inverter in dq vector
$V_{qdrefo}$	: Initial voltage reference of the inverter
$V_r$	: RMS rating voltage magnitude
$V_{ref}$	: Voltage amplitude reference (Q vs. V droop controller output)
$V_T$	: Voltage magnitude rating of each IGBT of the inverter
$X_g$	: Line impedance inductive component reactance
$X_g/R_g$	: Tie-line impedance ratio
$X_{gT}$	: Total line impedance inductive reactance ( $X_g+X_{vi}$ )
$X_v$	: Inductive component reactance of $Z_v$
$X_{vi}$	: Inductive virtual impedance reactance of the $i^{\text{th}}$ inverter
$Z_g$	: Line impedance magnitude
$Z_{Load}$	: Load impedance magnitude
$Z_v$	: Virtual impedance magnitude

$\delta$	: Phase angle between two ac voltage sources
$\delta_d$	: The phase angle of the new control loop
$\delta_o$	: Initial phase angle between two ac voltage sources
$\theta_g$	: Line impedance angle
$\theta_v$	: The virtual phase angle
$\theta_{vi}$	: The virtual phase angle of the $i^{\text{th}}$ inverter
$\xi$	: The damping ratio
$\tau$	: Voltage controller parameter
$\varphi_i$	: Output voltage phase angle of the $i^{\text{th}}$ ac voltage source
$\varphi_{qd}$	: The error between the voltage reference and the measured output voltage of the inverter
$\varphi_{qdi}$	: The error between the voltage reference and the measured output voltage of the $i^{\text{th}}$ inverter
$\omega_c$	: The LPF cut-off angular frequency
$\omega_{com}$	: The rotational speed of the common dq reference frame
$\omega_g$	: Grid's operating angular frequency
$\omega_i$	: Operating angular frequency of the $i^{\text{th}}$ inverter
$\omega_{Inv}$	: Operating angular frequency of the inverter
$\omega_{nL}$	: No-load angular frequency
$\omega_o$	: Operating angular frequency
$\omega_o$	: Steady-state operating angular frequency
$\omega_{ref}$	: Angular frequency reference (P vs. f droop controller output)



# Chapter 1 - Introduction

## 1.1 Introduction

In our time, the electricity has become an essential commodity, and without it, daily life would be difficult to envisage. Therefore, it is necessary to produce it efficiently and continuously. To meet the increasing consumption of electricity, the model in place today is based on relatively few power plants that can produce electricity in large quantities. Once produced, it must be brought up to the consumer since means for storing large quantities of electricity are still unavailable. In a country, the transmission and distribution systems ensure the transit of electrical energy between points of production and consumption, which in general, are located in urban areas. One issue with this model is that network (grid) expansion is often very expensive and not feasible in remote rural areas and islands. In such situations, mini-grids (isolated networks) would be a realistic alternative and the most cost-effective option to provide electricity to domestic and local businesses in those far off areas.

Conventionally, the main sources of electricity in mini-grids are diesel engine generator sets, or gensets, which provide electricity to the loads using a local distribution network. The main issue in diesel mini-grids is the high cost of electricity production due the high cost of diesel fuel and its transportation to those remote areas. Adding renewable energy sources (RESs), such as solar (Photovoltaic), wind energy, biomass or small scale hydro-generators, and battery storage units to a diesel based system gensets, results in a diesel hybrid mini-grids as Fig. 1.1 shows. These would be a very attractive solution to decrease the electrical energy cost in long term [1] because initial costs remain relatively high. Diesel hybrid mini-grids offer unique diesel fuel saving and ensuring reliable and least cost power supply [1].

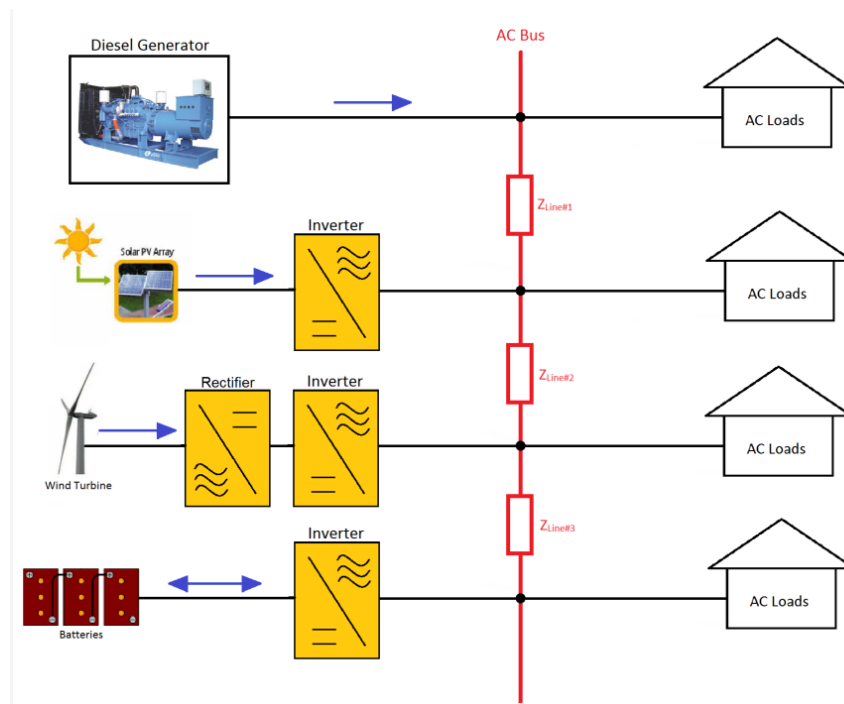


Figure 1.1: AC-Coupled Diesel Hybrid Mini-Grid

However, implementing sustainable energy sources in mini-grids involves complex technical issues [1], such as energy management, system stability, power quality and active and reactive power flow control. It should be noted that RESs which are interfaced into the AC bus through power electronic converters, act differently compared to conventional generation sources based on rotating machines. Because of that, the transient responses of diverse distributed energy sources (DESs) are not evident and the safe operation of diesel hybrid mini-grids requires in depth studies and analyses [2].

In remote rural areas, load variation is typically very high, and the peak load could reach 5 to 10 times the average load [3]. Consequently, in conventional mini-grids (where gensets are the only source of electricity) diesel generators might need to operate under light load conditions, where they are inefficient [3] [4]. On the other side, in diesel hybrid mini-grids, Gensets are usually turned off during light loads, letting the RESs or energy storage devices, such as battery inverters, feeding the loads.

The output power of each DES, in a hybrid mini-grid, should not exceed their ratings. To ensure that, Multi-Master droop control approach is widely used [5]. The droop control method consists on drooping the operating frequency of the AC voltage sources when their output power increases [6]. This allows avoiding the use of communication links between the Distributed Generators (DGs) and effectively reducing the investment costs [5]. Moreover, mini-grids extension would be possible [5].

Mini-grids are characterized by their low-voltage buses and by short distribution lines. This means that distribution lines' impedances amplitudes are very small. Hence, a very small perturbation on the operating frequency or the output voltage amplitude of those power electronic interfaced distributed generators (PEIDGs), due to their transient response characteristics, could generate high circulating current between them [5]. Therefore, multi-level control technique has to be used to ensure system stability and power quality [7]. The common technique employed for this case is the "Virtual Impedance control loop". It consists of adding "virtually" an inductive impedance at the output of inverters, without generating real losses, in order to put the system into the stability region [7]. However, the way this technique is implemented causes bad voltage regulation because the voltage drop across the virtual impedance affects the voltage references of the inverter. In other words, the conventional virtual impedance control loop affects the output voltage amplitude of the inverters hence it affects the reactive power sharing. This point will be taken into consideration in this thesis.

One of the major advantages of implementing RESs in parallel with a genset in a diesel hybrid mini-grid is the decreasing of the genset size which eventually reduces the diesel fuel consumption at the low load demands depending on RESs availability and load profile.

In case, where the load demand is high in a diesel hybrid mini-grid, genset and RESs should share loads proportionally to their apparent power ratings. As mentioned above, the PEIDGs and gensets have

different dynamic properties. Therefore, the parallel operation of a genset and PEIDGs should be analysed carefully.

## 1.2 Droop control theory

The droop control technique is commonly used in rotating (synchronous machine based) interfaces of power sources. The  $P$  vs.  $f$  droop loop allows parallel connected generators to operate in a safe way sharing variations in the load/demand in a pre-determined way without any dedicated communication means. Similarly, the  $Q$  vs.  $V$  droop loop is used to minimize the circulation currents that would appear if the impedance between the generators and a common load were not the same. In this section, theoretical studies of droop control have been done.

The values of the active and reactive powers flowing between two AC voltage sources, which are connected in parallel through line impedance as shown in Fig. 1.2, are given by Eq. 1.1 and 1.2 [8]-[10].

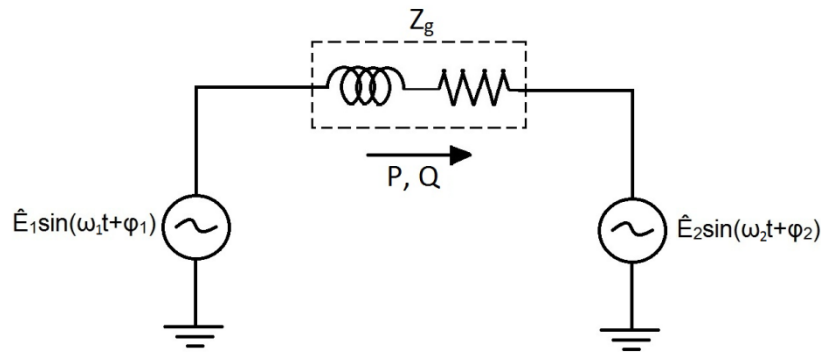


Figure 1.2: Two AC voltage sources connected in parallel through line impedance

$$P = \left[ \frac{E_1 E_2}{Z_g} \cos(\varphi_1 - \varphi_2) - \frac{E_2^2}{Z_g} \right] \cos(\theta_g) + \frac{E_1 E_2}{Z_g} \sin(\varphi_1 - \varphi_2) \sin(\theta_g) \quad (1.1)$$

$$Q = \left[ \frac{E_1 E_2}{Z_g} \cos(\varphi_1 - \varphi_2) - \frac{E_2^2}{Z_g} \right] \sin(\theta_g) - \frac{E_1 E_2}{Z_g} \sin(\varphi_1 - \varphi_2) \cos(\theta_g) \quad (1.2)$$



Where,  $Z_g$  and  $\theta_g$  are the line impedance amplitude and angle respectively.  $E_1$  and  $E_2$  are the RMS value of the AC voltage sources, and  $\varphi_1$  and  $\varphi_2$  are their phases respectively.

Assuming that the line impedance is highly inductive (Where,  $\theta_g \approx \pi/2$  rad in high-voltage networks; see Table 1.1). The equations 1.1 and 1.2 become;

$$P = \frac{E_1 E_2}{X_g} \sin(\varphi_1 - \varphi_2) \quad (1.3)$$

$$Q = \frac{E_1 E_2}{X_g} \cos(\varphi_1 - \varphi_2) - \frac{E_2^2}{Z_g} \quad (1.4)$$

Where,  $X_g$  is the inductive part of the line impedance  $Z_g$ . As it is shown by Eq. 1.3 and 1.4, the active power, flowing from voltage source 1 to 2 through a highly inductive line impedance, can be controlled by varying the phase  $\delta$  (Where,  $\delta = \varphi_1 - \varphi_2$ ). Also, that the reactive power supplied by source 1 can be controlled by controlling the magnitude of source 1 ( $E_1$ ). This forms the basis of the well-known P vs. f and Q vs. V droop control. The angle  $\delta$  is then generated by controlling the angular frequency dynamically (See Fig. 1.3) which makes  $P$  flow. Eq. 1.5 gives the relation between two angular frequencies of two interconnected AC voltage sources.

$$\delta = \int (\omega_1 - \omega_2) dt \quad (1.5)$$

The error between two AC voltage sources' angular frequencies generates a phase angle between them. Fig. 1.3 shows an example. Consider a generator (source 1) connected to an infinite bus. If a torque step is applied in the prime mover of the generator, at  $t_1$ , it will accelerate,  $\omega_1$  becoming bigger than  $\omega_2$ . This causes angle  $\delta$  to increase, increasing the active power flow from the generator what slows it down until it reaches the same speed as generator 2, when angle  $\delta$  becomes constant. Note that the active power flow depends also on the size of the magnitude of the line impedance ( $X_g$ ; for highly inductive line impedance) as given by Eq. 1.3. If  $X_g$  is very small which is the case in mini-grids, a small variation of  $\delta$

could lead to very large active power flows or to system instability. A precise control of the angle  $\delta$  of an inverter's output voltage when  $X_g$  is very small is almost impossible [11]. Therefore, selecting a larger size of  $X_g$  could solve the problem. However, the line impedances' values in a mini-grid are uncontrollable and mostly unknown and adding large inductive impedances in series to them could be costly. Bad transients caused by small line impedance amplitude will be discussed in the following chapters.

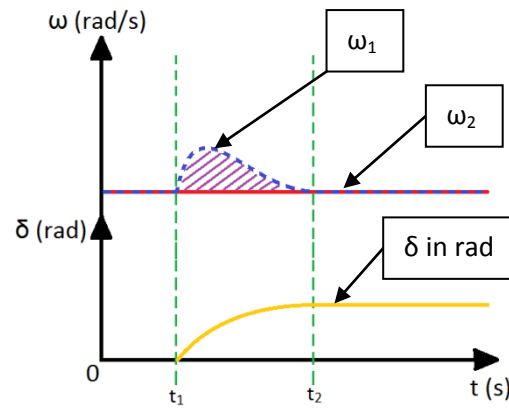


Figure 1.3: Phase angle generation curve

Practically it is difficult and costly to measure instantaneous frequencies of all parallel AC voltage sources, which form a mini-grid, in order to calculate and control their output voltage's phase angles using a centralized controller and communication links between the DGs [12]. Therefore, in isolated mini-grids, located generally in remote areas, decentralized methods, such as droop control that will be discussed shortly, should be adopted. It allows the DGs to be controlled and operated based only on local measurements (active and reactive power). This allows the easy expansion of the mini-grid, decreasing investments costs [13].

The conventional droop equations are given by;

$$\omega_{ref} = \omega_{nL} - m_p P \quad (1.6)$$

$$V_{ref} = V_{nL} - n_q Q \quad (1.7)$$

Where,  $\omega_{ref}$  and  $V_{ref}$  are the angular frequency and voltage magnitude references respectively,  $\omega_{nL}$  and  $V_{nL}$  are the no-load angular frequency and voltage respectively,  $m_p$  and  $n_q$  are the active and reactive droop slopes respectively, and  $P$  and  $Q$  are the output active and reactive power. When this technique is applied to power electronic converters, the angular frequency is usually “converted” into plain frequency (Hz).

From Eq. 1.6 and 1.7 the droop curves suitable for operation with inverters are shown in Fig. 1.4.

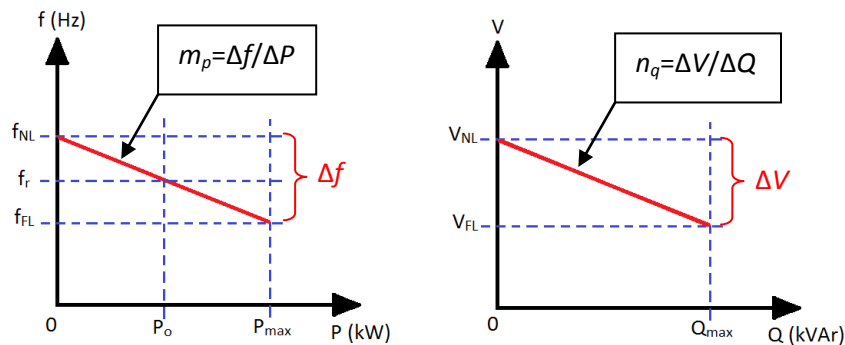


Figure 1.4: Droop curves

Where,  $f_r$  is the rated frequency which is equal to 60Hz or 50Hz. However, in some cases, the inverters' droop controllers must be designed regarding the droop characteristics of the paralleled source. For example, where an inverter operates in parallel with a Genset which has generally a full load frequency of 60Hz or 50Hz as it is discussed in Chapter 5, the inverter's droop controller must have the same configuration in order to ensure stability and good power sharing quality.

As mentioned above, the reactive droop controller's role is to minimize the circulating currents between DGs when feeders' impedances are not the same. This will limit the injection of reactive currents in order to make the DGs' maximum ratings available to face new load request [11]. The maximum output reactive power ( $Q_{max}$ ) supplied by the generator could be capacitive (negative) or inductive (positive). In

Eq. 1.4, the reactive power injected by  $G_1$  becomes positive if its output voltage ( $E_1$ ) is bigger than  $E_2$ , and it becomes negative when  $E_1$  is smaller than  $E_2$ . This means that one could regulate the output reactive power around zero by increasing or decreasing the output voltage amplitude when  $Q$  is inductive or capacitive respectively.

As it is well known, DGs in a mini-grid share load and each generator should provide apparent power depending on its maximum ratings. Therefore, from Eq. 1.6 and 1.7, neglecting the losses in the feeders, the DGs' droop equations should respect the following rule described by Eq. 1.8.

$$S_{Load} = S_{G1} + S_{G2} + \dots + S_{Gi} \quad (1.8)$$

Where,  $S_{Load}$  is the demanded apparent power and  $S_{Gi}$  is the output apparent power of the  $i^{\text{th}}$  generator.

From Eq. 1.6 and 1.7 one can derive the followings;

$$P_{Load} = \frac{\omega_{nL1} - \omega_{ref1}}{m_{p1}} + \frac{\omega_{nL2} - \omega_{ref2}}{m_{p2}} + \dots + \frac{\omega_{nLi} - \omega_{refi}}{m_{pi}} \quad (1.9)$$

And,

$$Q_{Load} = \frac{V_{nL1} - V_{ref1}}{n_{q1}} + \frac{V_{nL2} - V_{ref2}}{n_{q2}} + \dots + \frac{V_{nLi} - V_{refi}}{n_{qi}} \quad (1.10)$$

The DGs operating in the same mini-grid have to operate with the same frequency and voltage droop ranges ( $\Delta f$  and  $\Delta V$ ) in order to ensure stability and to operate with the same frequency in steady-state ( $\omega_{ref}$ ). Therefore, from Eq. 1.9 and 1.10 one can conclude that the droop slopes that determine the portion of the provided power by a DG to the mini-grid. Let's consider the following equations as an example (Eq. 1.11 and 1.12) which describes the total active power provided by two DGs that have different ratings.

$$P_{Load} = P_{G1} + P_{G2} \quad (1.11)$$

Where,

$$P_{G1\_max} = 0.75P_{Load\_max} ; P_{G2\_max} = 0.25P_{Load\_max} \quad (1.12)$$

Where  $P_{G1\_max}$  and  $P_{G2\_max}$  are the active power ratings of generator one and two respectively, and  $P_{Load\_max}$  is the maximum active power demanded by load.

From Eq. 1.6, 1.11 and 1.12, knowing that the steady-state frequency of the two DGs has to be the same, Eq. 1.13 describes an important aspect that should be taken into consideration in droop controller design in order to avoid ratings exceeding of DGs.

$$m_{p1}P_{G1} = m_{p2}P_{G2} \quad (1.13)$$

Hence,

$$m_{p1} = \frac{m_{p2}}{3} \quad (1.14)$$

From Eq. 1.14, one can see that  $m_{p1}$  has to be three times smaller than  $m_{p2}$  if the rating active power of the generator one is three times bigger than the rating active power of the generator two as shown in Fig.1.5. Note that the same rule applies to the reactive droop control as described by Eq. 1.15.

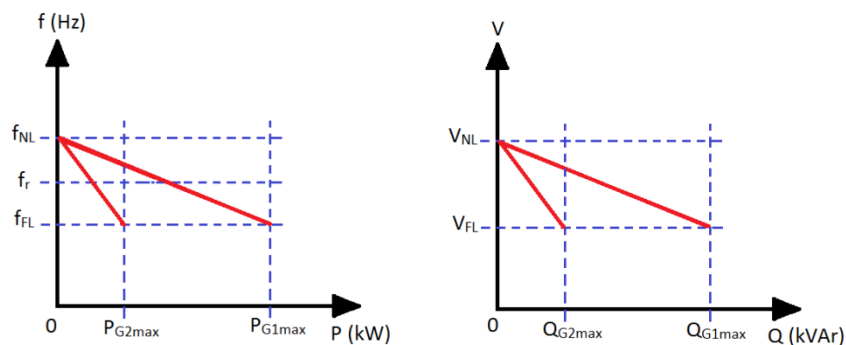


Figure 1.5: Droop curves of G1 and G2

$$n_{q1} = \frac{n_{q2}}{3} \quad (1.15)$$

Unlike what was assumed in Eq. 1.3 and 1.4, in low-voltage (LV) networks or in mini-grids, line impedances are mainly resistive where  $R_g \gg X_g$  [8], [10], [14], [15]. Table 1.1 shows typical line parameters for LV, MV (*Medium-voltage*) and HV networks [15].

**Table 1.1: Line parameters for different networks**

Type of network	$R_g$ ( $\Omega/\text{km}$ )	$X_g$ ( $\Omega/\text{km}$ )	$R_g/X_g$
LV	0.642	0.083	7.7
MV	0.161	0.190	0.85
HV	0.060	0.191	0.31

There is a very important aspect about droop control when  $Z_g$  is highly resistive ( $\theta_g \approx 0$ ; in Eq. 1.1 and 1.2) which has to be taken into consideration. Considering a feeder where  $R_g \gg X_g$ , Eq. 1.1 and 1.2 are reduced to the followings;

$$P = \frac{E_1 E_2}{R_g} \cos(\varphi_1 - \varphi_2) - \frac{E_2^2}{R_g} \quad (1.16)$$

$$Q = -\frac{E_1 E_2}{R_g} \sin(\varphi_1 - \varphi_2) \quad (1.17)$$

From Eq. 1.16 and 1.17, the droop control method is radically changed. In other words, the active and reactive power is no longer controlled by the phase angle and voltage amplitude respectively. Here one find out that P vs. V and Q vs. f droop control has to be adopted only where  $\theta_g \approx 0$ . Otherwise, the P vs. f and Q vs. V droop control could be used but the coupling between P and Q will be bigger as shown in Eq. 1.1 and 1.2. The smaller  $\theta_g$  is the larger the coupling between P and Q will be generated after a variation in frequency and/or voltage amplitude. This affects the system steady state responses as it is discussed in the following sections. The feeder impedance selected in this thesis is a resistive-inductive impedance where  $45^\circ < \theta_g < 0$ . Note that the coupling issue is not discussed in this thesis.

The implementation of the droop controllers in the inverter is discussed in chapter 3.

### 1.3 Thesis objectives

The main aim of this thesis is to solve some problems related to the modeling and control of a droop controlled voltage source inverter sharing loads with different sources separately (Stiff grid, voltage source inverter and genset). The mini-grid studied in this thesis has a three-phase three-wire configuration. The inverter interfaces the DC voltage bus (battery banks) into the AC voltage bus where loads are connected. For the sake of simplicity, ideal DC voltage sources have been assumed (without any voltage variations). The feeders' impedances which connect the DGs are resistive and have small magnitudes.

The research methodology will be developed as follows;

- Develop the three-phase voltage source inverter model with an output LC low-pass filter modeling using Park's transformation (dqo coordinates). The modeling is done for balanced linear loads.
- Design of the voltage controller for DC components (dqo values of voltage reference). This controller regulates the Inverter's output voltage amplitude, frequency and phase under balanced loads conditions.
- In order to define all parameters that influence significantly the system stability, an accurate model will be derived for a droop controlled voltage source inverter connected in parallel with a stiff grid through a tie-line. The study is based on small-signal analysis, frequency domain behavior and root locus diagrams. The same thing is done for a system composed with two drooped controlled inverters, two local loads and a tie-line. Time domain simulations are done to see the effect of some parameters on the system steady-state responses.

- Analyze and develop the virtual impedance control loop in order to reduce the inverters' output impedance issues and its impact on the system stability. Based on the derived small-signal model of the system including the virtual impedance loop, frequency domain analysis will be done to see the effect of the virtual impedance loop on the system's transients. Then, time domain simulations will be done to discuss the effect of the virtual impedance loop on the system steady-state responses and on the inverter's voltage regulation.
- A new virtual impedance control loop will be proposed which is based on phase shift control of the inverters' output voltage. This new virtual impedance control loop provides more robust transient response improvement and much better voltage regulation.
- Analyse the behavior of the genset operating in parallel with one voltage source inverter sharing local loads through a feeder.
- Analyse and develop a new control loop permitting the control of the settling time of the inverter's active power in order to make it slower as the genset. This new control loop improves the inverter's transients since the latter has a quicker speed response and consequently it takes all the dynamics when a load step occurs.
- The system performance is verified by means of simulations using Simulink/Matlab.

## 1.4 Outline of the Thesis

This thesis is organized in 6 chapters, as follows;

- **Chapter 2** contains the modeling of a three-phase voltage source inverter with its output LC filter using Park's transformation. This allows designing of the voltage controller in order to regulate the output voltage under balanced linear loads conditions. A PI type-3 controller is chosen to get zero steady-state error and to damp the transient response of the inverter under light load condition. For system performance verification, the inverter has been put



- under various tests which could face when sharing load with parallel DGs. This has been efficacy validated through time domain simulations.
- In **Chapter 3**, a small-signal state-space model, based on dq components, of a system composed of a droop controlled three-phase voltage source inverter with an output LC low-pass filter and a local load connected in parallel to a stiff grid through line impedance is developed. This is to define the elements affect the system stability. This model allows also an accurate analysis of the system, in frequency domain, in order to design appropriate parameters of power droop controllers to make the system having better dynamics. This is verified through time domain simulations.
  - Based on the small-signal model derived in Chapter 3, a small-signal model of a system composed by two three-phase voltage source inverters with their output LC low-pass filters, two local loads and one line impedance is derived in **Chapter 4**. After defining the most influencing elements to the system transient responses using root locus, the virtual impedance loop is designed then included in the small-signal model in order to see its effects on the system dynamics. Time domain simulations are done to verify the latter. However, the virtual impedance loop affects also the inverters' output voltage amplitude. Therefore, a new virtual impedance loop is proposed which consists on controlling the inverters' output voltage phase angle without affecting the Ac voltage amplitude and the system steady-states. This is verified by frequency and time domain analysis.
  - In **Chapter 5**, the parallel operation of a genset with a droop controlled voltage source inverter through a tie-line is investigated. The analysis is done based only on simulations due to system complexity. As discussed before, the inverter has a much quicker dynamic response compared to the genset. Two DGs operating in parallel, and which have different dynamic properties, tend to lead to a more oscillatory transient response. A proposed phase

angle control loop is proposed allowing the increasing of the inverter settling time; hence improving its dynamics when operating with the Genset. Some time domain simulations are done to verify this technique.

- **Chapter 6** presents the final conclusions of the research and some suggestions for future work.

# Chapter 2 - Three-phase voltage source inverter design

## 2.1 Introduction

This chapter contains the design and testing of a 10kVA, 120/208V, 60Hz three-phase voltage source inverter (VSI), which is used as the interface of renewable energy sources and energy storage units to a distribution grid. A conventional sinusoidal pulse-width modulation (SPWM) scheme, with a triangular carrier of 20 kHz, has been employed. The most suitable power gates for such application are the Insulated Gate Bipolar Transistors (IGBTs). A 2<sup>nd</sup> order LC low pass filter for attenuating switching harmonics is then designed. For regulating the voltage at the output of the LC filter, across the capacitor, a dq (vector) control scheme employing a simple PI-type controller is used. The performance of the inverter is verified by means of simulations with Simulink/Matlab.

## 2.2 Design of the power stage of the inverter

### 2.2.1 The 2<sup>nd</sup> order low pass harmonic filter

The power stage of the three-phase voltage source inverter with an LC filter supplying a load is shown in Fig. 2.1. Both the inductor and the capacitor present intrinsic equivalent series resistances (ESR).

Considering that the inverter operates with SPWM at a switching frequency ( $f_{sw}$ ) of 20 kHz, the cut-off frequency ( $f_{LCF}$ ) of the LC filter is selected as 2 kHz, using the rule-of-thumb of 10% of  $f_{sw}$ . This in turn will allow the choice of the values of  $L_f$  and  $C_f$  according to Eq. 2.1.

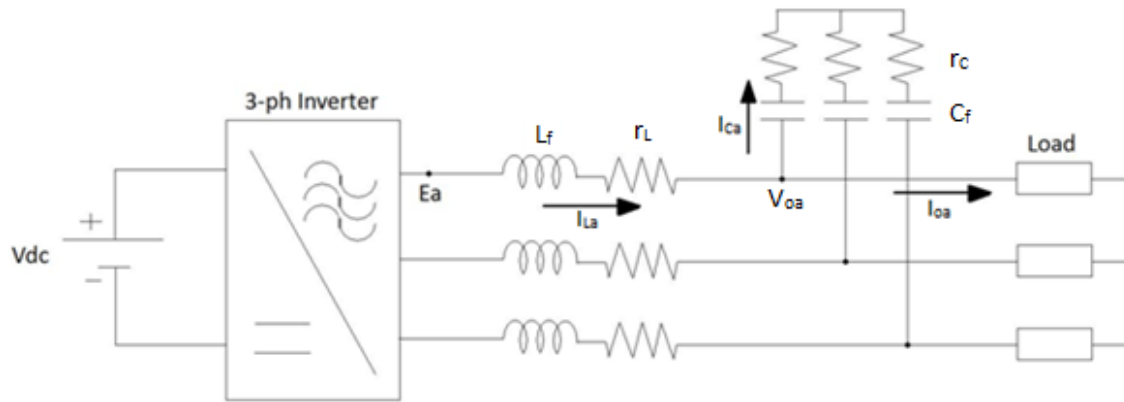


Figure 2.1: The power stage of the three-phase voltage source inverter with the output LC filter and load

$$f_{LCF} = 2\text{kHz} = \frac{1}{2\pi\sqrt{L_f C_f}} \quad (2.1)$$

By fixing the value of capacitor at 20 $\mu$ F, one calculates the inductor as 316.6 $\mu$ H.

Typical values for the ESRs of the inductor and capacitor are shown in Table 2.1.

Table 2.1: LC filter components

Element	Size	ESR
Inductor	320 $\mu$ H	500m $\Omega$
Capacitor	20 $\mu$ F	100m $\Omega$

The inverter has a rated output apparent power of 10kVA with a minimum power factor of 0.8, and its output AC voltage is rated at a RMS value of 208 V<sub>LL</sub>. For Y-connected filter capacitors, the rated voltage could be selected to be at least 25% bigger than the rated peak voltage at the AC side, or 212.13 V. Hence, we can use the polycarbonate capacitor of “Venture Lighting Inc.” having a product number of “R1008HP200P25M” and rated at 250V. Regarding the filter inductors, they should be able to conduct a fundamental line current given by Eq. 2.2 ([1]; Eq. 8-62) plus current harmonics;

$$I_{o,rms} = \frac{S_{3ph}}{\sqrt{3} \times V_{LL,rms}} = \frac{10\text{kVA}}{\sqrt{3} \times 208} = 27.8 \text{ A} \quad (2.2)$$

Where,  $S_{3ph}$  is the rated apparent power, and  $V_{LL,rms}$  is the RMS value of the fundamental component of the switched voltage of the inverter. Therefore, an inductor rated at 32 A<sub>rms</sub> will be selected for this application.

### 2.2.2 Selection of the DC bus voltage magnitude

The value of the DC bus voltage is selected so that the magnitude of the fundamental component of the output voltage of the inverter can be varied by  $\pm 10\%$  while operating with linear SPWM. In this case, the modulation index ( $m_a$ ), the parameter used for controlling the magnitude of the inverter voltage, should be smaller or equal to 1.

The relationship between the dc bus voltage and the fundamental component of the line-to-line voltage in the output of a SPWM controlled inverter ( $V_{LL}$ ) is given by;

$$V_{DC} = \frac{V_{LL,rms}}{0.612 \times m_a} \quad (2.3)$$

Therefore, one shall use  $m_a = 0.8$  when to obtain  $V_{LL} = 228.8$  V what requires  $V_{DC}$  to be equal to 467.3 V. Since the switches are not ideal, presenting voltage drops of a few V, and there will also be a voltage drop across the output filter inductor, the dc bus voltage is selected as 500 V.

### 2.2.3 Design of the power switches

It is very important to determine the current and voltage ratings of the inverter's switches in order to avoid damaging them. In this study, it is assumed that the voltage of the DC bus is constant, and also that the output current is free of harmonics at maximum loading. The peak ratings of each switch are (Eq. 2.4 and 2.5 are obtained from [1]; Eq. 8-60 and Eq. 8-61 respectively);

$$V_T = V_{DC} = 500 \text{ V} \quad (2.4)$$

And,

$$I_T = \sqrt{2}I_{o,max} = \sqrt{2} \times 27.8 A = 39.3 A \quad (2.5)$$

Where,  $V_T$  and  $I_T$  are the maximum voltage and current of each switch respectively. The IGBT switch from the manufacturer "FAIRCHILD SEMICONDUCTOR" having the part number of "FGA50N100BNTD2" is suitable for our application. The Table 2.2 gives a brief summary of the IGBT's maximum ratings It presents an 100% safety margin in terms of the voltage ratings and 21.4% safety for the current ratings what is desirable since parasitic inductance in the dc bus can result in over-voltages during the commutations of the switches.

Table 2.2: The IGBT's maximum ratings

Symbol	Description	Ratings	Units
$V_{CES}$	Collector to Emitter Voltage	1000	V
$I_c$	Collector Current @ $T_c = 25^\circ\text{C}$	50	A
$I_{CM}$	Pulsed Collector Current	200	A
$I_{FM}$	Diode Maximum Forward Current	150	A
$P_D$	Maximum Power Dissipation @ $T_c = 25^\circ\text{C}$	156	W

### 2.3 Three-phase Voltage Source Inverter modeling in dqo coordinates for balanced linear load

To obtain an accurate and reliable voltage regulation for a three-phase Inverter using a simple PI-type controller, one needs to use DC, not AC, components as inputs to the controller. Therefore, the power system model of the inverter should be transformed from ABC coordinates to dqo coordinates (called also Park's transformation).

From Fig. 2.1, the following equations describe the Inverter's inductors' currents and capacitors' voltages behavior in ABC coordinates, assuming that the DC voltage and switches are ideal;

$$\frac{d}{dt} \begin{bmatrix} i_{La} \\ i_{Lb} \\ i_{Lc} \end{bmatrix} = \frac{1}{L_f} \times \begin{bmatrix} E_a \\ E_b \\ E_c \end{bmatrix} - \frac{r_L}{L_f} \times \begin{bmatrix} i_{La} \\ i_{Lb} \\ i_{Lc} \end{bmatrix} - \frac{1}{L_f} \times \begin{bmatrix} V_{oa} \\ V_{ob} \\ V_{oc} \end{bmatrix} \quad (2.6)$$

$$\frac{d}{dt} \begin{bmatrix} V_{oa} \\ V_{ob} \\ V_{oc} \end{bmatrix} = \frac{1}{C_f} \times \begin{bmatrix} i_{La} \\ i_{Lb} \\ i_{Lc} \end{bmatrix} - \frac{1}{C_f Z_{Load}} \times \begin{bmatrix} V_{oa} \\ V_{ob} \\ V_{oc} \end{bmatrix} \quad (2.7)$$

Where,  $i_{La}$ ,  $i_{Lb}$  and  $i_{Lc}$  are the inductor's currents,  $E_a$ ,  $E_b$  and  $E_c$  are the output switched voltages,  $V_{oa}$ ,  $V_{ob}$  and  $V_{oc}$  are the capacitor voltages, and  $Z_{Load}$  is the load impedance. Note that the ESR of the capacitor ( $r_c$ ), which is usually very small, has been neglected for the sake of simplicity.

The following equation describes the Park's transformation matrix " $T_1$ ";

$$\begin{bmatrix} x_q \\ x_d \\ x_o \end{bmatrix} = \frac{2}{3} \begin{bmatrix} \sin\omega t & \sin\left(\omega t - \frac{2\pi}{3}\right) & \sin\left(\omega t + \frac{2\pi}{3}\right) \\ \cos\omega t & \cos\left(\omega t - \frac{2\pi}{3}\right) & \cos\left(\omega t + \frac{2\pi}{3}\right) \\ \frac{1}{2} & \frac{1}{2} & \frac{1}{2} \end{bmatrix} \times \begin{bmatrix} x_a \\ x_b \\ x_c \end{bmatrix} = T_1 \times \begin{bmatrix} x_a \\ x_b \\ x_c \end{bmatrix} \quad (2.8)$$

Where,  $\omega$  is the operating angular frequency. Before converting Eq. 2.6 and 2.7 to dqo values some mathematical developments should be done. The derivative of Eq. 2.8 is given by;

$$\frac{d}{dt} \begin{bmatrix} x_a \\ x_b \\ x_c \end{bmatrix} = \frac{d}{dt} \left\{ T_1^{-1} \times \begin{bmatrix} x_q \\ x_d \\ x_o \end{bmatrix} \right\} = \frac{d}{dt} \{ T_1^{-1} \} \times \begin{bmatrix} x_q \\ x_d \\ x_o \end{bmatrix} + T_1^{-1} \times \frac{d}{dt} \begin{bmatrix} x_q \\ x_d \\ x_o \end{bmatrix} \quad (2.9)$$

Hence,

$$T_1 \times \frac{d}{dt} \begin{bmatrix} x_a \\ x_b \\ x_c \end{bmatrix} = T_1 \times \frac{d}{dt} \left\{ T_1^{-1} \times \begin{bmatrix} x_q \\ x_d \\ x_o \end{bmatrix} \right\} = T_1 \times \frac{d}{dt} \{ T_1^{-1} \} \times \begin{bmatrix} x_q \\ x_d \\ x_o \end{bmatrix} + \frac{d}{dt} \begin{bmatrix} x_q \\ x_d \\ x_o \end{bmatrix} \quad (2.10)$$

Where the inverse of the matrix  $T_1$  is;

$$T_1^{-1} = \begin{bmatrix} \sin\theta & \cos\theta & 1 \\ \sin\left(\theta - \frac{2\pi}{3}\right) & \cos\left(\theta - \frac{2\pi}{3}\right) & 1 \\ \sin\left(\theta + \frac{2\pi}{3}\right) & \cos\left(\theta + \frac{2\pi}{3}\right) & 1 \end{bmatrix} \quad (2.11)$$

And,

$$T_1 \times \frac{d}{dt} T_1^{-1} = \begin{bmatrix} 0 & -\omega & 0 \\ \omega & 0 & 0 \\ 0 & 0 & 0 \end{bmatrix} \quad (2.12)$$

Applying Eq. 2.8, 2.10 and 2.12 into Eq. 2.6 and 2.7 one can get the followings;

$$\frac{d}{dt} \begin{bmatrix} I_{Lq} \\ I_{Ld} \\ I_{Lo} \end{bmatrix} = \frac{1}{L_f} \begin{bmatrix} E_q \\ E_d \\ E_o \end{bmatrix} - \frac{r_L}{L_f} \begin{bmatrix} I_{Lq} \\ I_{Ld} \\ I_{Lo} \end{bmatrix} - \frac{1}{L_f} \begin{bmatrix} V_{oq} \\ V_{od} \\ V_{oo} \end{bmatrix} - \begin{bmatrix} -\omega I_{Ld} \\ \omega I_{Lq} \\ 0 \end{bmatrix} \quad (2.13)$$

$$\frac{d}{dt} \begin{bmatrix} V_{oq} \\ V_{od} \\ V_{oo} \end{bmatrix} = \frac{1}{C_f} \begin{bmatrix} I_{Lq} \\ I_{Ld} \\ I_{Lo} \end{bmatrix} - \frac{1}{C_f Z_{Load}} \begin{bmatrix} V_{oq} \\ V_{od} \\ V_{oo} \end{bmatrix} - \begin{bmatrix} -\omega V_{od} \\ \omega V_{oq} \\ 0 \end{bmatrix} \quad (2.14)$$

From Eq. 2.13 and 2.14, one can draw the equivalent circuit of the three-phase voltage source Inverter in dqo coordinates shown in Fig 2.2;

It can be seen from Fig. 2.2 that there is a coupling effect between q and d channels. However, the 0 channel is not affected by the other channels.

The next Figure shows the block diagrams, which is equivalent to the equations 2.13 and 2.14;

The bode diagram of the transfer functions  $V_{oq}/E_q$ ,  $V_{od}/E_d$  and  $V_o/E_o$  (obtained from Fig. 2.3 for a load with unity power factor) is shown in Fig. 2.4. There one sees that it presents a very small damping factor under light load condition. This could make the system response too oscillatory.



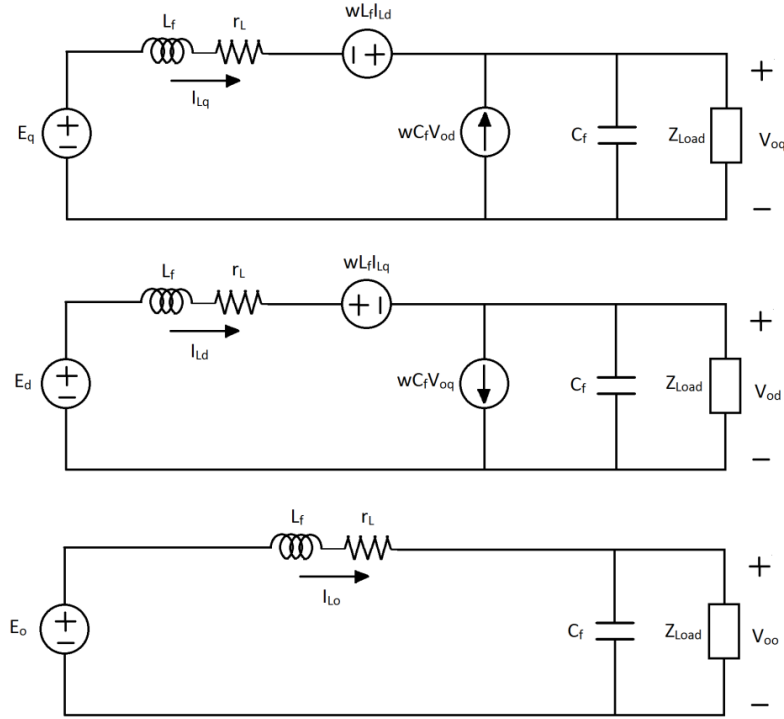


Figure 2.2: dqo equivalent circuit of a three-phase voltage source inverter

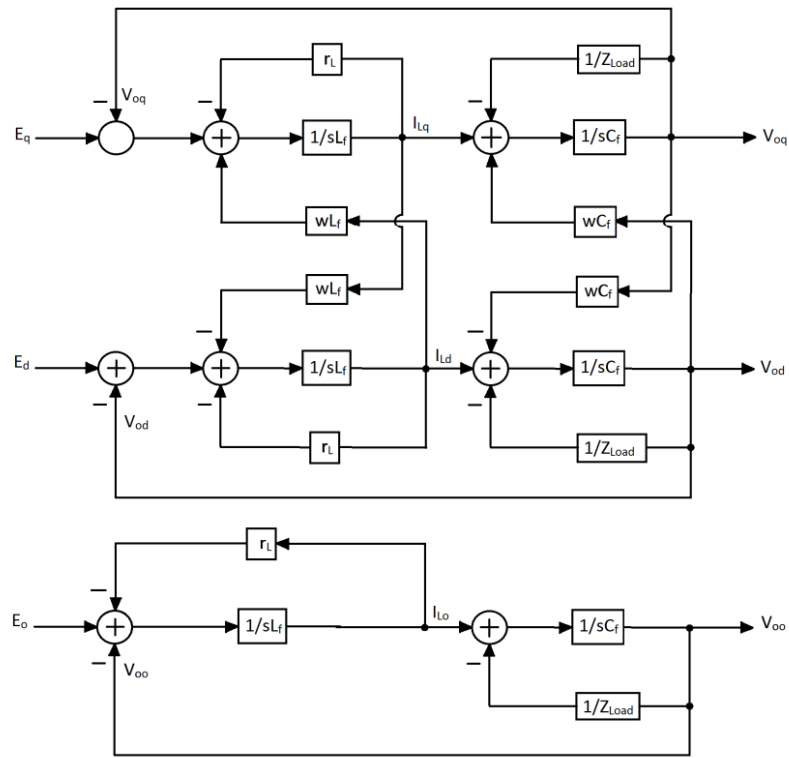


Figure 2.3: dqo block diagrams of a three-phase voltage source inverter

## 2.4 Voltage controller design 22

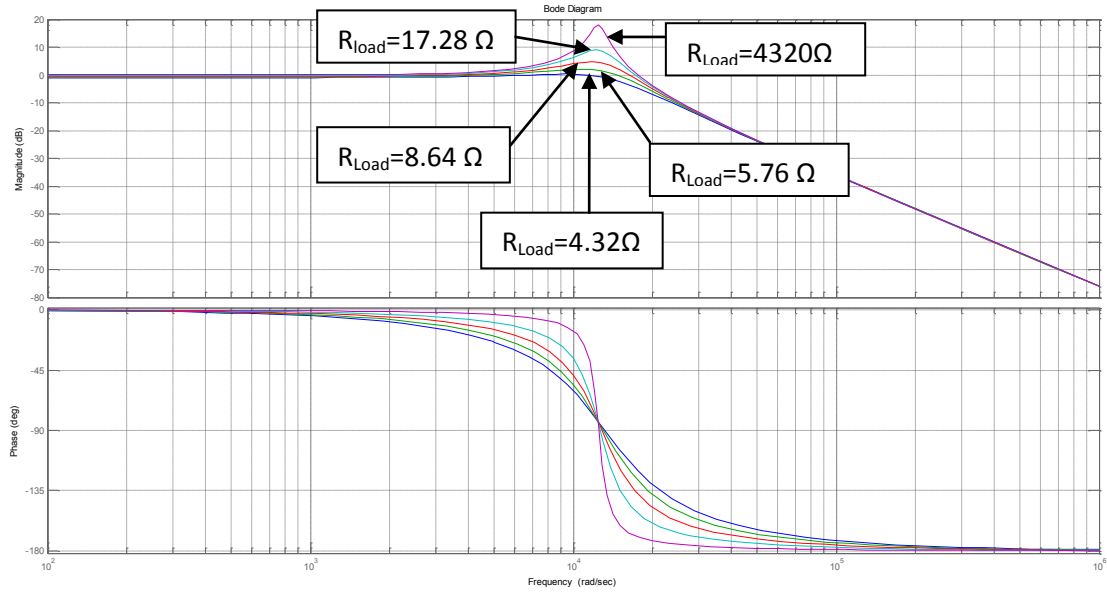


Figure 2.4:  $V_{oq}/E_q$  Bode diagram with different load values

Note that  $V_{od}/E_d$  and  $V_{oo}/E_o$  transfer functions have the same Bode diagram as  $V_{oq}/E_q$  because the couplings are not included in their transfer functions. The following table shows values of the damping ratios which correspond to different values of output load.

Table 2.3: Damping ratios with various load values

Inverter's Output Power (kW)	Load ( $\Omega$ )	Damping ratio ' $\xi$ '
0.01	4320	0.063
2.5	5.76	0.176
5	8.64	0.286
7.5	17.28	0.393
10	4.32	0.497

To avoid getting poor and oscillatory transient responses, the voltage controller should be designed for the worst case, that is, when the system is under light load. Note that the 0 channel is not used because only balanced loads condition has been taken into consideration in the system.

## 2.4 Voltage controller design

The main role of the voltage controller is to regulate the inverter's output voltage when perturbations occur due to load and/or voltage reference variations. A PI-type controller has been

chosen in order to get zero steady-state error and to provide a good, fast transient response with a good damping.

As mentioned above, the voltage controller should be designed when the system operates under the worst condition which is under light load condition. Fig. 2.5 shows the bode diagram of the system under light load condition ( $P_{Load}=0.01kW$ );

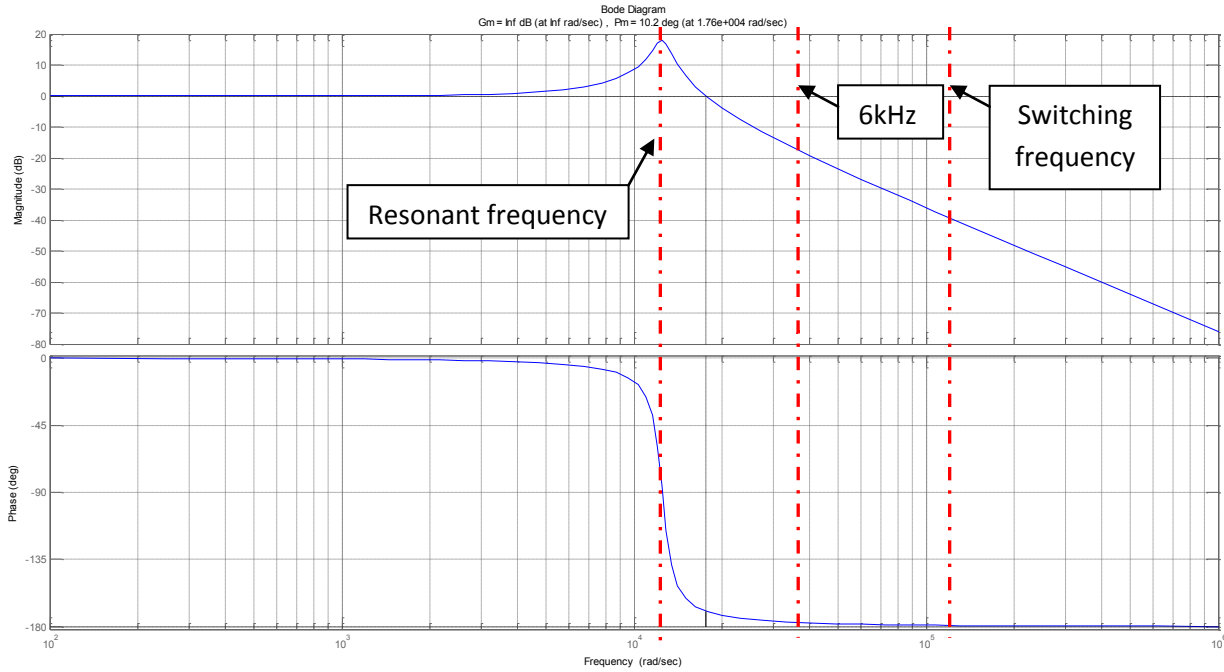


Figure 2.5: Bode diagram of the system under light load condition

The cross-over frequency ( $f_x$ ) has been selected as 6 kHz in order to get fast transient response and to impose enough gain at the switching harmonics frequencies to suppress them. For this purpose, a PI type-3 controller has been designed, which will allow getting enough phase-margin and large negative slope ( $db/Dec$ ) at high frequencies. Because the ESR of the capacitor ( $r_c$ ) has been neglected in the inverter's modeling, a large phase-margin ( $PM$ ) of  $60^\circ$  has been chosen.

The transfer function of a PI type-3 controller is given by Eq. 2.15.

$$G_{c,PI3} = \frac{K_{pi} (1 + s\tau)^2}{s\tau (1 + sT_p)^2} \quad (2.15)$$

Note that only a voltage control loop has been designed due to the high cross-over frequency, and corresponding fast transient response that is desired. Fig. 2.6 shows the inverter’s power stage including the voltage control loop scheme. The “Voltage Reference Generator” block computes the voltage references in dq by converting the inputs ( $V_{ref}$  and  $\omega_{ref}$ ) to a three-phase balanced signal than to dq signals.

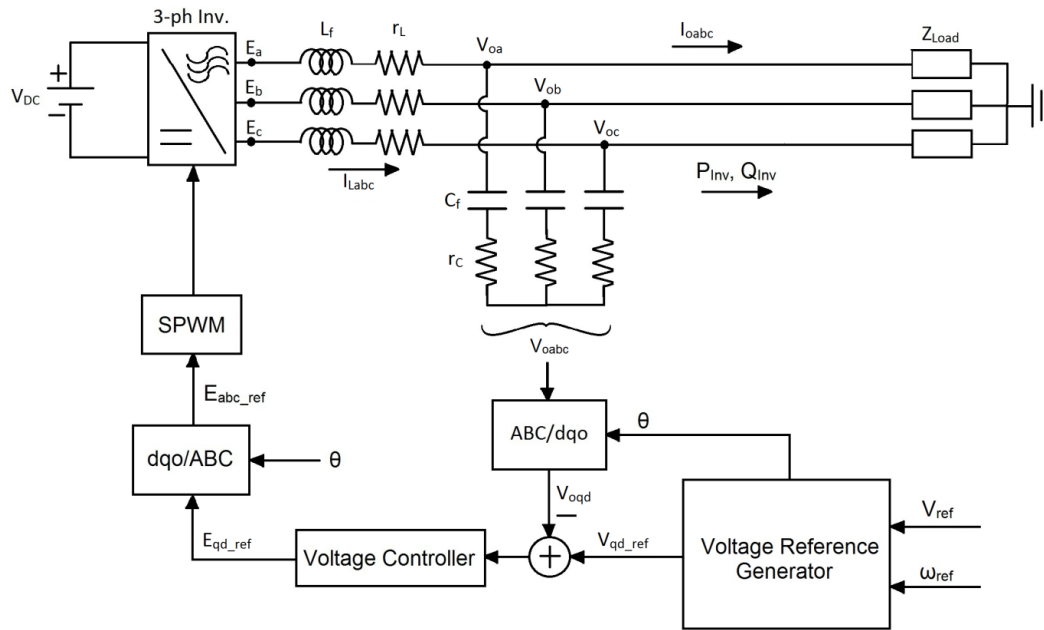


Figure 2.6: Voltage control loop scheme

$V_{ref}$  (Peak value of the phase voltage) and  $\omega_{ref}$  have been set as 169.7V and 377rad/s respectively. By choosing the cross-over frequency as 6 kHz and the phase-margin as  $60^\circ$ , one gets the voltage controller parameters shown in Table 2.4.

Table 2.4: Voltage controller parameters

Controller’s channel	Crossover frequency (Hz)	Phase margin (degree)	$K_{pi}$	$\tau$	$T_p$
q and d	6k	60	1.1614	182.94u	3.846u

The voltage controller has been designed such a way when multiplying it with the system transfer function shown in Fig. 2.5, the loop transfer function has to have a null gain at the cross-over frequency

and a large negative db/Dec slope at high frequencies. Fig. 2.7 shows the bode diagram of the voltage controller.

Note that the same voltage controller has been used for q and d channels.

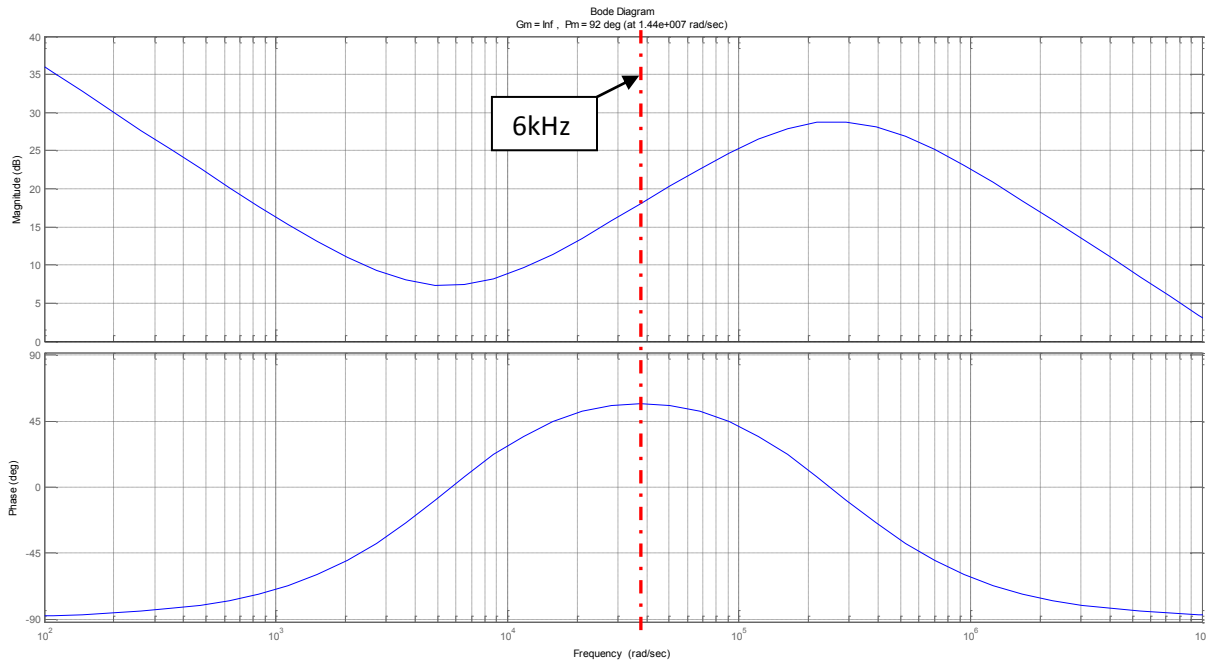


Figure 2.7: Bode diagram of the voltage controller

Fig. 2.8 shows the Bode diagram of the loop transfer function (LTF) (multiplication of the system transfer function under light load condition with the voltage controller transfer function) under light load condition ( $P_{\text{Load}}=0.01\text{kW}$ ).

As it seen shown in Fig. 2.8,  $f_x$  and PM obtained in the LTF are as expected; hence the voltage controller has been well designed. The gain that has been obtained at the switching frequency (-13.2 dB) is large enough to suppress the dominant voltage harmonics. Fig 2.9 shows the bode diagram of the LTF under heavy load condition ( $P_{\text{Load}}=10\text{kW}$ ).

As one can see in Fig. 2.9, the system's cross-over frequency did not vary significantly when the load has been increased, which means that the speed response of the system is about the same under various load conditions. However, the PM has increased making the system dynamics less oscillatory. Moreover,

the gain imposed by the voltage controller at the switching frequency did not change allowing good attenuation of the later under various load conditions.

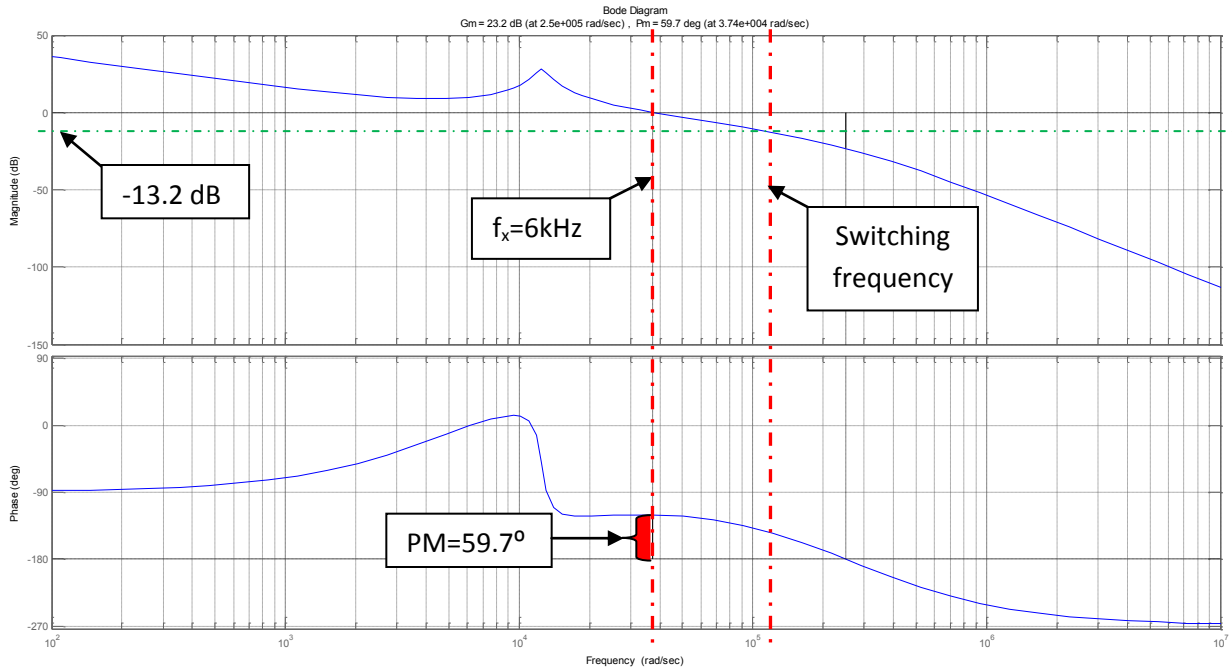


Figure 2.8: Bode diagram of the loop transfer function under light load condition

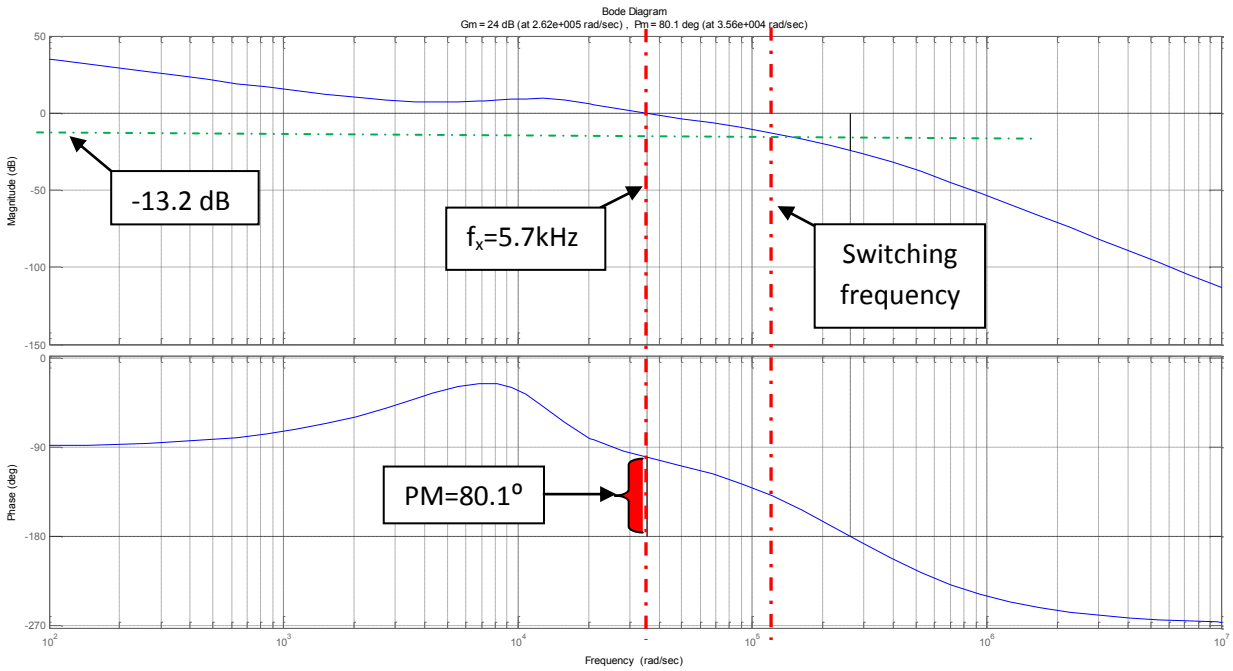


Figure 2.9: Bode diagram of the loop transfer function under heavy load condition

## 2.5 Performance verification

The performance of the inverter has been verified by means of simulations with Simulink/Matlab. The system has been tested under various conditions and perturbations. Note that the ESR of the capacitor " $r_c$ " has been included in the system to verify the inverter's performance when  $r_c$  has been neglected in the inverter's model and voltage controller design. Table 2.5 contains a summary of the system's parameters.

### 2.5.1 Performance of the inverter in steady-state

The inverter should be able to regulate its output voltage when feeding a balanced linear load. As mentioned above the inverter's rating apparent power is 10kVA with a minimum power factor of 0.8. In this section, some simulation results are shown with the inverter feeding an inductive load of  $P_{Load}=8kW$  and  $Q_{Load}=6kVAR$  ( $S_{3ph} = 10$  kVA and PF=0.8 lagging).

Table 2.5: The system parameters

Parameter	Value	Unit
Operating frequency ( $f_{Inv}$ )	60	Hz
Line-to-neutral output voltage " $V_{o,peak}$ "	169.7	V
Apparent power " $S_{3ph}$ "	10	kVA
Minimum power factor	0.8	W/VA
DC bus voltage " $V_{DC}$ "	500	V
LC filter inductor " $L_f$ "	320	uH
ESR of $L_f$ " $r_L$ "	0.5	$\Omega$
LC filter capacitor " $C_f$ "	20	uF
ESR of $C_f$ " $r_C$ "	0.1	$\Omega$
Light load power demand " $P_{Low}$ "	0.01	kW
Heavy load power demand " $P_{High}$ "	10	kW

As one can see in Fig. 2.10-14, the inverter's output voltage has a good sinusoidal shape, the steady-state error is equal to zero, and the Total Voltage Harmonics Distortion (THDv) is very small which has been obtained with Matlab see Fig. 2.13 and 2.14 (THDv=0.2%). This means that the gain (-13.2 dB)

imposed by the voltage controller at the switching frequencies is enough to suppress the later. Note that the same THDv, and a zero steady-state error have been obtained when PF=0.8 leading.

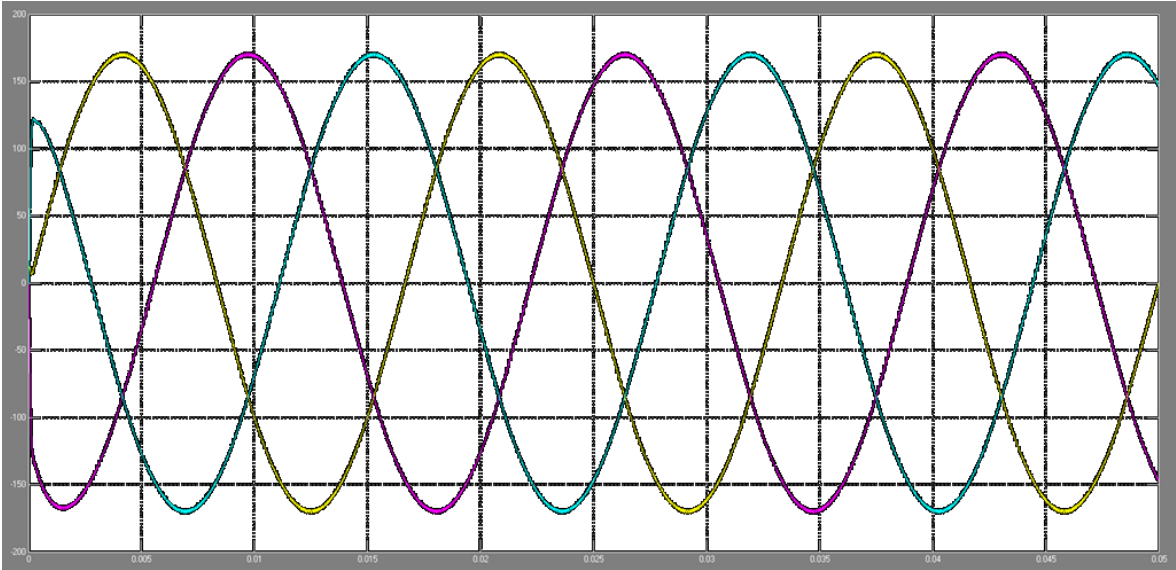


Figure 2.10: Inverter's output voltage when PF=0.8 (lagging) (V) vs. Time (s)

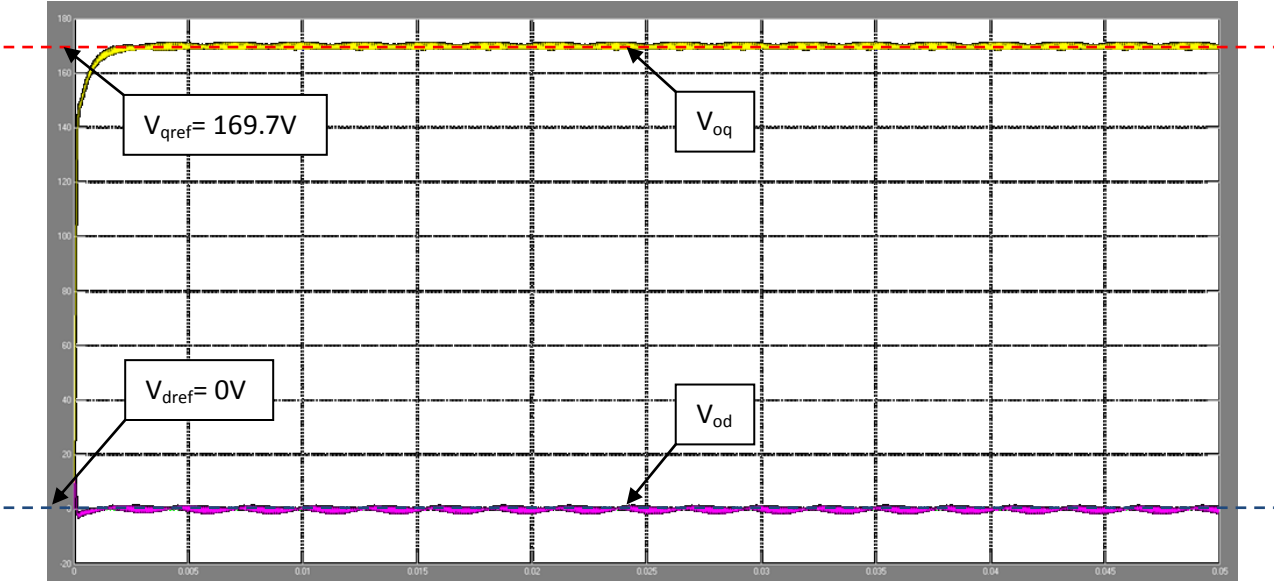


Figure 2.11:  $V_{oq}$  and  $V_{od}$  when PF=0.8 (lagging) (V) vs. Time (s)



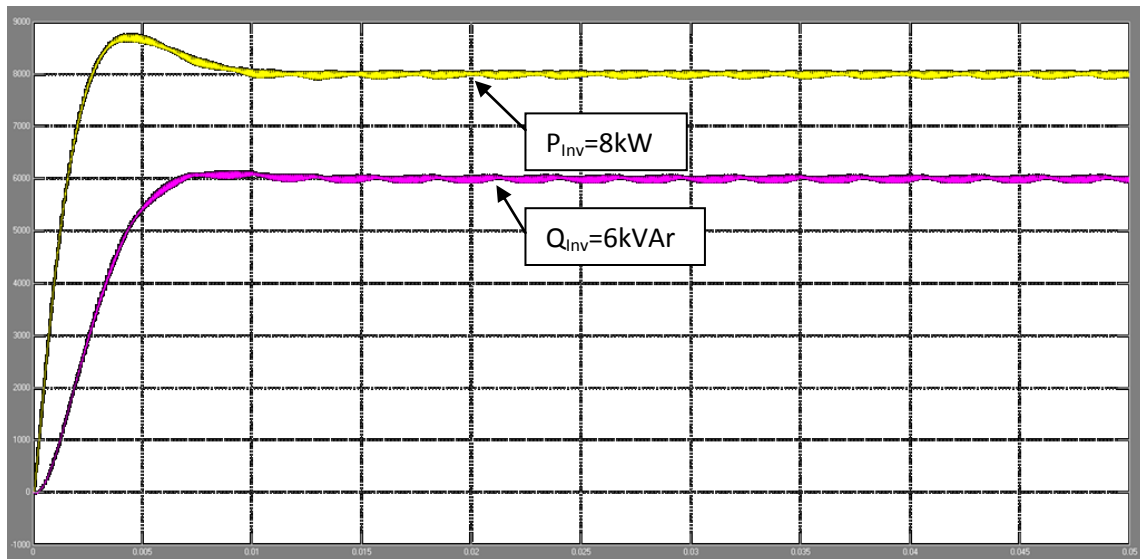


Figure 2.12: Inverter's output active and reactive power (W & VAR) vs. Time (s)

### 2.5.2 Transient response of the inverter

In isolated power systems, also known as mini-grids, AC voltage sources operate with variable voltage magnitude and frequency, and load variations can be very big and frequent. Therefore, the inverter's voltage controller should be able to satisfy those requirements. Table 2.6 describes simulation steps that have been done for the verification of the transient response of the inverter.

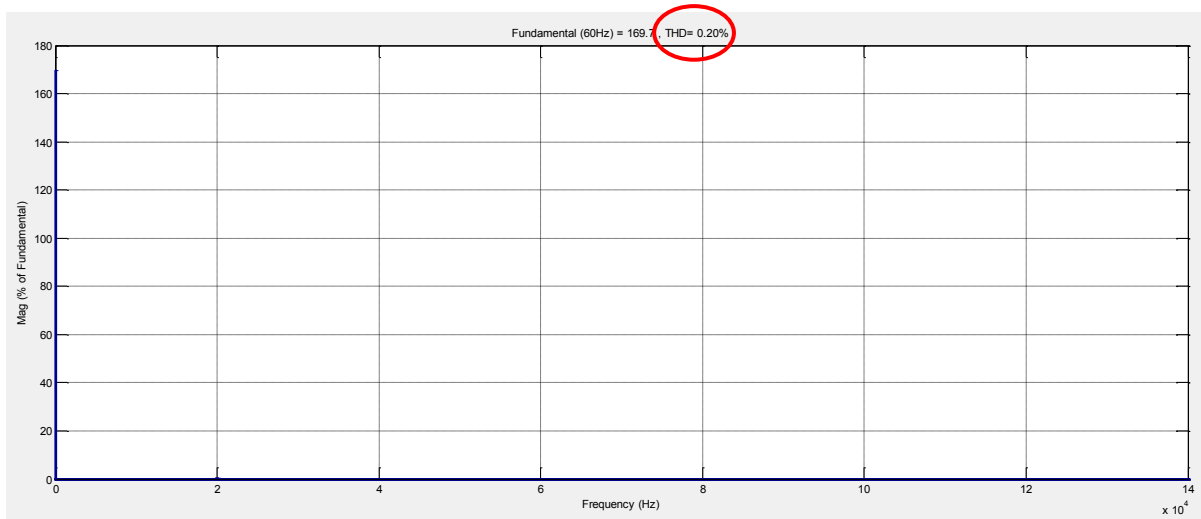


Figure 2.13: FFT of the inverter's output voltage when PF=0.8 (lagging) (V) vs. Frequency (Hz)

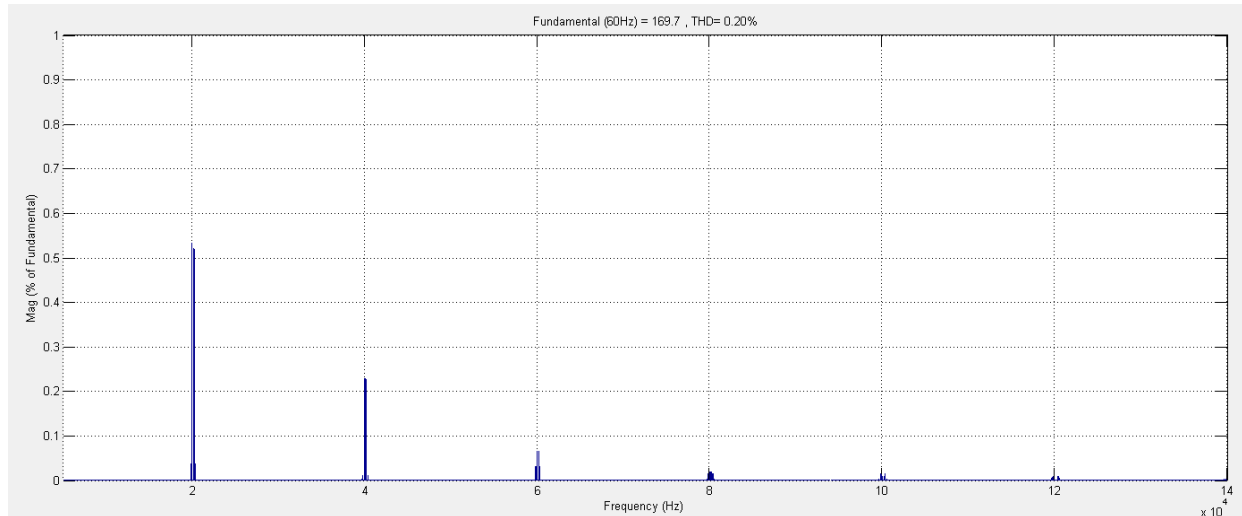


Figure 2.14: Zoom on switching frequency harmonics (From Fig. 2.13) (V) vs. Frequency (Hz)

Table 2.6: Simulation steps for transient response verification when voltage reference and load variations occur

Condition	Time (s)
$P_{Load}=0.01kW, V_{q\_ref}=169.7V$	0
$P_{Load}=0.01kW, V_{q\_ref}=152.7V$	0.05
$P_{Load}=10kW, V_{q\_ref}=152.7V$	0.1
$P_{Load}=10kW, V_{q\_ref}=186.7V$	0.15

From Fig. 2.15 to Fig. 2.21, one can see that the transient response of the inverter is very good in terms of rise time which is very short, and overshoot which is very small. The THDv under light and heavy load conditions is very low (0.28% and 0.21% respectively). Finally, the steady-state error obtained for various conditions is null (see Fig 2.16).

Note that in Fig 2.18 the switching harmonics amplitudes are smaller than in Fig.2.20 yet the THDv in the later is smaller. This is due to the larger voltage reference amplitude used in Fig 2.20 ( $V_{qref}=186.7 V$ ). Noting also that it is this large voltage reference which makes the inverter's output current increase (see Fig. 2.21).

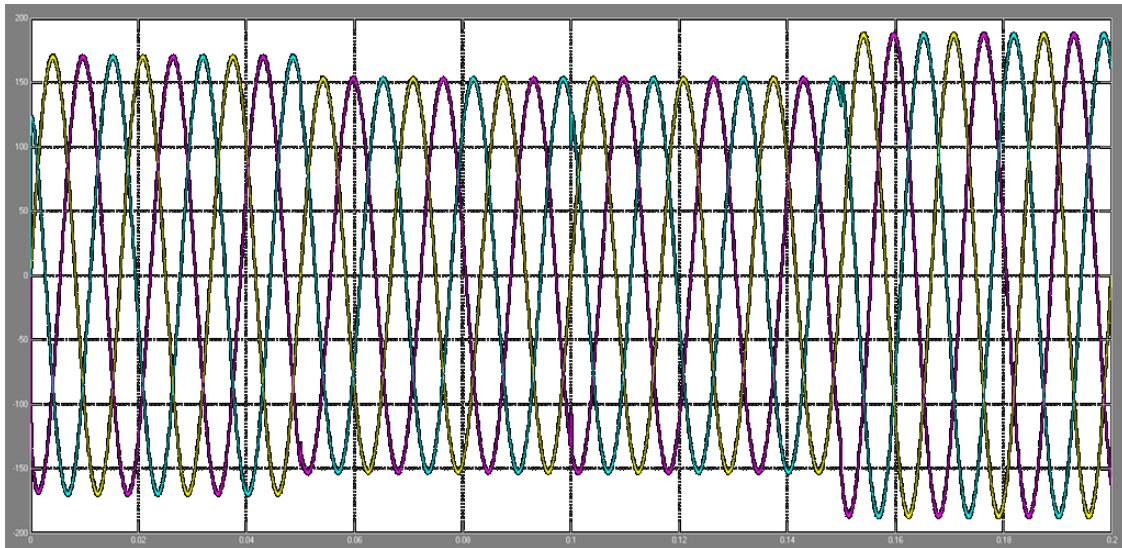


Figure 2.15: Inverter's output voltage under various conditions (V) vs. Time (s)

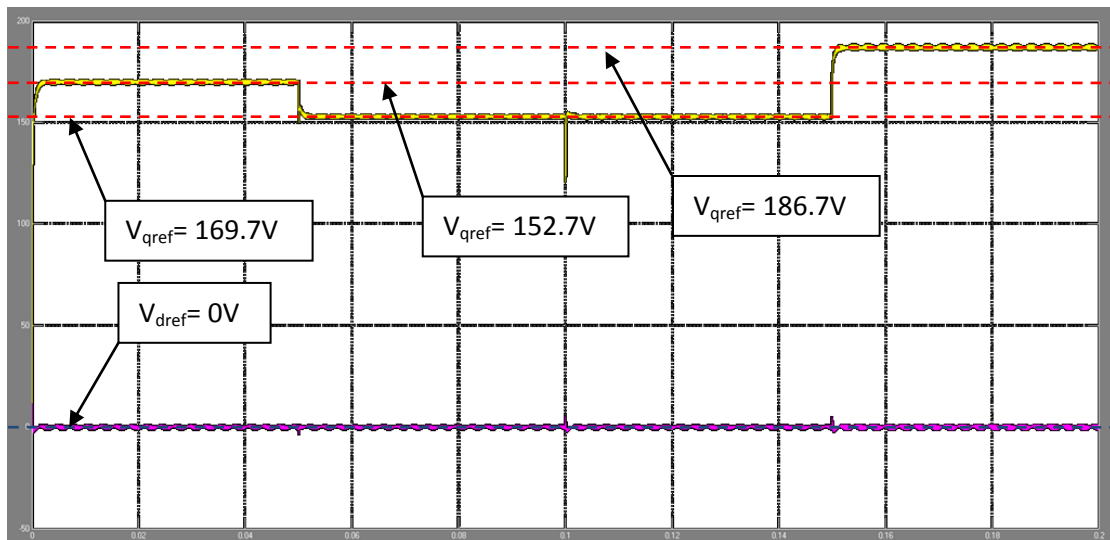


Figure 2.16:  $V_{oq}$  and  $V_{od}$  under various conditions (V) vs. Time (s)

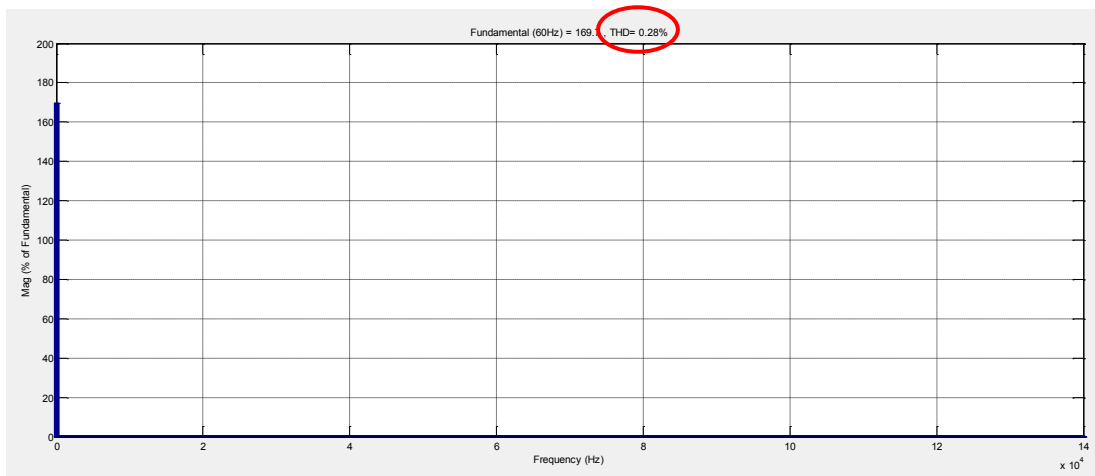


Figure 2.17: FFT of the inverter's output voltage under light load (V) vs. Frequency (Hz)

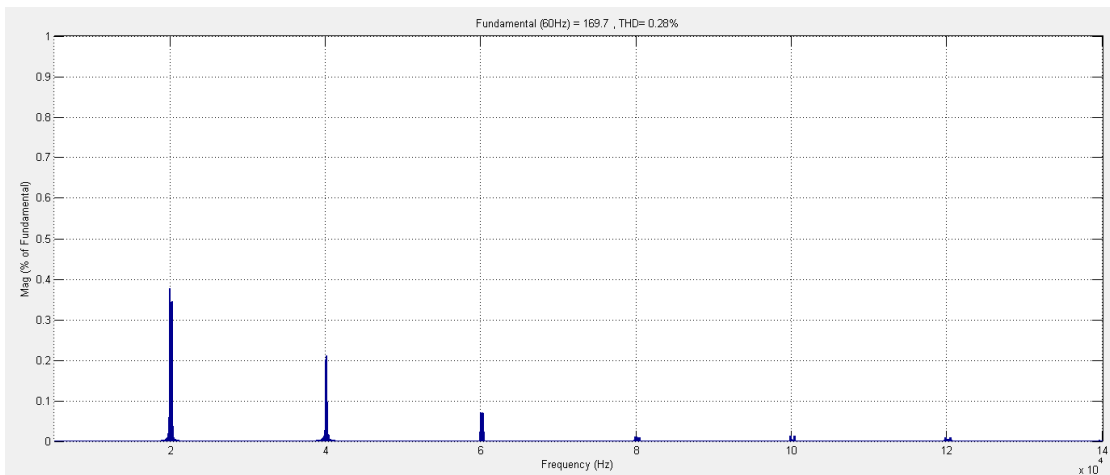


Figure 2.18: Zoom on switching frequency harmonics under light load (From Fig. 2.17) (V) vs. Frequency (Hz)

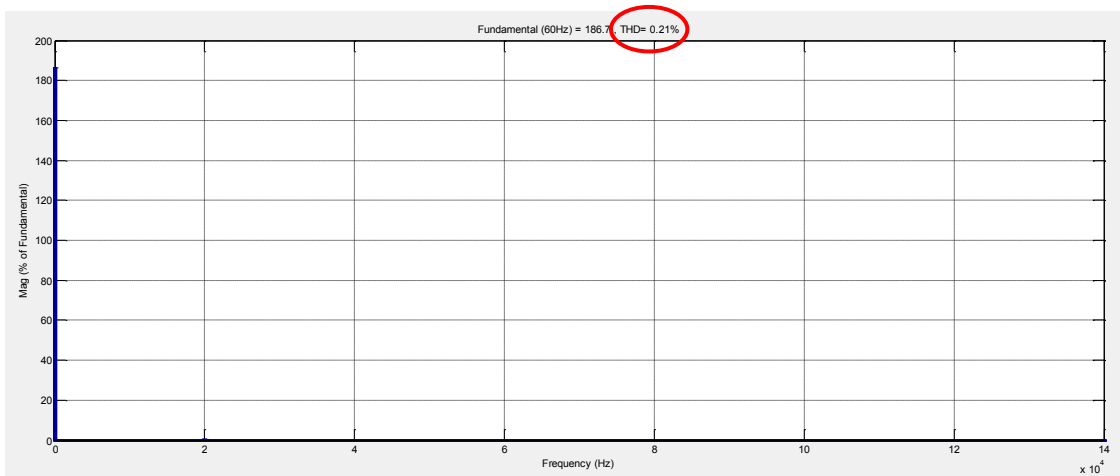


Figure 2.19: FFT of the inverter's output voltage under heavy load (V) vs. Frequency (Hz)

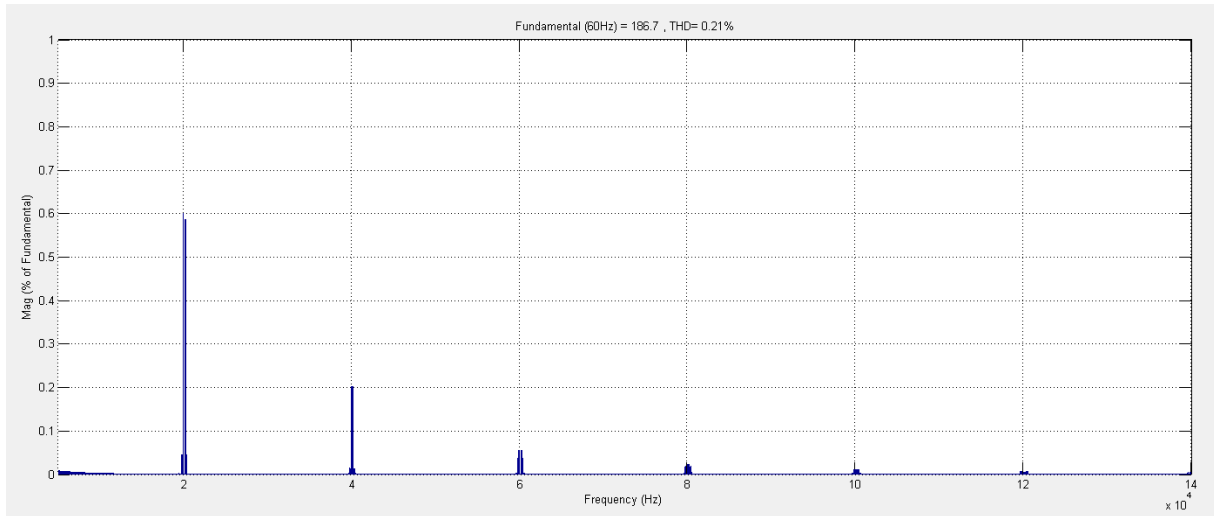


Figure 2.20: Zoom on switching frequency harmonics under light load (From Fig. 2.19) (V) vs. Frequency (Hz)

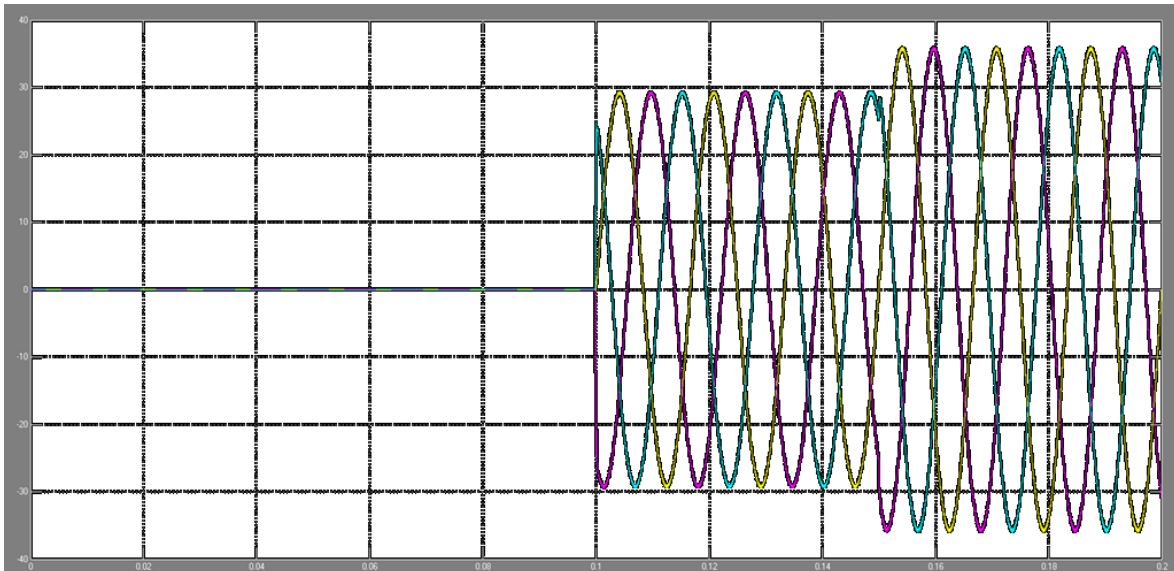


Figure 2.21: Inverter's output current (A) vs. Time (s)

As mentioned before, the voltage source inverter has to be able to operate with variable frequency when sharing loads with other paralleled AC voltage sources. To verify this, a simulation has been done using Simulink/Matlab. Table 2.7 describes the simulation steps.

Table 2.7: Simulation steps for transient response verification when voltage reference and load variations occur

Condition	Time (s)
$P_{Load}=5kW$ ; $V_{qref}=169.7V$ ; $f_{ref}=62Hz$	0
$P_{Load}=5kW$ ; $V_{qref}=169.7V$ ; $f_{ref}=58Hz$	0.5
$P_{Load}=5kW$ ; $V_{qref}=169.7V$ ; $f_{ref}=60Hz$	1

The inverter's operating frequency has been measured by the three-phase phase-locked loop system (*PLL*). Note that the latter has a variable measurement delay as it is shown in Fig. 2.22.

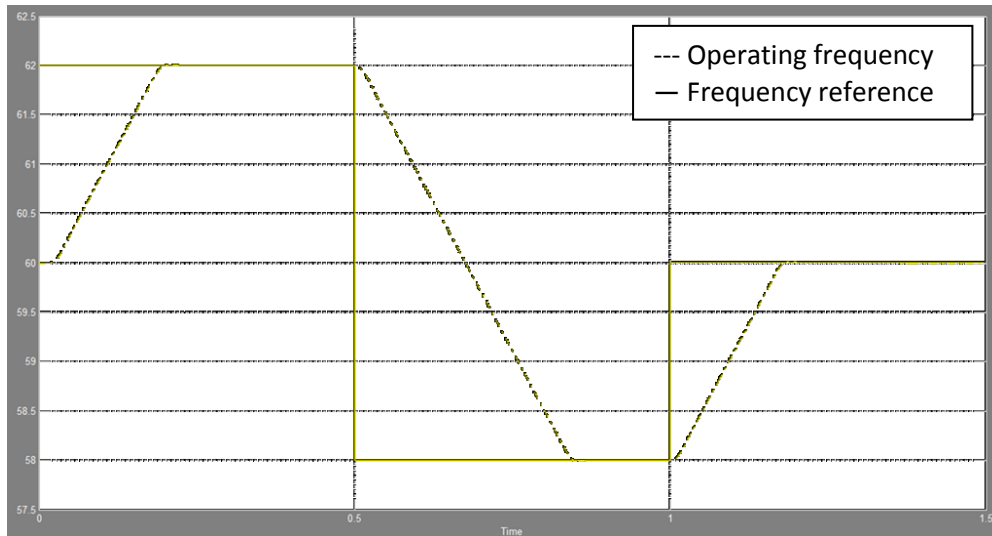


Figure 2.22: Inverter's operating frequency (Hz) vs. Time (s)

In order to see the effect of varying the operating frequency on the inverter's output voltage waveform, Fig. 2.23 shows the latter. The same simulation steps listed in Table 2.7 have been used. However, the time intervals are divided by ten in order to decrease the number of cycles by interval. As one can see in Fig. 2.23, the inverter is robust enough to handle the variations in its operating frequency.

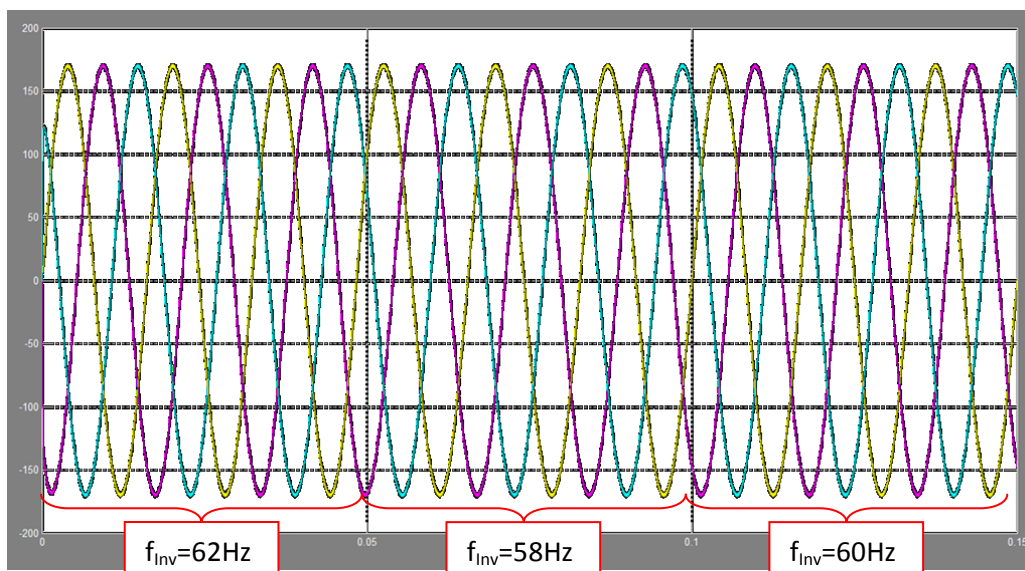


Figure 2.23: Inverter's output voltage when the operating frequency varies (V) vs. Time (s)

## 2.6 Conclusion

This chapter presented the analysis, modeling and design of a three-phase voltage source inverter operating with dq control and linear carrier based SPWM, what is required for interfacing power sources and energy storage units to a distribution grid. The choice of dq control was due to the possibility of having zero output voltage error in the steady state using a simple PI type controller. The performance of the inverter operating at stand-alone and feeding a variable linear balanced load was verified by means of simulation. Its output voltage presented good power quality, with low THDv for both minimum and rated load conditions, much lower than the 5% maximum THDv recommended by the IEEE standards [2]. It also presented good transient response for load and output voltage reference variations (in amplitude and frequency).

In the next chapters, this inverter equipped with droop-base active and reactive power control loops will be connected to other components commonly found in distribution power systems with renewable power sources and energy storage units.

# **Chapter 3 - Parallel operation of a droop controlled three-phase voltage source inverter with a stiff grid**

## **3.1 Introduction**

This chapter focuses on the operation of a droop controlled inverter connected to a stiff grid, that is, a bus where the magnitude and frequency of the voltage are essentially constant. The main blocks required for the implementation of the droop controllers in a three-phase inverter are described in details, including their Simulink realizations. Then a complete small-signal model of the system, including the droop loops and the impedance of the feeder through which the inverter is connected to the stiff grid, is presented. It is used for analyzing by means of root locus of the system to various system parameters. Finally, time domain simulations in Simulink/Matlab are done to verify the results obtained in frequency domain analysis.

## **3.2 P vs. f and Q vs. V droop loops implementation**

The implementation of the droop controllers in the inverter's control loop is shown in Fig. 3.1. The inverter presents an output LC filter and a local load and connected in parallel to the grid by a feeder. As the inverter's output voltage is regulated using dq control technique, the voltage references in dq are obtained from the "Voltage Reference Generator" block which converts the voltage and frequency references from droop controllers to three-phase balanced signal. Then these voltage references in dq



are compared to the dq voltage across the filter capacitors ( $V_{oabc}$ ). Note that the low-pass filter is used to filter the instantaneous P and Q and to slow down their variations.

From Eq. 1.6 and 1.7, the voltage and frequency references for the voltage controller (see Fig 2.6) have been calculated from the filtered inverter's output active and reactive power. These equations could be written as follows;

$$P = \frac{\omega_{nL} - \omega_{ref}}{m_p} \quad (3.1)$$

$$Q = \frac{V_{nL} - V_{ref}}{n_q} \quad (3.2)$$

One could get from Eq. 3.1 and 3.2 that the active and reactive power can be controlled (increased or decreased) by varying the no-load frequency and voltage ( $\omega_{nL}$  and  $V_{nL}$ ) respectively. This point could be very beneficial and interesting for the case when a droop controlled voltage source inverter, having a DC source as battery banks or renewable energy sources, operates in parallel with a grid. The element  $\omega_{nL}$  could be used to control the inverter's output voltage in order to charge or discharge the battery banks, or to make the inverter providing continuously the maximum power available from the renewable energy sources (e.g. MPPT for a photovoltaic source). Note that in this chapter only the system dynamics and steady-states will be investigated.

The block that calculates the instantaneous active and reactive power uses the Eq. 3.3 and 3.4 applied to the inverter's output voltage and current ( $V_{oabc}$  and  $I_{oabc}$ ).

$$P_{Inv} + \tilde{p}_{Inv} = V_{oa}I_{oa} + V_{ob}I_{ob} + V_{oc}I_{oc} \quad (3.3)$$

$$Q_{Inv} + \tilde{q}_{Inv} = \frac{1}{\sqrt{3}} [(V_{ob} - V_{oc})I_{oa} + (V_{oc} - V_{oa})I_{ob} + (V_{oa} - V_{ob})I_{oc}] \quad (3.4)$$

Where,  $\tilde{p}_{inv}$  and  $\tilde{q}_{inv}$  are the active and reactive power ripples respectively. Note that the non-linear loads are not taken into consideration in this thesis.

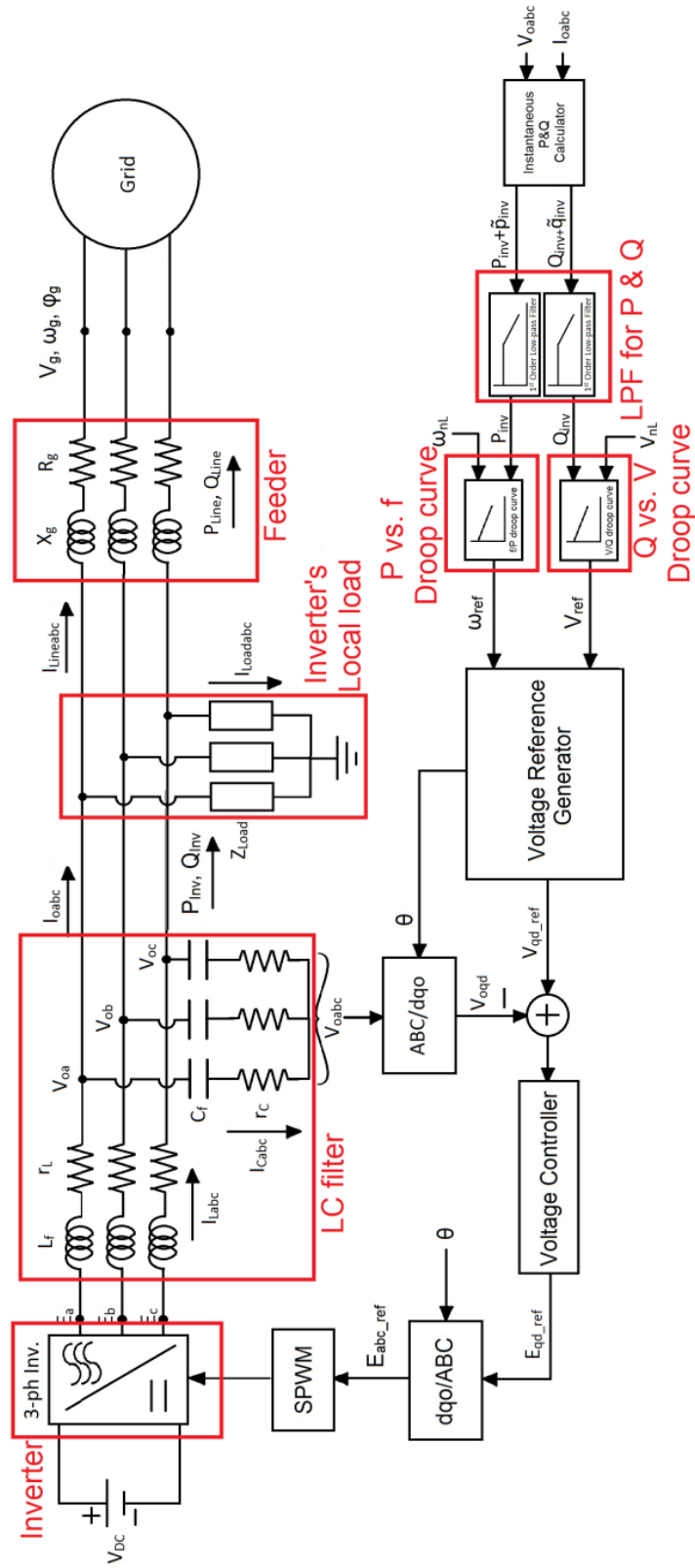


Figure 3.1: Parallel three-phase voltage source inverter and stiff grid

The droop controller blocks in Fig. 3.1 labeled by “P vs.  $f$  droop curve” and “Q vs.  $V$  droop curve” ensure the tracking of the requested active and reactive power when the inverter is connected in parallel to a grid with fixed and known values of  $f$  and  $V$  by adjusting  $\omega_{nL}$  and  $V_{nL}$ . However, in isolated mini-grid the inverter will share the demanded power with other DGs [11].

The low-pass filter (*LPF*) is required to filter the active and reactive power since the inverter’s control loops (Voltage control loop and droop control loop) are implemented in parallel; hence the outer loop which is the droop control loop has to be slower than the inner loop (Voltage control loop). Therefore, a LPF has been used to slow down active and reactive power measurements which provide references to the inner loop. The cut-off frequency value of the LPF is investigated in this chapter.

### 3.3 Small-signal model

The small signal analysis technique is used in this chapter in order to evaluate the system stability. This technique is based on finding eigenvalues of linearized equations of the system. The frequency domain results obtained by this technique are verified by time domain simulations using Simulink/Matlab.

The idea behind this modeling is to see the effect of every element (LC filter, voltage controller, power controller, LPF, line impedance, etc) on the system stability. Finding the conditions for which the line impedance current presents good transient and steady-state responses are the main objectives of this study.

The system shown in Fig 3.1 is modeled in dq coordinates. Assuming that the grid’s voltage and frequency are fixed, and its phase is always at zero. Eq. 3.7 shows the grid’s parameters.

$$V_{gq} = 169.7 \text{ V}; \quad V_{gd} = 0 \text{ V}; \quad \text{and } \omega_g = 377 \frac{\text{rad}}{\text{s}} \quad (3.5)$$

Fig. 3.2 shows the block diagram of the system model in dq coordinates. The line current is calculated from two elements; the grid and the inverter output voltage amplitudes. Where, the first one is fixed but the second element depends on the phase angle ( $\delta$ ) between the two reference frames as shown in Fig. 3.3. The grid and the inverter output voltages have to be on the same reference frame to allow generating the line currents.

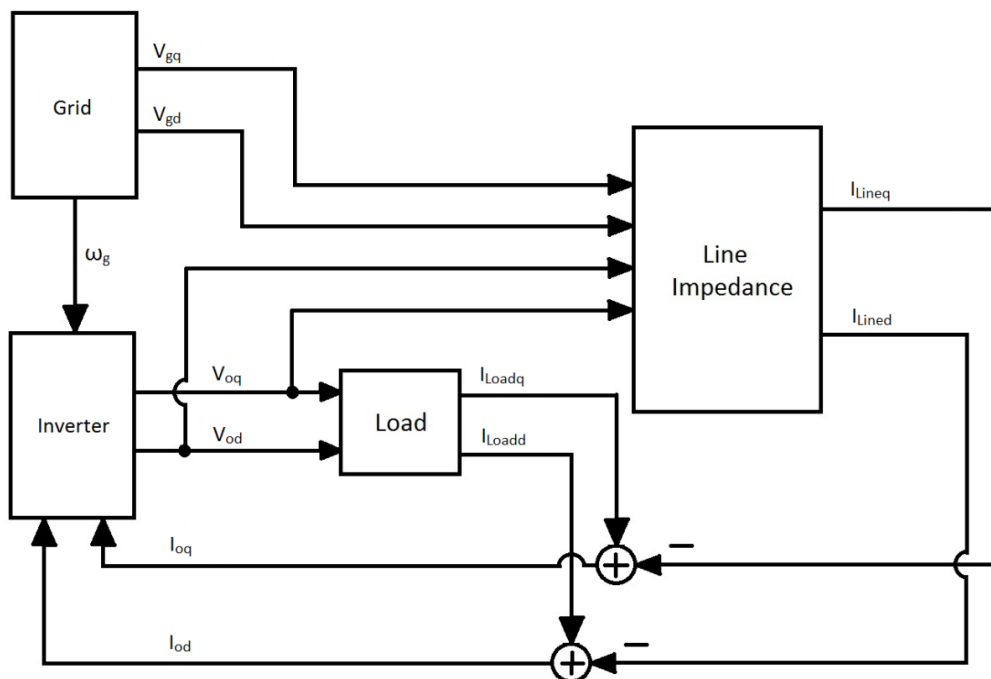


Figure 3.2: Bloc diagram of parallel grid and inverter in dq coordinates

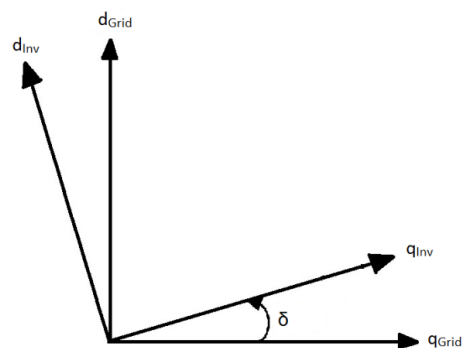


Figure 3.3: Reference frames of the grid and the inverter

The “Inverter” block in Fig. 3.2 is shown in details in Fig. 3.4. The blocks “Line Impedance” and “Load” in Fig. 3.2, and “P & Q calculator”, “1<sup>st</sup> Order LPF”, “Droop curves”, “Voltage reference generator” and “LC filter” in Fig 3.4 contain the appropriate equations that are derived below.

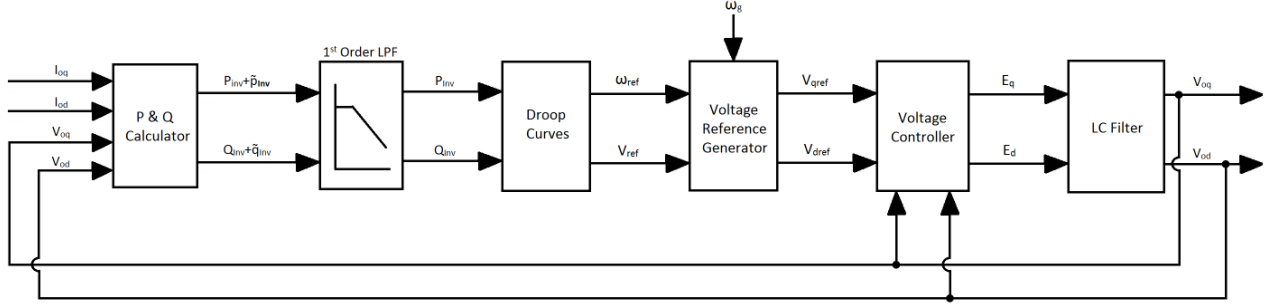


Figure 3.4: Inverter's bloc diagram

The inverter's instantaneous output active and reactive powers are calculated using the following equations;

$$P_{Inv} = \frac{\omega_c}{s + \omega_c} \times \frac{3}{2} (V_{oq} I_{oq} + V_{od} I_{od}) \quad (3.6)$$

$$Q_{Inv} = \frac{\omega_c}{s + \omega_c} \times \frac{3}{2} (V_{od} I_{oq} - V_{oq} I_{od}) \quad (3.7)$$

Where,  $\omega_c$  is the cut-off frequency of the Low-Pass Filter used to measure the active and reactive power.

The small-signal terms of Eq. 3.6 and 3.7 are given by the following equations;

$$\Delta \dot{P}_{Inv} = -\omega_c \Delta P_{Inv} + \frac{3}{2} \omega_c (V_{oq0} \Delta I_{oq} + I_{oq0} \Delta V_{oq} + V_{od0} \Delta I_{od} + I_{od0} \Delta V_{od}) \quad (3.8)$$

$$\Delta \dot{Q}_{Inv} = -\omega_c \Delta Q_{Inv} + \frac{3}{2} \omega_c (V_{od0} \Delta I_{oq} + I_{oq0} \Delta V_{od} - V_{oq0} \Delta I_{od} - I_{od0} \Delta V_{oq}) \quad (3.9)$$

The terms;  $V_{oq0}$ ,  $V_{od0}$ ,  $I_{oq0}$  and  $I_{od0}$  are the initial values which are calculated using Simulink/Matlab.

The droop equations described by Eq. 1.6 and 1.7 are now reduced, using linearization process, to the following;

$$\Delta\omega_{ref} = -m_p\Delta P_{Inv} \quad (3.10)$$

$$\Delta V_{ref} = -n_q\Delta Q_{Inv} \quad (3.12)$$

The angle  $\delta$  equation for this case is given by Eq. 3.13.

$$\delta = \int (\omega_{Inv} - \omega_g) dt \quad (3.13)$$

The operating angular frequency of the inverter ( $\omega_{inv}$ ) can be replaced by the angular frequency ( $\omega_{ref}$ ) obtained from the droop equation since the latter is not delayed. The small signal of the angle  $\delta$  is given by the following equation;

$$\dot{\Delta\delta} = \Delta\omega_{ref} - \Delta\omega_g \quad (3.14)$$

Since the grid's frequency is fixed, Eq. 3.15 is reduced to Eq.15.

$$\dot{\Delta\delta} = \Delta\omega_{ref} = -m_p\Delta P_{Inv} \quad (3.15)$$

Based on Fig. 3.3, the voltage reference values for the inverter calculated on the grid reference frame are given by the following matrix.

$$\begin{bmatrix} V_{qrefcom} \\ V_{drefcom} \end{bmatrix} = \begin{bmatrix} \cos\delta & -\sin\delta \\ \sin\delta & \cos\delta \end{bmatrix} \begin{bmatrix} V_{qref} \\ V_{dref} \end{bmatrix} \quad (3.16)$$

Where,  $V_{qrefcom}$  and  $V_{drefcom}$  are the inverter's voltage references projected on the grid's reference frame (The common reference frame). The small signal of Eq. 3.16 is given by Eq. 3.17.

$$\begin{bmatrix} \Delta V_{qrefcom} \\ \Delta V_{drefcom} \end{bmatrix} = \begin{bmatrix} \cos\delta_o & -\sin\delta_o \\ \sin\delta_o & \cos\delta_o \end{bmatrix} \begin{bmatrix} \Delta V_{qref} \\ \Delta V_{dref} \end{bmatrix} + \begin{bmatrix} -V_{qrefo}\sin\delta_o - V_{drefo}\cos\delta_o \\ V_{qrefo}\cos\delta_o - V_{drefo}\sin\delta_o \end{bmatrix} [\Delta\delta] \quad (3.17)$$

Where,  $V_{qrefo}$ ,  $V_{drefo}$  and  $\delta_o$  are the initial values. From Eq. 3.12, the Eq. 3.17 is now written as given by Eq. 3.19. Note that the voltage references for the inverter on its own reference frame are  $V_{qref}=169.7V$  and  $V_{dref}=0V$ .

$$\begin{bmatrix} \Delta V_{qrefcom} \\ \Delta V_{drefcom} \end{bmatrix} = \begin{bmatrix} -n_q \cos \delta_o \\ -n_q \sin \delta_o \end{bmatrix} [\Delta Q_{Inv}] + \begin{bmatrix} -V_{qrefo} \sin \delta_o - V_{drefo} \cos \delta_o \\ V_{qrefo} \cos \delta_o - V_{drefo} \sin \delta_o \end{bmatrix} [\Delta \delta] \quad (3.19)$$

As mentioned in Chapter 2, the voltage controller which has been used is a PI type-3 controller whose transfer function is given by the following equation.

$$G_{PI3}(s) = \frac{K_{pi} (\tau s + 1)^2}{\tau s (T_p s + 1)^2} \quad (3.20)$$

The voltage controller has two inputs and one output as Fig. 3.5 shows. Note that the same voltage controller has been used for q and d channels.

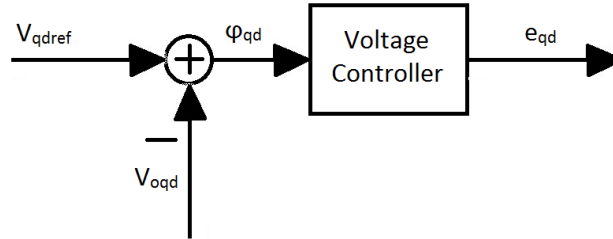


Figure 3.5: Inverter's voltage control loop

Where,  $\varphi_{qd}$  is the error between the voltage reference and the measured output voltage, and  $e_{qd}$  is the command to the inverter's gates.

From Fig. 3.5, one can get the following equation;

$$e_{qd} = \frac{K_{pi} (\tau s + 1)^2}{\tau s (T_p s + 1)^2} \varphi_{qd} \quad (3.21)$$

Developing Eq. 3.21, one gets the following;

$$\tau T_p^2 \ddot{e}_{qd} + 2\tau T_p \dot{e}_{qd} + \tau e_{qd} = K_{pi} \tau^2 \ddot{\varphi}_{qd} + 2\tau K_{pi} \dot{\varphi}_{qd} + K_{pi} \varphi_{qd} \quad (3.22)$$

Hence,

$$\ddot{e}_{qd} = -\frac{2}{T_p} \dot{e}_{qd} - \frac{1}{T_p^2} e_{qd} + \frac{K_{pi}\tau}{T_p^2} \dot{\varphi}_{qd} + \frac{2K_{pi}}{T_p^2} \varphi_{qd} + \frac{K_{pi}}{\tau T_p^2} \varphi_{qd} \quad (3.23)$$

Then, the small-signal model of the voltage controller is given by Eq. 3.24.

$$\Delta \ddot{e}_{qd} = -\frac{2}{T_p} \Delta \dot{e}_{qd} - \frac{1}{T_p^2} \Delta e_{qd} + \frac{K_{pi}\tau}{T_p^2} \Delta \dot{\varphi}_{qd} + \frac{2K_{pi}}{T_p^2} \Delta \varphi_{qd} + \frac{K_{pi}}{\tau T_p^2} \Delta \varphi_{qd} \quad (3.24)$$

The next step is to model the LC filter by linearizing the inductor current and the capacitor voltage. The equivalent circuit of the three-phase LC filter in dq coordinates (including the load impedance and Line current) is illustrated in Fig. 3.6.

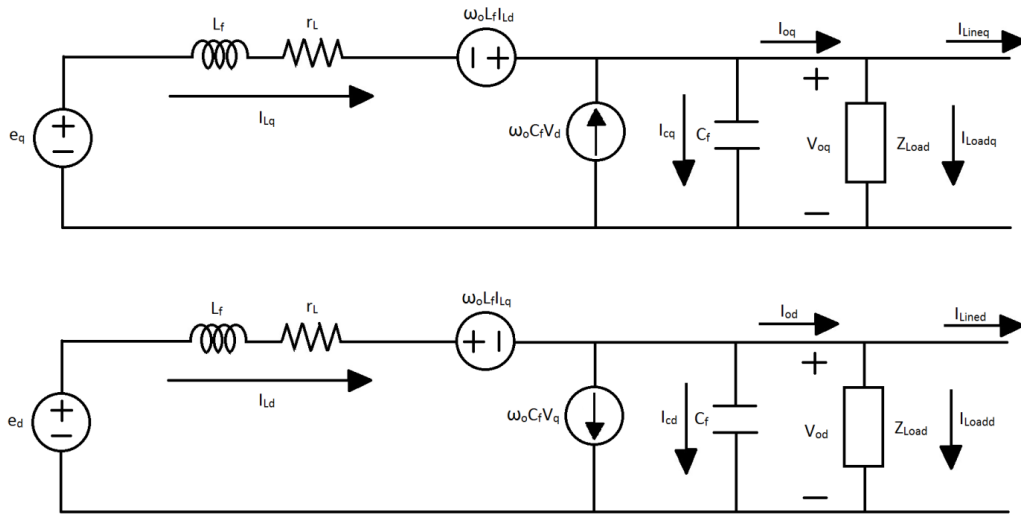


Figure 3.6: dq equivalent circuit of a three-phase LC filter including local load

From Fig 3.10, the following equations of filter inductor current and filter capacitor voltage in dq coordinates can be derived.

From voltage loops,

$$\frac{di_{Lq}}{dt} = \frac{1}{L_f} e_q - \frac{r_L}{L_f} i_{Lq} + \omega_o i_{Ld} - v_{oq} \quad (3.25)$$

$$\frac{di_{Ld}}{dt} = \frac{1}{L_f} e_d - \frac{r_L}{L_f} i_{Ld} - \omega_o i_{Lq} - v_{od} \quad (3.26)$$

And from current nodes,



$$\frac{dv_{oq}}{dt} = \frac{1}{C_f} i_{Lq} - \frac{1}{C_f} i_{oq} + \omega_o v_{od} \quad (3.27)$$

$$\frac{dv_{od}}{dt} = \frac{1}{C_f} i_{Ld} - \frac{1}{C_f} i_{od} - \omega_o v_{oq} \quad (3.28)$$

The small-signal model of the LC filter is then given by;

$$\Delta \dot{I}_{Lq} = \frac{1}{L_f} \Delta E_q - \frac{r_L}{L_f} \Delta I_{Lq} + \omega_o \Delta I_{Ld} - \Delta V_{oq} \quad (3.29)$$

$$\Delta \dot{I}_{Ld} = \frac{1}{L_f} \Delta E_d - \frac{r_L}{L_f} \Delta I_{Ld} - \omega_o \Delta I_{Lq} - \Delta V_{od} \quad (3.30)$$

And,

$$\Delta \dot{V}_{oq} = \frac{1}{C_f} \Delta I_{Lq} - \frac{1}{C_f} \Delta I_{oq} + \omega_o \Delta V_{od} \quad (3.31)$$

$$\Delta \dot{V}_{od} = \frac{1}{C_f} \Delta I_{Ld} - \frac{1}{C_f} \Delta I_{od} - \omega_o \Delta V_{oq} \quad (3.32)$$

The dq equivalent circuit of an inductive load is shown in the next figure.

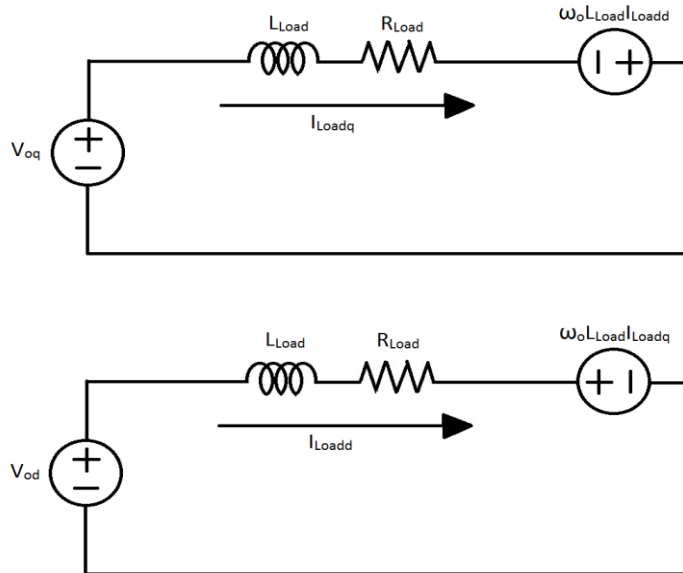


Figure 3.7: dq equivalent circuit of an inductive load

Where,  $R_{Load}$  and  $L_{Load}$  are the resistive and inductive components of the load impedance ( $Z_{Load}$ ) respectively. The inductive load current is then calculated by the following equations;

$$\frac{di_{Loadq}}{dt} = \frac{1}{L_{Load}} v_{oq} + \omega_o i_{Loadd} - \frac{R_{Load}}{L_{Load}} i_{Loadq} \quad (3.33)$$

$$\frac{di_{Loadd}}{dt} = \frac{1}{L_{Load}} v_{od} - \omega_o i_{Loadq} - \frac{R_{Load}}{L_{Load}} i_{Loadd} \quad (3.34)$$

Hence the small-signal model of the inductive load current is given by Eq. 3.35 and 3.36.

$$\Delta I_{Loadq} \dot{\phantom{I}} = \frac{1}{L_{Load}} \Delta V_{oq} + \omega_o \Delta I_{Loadd} - \frac{R_{Load}}{L_{Load}} \Delta I_{Loadq} \quad (3.35)$$

$$\Delta I_{Loadd} \dot{\phantom{I}} = \frac{1}{L_{Load}} \Delta V_{od} - \omega_o \Delta I_{Loadq} - \frac{R_{Load}}{L_{Load}} \Delta I_{Loadd} \quad (3.36)$$

Finally, the line impedance dq equivalent circuit is shown in Fig. 3.8.

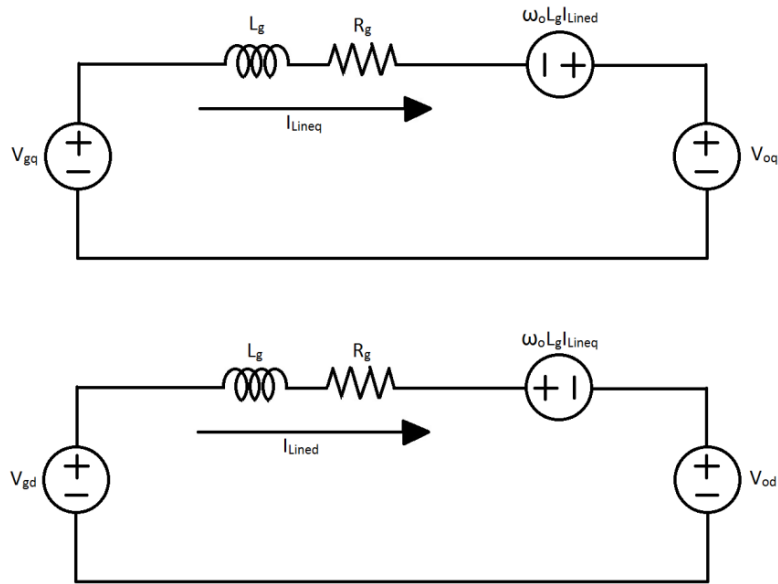


Figure 3.8: dq equivalent circuit of the line impedance

The line impedance current is given by;

$$\frac{di_{Lineq}}{dt} = \frac{1}{L_g} v_{gq} + \omega_o i_{Lined} - \frac{R_g}{L_g} i_{Lineq} - \frac{1}{L_g} v_{oq} \quad (3.37)$$

$$\frac{di_{Lined}}{dt} = \frac{1}{L_g} v_{gd} - \omega_o i_{Lineq} - \frac{R_g}{L_g} i_{Lined} - \frac{1}{L_g} v_{od} \quad (3.38)$$

Then, the small-signal equations of the line impedance current are given by the following;

$$\Delta \dot{I}_{Lineq} = \omega_o \Delta I_{Lined} - \frac{R_g}{L_g} \Delta I_{Lineq} - \frac{1}{L_g} \Delta V_{oq} \quad (3.39)$$

$$\Delta \dot{I}_{Lined} = -\omega_o \Delta I_{Lineq} - \frac{R_g}{L_g} \Delta I_{Lined} - \frac{1}{L_g} \Delta V_{od} \quad (3.40)$$

Each block of the system, shown in Fig. 3.2 and 3.4, is now modeled. Therefore, in order to study the system stability in the frequency domain, one needs to link all the small-signal equations of the system in one matrix. Therefore, state-space modeling is needed. From all the small-signal equations (Eq. 3.8, 3.9, 3.10, 3.19, 3.24, 3.29, 3.30, 3.31, 3.32, 3.35, 3.36, 3.39 and 3.40), the state-space matrices of the system are given by the followings;

The state-space matrices of the droop controller's model are as follows.

$$\begin{bmatrix} \Delta \dot{\delta} \\ \Delta \dot{P}_{Inv} \\ \Delta \dot{Q}_{Inv} \end{bmatrix} = A_{PQ} \begin{bmatrix} \Delta \delta \\ \Delta P_{Inv} \\ \Delta Q_{Inv} \end{bmatrix} + B_{PQ} \begin{bmatrix} \Delta V_{oq} \\ \Delta V_{od} \\ \Delta I_{Loadq} \\ \Delta I_{Loadd} \\ \Delta I_{Lineq} \\ \Delta I_{Lined} \end{bmatrix} \quad (3.41)$$

And,

$$\begin{bmatrix} \Delta V_{qrefcom} \\ \Delta V_{drefcom} \end{bmatrix} = C_{PQ} \begin{bmatrix} \Delta \delta \\ \Delta P_{Inv} \\ \Delta Q_{Inv} \end{bmatrix} + D_{PQ} \begin{bmatrix} \Delta V_{oq} \\ \Delta V_{od} \\ \Delta I_{Loadq} \\ \Delta I_{Loadd} \\ \Delta I_{Lineq} \\ \Delta I_{Lined} \end{bmatrix} \quad (3.42)$$

Where,  $\Delta V_{oq}$ ,  $\Delta V_{od}$ ,  $\Delta I_{Loadq}$ ,  $\Delta I_{Loadd}$ ,  $\Delta I_{Lineq}$  and  $\Delta I_{Lined}$  are the inputs and  $\Delta V_{qrefcom}$  and  $\Delta V_{drefcom}$  are the outputs of the droop controller. The state-space matrices are defined by the followings;

$$A_{PQ} = \begin{bmatrix} 0 & -m_p & 0 \\ 0 & -\omega_c & 0 \\ 0 & 0 & -\omega_c \end{bmatrix} \quad (3.43)$$

$$B_{PQ} = \frac{3}{2} \omega_c \begin{bmatrix} 0 & 0 & 0 & 0 & 0 & 0 \\ (I_{Loadqo} - I_{Lineqo}) & (I_{Loaddo} - I_{Linedo}) & V_{oqo} & V_{odo} & -V_{oqo} & -V_{odo} \\ -(I_{Loaddo} - I_{Linedo}) & (I_{Loadqo} - I_{Lineqo}) & V_{odo} & -V_{oqo} & -V_{odo} & V_{oqo} \end{bmatrix} \quad (3.44)$$

$$C_{PQ} = \begin{bmatrix} -V_{qrefo} \sin \delta_o - V_{drefo} \cos \delta_o & 0 & -n_q \cos \delta_o \\ V_{qrefo} \cos \delta_o - V_{drefo} \sin \delta_o & 0 & -n_q \sin \delta_o \end{bmatrix} \quad (3.45)$$

$$D_{PQ} = \begin{bmatrix} 0 & 0 & 0 & 0 & 0 & 0 \\ 0 & 0 & 0 & 0 & 0 & 0 \\ 0 & 0 & 0 & 0 & 0 & 0 \end{bmatrix} \quad (3.46)$$

From Eq. 3.24, the voltage controller's state-space matrices are given by;

$$\begin{bmatrix} \Delta \ddot{\varphi}_q \\ \Delta \dot{\varphi}_q \\ \Delta \varphi_q \\ \Delta \ddot{\varphi}_d \\ \Delta \dot{\varphi}_d \\ \Delta \varphi_d \end{bmatrix} = A_{PI3} \begin{bmatrix} \Delta \ddot{\varphi}_q \\ \Delta \dot{\varphi}_q \\ \Delta \varphi_q \\ \Delta \ddot{\varphi}_d \\ \Delta \dot{\varphi}_d \\ \Delta \varphi_d \end{bmatrix} + B_{PI3} \begin{bmatrix} \Delta V_{qrefcom} \\ \Delta V_{drefcom} \\ \Delta V_{oq} \\ \Delta V_{od} \end{bmatrix} \quad (3.47)$$

And,

$$\begin{bmatrix} \Delta e_q \\ \Delta e_d \end{bmatrix} = C_{PI3} \begin{bmatrix} \Delta \ddot{\varphi}_q \\ \Delta \dot{\varphi}_q \\ \Delta \varphi_q \\ \Delta \ddot{\varphi}_d \\ \Delta \dot{\varphi}_d \\ \Delta \varphi_d \end{bmatrix} + D_{PI3} \begin{bmatrix} \Delta V_{qrefcom} \\ \Delta V_{drefcom} \\ \Delta V_{oq} \\ \Delta V_{od} \end{bmatrix} \quad (3.48)$$

Where,

$$A_{PI3} = \begin{bmatrix} -2/T_p & -1/T_p^2 & 0 & 0 & 0 & 0 \\ 1 & 0 & 0 & 0 & 0 & 0 \\ 0 & 1 & 0 & 0 & 0 & 0 \\ 0 & 0 & 0 & -2/T_p & -1/T_p^2 & 0 \\ 0 & 0 & 0 & 1 & 0 & 0 \\ 0 & 0 & 0 & 0 & 1 & 0 \end{bmatrix} \quad (3.49)$$

$$B_{PI3} = \begin{bmatrix} 1 & 0 & -1 & 0 \\ 0 & 0 & 0 & 0 \\ 0 & 0 & 0 & 0 \\ 0 & 1 & 0 & -1 \\ 0 & 0 & 0 & 0 \\ 0 & 0 & 0 & 0 \end{bmatrix} \quad (3.50)$$

$$C_{PI3} = \begin{bmatrix} K_{pi}\tau/T_p^2 & 2K_{pi}/T_p^2 & K_{pi}/\tau T_p^2 & 0 & 0 & 0 \\ 0 & 0 & 0 & K_{pi}\tau/T_p^2 & 2K_{pi}/T_p^2 & K_{pi}/\tau T_p^2 \end{bmatrix} \quad (3.51)$$

$$D_{PI3} = \begin{bmatrix} 0 & 0 & 0 & 0 \\ 0 & 0 & 0 & 0 \end{bmatrix} \quad (3.52)$$

Note that the inverter's output voltage  $V_{odq}$  is automatically on the common reference frame since the voltage reference has been converted in the droop controller state-space matrices (Eq. 3.41 and 3.42).

The LC filter's current and voltage state-space matrices for the Inverter are given by the followings;

$$\begin{bmatrix} \Delta \dot{I}_{Lq} \\ \Delta \dot{I}_{Ld} \\ \Delta \dot{V}_{oq} \\ \Delta \dot{V}_{od} \end{bmatrix} = A_{LCF} \begin{bmatrix} \Delta I_{Lq} \\ \Delta I_{Ld} \\ \Delta V_{oq} \\ \Delta V_{od} \end{bmatrix} + B_{LCF} \begin{bmatrix} \Delta e_q \\ \Delta e_d \\ \Delta I_{Loadq} \\ \Delta I_{Loadd} \\ \Delta I_{Lineq} \\ \Delta I_{Lined} \end{bmatrix} \quad (3.53)$$

And,

$$\begin{bmatrix} \Delta V_{oq} \\ \Delta V_{od} \end{bmatrix} = C_{LCF} \begin{bmatrix} \Delta I_{Lq} \\ \Delta I_{Ld} \\ \Delta V_{oq} \\ \Delta V_{od} \end{bmatrix} + D_{LCF} \begin{bmatrix} \Delta e_q \\ \Delta e_d \\ \Delta I_{Loadq} \\ \Delta I_{Loadd} \\ \Delta I_{Lineq} \\ \Delta I_{Lined} \end{bmatrix} \quad (3.54)$$

Where,

$$A_{LCF} = \begin{bmatrix} -r_L/L_f & \omega_o & -1/L_f & 0 \\ -\omega_o & -r_L/L_f & 0 & -1/L_f \\ 1/C_f & 0 & 0 & \omega_o \\ 0 & 1/C_f & -\omega_o & 0 \end{bmatrix} \quad (3.55)$$

$$B_{LCF} = \begin{bmatrix} 1/L_f & 0 & 0 & 0 & 0 & 0 \\ 0 & 1/L_f & 0 & 0 & 0 & 0 \\ 0 & 0 & -1/C_f & 0 & 1/C_f & 0 \\ 0 & 0 & 0 & -1/C_f & 0 & 1/C_f \end{bmatrix} \quad (3.56)$$

$$C_{LCF} = \begin{bmatrix} 0 & 0 & 1 & 0 \\ 0 & 0 & 0 & 1 \end{bmatrix} \quad (3.57)$$

$$D_{LCF} = \begin{bmatrix} 0 & 0 & 0 & 0 & 0 & 0 \\ 0 & 0 & 0 & 0 & 0 & 0 \end{bmatrix} \quad (3.58)$$

Now the load current's state-space matrices are as the followings;

$$\begin{bmatrix} \Delta \dot{I}_{Loadq} \\ \Delta \dot{I}_{Loadd} \end{bmatrix} = A_{Load} \begin{bmatrix} \Delta I_{Loadq} \\ \Delta I_{Loadd} \end{bmatrix} + B_{Load} \begin{bmatrix} \Delta V_{oq} \\ \Delta V_{od} \end{bmatrix} \quad (3.59)$$

And,

$$\begin{bmatrix} \Delta I_{Loadq} \\ \Delta I_{Loadd} \end{bmatrix} = C_{Load} \begin{bmatrix} \Delta I_{Loadq} \\ \Delta I_{Loadd} \end{bmatrix} + D_{Load} \begin{bmatrix} \Delta V_{oq} \\ \Delta V_{od} \end{bmatrix} \quad (3.60)$$

Where,

$$A_{Load} = \begin{bmatrix} -R_{Load}/L_{Load} & \omega_o \\ -\omega_o & -R_{Load}/L_{Load} \end{bmatrix} \quad (3.61)$$

$$B_{Load} = \begin{bmatrix} 1/L_{Load} & 0 \\ 0 & 1/L_{Load} \end{bmatrix} \quad (3.62)$$

$$C_{Load} = \begin{bmatrix} 1 & 0 \\ 0 & 1 \end{bmatrix} \quad (3.63)$$

$$D_{Load} = \begin{bmatrix} 0 & 0 \\ 0 & 0 \end{bmatrix} \quad (3.64)$$

Finally, the state-space matrices of the line current are given by;

$$\begin{bmatrix} \Delta \dot{I}_{Lineq} \\ \Delta \dot{I}_{Lined} \end{bmatrix} = A_{Line} \begin{bmatrix} \Delta I_{Lineq} \\ \Delta I_{Lined} \end{bmatrix} + B_{Line} \begin{bmatrix} \Delta V_{oq} \\ \Delta V_{od} \end{bmatrix} \quad (3.65)$$

And,

$$\begin{bmatrix} \Delta I_{Lineq} \\ \Delta I_{Lined} \end{bmatrix} = C_{Line} \begin{bmatrix} \Delta I_{Lineq} \\ \Delta I_{Lined} \end{bmatrix} + D_{Line} \begin{bmatrix} \Delta V_{oq} \\ \Delta V_{od} \end{bmatrix} \quad (3.66)$$

Where,

$$A_{Line} = \begin{bmatrix} -R_g/L_g & \omega_o \\ -\omega_o & -R_g/L_g \end{bmatrix} \quad (3.67)$$

$$B_{Line} = \begin{bmatrix} -1/L_g & 0 \\ 0 & -1/L_g \end{bmatrix} \quad (3.68)$$

$$C_{Line} = \begin{bmatrix} 1 & 0 \\ 0 & 1 \end{bmatrix} \quad (3.69)$$

$$D_{Line} = \begin{bmatrix} 0 & 0 \\ 0 & 0 \end{bmatrix} \quad (3.70)$$

From the state-space equations (Eq. 3.41-70), one can see that the whole system has 17 states which can be linked in one matrix as shown in Eq. 3.71.

Note that the matrix “ $A_{mg}$ ” has to be an n-by-n matrix (17-by-17 in this case) unless eigenvalues could not be calculated. These later are used to analyze the stability and dynamic behaviors of the system.

$$\begin{bmatrix} \dot{\Delta\delta} \\ \Delta\dot{P}_{Inv} \\ \Delta\dot{Q}_{Inv} \\ \Delta\ddot{\varphi}_q \\ \Delta\dot{\varphi}_q \\ \Delta\dot{\varphi}_q \\ \Delta\ddot{\varphi}_d \\ \Delta\dot{\varphi}_d \\ \Delta\dot{\varphi}_d \\ \Delta\dot{I}_{Lq} \\ \Delta\dot{I}_{Ld} \\ \Delta\dot{V}_{oq} \\ \Delta\dot{V}_{od} \\ \Delta\dot{I}_{Loadq} \\ \Delta\dot{I}_{Loadd} \\ \Delta\dot{I}_{Lineq} \\ \Delta\dot{I}_{Lined} \end{bmatrix} = A_{mg} \begin{bmatrix} \Delta\delta \\ \Delta P_{Inv} \\ \Delta Q_{Inv} \\ \Delta\ddot{\varphi}_q \\ \Delta\dot{\varphi}_q \\ \Delta\dot{\varphi}_q \\ \Delta\ddot{\varphi}_d \\ \Delta\dot{\varphi}_d \\ \Delta\dot{\varphi}_d \\ \Delta I_{Lq} \\ \Delta I_{Ld} \\ \Delta V_{oq} \\ \Delta V_{od} \\ \Delta I_{Loadq} \\ \Delta I_{Loadd} \\ \Delta I_{Lineq} \\ \Delta I_{Lined} \end{bmatrix} \quad (3.71)$$

Where,

$$A_{mg} = \begin{bmatrix} 0 & A_1 & 0 & 0 & 0 & 0 & 0 & 0 & 0 & 0 & 0 & 0 & 0 & 0 & 0 & 0 & 0 \\ 0 & A_2 & 0 & 0 & 0 & 0 & 0 & 0 & 0 & 0 & 0 & A_2 & A_4 & A_5 & A_6 & -A_5 & -A_6 \\ 0 & 0 & A_2 & 0 & 0 & 0 & 0 & 0 & 0 & 0 & 0 & -A_4 & A_3 & A_6 & -A_5 & -A_6 & A_5 \\ A_7 & 0 & A_8 & A_9 & A_{10} & 0 & 0 & 0 & 0 & 0 & 0 & -1 & 0 & 0 & 0 & 0 & 0 \\ 0 & 0 & 0 & 1 & 0 & 0 & 0 & 0 & 0 & 0 & 0 & 0 & 0 & 0 & 0 & 0 & 0 \\ 0 & 0 & 0 & 0 & 1 & 0 & 0 & 0 & 0 & 0 & 0 & 0 & 0 & 0 & 0 & 0 & 0 \\ A_{11} & 0 & A_{12} & 0 & 0 & 0 & A_9 & A_{10} & 0 & 0 & 0 & 0 & -1 & 0 & 0 & 0 & 0 \\ 0 & 0 & 0 & 0 & 0 & 0 & 1 & 0 & 0 & 0 & 0 & 0 & 0 & 0 & 0 & 0 & 0 \\ 0 & 0 & 0 & 0 & 0 & 0 & 0 & 1 & 0 & 0 & 0 & 0 & 0 & 0 & 0 & 0 & 0 \\ 0 & 0 & 0 & A_{13} & A_{14} & A_{15} & 0 & 0 & 0 & A_{16} & A_{17} & A_{18} & 0 & 0 & 0 & 0 & 0 \\ 0 & 0 & 0 & 0 & 0 & 0 & A_{13} & A_{14} & A_{15} & -A_{17} & A_{16} & 0 & A_{18} & 0 & 0 & 0 & 0 \\ 0 & 0 & 0 & 0 & 0 & 0 & 0 & 0 & 0 & A_{19} & 0 & 0 & A_{17} & -A_{19} & 0 & A_{19} & 0 \\ 0 & 0 & 0 & 0 & 0 & 0 & 0 & 0 & 0 & 0 & A_{19} & -A_{17} & 0 & 0 & -A_{19} & 0 & A_{19} \\ 0 & 0 & 0 & 0 & 0 & 0 & 0 & 0 & 0 & 0 & 0 & A_{20} & 0 & A_{21} & A_{17} & 0 & 0 \\ 0 & 0 & 0 & 0 & 0 & 0 & 0 & 0 & 0 & 0 & 0 & 0 & A_{20} & -A_{17} & A_{21} & 0 & 0 \\ 0 & 0 & 0 & 0 & 0 & 0 & 0 & 0 & 0 & 0 & 0 & A_{22} & 0 & 0 & 0 & A_{23} & A_{17} \\ 0 & 0 & 0 & 0 & 0 & 0 & 0 & 0 & 0 & 0 & 0 & 0 & A_{22} & 0 & 0 & -A_{17} & A_{23} \end{bmatrix} \quad (3.72)$$

Where,

$$A_1 = -m_p$$

$$A_2 = -\omega_c$$

$$A_3 = 1.5\omega_c(I_{Loadqo} - I_{Lineqo})$$

$$A_4 = 1.5\omega_c(I_{Loaddo} - I_{Linedo})$$

$$A_5 = 1.5\omega_c V_{oqo}$$

$$A_6 = 1.5\omega_c V_{odo}$$

$$A_7 = V_{qrefo} \sin(\delta_o) - V_{drefo} \cos(\delta_o)$$

$$A_8 = -n_q \cos(\delta_o)$$

$$A_9 = -2/T_p$$



$$\begin{array}{lll}
A_{10} = -1/T_p^2 & A_{11} = V_{qref0} \cos(\delta_o) - V_{dref0} \sin(\delta_o) & A_{12} = -n_q \sin(\delta_o) \\
A_{13} = (K_{pi} \tau) / (L_f T_p^2); & A_{14} = (2K_{pi}) / (L_f T_p^2) & A_{15} = K_{pi} / (L_f \tau T_p^2) \\
A_{16} = -r_L / L_f & A_{17} = \omega_o & A_{18} = -1/L_f \\
A_{19} = 1/C_f & A_{20} = 1/L_{Load} & A_{21} = -R_{Load} / L_{Load} \\
A_{22} = -1/L_g & A_{23} = -R_g / L_g & 
\end{array}$$

The eigenvalues of the matrix ( $A_{mg}$ ) have been calculated using Matlab. As mentioned before, the initial values of each case have been obtained from Simulink/Matlab simulation of the average model (dq model) of the system shown in Fig. 3.2. The results of the latter will be verified in the next section. The .m file of Matlab which contains the small-signal state-space model of the complete system is given in the Appendix-A.

### 3.4 Schematics of the simulation file

Based on Fig. 3.1 and Fig. 3.2, the schematics of Simulink/Matlab simulation file of the average system and the average dq model are shown in Fig. 3.9 and 3.10 respectively. The purpose of the latter is to verify the modeling that has been done in the previous section by comparing its results with the Simulink/Matlab file simulation results.

Note that in order to make the simulations run fast, the three-phase inverter, in Fig. 3.9, is represented by three controllable AC voltage sources. The switching harmonics in this case are neglected but this is not a problem since the main interest is the investigation of the stability of the system and the behavior of the active and reactive power flows, which are not influenced by the harmonics.

The dq model shown in Fig. 3.10, as described before, has three main blocks (The grid, the inverter and the line impedance). Where, each block contains the appropriate mathematical models derived in the previous section (Eq. 1.6, 1.7, 3.6, 3.7, 3.13, 3.16, 3.20, 3.25-3.28, 3.33, 3.34, 3.37 and 3.38).

Setting the system parameters as listed in Table 3.1, the comparison results of the system in Fig. 3.9 and its dq average model shown in Fig. 3.10 are shown in Fig 3.11 and 3.12. These latter shows the transient and the steady-state responses of the inverter's output active and reactive power respectively when a change in the no-load frequency ( $f_{nL}$ ) occurs in the P vs. f droop controller. As discussed previously, the active power could be controlled by varying also the no-load frequency as shown by Eq. 3.1. Note that the reactive power controller has been disabled ( $n_q=0$ ) in order to see the coupling effect between P and Q caused by the line impedance characteristics.

**Table 3.1: System parameters**

Parameter	Value	Unit
$V_g$	120/208	$V_{rms}$
$f_g$	60	Hz
$m_p (\Delta f)$	2.513m (4)	rad/s/W (Hz)
$n_q$	0	V/VAr
$X_g$	0.1	$\Omega$
$R_g$	0.23	$\Omega$
$f_c$ (LPF cut-off frequency)	30	Hz

Note that the line impedance values ( $X_g$  and  $R_g$ ) have been obtained from [16].

The next table describes the simulations' steps.

**Table 3.2: Simulation steps**

Condition	Time (s)
$P_{Load}=5kW; f_{nL}=62Hz$	0
$P_{Load}=5kW; f_{nL}=63Hz$	0.25
$P_{Load}=5kW; f_{nL}=59Hz$	0.5

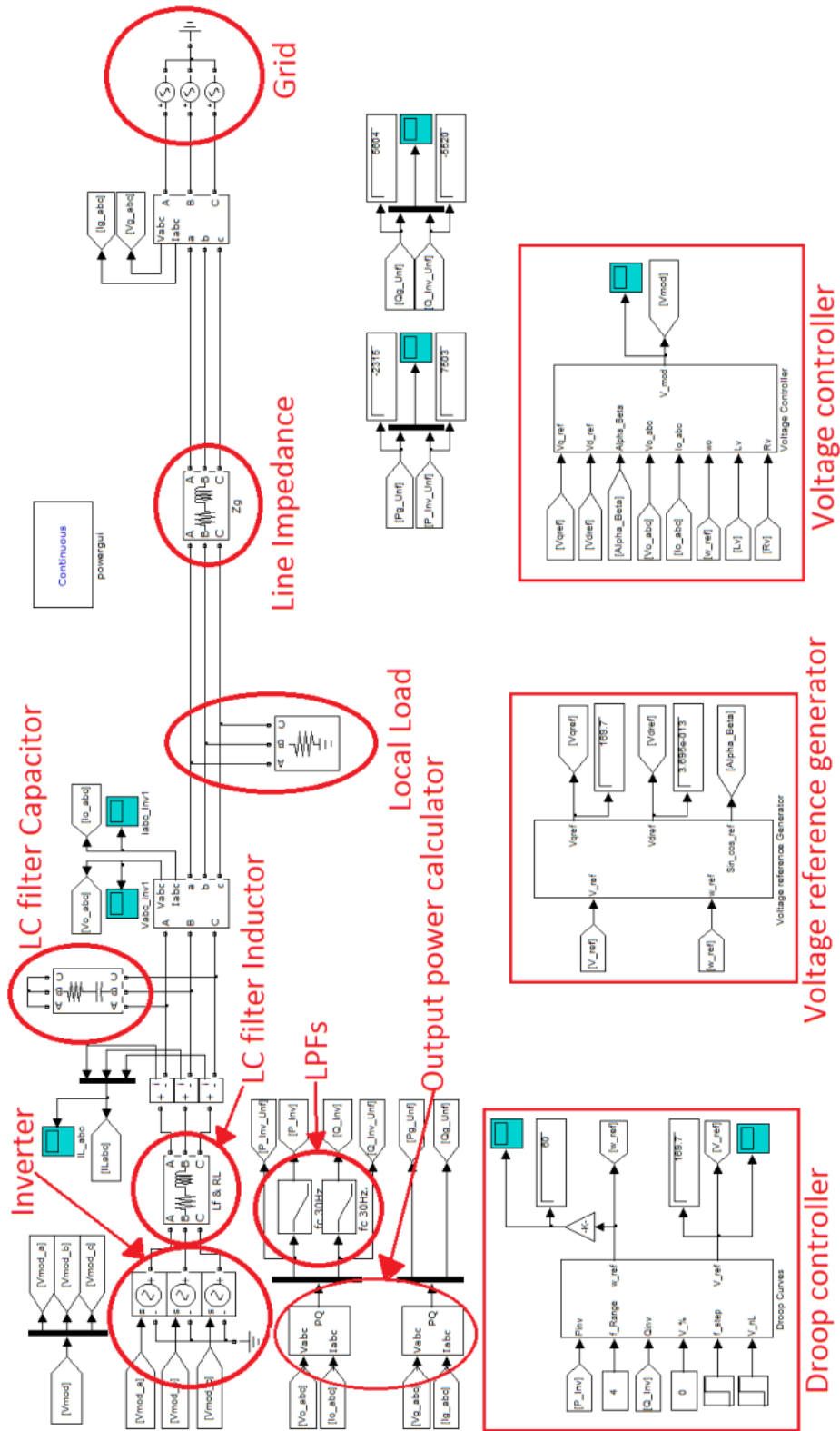


Figure 3.9: The system's Simulink/Matlab simulation file scheme

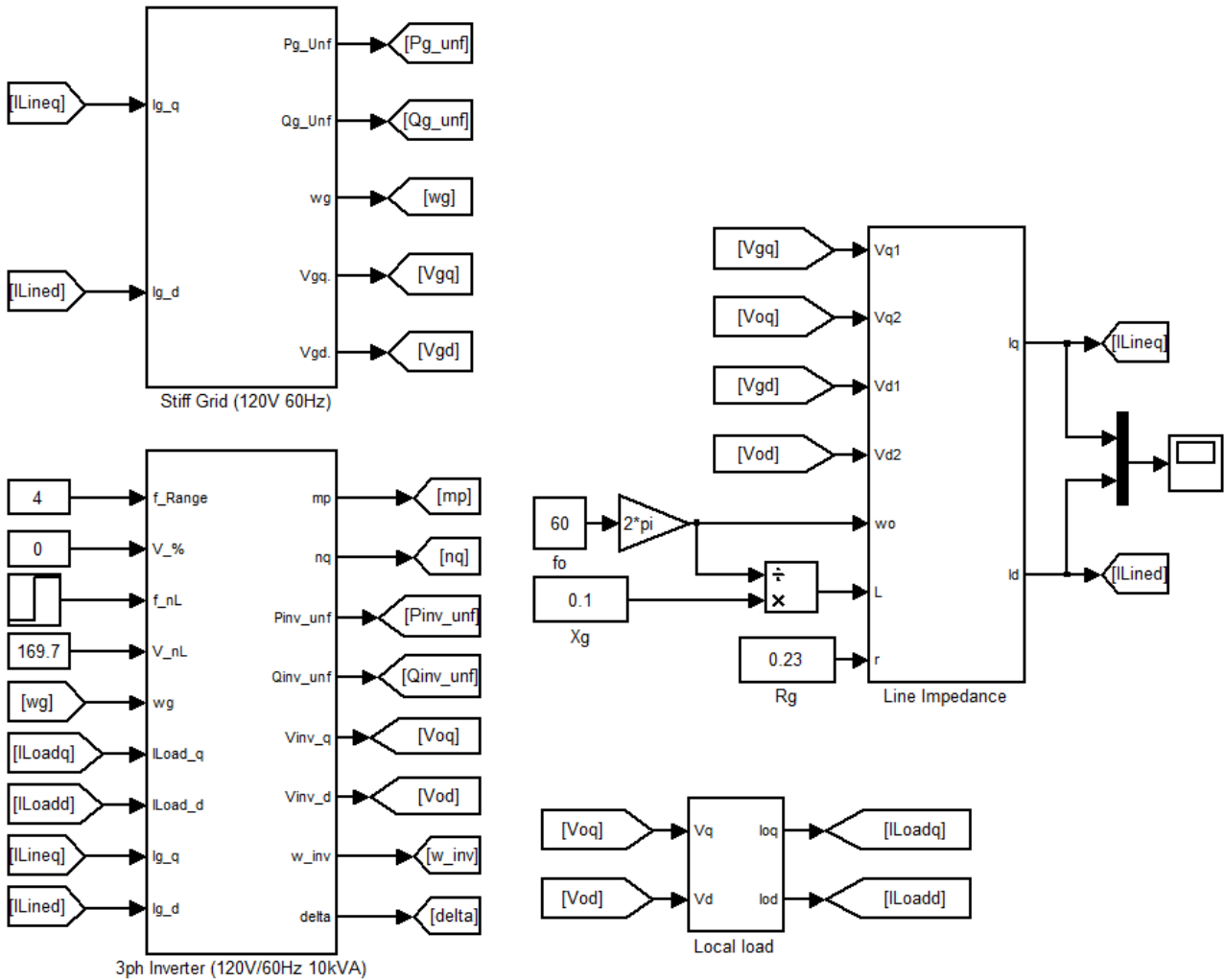


Figure 3.10: The system's dq average model in Simulink/Matlab

It is shown in Fig 3.11 and 3.12, that the mathematical average model of the system derived on dq coordinates gives the same results as the simulation file on Simulink/Matlab. There is only a difference in the magnitude at the synchronization between the inverter and the grid. However, this does not have any influence on the outcome of the analysis.

Note that the inverter has a local load of 5kW which is entirely supplied by the inverter. This makes the operating frequency of the inverter settle at 60Hz and preventing the inverter to provide active power to the grid.

The increase in the no-load frequency in the droop controller generates a positive phase angle ( $\delta$ ) which makes the inverter provide active power to the grid. On the other side, decreasing  $f_{nL}$  (below the rated frequency 60Hz) makes the inverter absorb active power. This is suitable in case the batteries bank in the DC bus need to be charged.

The coupling between P and Q is shown in Fig 3.11 and 3.12. The frequency range ( $\Delta f$ ) used in the P vs. f droop controller is 4Hz. Knowing that inverter's rated apparent power is 10kVA, an increasing of 1Hz in the no-Load frequency generates an increasing of 2.5kW in the inverter's output active power. However, in case when line impedance is not purely inductive, an increasing in the reactive power occurs. The amount of the latter depends on the ratio  $X_g/R_g$ . As mentioned before, the P and Q coupling issue is not discussed in this thesis.

As described in Table 3.2, when a step-up of 1Hz occurs at 0.25s in  $f_{nL}$ , the inverter provides an additional 2.5kW to the grid as shown in Fig 3.11. However, when  $f_{nL}$  becomes smaller (59Hz at 0.5s) than the rating frequency 60Hz, the inverter absorbs 2.5kW.

The reactive power droop controller does not solve the coupling issue between P and Q. However, the increasing of the reactive droop gain ( $n_q$ ) makes the reactive power decreases since it has an influence on the voltage amplitude. As it is shown in the following paragraphs, the system stability is very sensitive to the value of  $n_q$  and its value depends on other slow elements of the system.

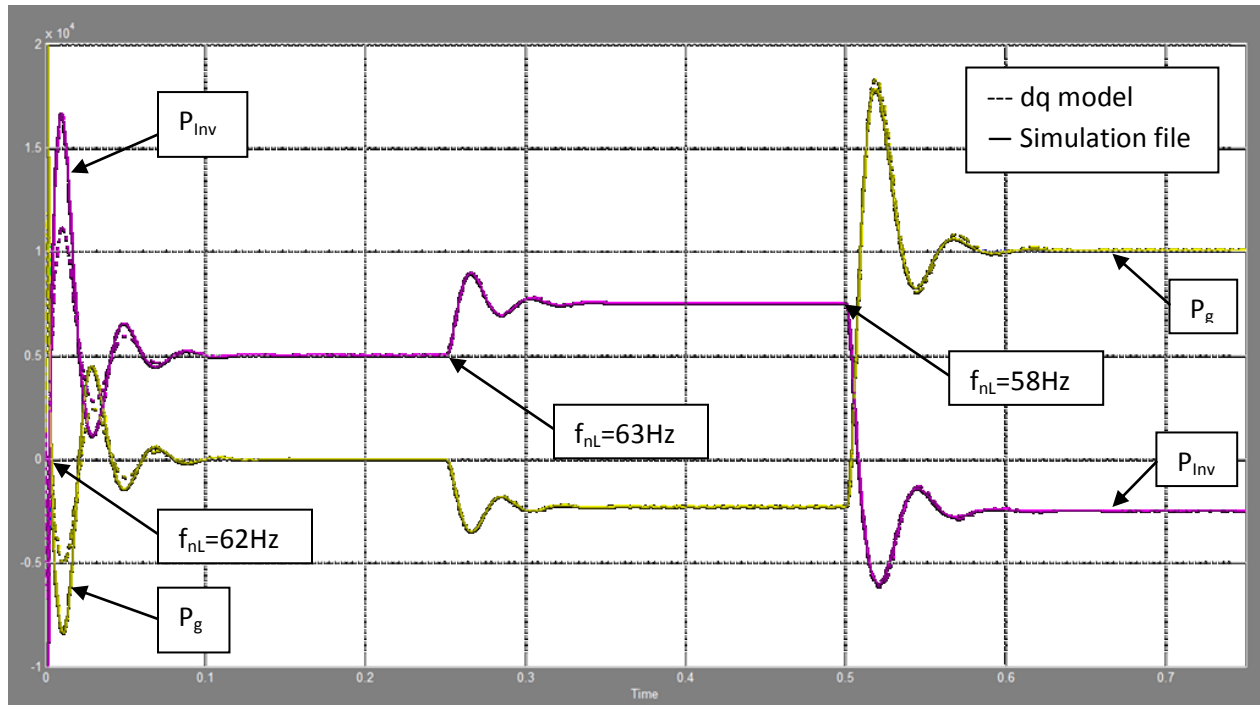


Figure 3.11: Inverter and grid's output active power (W) vs. Time (s)

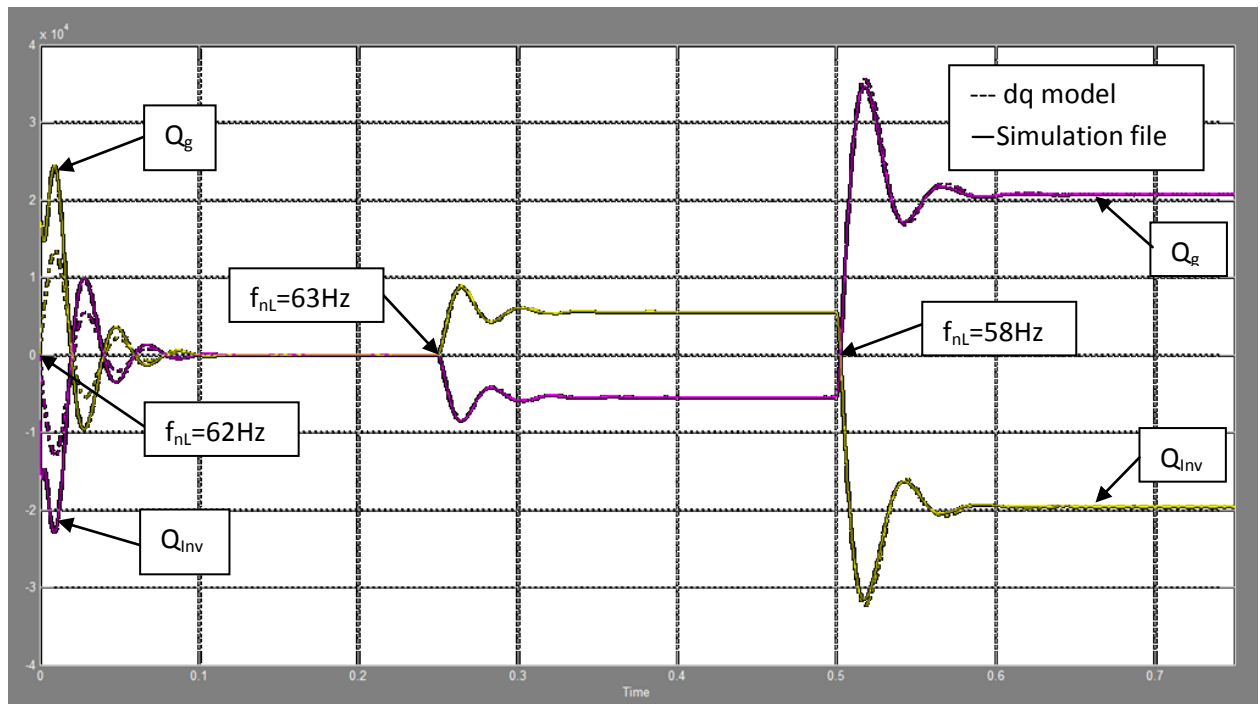


Figure 3.12: Inverter and grid's output reactive power (VAr) vs. Time (s)

### 3.5 Root locus of the system to various parameters

After linearizing the various blocks of the system using the small-signal approach and combining them in one state-space matrix, the roots of the system model are shown in Fig. 3.17. The system parameters are the same as in Table 3.1.

There are three clusters of poles, as it is seen in Fig 3.13. Clusters #2 and #3 contain high frequency poles which are directly influenced by the voltage controller and the LC Filter. However, cluster #1 contains the low frequency poles which are directly influenced by the droop controllers, the output impedance and the LPF. According to [12], the fast elements as the voltage regulator and the LC filter could be neglected in the system modeling since they have a very small influence on the system behavior. To verify this, a reduced system model needs to be derived. Neglecting the voltage controller, the LC filter and the local load (for the sake of simplicity since the large load impedance does not influence a lot the inverter's output impedance), the system states are reduced now to 5 as shown by the following equations.

$$\begin{bmatrix} \Delta \dot{\delta} \\ \Delta \dot{P}_{Inv} \\ \Delta \dot{Q}_{Inv} \\ \Delta \dot{I}_{Lineq} \\ \Delta \dot{I}_{Lined} \end{bmatrix} = A_{rmg} \begin{bmatrix} \Delta \delta \\ \Delta P_{Inv} \\ \Delta Q_{Inv} \\ \Delta I_{Lineq} \\ \Delta I_{Lined} \end{bmatrix} \quad (3.73)$$

Where,

$$A_{rmg} = \begin{bmatrix} 0 & Ar_1 & 0 & 0 & 0 \\ Ar_2 & Ar_3 & Ar_4 & Ar_5 & Ar_6 \\ Ar_7 & 0 & Ar_8 & Ar_6 & -Ar_5 \\ Ar_9 & 0 & Ar_{10} & Ar_{11} & Ar_{12} \\ Ar_{13} & 0 & Ar_{14} & -Ar_{12} & Ar_{11} \end{bmatrix} \quad (3.74)$$

Where,

$$Ar_1 = -m_p$$

$$Ar_2 = 1.5 * \omega_c * (-I_{Lineqo} * (-V_{qrefo} * \sin(\delta_o) - V_{drefo} * \cos(\delta_o)) - I_{Linedo} * (V_{qrefo} * \cos(\delta_o) - V_{drefo} * \sin(\delta_o)))$$

$$Ar_3 = -\omega_c$$

$$Ar_4 = -1.5 * \omega_c * n_q * (-I_{Lineqo} * \cos(\delta_o) - I_{Linedo} * \sin(\delta_o))$$

$$Ar_5 = -1.5 * \omega_c * V_{oqo}$$

$$Ar_6 = -1.5 * \omega_c * V_{odo}$$

$$Ar_7 = 1.5 * \omega_c * (I_{Linedo} * (-V_{qrefo} * \sin(\delta_o) - V_{drefo} * \cos(\delta_o)) - I_{Lineqo} * (V_{qrefo} * \cos(\delta_o) - V_{drefo} * \sin(\delta_o)))$$

$$Ar_8 = -\omega_c + 1.5 * \omega_c * n_q * (-I_{Linedo} * \cos(\delta_o) + I_{Lineqo} * \sin(\delta_o))$$

$$Ar_9 = -(V_{qrefo} * \sin(\delta_o) - V_{drefo} * \cos(\delta_o)) / L_g$$

$$Ar_{10} = n_q * \cos(\delta_o) / L_g$$

$$Ar_{11} = -R_g / L_g$$

$$Ar_{12} = \omega_o$$

$$Ar_{13} = -(V_{qrefo} * \cos(\delta_o) - V_{drefo} * \sin(\delta_o)) / L_g$$

$$Ar_{14} = n_q * \sin(\delta_o) / L_g$$

The characteristic polynomial (known also as the characteristic equation) of the reduced system model's matrix ( $A_{rmg}$ ) is calculated using the following equation.

$$\det|A_{rmg} - xI| = 0 \quad (3.75)$$

Where,  $I$  is a 5x5 identity matrix. Using the mathematical software "MathCAD", the characteristic equation of the reduced system model is given by;

$$x^5 + \alpha x^4 + \beta x^3 + \gamma x^2 + \lambda x + \zeta = 0 \quad (3.76)$$



Where,

$$\alpha = -Ar_3 - Ar_8 - 2Ar_{11}$$

$$\beta = Ar_{11}^2 + Ar_{12}^2 - Ar_1Ar_2 + Ar_3Ar_8 + 2Ar_3Ar_{11} - Ar_6Ar_{10} + Ar_5Ar_{14} + 2Ar_8Ar_{11}$$

$$\begin{aligned} \gamma = & -Ar_3Ar_{11}^2 - Ar_3Ar_{12}^2 - Ar_8Ar_{11}^2 - Ar_8Ar_{12}^2 + Ar_1Ar_2Ar_8 - Ar_1Ar_4Ar_7 - Ar_1Ar_5Ar_9 + 2Ar_1Ar_2Ar_{11} + Ar_3Ar_6Ar_{10} - Ar_1Ar_6Ar_{13} - \\ & Ar_3Ar_5Ar_{14} - 2Ar_3Ar_8Ar_{11} - Ar_5Ar_{10}Ar_{12} + Ar_6Ar_{10}Ar_{11} - Ar_5Ar_{11}Ar_{14} - Ar_6Ar_{12}Ar_{14} \end{aligned}$$

$$\begin{aligned} \lambda = & -Ar_1Ar_2Ar_{11}^2 - Ar_1Ar_2Ar_{12}^2 + Ar_3Ar_8Ar_{11}^2 + Ar_3Ar_8Ar_{12}^2 - Ar_1Ar_4Ar_6Ar_9 + Ar_1Ar_5Ar_8Ar_9 + Ar_1Ar_2Ar_6Ar_{10} - \\ & Ar_1Ar_2Ar_5Ar_{14} - 2Ar_1Ar_2Ar_8Ar_{11} + Ar_1Ar_4Ar_5Ar_{13} + 2Ar_1Ar_4Ar_7Ar_{11} - \\ & Ar_1Ar_5Ar_7Ar_{10} + Ar_1Ar_5Ar_9Ar_{11}Ar_6Ar_7Ar_{14} + Ar_1Ar_6Ar_8Ar_{13} + Ar_1Ar_6Ar_9Ar_{12} + Ar_3Ar_5Ar_{10}Ar_{12} - Ar_3Ar_6Ar_{10}Ar_{11} - \\ & Ar_1Ar_5Ar_{12}Ar_{13} + Ar_1Ar_6Ar_{11}Ar_{13} + Ar_3Ar_5Ar_{11}Ar_{14} + Ar_3Ar_6Ar_{12}Ar_{14} \end{aligned}$$

$$\begin{aligned} \zeta = & Ar_1Ar_2Ar_8Ar_{11}^2 + Ar_1Ar_2Ar_8Ar_{12}^2 - Ar_1Ar_4Ar_7Ar_{11}^2 - Ar_1Ar_4Ar_7Ar_{12}^2 - Ar_1Ar_5^2Ar_9Ar_{14} - \\ & Ar_1Ar_6^2Ar_9Ar_{14} + Ar_1Ar_5^2Ar_{10}Ar_{13} + Ar_1Ar_6^2Ar_{10}Ar_{13} - Ar_1Ar_4Ar_5Ar_9Ar_{12} + Ar_1Ar_4Ar_6Ar_9Ar_{11} - Ar_1Ar_5Ar_8Ar_9Ar_{11} - \\ & Ar_1Ar_6Ar_8Ar_9Ar_{12} + Ar_1Ar_2Ar_5Ar_{10}Ar_{12} - Ar_1Ar_2Ar_6Ar_{10}Ar_{11} + Ar_1Ar_2Ar_5Ar_{11}Ar_{14} - \\ & Ar_1Ar_4Ar_5Ar_{11}Ar_{13} + Ar_1Ar_5Ar_7Ar_{10}Ar_{11} + Ar_1Ar_2Ar_6Ar_{12}Ar_{14} - Ar_1Ar_4Ar_6Ar_{12}Ar_{13} + Ar_1Ar_6Ar_7Ar_{10}Ar_{12} - \\ & Ar_1Ar_5Ar_7Ar_{12}Ar_{14} + Ar_1Ar_5Ar_8Ar_{12}Ar_{13} + Ar_1Ar_6Ar_7Ar_{11}Ar_{14} - Ar_1Ar_6Ar_8Ar_{11}Ar_{13} \end{aligned}$$

The characteristic equation 3.76 is a 5<sup>th</sup> order function which is very complicated to calculate its roots manually as function of  $A_{r_{mg}}$  components  $A_{r_i}$ . Therefore, Matlab has been used to calculate and to plot those roots as shown in Fig. 3.14.

Note that the .m file of Matlab which contains the small-signal state-space model of the reduced system is given in the Appendix-B. The eigenvalues of the state-space matrix have been calculated using the Matlab command "eig".

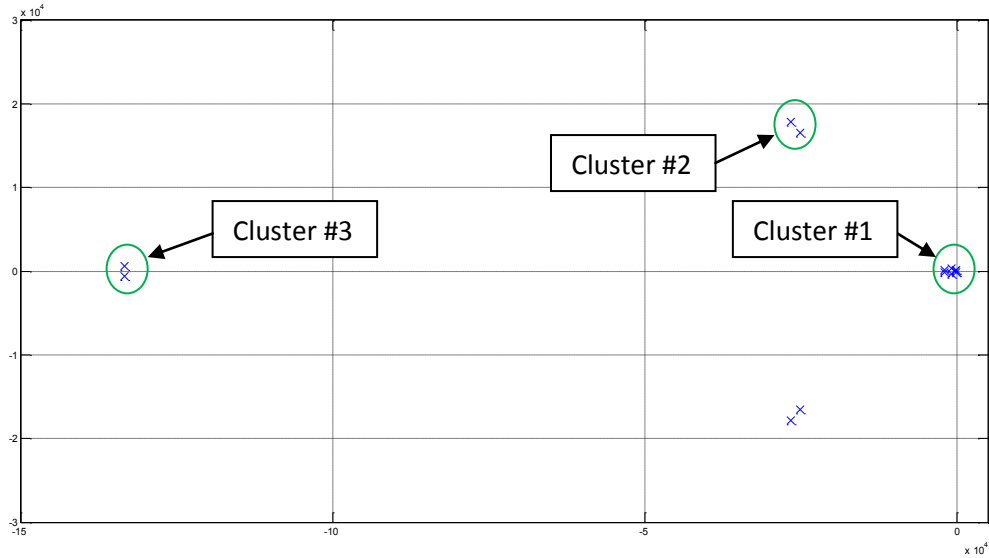


Figure 3.13: Roots of the complete system small-signal model

As one can see in Fig. 3.13 and 3.14 that clusters #2 and #3 disappear in the reduced system model and only the low-frequency poles are shown.

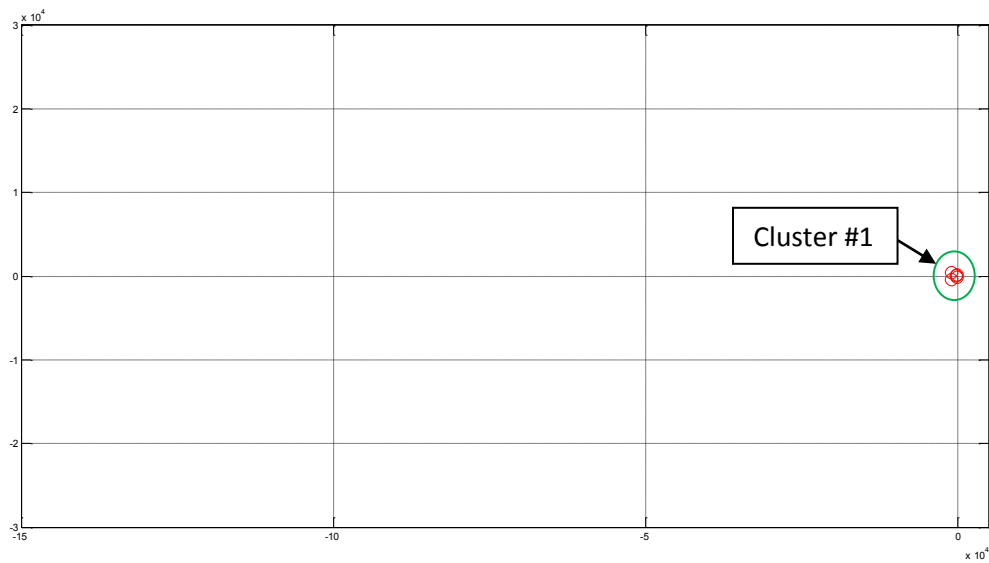


Figure 3.14: Roots of the reduced system small-signal model

In order to compare the position of the roots of the detailed and the reduced system models, Fig. 3.15 shows a zoom on cluster #1 of Fig. 3.13 and 3.14. The dominant poles of the two models are similar but the intermediate poles, which are around  $-800 \pm j250$ , are significantly different due to the difference of

the output impedance in the two models. In the following sections, the influence of the output impedance on the intermediate pole is verified using the reduced system model. Therefore, only the reduced system model is used for following studies since the latter gives accurate system behavior which is dictated by the dominant pole. Finally, the fast elements of the system could be neglected in the modeling because they have a negligible influence on the dominant pole.

The system is actually stable since all the poles are in the left side of the imaginary axes. As mentioned above, the dominant poles shown in Fig 3.15 are influenced by the droop controller slopes, the line impedance characteristic and the LPF cut-off frequency.

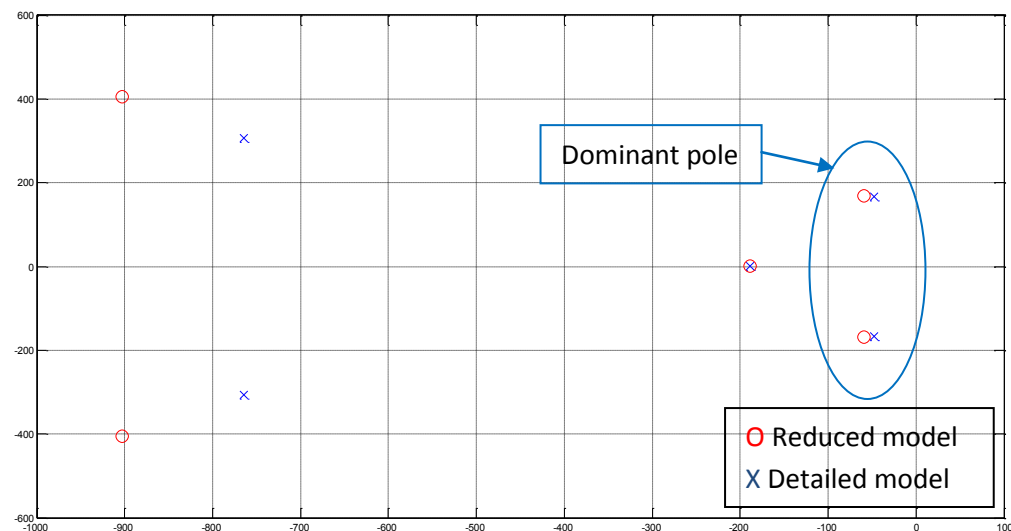


Figure 3.15: Low frequency poles of the detailed and reduced system's small-signal models

In order to see the influence of those elements on the system dynamics, a root locus has been gotten showing the poles displacement when varying those elements' parameters. Fig. 3.16 shows the root locus of the reduced and the detailed system when  $m_p$  is increased ( $\Delta f$  is varied from 0Hz to 15Hz). The system parameters are shown in Table 3.1.

As one can see in Fig. 3.16, the dominant roots of the reduced system behave exactly as those of the detailed system. By increasing the active power droop gain, the dominant complex poles moves to the

right. In other words the real part of the dominant pole increases and its imaginary part decreases. This makes the system quicker but more oscillatory. Just for information purposes, the detailed system becomes unstable when  $\Delta f$  is bigger than 10.7Hz which larger than the standards. In the next section, time domain simulations will be done for the complete system shown in Fig. 3.9 in order to verify the frequency domain results.

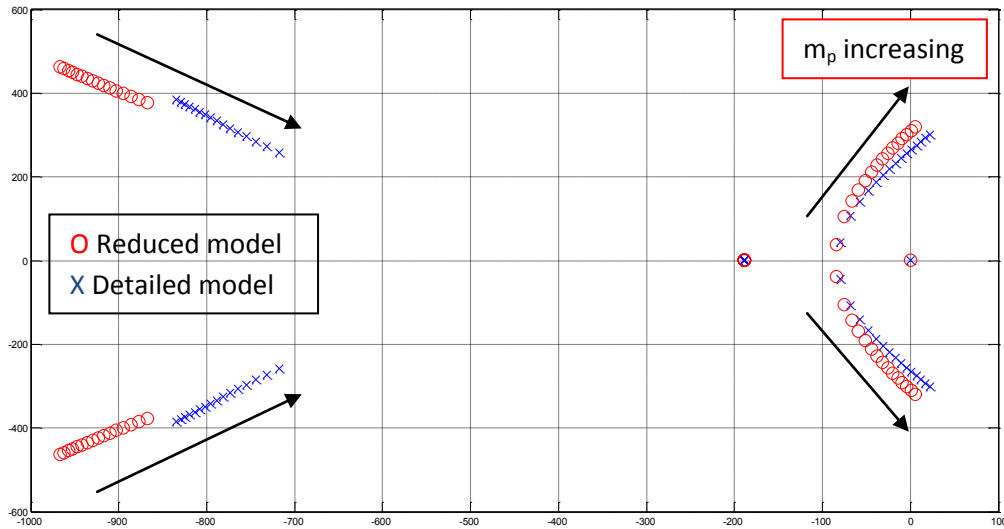


Figure 3.16: Dominant poles of the detailed and reduced system models when  $m_p$  or  $\Delta f$  is increasing

Now to verify the effect of the reactive droop gain ( $n_q$ ) on the system behavior, the roots of Eq. 3.76 have been obtained by fixing all the system parameters shown in Table 3.1 but  $n_q$  or  $\Delta V\%$  (the percentage of the voltage range with respect to the no-load voltage 169.7V) has been increased. In the frequency domain simulation shown in Fig. 3.17, the  $\Delta V\%$  is increased from 0% to 3%. As one can see, the increasing of  $n_q$  leads the system towards instability. However, small values of the reactive droop gain generate large reactive power steady-state error as it is verified in the next section. Note that the complete system becomes unstable when  $\Delta V\%$  is above 2%.

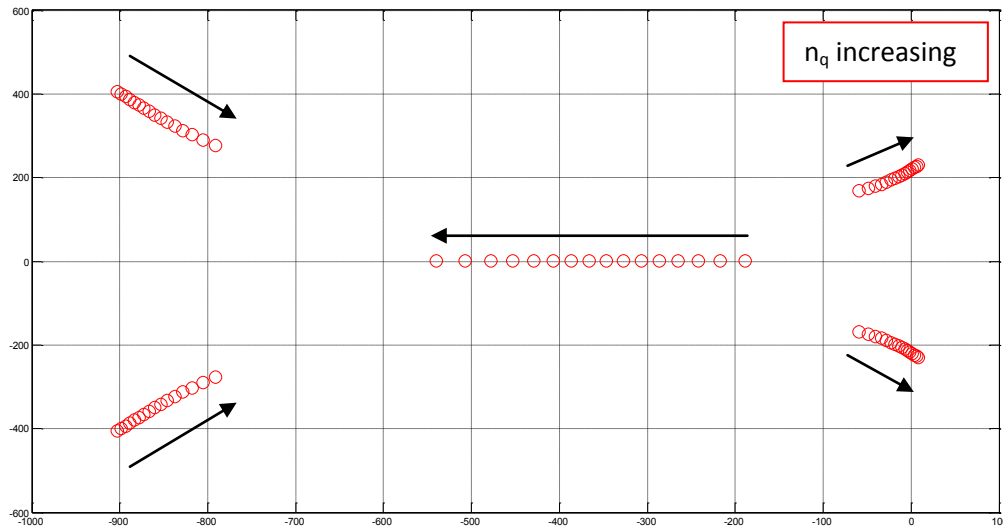


Figure 3.17: Roots of the reduced system model when  $n_q$  or  $\Delta V\%$  is increasing

Fig. 3.18 shows the system's root locus when the ratio  $X_g/R_g$  is increased from 0.1 to 15 while the resistive component of the line impedance ( $R_g$ ) is fixed at  $0.23\Omega$ . There the system (in frequency domain) never becomes unstable when increasing the inductive part of the line impedance. However, when the ratio  $X_g/R_g$  is equal or bigger than 4, the system is dominated by two poles since they are both close to the imaginary axes. The time domain results are shown in the next section. Note that the large variations in the line impedance study may not correspond to actual line impedance parameters but they help to visualize the trend of the line impedance ratio variations on the change of position of the roots.

Fig. 3.19 shows the system root locus when decreasing  $X_g/R_g$  from 2 to 0.125 while  $X_g$  is fixed at  $0.1\Omega$ . The system becomes more stable when the ratio  $X_g/R_g$  decreases and it becomes unstable when  $R_g$  is smaller than  $0.15\Omega$ . From Fig. 3.18 and 3.19, the increasing of the ratio  $X_g/R_g$  turns the system stable since the P vs. f and the Q vs. V droop control has been adopted. However,  $R_g$  must be higher than a certain value to make the dominant pole at the left side of the imaginary axes.

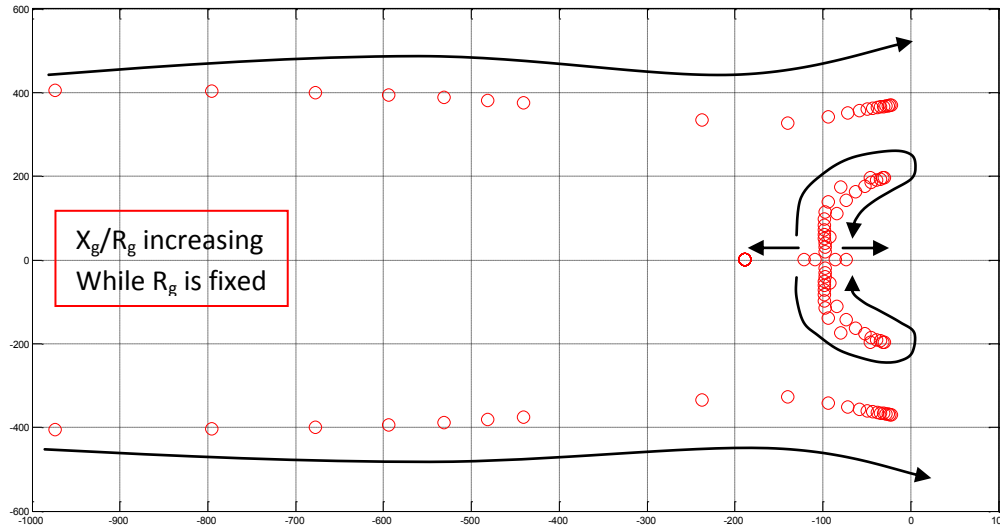


Figure 3.18: Root locus of the reduced system model when  $R_g$  is fixed and  $X_g$  is increasing

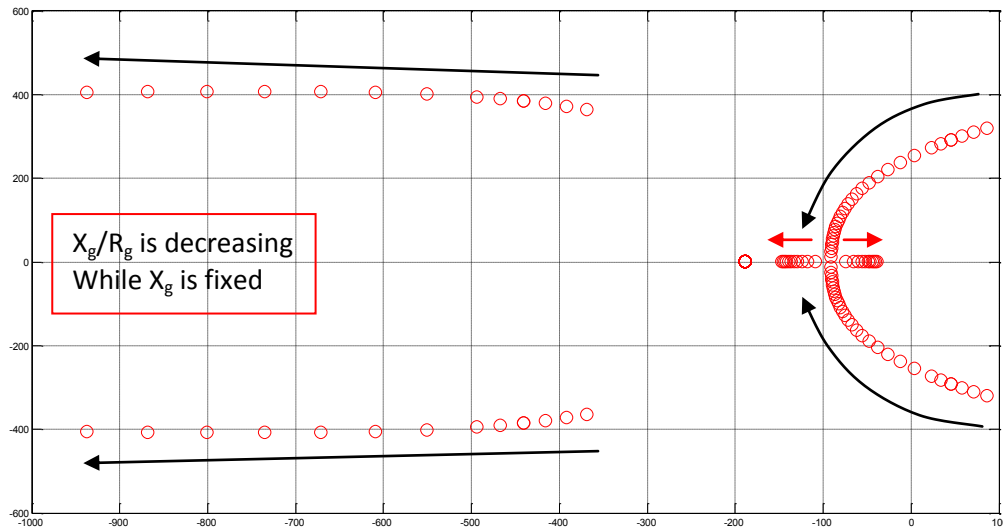


Figure 3.19: Root locus of the reduced system model when  $X_g$  is fixed and  $R_g$  is increasing

The last element which is investigated in this section is the cut-off frequency of the low-pass filter ( $f_c$ ). The latter is used to filter the measured inverter’s output power for the droop controllers. The Q vs. V droop control loop is an outer control loop as shown in Fig. 3.1 since it provides the voltage reference to the voltage control loop; hence to avoid conflicts between the two cascaded loops, the outer control loop must be slower than the inner loop. Therefore, a LPF is needed to slow down the variation of the reactive power supplied to the droop block. Since the droop controlled inverter is designed to share

active and reactive power, conventionally same LPF should be used for the P vs. f droop controller. However the LPF influences directly the system dynamics. Fig. 3.20 shows the root locus of the system when  $f_c$  is increasing from 1Hz to 60Hz. The system parameters are the same as in Table 3.1.

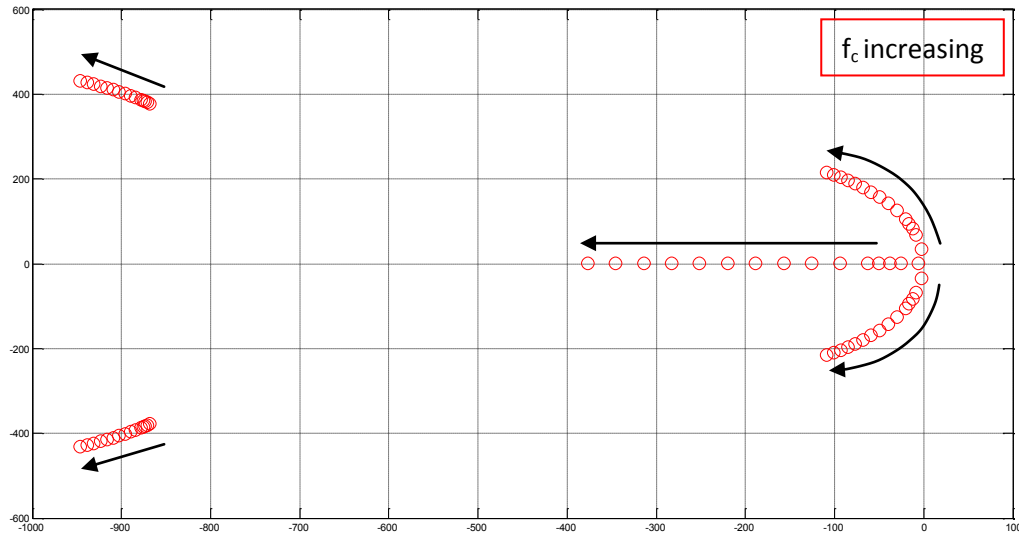


Figure 3.20: Root locus of the reduced system model when  $f_c$  is increasing

The way the low-frequency poles move in Fig 3.20 means that the higher  $f_c$  is the more stable the system is. This is uncommon since LPF are normally used to slow down any variations. However in this case, the LPF is used only in the feedback loop as Fig. 3.21 shows. From the latter, the equation of the phase angle  $\delta$  is given by Eq. 3.77 where its dynamic response is dictated by two poles ( $\lambda=0$  and  $\lambda=-\omega_c$ ). The bigger  $\omega_c$  is the more stable the system will be. This is the reason why the system becomes less oscillatory when increasing  $f_c$ . This is verified by time domain simulations in the next section.

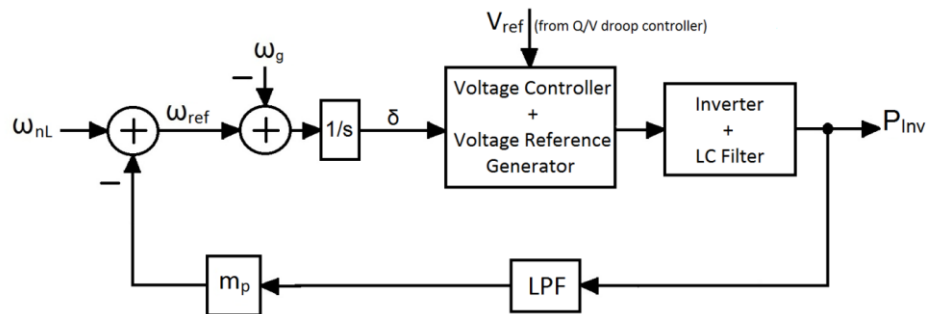


Figure 3.21: P vs. f droop control loop

$$\delta = \frac{(\omega_{nL} - \omega_g)s + (\omega_{nL} - \omega_g)\omega_c - m_p\omega_c P_{Inv}}{s(s + \omega_c)} \quad (3.77)$$

Note that Fig. 3.16-19 show that the intermediate poles are more influenced by the feeder impedance than by the droop gains. This explains the difference in that pole in Fig. 3.15 and 3.16 due to the difference in the output impedance since the voltage controller and the LC filter have been neglected in the reduced system model.

## 3.6 Performance verification

### 3.6.1 Response of the system due to reference signal variations

In the previous section, frequency domain modeling and analysis have been done showing how the system behaves dynamically under some specific parameters variations. In this section, the previous modeling is verified by time domain simulations using Simulink/Matlab.

#### 3.6.1.1 The active power droop gain ( $m_p$ ) varies

As it is seen in Fig. 3.16, the system is lead to instability and its transient response becomes faster and more oscillatory when the P vs. f droop gain is increased. To verify this, time domain simulations have been done with three different values of  $m_p$ . Table 3.3 shows the system parameters used for the simulations.

Fig. 3.22 presents simulation results when  $\Delta f$  equal 2Hz, 4Hz and 8Hz. A step of  $\Delta f/4$  in the no-load frequency signal occurs at 0.5s. There one sees that the increasing of  $m_p$  reduces the damping factor, shortens the rise time and increases the overshoot.

In the s-plane a pole is described by the following equation below where,  $\sigma$  is the real part and  $\omega$  is the imaginary part called the damped frequency of oscillation.



$$s = \sigma \pm j\omega \quad (3.78)$$

Table 3.4 gives the dominant pole shown in Fig. 3.23, the damping coefficient ( $\xi$ ) and the estimated rise time of the system for each value of  $m_p$ .

Table 3.3: system parameters for  $m_p$  increasing simulations

Parameter	Value	Unit
$V_g$	120/208	$V_{rms}$
$f_g$	60	Hz
$m_p$	1.257m, 2.513m, 5.027m	rad/s/W
$n_q$	0	V/VAr
$\Delta f$	2, 4, 8	Hz
$X_g$	0.1	$\Omega$
$R_g$	0.23	$\Omega$
$f_c$	30	Hz

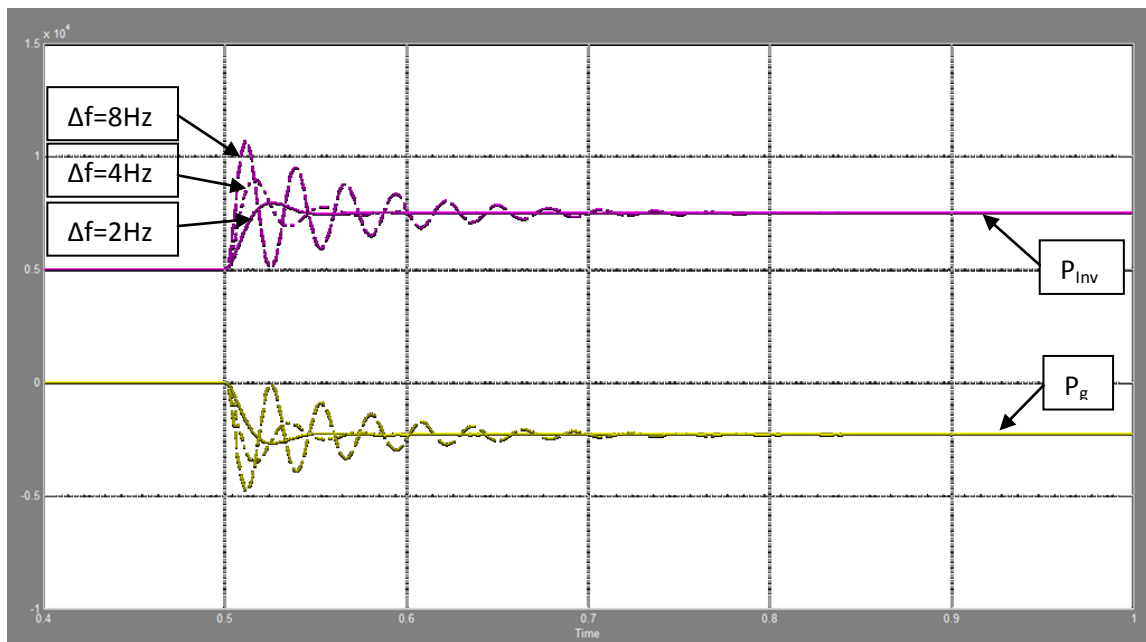


Figure 3.22: Inverter and grid's output active power when  $m_p$  varies (W) vs. Time (s)

Note that the role of the P vs. f droop slope ( $m_p$ ) in the inverter's outer control loop is similar to a proportional controller represented by a constant ( $K_p$ ) which is being used to damp the transient response. In droop control, the zero steady-state of the operating frequency is already gotten without using any integral controller. However, adding a derivative component in the droop control, as Eq. 3.79

and 3.80 show, enhances the system's transient response [12]. The impact of the derivative gains  $m_d$  and  $n_d$  on the system behavior is not investigated in this thesis.

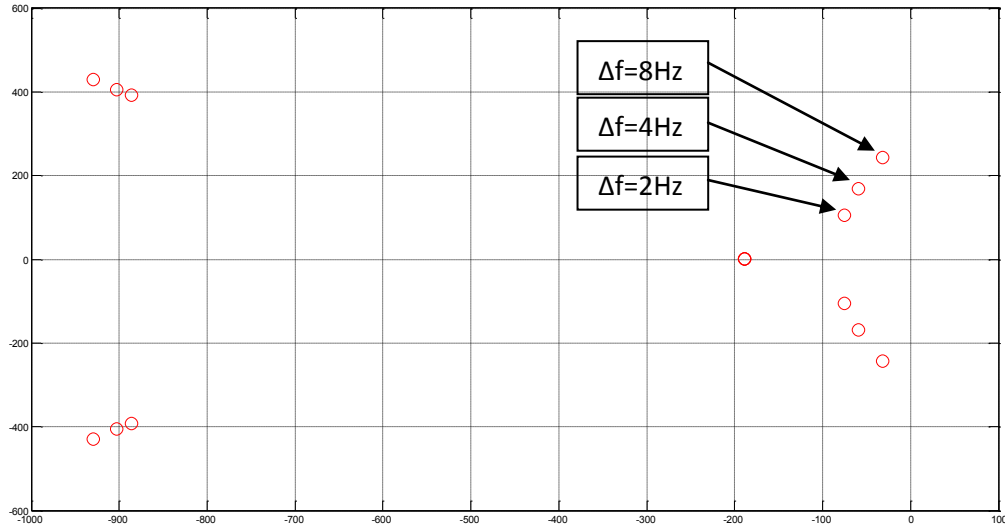


Figure 3.23: Roots of the reduced system model with different values of  $m_p$

Table 3.4: The dominant pole with different  $m_p$

$\Delta f$ (Hz)	$\sigma$	$\omega$ (rad/s)	$\xi$	$t_r$ , 10% to 90% (s)
2	-66.535	119.14	0.4874	10.91m
4	-45.418	181.05	0.2433	5.739m
8	-13.234	250.92	0.053	3.924m

$$\omega_{ref} = \omega_{nL} - m_p P_{Inv} - m_d \frac{dP_{Inv}}{dt} \quad (3.79)$$

$$V_{ref} = V_{nL} - n_q Q_{Inv} - n_d \frac{dQ_{Inv}}{dt} \quad (3.80)$$

### 3.6.1.2 The reactive power droop gain ( $n_q$ ) varies

In order to verify the results shown in Fig. 3.17, time domain simulations have been done. Table 3.5 shows the system parameters for these simulations. Like the active power droop controller, the increasing of the no-load voltage ( $V_{nL}$ ) generates more reactive power at the inverter's output and vice

versa. Therefore, a step-up in  $V_{nL}$  of  $V_{nL} \times \Delta V\% / 100$  occurs at 1s in order to make the inverter provide half of its rated reactive power: 3kVAR. Fig. 3.24 shows the simulations results.

Table 3.5: System parameters for  $n_q$  increasing simulations

Parameter	Value	Unit
$V_g$	120/208	$V_{rms}$
$f_g$	60	Hz
$m_p$	2.513m	rad/s/W
$n_q$	183.8u, 282.8u, 381.8u	V/VAr
$\Delta f$	4	Hz
$\Delta V\%$	0.65, 1, 1.35	%
$X_g$	0.1	$\Omega$
$R_g$	0.23	$\Omega$
$f_c$	30	Hz

It is shown in Fig. 3.24 that the steady-state error decreases, which is the difference to 3 kVAR, when  $n_q$  increases but the system dynamics become more oscillatory leading to instability. Fig. 3.25 shows the root locus of system for the three different values of  $n_q$ . The choice of this parameter should be done in order to satisfy two conditions: Good system transient response and small steady-state error. Until now, the only solution to get zero steady-state error is to increase  $n_q$ . However, to get good dynamics one can decrease the active power droop gain ( $m_p$ ) since the inverter is connected to a fixed frequency voltage source. Fig. 3.26 shows the time domain simulations results for different values of  $\Delta f$  or  $m_p$  while  $\Delta V\%$  or  $n_q$  is fixed to a large value 1.35% that makes the system have the poor transient response shown in Fig. 3.24. One can see in Fig. 3.26 that indeed, decreasing  $m_p$  damps the system transient response and generates good dynamic. Fig. 3.27 shows the system's root locations corresponding to the simulations. The dominant poles move to the left when  $m_p$  decreases.

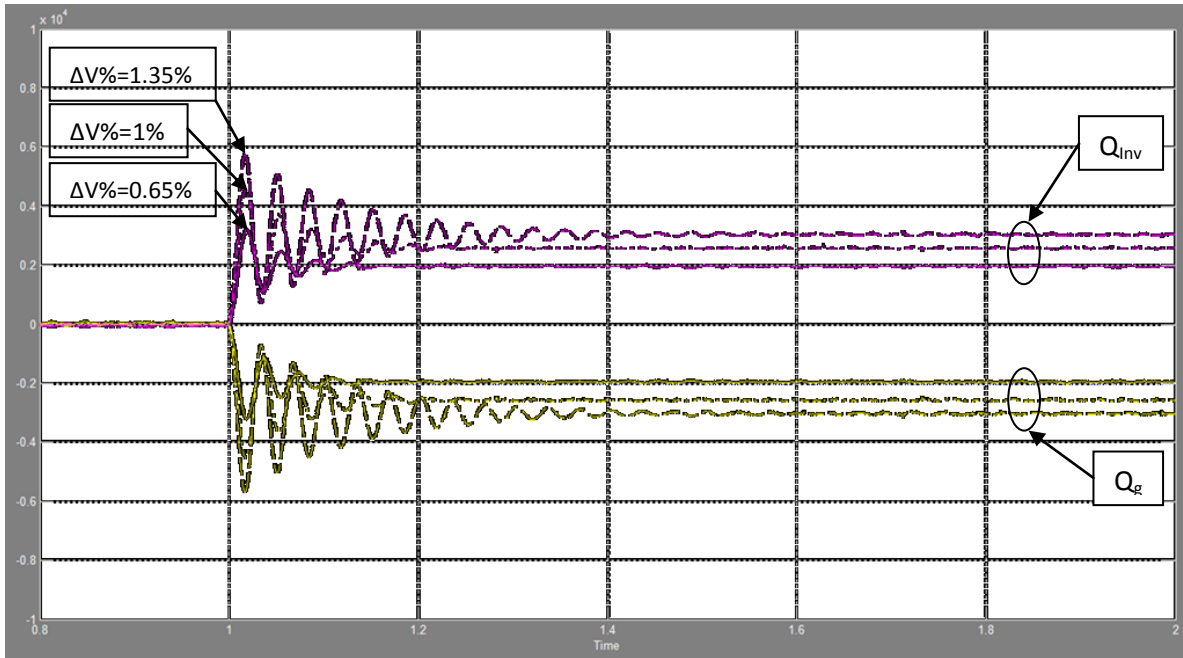


Figure 3.24: Inverter and grid's reactive power when  $n_q$  varies (VAR) vs. Time (s)

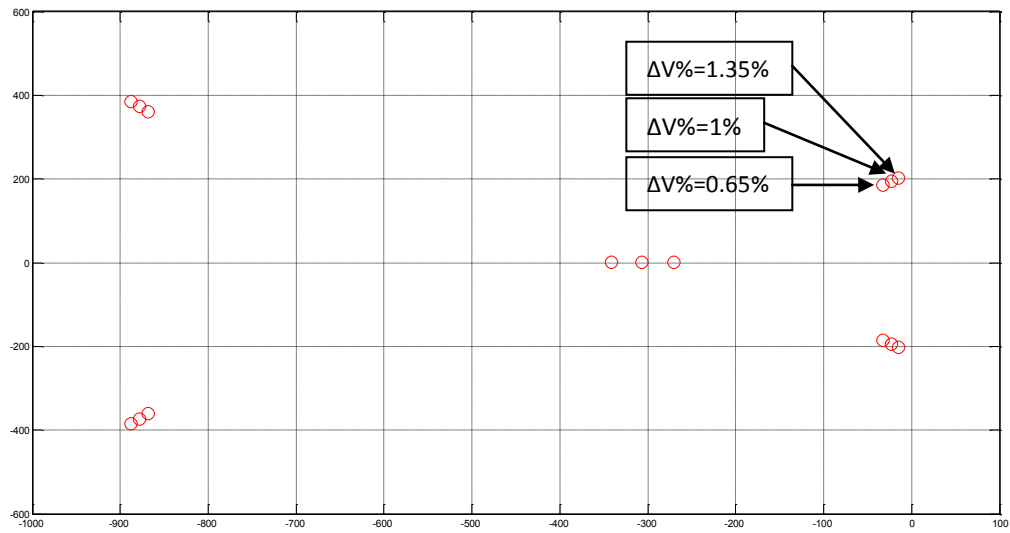


Figure 3.25: Roots of the reduced system model with different values of  $n_q$

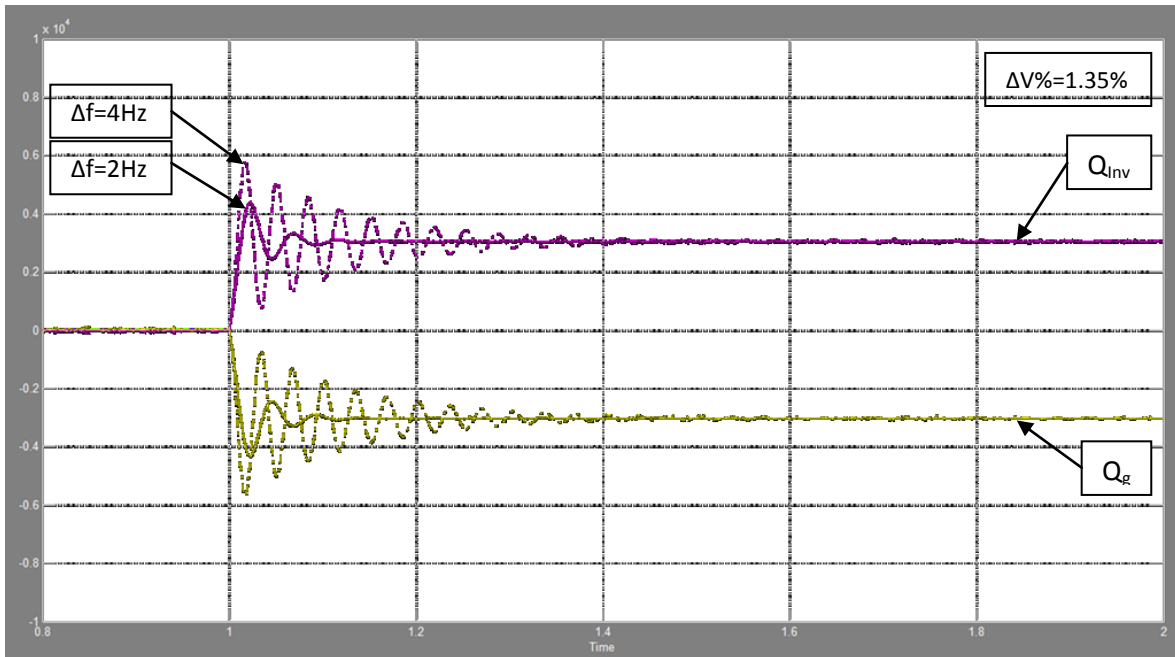


Figure 3.26: Inverter and grid's reactive power damped with  $m_p$  decreasing (VAr) vs. Time (s)

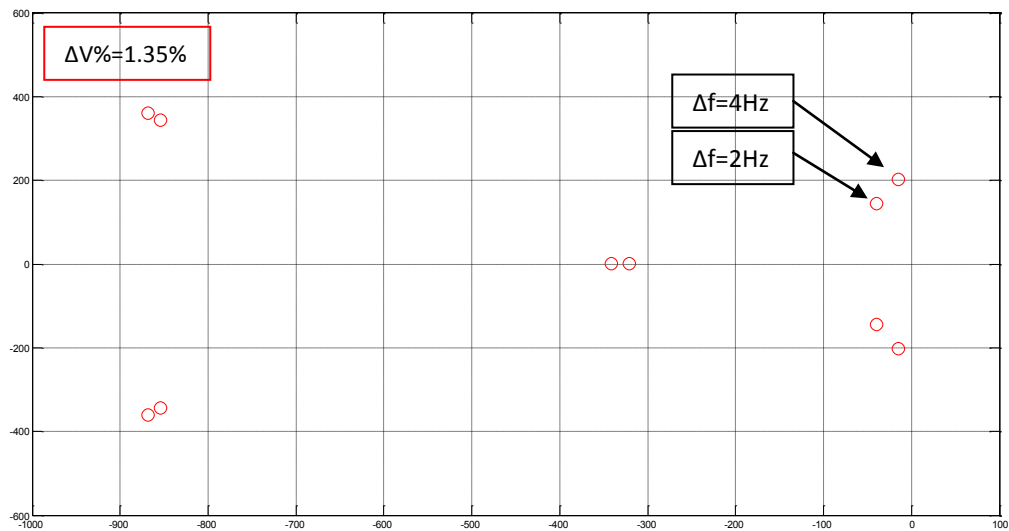


Figure 3.27: Root locus of the reduced system model when decreasing  $m_p$  while  $n_q$  is large

### 3.6.1.3 The Grid impedance ( $Z_g$ ) varies

As mentioned before, the ratio  $X_g/R_g$  has a direct impact on the system dynamics. Moreover, it has an impact on the steady-state response as Fig. 3.28 shows. The increasing of  $X_g$  while  $R_g$  is fixed to  $0.23\Omega$

leads to zero steady-state error since the coupling effect becomes negligible. Note that the simulations used for this section have fixed  $\Delta f$  at 4Hz and  $f_c$  to 30Hz.

The resistive part of the line impedance ( $R_g$ ) damps the transient response when it is increased. Fig. 3.29 shows the dynamics of the system with different values of  $R_g$  but with the same  $X_g/R_g$  ratio of 10. The value of  $R_g$  influences significantly the transient response, more than  $X_g$  but the latter should be considerably bigger than  $R_g$  in order to eliminate the coupling effect and to get zero steady-state error. Fig. 3.30 shows the system's root locus that corresponds to the time domain simulation results shown in Fig. 3.29. There are two pairs of conjugate poles near of the imaginary axes and both influence the dynamics of the system.

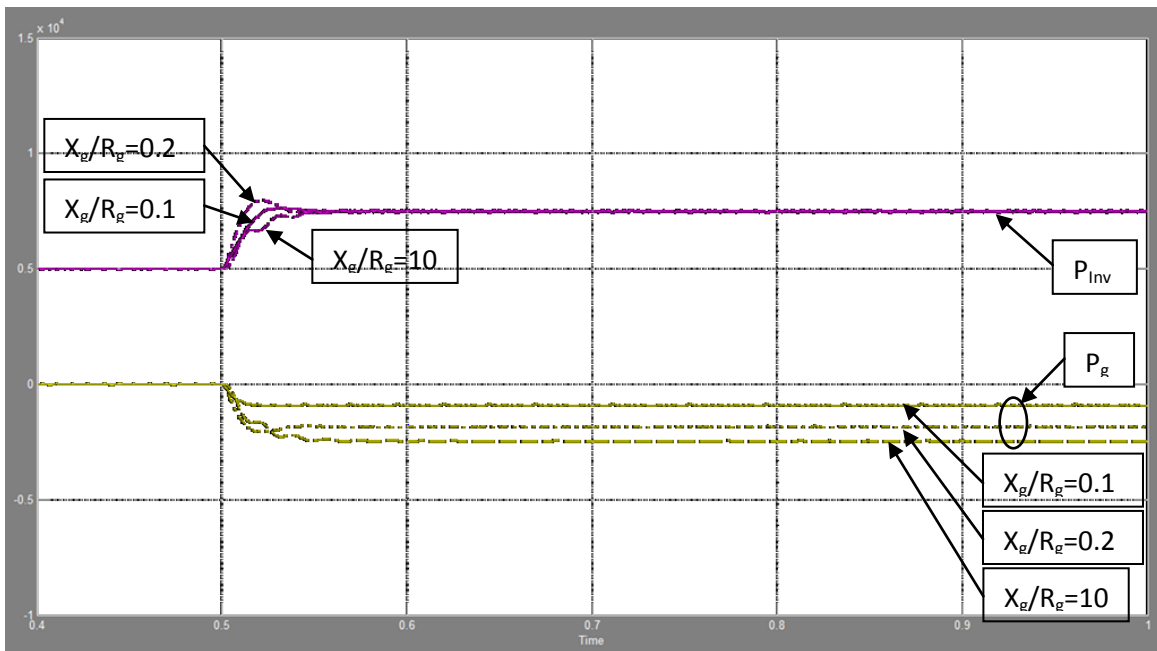


Figure 3.28: Inverter and grid's output active power when the ratio  $X_g/R_g$  varies while  $R_g$  is fixed (W) vs. Time (s)

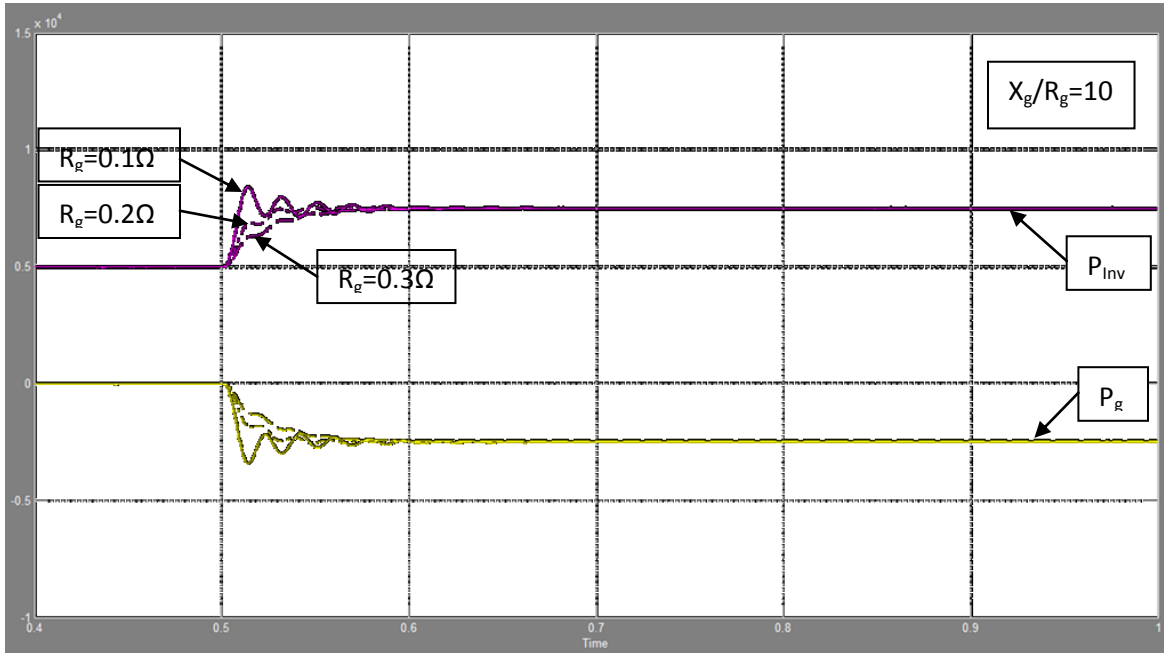


Figure 3.29: Inverter and grid's output active power when  $R_g$  varies while  $X_g/R_g$  is fixed (W) vs. Time (s)

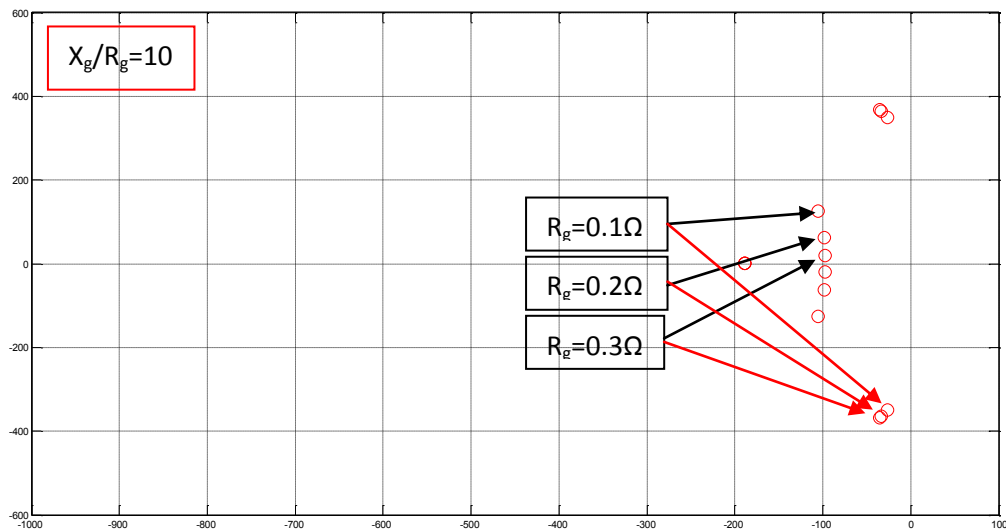


Figure 3.30: Root locus of the reduced system model when  $R_g$  varies while  $X_g/R_g$  is fixed

The values of  $X_g$  and  $R_g$  are not controllable and are usually unknown, hence, enhancing the inverter's transient and steady-state response is impossible when conventional droop and voltage control loops are used. In the next chapter, a well-known approach to enhance the system behavior, called virtual impedance, is analyzed and a new one is proposed.

### 3.6.1.4 The cut-off frequency of the LPF ( $f_c$ ) varies

The low-pass filter used to filter active and reactive power measurements has also an effect on the system dynamics. Time domain simulations have been done to verify this statement. Fig. 3.31 shows the system behavior for three different values of  $f_c$  while the other parameters are fixed as given by Table 3.1. As previously mentioned the LPF adds a zero to the system (Eq. 3.73) which increases its phase margin and making its transient response having less oscillation and shorter settling time as shown in Fig. 3.31. However, the rise time doesn't change for the different values of  $f_c$ . Note that in Fig. 3.31, a step of 1Hz occurs at 0.5s resulting in an active power flow of 2.5kW between the inverter and the grid.

The increasing of  $f_c$  could be also a solution for highly oscillatory transient responses obtained when  $n_q$  is large. Using the same simulation steps as in Fig. 3.24, Fig. 3.33 shows the system behavior in case where a step occurs in  $V_{nl}$ , for two different values of  $f_c$  when  $n_q$  is large ( $\Delta V\%=1.35\%$ ). As one can see in Fig. 3.33, that indeed increasing the cut-off frequency of the LPF damps the system's transient response in time domain and in frequency domain (see Fig. 3.32 and 3.34). However, like  $m_p$  and  $n_q$ , the value of  $f_c$  is limited. Therefore, in purpose to obtain good transients, all the influencing parameters should be adjusted.

Note that the simulation steps are the same as in Fig. 3.26 when  $\Delta f$  is equal to 4Hz,  $X_g$  and  $R_g$  is still equal to  $0.1\Omega$  and  $0.23\Omega$  respectively.

From Eq. 1.4, an increase of  $Z_g$  imposes an increase of the voltage magnitude difference which means an increase of the reactive power droop gain ( $n_q$ ) to get the same value of Q. This means that the increasing of the  $X_g/R_g$  ratio in order to get zero steady-state error in the active power provided to or absorbed from the grid, implies an increase of  $n_q$  to get zero steady-state error in the generated or absorbed



reactive power. However, the magnitude of  $\Delta V\%$  is limited at a certain value by the standards and because it leads the system to instability as shown in Fig. 3.25.

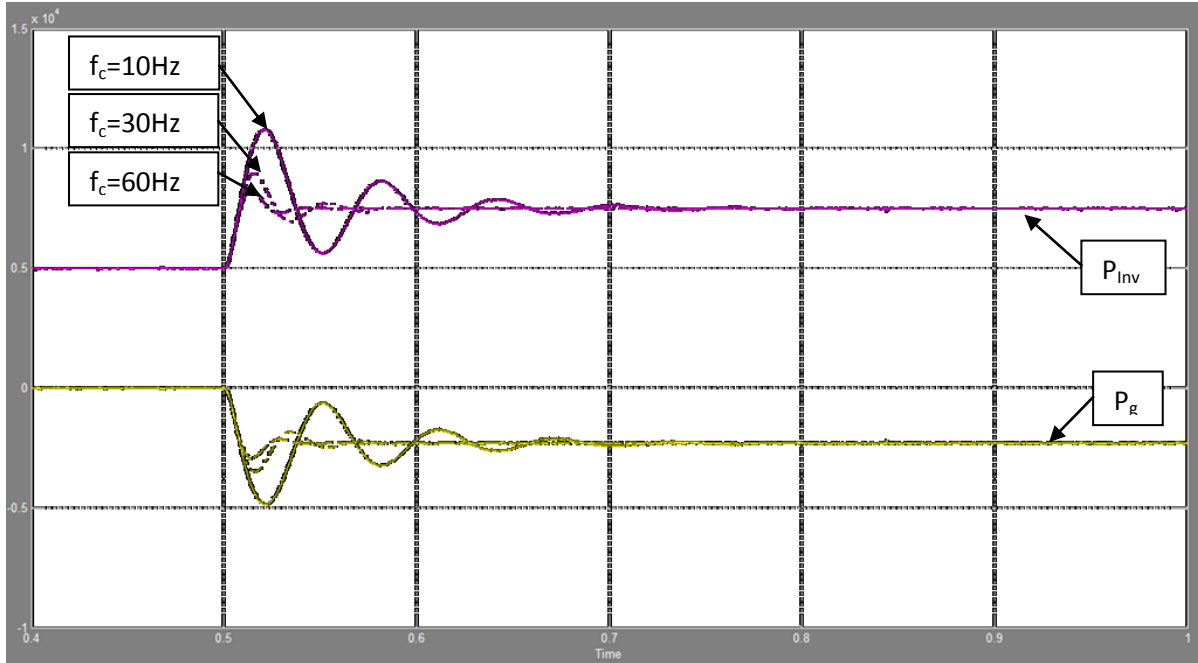


Figure 3.31: Inverter and grid's output active power when  $f_c$  varies (W) vs. Time (s)

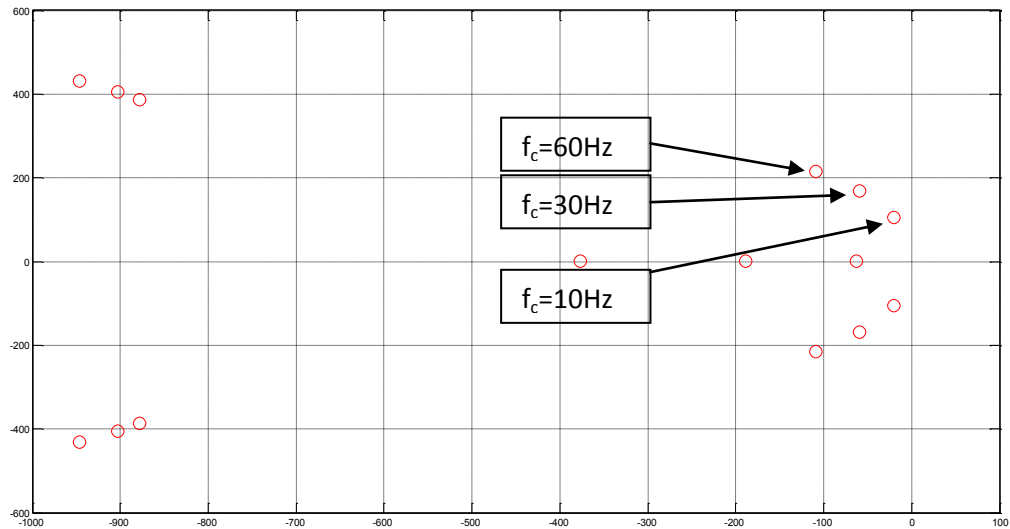


Figure 3.32: Root locus of the reduced system model when  $f_c$  varies

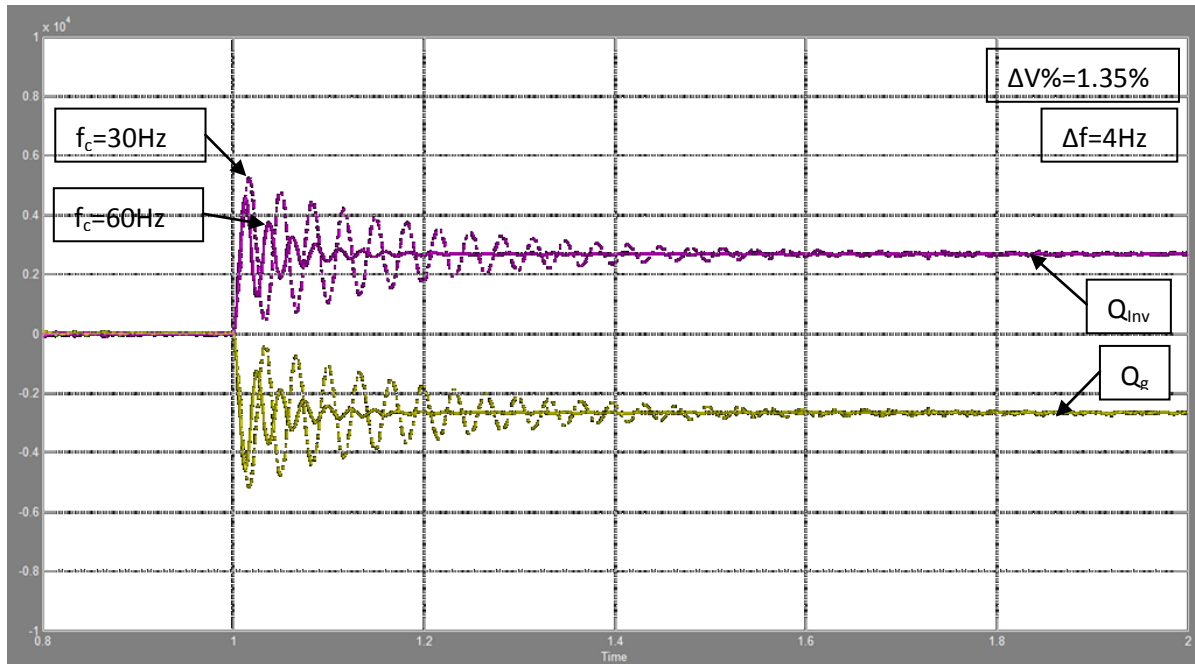


Figure 3.33: Inverter and grid's reactive power damped when  $f_c$  is increased (VAR) vs. Time (s)

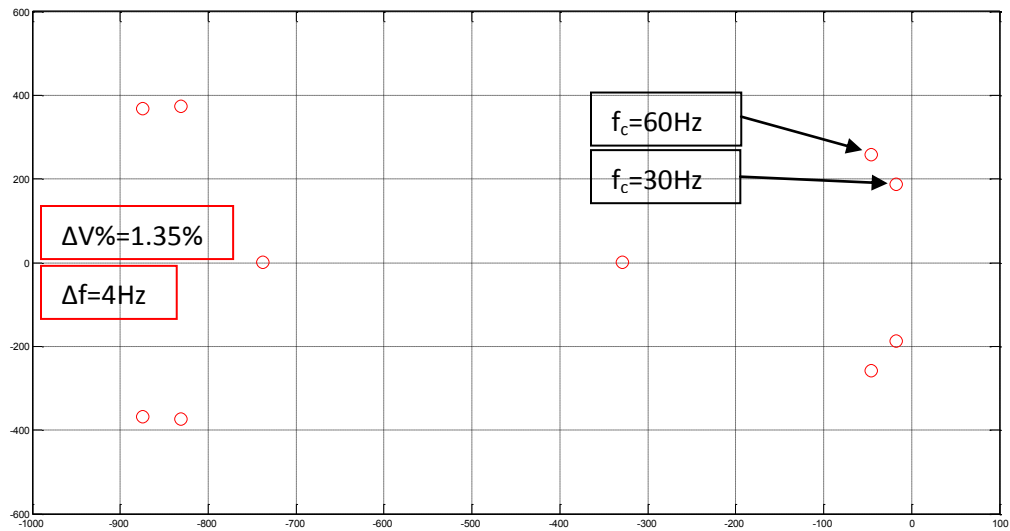


Figure 3.34: Roots of the reduced system model when  $f_c$  is increased while  $n_q$  is large

### 3.6.2 Response of the system during a grid disconnection

Detailed studies and analysis have been done so far for a system composed by a droop controlled voltage source inverter connected to a stiff grid through a feeder showing all the parameters that influence significantly the system transient and steady-state responses. However, the inverter has to be

able to meet the demanded power by the local load during grid disconnection caused by faults or bad power quality.

Fig. 3.35 shows the result of a simulation of the grid disconnection. Initially, the inverter shares its maximum local load ( $S_o=8000+j6000$  VA) with the grid by 50% by selecting properly  $f_{nL}$  and  $V_{nL}$ , then the grid is disconnected at 0.5s. After grid disconnection, the inverter is the only voltage source which feeds its local load and regulates the AC bus voltage and frequency. However, the inverter's droop controllers are still active making the output voltage and frequency decrease. Therefore, droop controllers should be disabled (or designing another loop that regulates the AC voltage amplitude and frequency to be near the rated V and f) in order to get rated voltage amplitude and frequency. Therefore, active and reactive droop gains ( $m_p$  and  $n_q$  respectively) become zero at 0.7s in Fig. 3.35. The latter shows also that the grid disconnection has been done smoothly, and the inverter takes over the local load power demand.

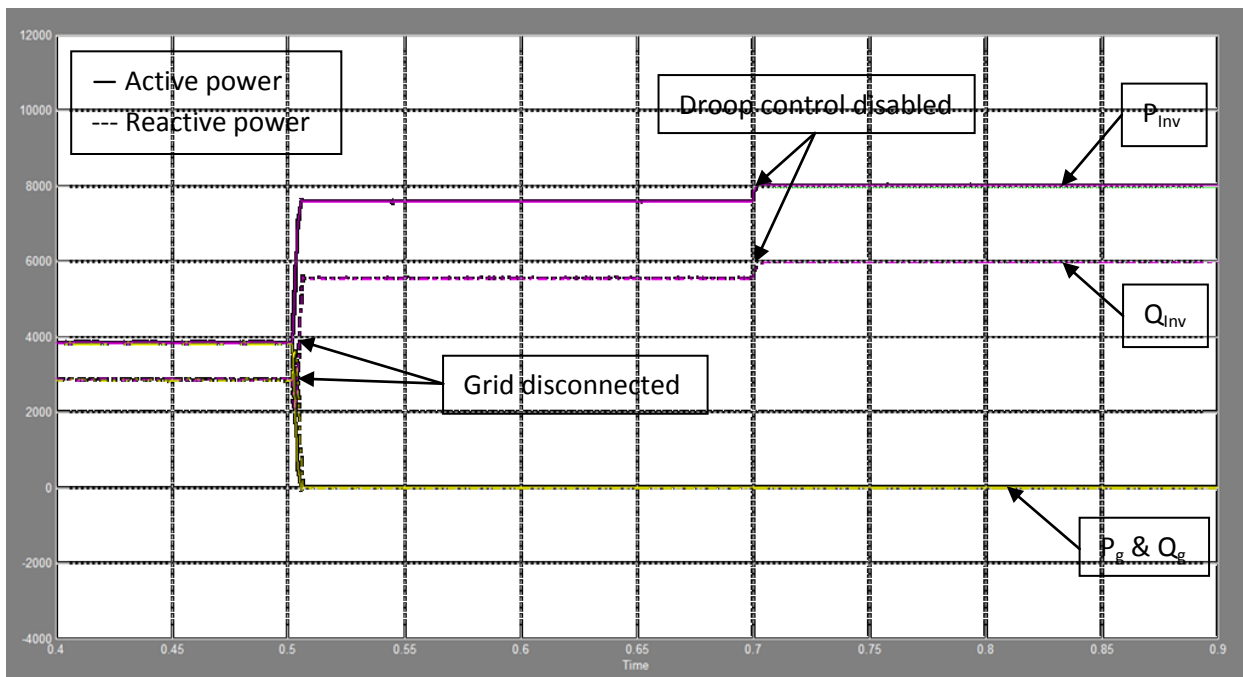


Figure 3.35: Inverter and grid's active and reactive power during grid disconnection (W & VAR) vs. Time (s)

### 3.7 Conclusions

In this chapter, the implementation of the P vs. f and Q vs. V droop controllers in dq control loops of a three phase voltage source inverter has been shown. As the mini-grids have different characteristics in terms of line impedance among the other networks, the line impedance amplitudes are very small which makes the system's dynamics oscillatory, and the ratio  $X_g/R_g$  is smaller than 1 making the P and Q control complicated. A small-signal model of the system has been developed in order to make a detailed analysis and to identify the system elements and parameters which influences directly and significantly the transient response.

Also, a reduced system model was derived neglecting the voltage controller and the LC filter. The roots of this simplified model were compared to the roots of the detailed system model, showing the similarity of their dominant poles.

It has been found out that the most influencing parameters are; the droop gains ( $m_p$  and  $n_q$ ), the line impedance components ( $R_g$  and  $X_g$ ) and the LPF cut-off frequency ( $f_c$ ). The dominant pole of the system moves to the instability region when  $m_p$  and  $n_q$  are increased but contrary to  $f_c$  which damps the system's dynamics when it is increased. The  $X_g/R_g$  ratio influences much the steady-state response rather than the transient response. However, to get the latter damped,  $R_g$  needs to be larger than a certain value.

Time domain simulations have been done to support the frequency domain results. However, besides transient responses verifications, it has been found that some parameters influence significantly the steady-state response of the system. The ratio  $X_g/R_g$  has to be relatively large to get zero steady-state error in the generated or absorbed active power. However, this requires an increase of  $n_q$  to get the same steady-state error in the generated or absorbed reactive power, but at the same time, high values

of  $n_q$  leads the system to instability. This means that the droop control method used in this chapter, which is known as the conventional droop control method, is not reliable and not robust enough to get accurate steady-state and damped transient responses whatever the characteristic of the feeder is. Many new droop control methods have been designed in order to enhance the transient response and to eliminate the coupling effect between P and Q when the line impedance amplitude and angle are small. However, none of these new droop control approaches have taken into consideration the fact that the line impedance is usually unknown.

It has been shown in this chapter that the inverter was capable to feed its local load after the grid disconnection. Since the inverter shared the local inductive load with the grid which implied a changing in the no-load frequency and voltage, the droop controllers should be disabled after the grid disconnection in order to get rated frequency and voltage at the load after grid disconnection.

In the next chapter, the parallel operation of two droop-controlled voltage source inverters is studied. This system called mini-grid is totally autonomous and independent on the main grid where only local energy sources are used to power the customers' loads. This system is more challenging since both inverters are variable voltage and frequency sources.

# Chapter 4 - Parallel operation of two droop controlled three-phase voltage source inverters

## 4.1 Introduction

This chapter focuses on the operation of two droop controlled voltage source inverters connected in parallel through a feeder forming an autonomous micro-grid. In this case, the AC bus at which the voltage source inverters are connected appear as an AC bus with variable voltage magnitude and frequency which makes the system stability more challenging than the case in Chapter 3. The complete small-signal model of the system is presented allowing the detailed analysis of the transient response of the system. Then a conventional virtual impedance control technique is explained and implemented into the inverters' control loops showing its benefits in term of system stability and steady-state response accuracy. A new virtual impedance control loop is proposed making the voltage regulation enhanced. The time domain simulation results of the system, obtained with Simulink using the average model, are presented in order to support the frequency domain analysis.

## 4.2 Small-signal model

The system shown in Fig 4.1 represents a simple micro-grid where two voltage source inverters assist each other in case of power shortage. The inverter #1 is two times bigger than inverter #2 (where the rated apparent power of inverter #1 is;  $S_{max1}=20\text{kVA}$ , so  $S_{max2}=10\text{kVA}$ ). Therefore, as mentioned in Chapter 1, the droop gains of the inverters should be different (from Eq. 1.13,  $m_{p1}=m_{p2}/2$ ) if they are to share load variations proportionally to their power capacities. The inverters have the same voltage

controller and LC Filter designed in Chapter 2, and both use SPWM as modulation scheme. Since the inverters are droop controlled, the voltage amplitude and frequency across the feeder are variable making the design of a system with good transients more challenging. Therefore, a small-signal model needs to be derived so that one can have a better understanding of how the main system parameters affect the system behavior.

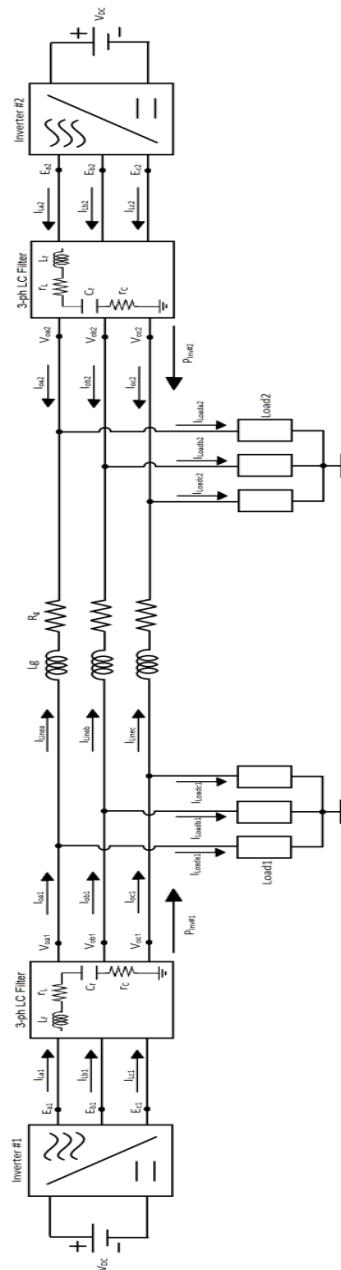


Figure 4.1: Micro-grid composed by two droop controlled inverters, a feeder and local loads

In Fig. 4.1, the dc sources are assumed to be ideal and  $V_{DC}$  is the DC bus voltage amplitude,  $E_{abc1}$  and  $E_{abc2}$  are the output switched voltages of Inverter #1 and Inverter #2,  $I_{Labc1}$  and  $I_{Labc2}$  are the filter inductors' currents of Inverter #1 and Inverter #2,  $V_{oabc1}$  and  $V_{oabc2}$  are the filter capacitors' voltages of Inverter #1 and Inverter #2,  $I_{oabc1}$  and  $I_{oabc2}$  are the output currents of Inverter #1 and Inverter #2,  $I_{Loadabc1}$  and  $I_{Loadabc2}$  are the local loads' currents for Inverter #1 and Inverter #2,  $I_{Lineabc}$  are the line currents drawn from Inverter #1 to Inverter #2,  $L_f$  and  $r_L$  are the filter inductor and its parasite resistance of the LC filter,  $C_f$  and  $r_c$  are the filter capacitor and its parasite resistance of the LC filter,  $L_g$  and  $R_g$  are the feeder's inductor and resistor respectively.

The inverters are droop controlled using the approach P vs. f (active power vs. frequency) and Q vs. V (reactive power vs. voltage amplitude), and the voltage regulation is ensured by a voltage controller (only one voltage control loop is used). Fig. 4.2 shows the block diagram of the system in dq coordinates using Park's transformation.

The idea behind this modeling is to see the effect of every element (LC filter, voltage controller, power controller, line impedance, etc) on the system dynamics and steady-state responses. Finding the conditions for which the line impedance current presents good transient and steady-state responses are the main objectives of this study.

In Fig. 4.2, the line impedance's current is calculated from the output voltages of the Inverters. Where, these latter are controlled and influenced by the power (droop) controllers and the voltage controllers. The line current depends also on the amplitude and the angle of the line impedance.

For the analysis of the system using small-signal models Inverter #1 has been chosen as the reference since it has the biggest ratings. This means that the operating frequency of Inverter #1 is used as an input for Inverter #2 to calculate the phase angle " $\delta$ " between the Inverters' output voltages, then the voltage reference generator of Inverter #2 calculates new values of voltage reference depending on that



angle “ $\delta$ ,” using Eq. 3.17. This allows the output voltages of the Inverters to be on a common reference frame as Fig. 4.3 shows. The values of the output voltage of Inverter #1 and #2 allow the calculation of the line impedance current.

In Fig. 4.2,  $V_{odq1}$  and  $V_{odq2}$  are the voltage across the capacitor filters of inverter #1 and inverter #2,  $I_{odq1}$  and  $I_{odq2}$  are the output currents of inverter #1 and inverter #2,  $I_{Loaddq1}$  and  $I_{Loaddq2}$  are the local loads’ currents of inverter #1 and inverter #2,  $I_{linedq}$  are the feeder’s currents, and  $\omega_1$  is the frequency reference of inverter #1’s P vs. f droop controller.

The blocks “Inv#1” and “Inv#2” in Fig. 4.2 contain the power controller (P&Q droop curves), the voltage reference generator, the voltage controller and the LC filter as Fig. 3.4 shows. Note that the  $\omega_g$  in Fig. 3.4 becomes, in this case,  $\omega_1$  only for inverter #2 in order to calculate  $\delta$ , since inverter #1 has been considered as the reference for the system.

Where, the angle delta “ $\delta$ ” is calculated by the following equation;

$$\delta = \int (\omega_2 - \omega_1) dt \quad (4.16)$$

The angle “ $\delta$ ” is actually the phase angle between the output voltages of Inverter #1 and #2. Note that Inverter #1 has two inputs and three outputs but Inverters #2 has three inputs and only two outputs (see Fig. 4.2).

The system modeling has been done following the same steps in Chapter 3. However, some variations have to be taken into consideration like  $\omega_1$  variations and inverter’s #1 output current variations.

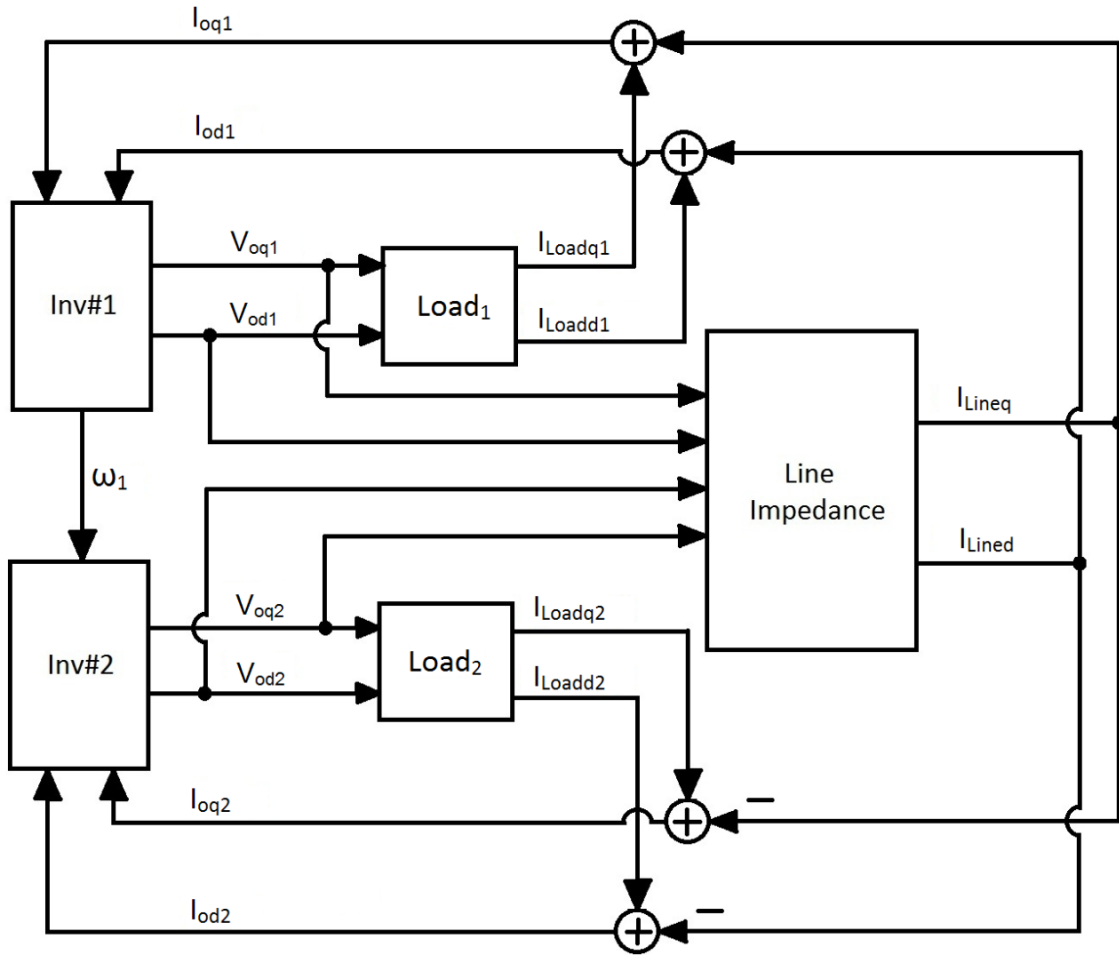


Figure 4.2: The system bloc diagram on dq coordinates

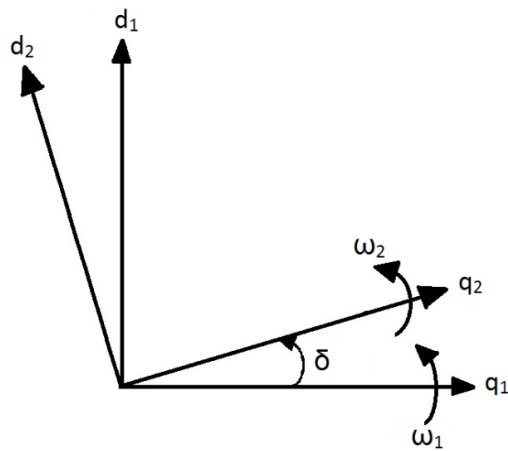


Figure 4.3: Reference frames of the inverters

Based on Eq. 3.8-3.40, the small-signal model of the complete system is as follows.

- Droop controller of inverter #1:

$$\begin{bmatrix} \Delta \dot{P}_{Inv1} \\ \Delta \dot{Q}_{Inv1} \end{bmatrix} = A_{PQ1} \begin{bmatrix} \Delta P_{Inv1} \\ \Delta Q_{Inv1} \end{bmatrix} + B_{PQ1} \begin{bmatrix} \Delta V_{oq1} \\ \Delta V_{od1} \\ \Delta I_{Loadq1} \\ \Delta I_{Loadd1} \\ \Delta I_{Lineq} \\ \Delta I_{Lined} \end{bmatrix} \quad (4.17)$$

$$\begin{bmatrix} \Delta \omega_1 \\ \Delta V_{qref1} \\ \Delta V_{dref1} \end{bmatrix} = C_{PQ1} \begin{bmatrix} \Delta P_{Inv1} \\ \Delta Q_{Inv1} \end{bmatrix} + D_{PQ1} \begin{bmatrix} \Delta V_{oq1} \\ \Delta V_{od1} \\ \Delta I_{Loadq1} \\ \Delta I_{Loadd1} \\ \Delta I_{Lineq} \\ \Delta I_{Lined} \end{bmatrix} \quad (4.18)$$

Where,

$$A_{PQ1} = \begin{bmatrix} -\omega_c & 0 \\ 0 & -\omega_c \end{bmatrix} \quad (4.19)$$

$$B_{PQ1} = \frac{3}{2} \omega_c \begin{bmatrix} (I_{Loadq1o} + I_{Lineqo}) & (I_{Loadd1o} + I_{Linedo}) & V_{oq1o} & V_{od1o} & V_{oq1o} & V_{od1o} \\ -(I_{Load1o} + I_{Linedo}) & (I_{Loadq1o} + I_{Lineqo}) & V_{od1o} & -V_{oq1o} & V_{od1o} & -V_{oq1o} \end{bmatrix} \quad (4.20)$$

$$C_{PQ1} = \begin{bmatrix} -mp_1 & 0 \\ 0 & -nq_1 \\ 0 & 0 \end{bmatrix} \quad (4.21)$$

$$D_{PQ1} = \begin{bmatrix} 0 & 0 & 0 & 0 & 0 & 0 \\ 0 & 0 & 0 & 0 & 0 & 0 \end{bmatrix} \quad (4.22)$$

- Droop controller of inverter #2:

$$\begin{bmatrix} \Delta \dot{\delta} \\ \Delta \dot{P}_{Inv2} \\ \Delta \dot{Q}_{Inv2} \end{bmatrix} = A_{PQ2} \begin{bmatrix} \Delta \delta \\ \Delta P_{Inv2} \\ \Delta Q_{Inv2} \end{bmatrix} + B_{PQ2} \begin{bmatrix} \Delta \omega_1 \\ \Delta V_{oq2} \\ \Delta V_{od2} \\ \Delta I_{Loadq2} \\ \Delta I_{Loadd2} \\ \Delta I_{Lineq} \\ \Delta I_{Lined} \end{bmatrix} \quad (4.23)$$

$$\begin{bmatrix} \Delta V_{qref2com} \\ \Delta V_{dref2com} \end{bmatrix} = C_{PQ2} \begin{bmatrix} \Delta \delta \\ \Delta P_{Inv2} \\ \Delta Q_{Inv2} \end{bmatrix} + D_{PQ2} \begin{bmatrix} \Delta \omega_1 \\ \Delta V_{oq2} \\ \Delta V_{od2} \\ \Delta I_{Loadq2} \\ \Delta I_{Loadd2} \\ \Delta I_{Lineq} \\ \Delta I_{Lined} \end{bmatrix} \quad (4.24)$$

Where,

$$A_{PQ2} = \begin{bmatrix} 0 & -mp_2 & 0 \\ 0 & -\omega_c & 0 \\ 0 & 0 & -\omega_c \end{bmatrix} \quad (4.25)$$

$$B_{PQ2} = \frac{3}{2} \omega_c \begin{bmatrix} -2/3\omega_c & 0 & 0 & 0 & 0 & 0 & 0 \\ 0 & (I_{Loadq2o} - I_{Lineqo}) & (I_{Loadd2o} - I_{Linedo}) & V_{oq2o} & V_{od2o} & -V_{oq2o} & -V_{od2o} \\ 0 & -(I_{Load2o} - I_{Linedo}) & (I_{Loadq2o} - I_{Lineqo}) & V_{od2o} & -V_{oq2o} & -V_{od2o} & V_{oq2o} \end{bmatrix} \quad (4.26)$$

$$C_{PQ2} = \begin{bmatrix} -V_{qref2o} \sin \delta_o - V_{dref2o} \cos \delta_o & 0 & -nq_2 \cos \delta_o \\ V_{qref2o} \cos \delta_o - V_{dref2o} \sin \delta_o & 0 & -nq_2 \sin \delta_o \end{bmatrix} \quad (4.27)$$

$$D_{PQ2} = \begin{bmatrix} 0 & 0 & 0 & 0 & 0 & 0 & 0 \\ 0 & 0 & 0 & 0 & 0 & 0 & 0 \end{bmatrix} \quad (4.28)$$

- Voltage controller:

The same small-signal state space equations of the voltage controller presented in Chapter 3 (Eq. 3.47-3.52) are used in this section.

- LC filter of inverter #1:

$$\begin{bmatrix} \Delta \dot{I}_{Lq1} \\ \Delta \dot{I}_{Ld1} \\ \Delta \dot{V}_{oq1} \\ \Delta \dot{V}_{od1} \end{bmatrix} = A_{LCF1} \begin{bmatrix} \Delta I_{Lq1} \\ \Delta I_{Ld1} \\ \Delta V_{oq1} \\ \Delta V_{od1} \end{bmatrix} + B_{LCF1} \begin{bmatrix} \Delta e_{q1} \\ \Delta e_{d1} \\ \Delta I_{Loadq1} \\ \Delta I_{Loadd1} \\ \Delta I_{Lineq} \\ \Delta I_{Lined} \end{bmatrix} \quad (4.29)$$

$$\begin{bmatrix} \Delta V_{oq1} \\ \Delta V_{od1} \end{bmatrix} = C_{LCF1} \begin{bmatrix} \Delta I_{Lq1} \\ \Delta I_{Ld1} \\ \Delta V_{oq1} \\ \Delta V_{od1} \end{bmatrix} + D_{LCF1} \begin{bmatrix} \Delta e_{q1} \\ \Delta e_{d1} \\ \Delta I_{Loadq1} \\ \Delta I_{Loadd1} \\ \Delta I_{Lineq} \\ \Delta I_{Lined} \end{bmatrix} \quad (4.30)$$

Where,

$$A_{LCF1} = \begin{bmatrix} -r_L/L_f & \omega_o & -1/L_f & 0 \\ -\omega_o & -r_L/L_f & 0 & -1/L_f \\ 1/C_f & 0 & 0 & \omega_o \\ 0 & 1/C_f & -\omega_o & 0 \end{bmatrix} \quad (4.31)$$

$$B_{LCF1} = \begin{bmatrix} 1/L_f & 0 & 0 & 0 & 0 & 0 \\ 0 & 1/L_f & 0 & 0 & 0 & 0 \\ 0 & 0 & -1/C_f & 0 & -1/C_f & 0 \\ 0 & 0 & 0 & -1/C_f & 0 & -1/C_f \end{bmatrix} \quad (4.32)$$

$$C_{LCF1} = \begin{bmatrix} 0 & 0 & 1 & 0 \\ 0 & 0 & 0 & 1 \end{bmatrix} \quad (4.33)$$

$$D_{LCF1} = \begin{bmatrix} 0 & 0 & 0 & 0 & 0 & 0 \\ 0 & 0 & 0 & 0 & 0 & 0 \end{bmatrix} \quad (4.34)$$

- LC filter of inverter #2:

$$\begin{bmatrix} \Delta \dot{I}_{Lq2} \\ \Delta \dot{I}_{Ld2} \\ \Delta \dot{V}_{oq2} \\ \Delta \dot{V}_{od2} \end{bmatrix} = A_{LCF2} \begin{bmatrix} \Delta I_{Lq2} \\ \Delta I_{Ld2} \\ \Delta V_{oq2} \\ \Delta V_{od2} \end{bmatrix} + B_{LCF2} \begin{bmatrix} \Delta e_{q2} \\ \Delta e_{d2} \\ \Delta I_{Loadq2} \\ \Delta I_{Loadd2} \\ \Delta I_{Lineq} \\ \Delta I_{Lined} \end{bmatrix} \quad (4.35)$$

$$\begin{bmatrix} \Delta V_{oq2} \\ \Delta V_{od2} \end{bmatrix} = C_{LCF1} \begin{bmatrix} \Delta I_{Lq2} \\ \Delta I_{Ld2} \\ \Delta V_{oq2} \\ \Delta V_{od2} \end{bmatrix} + D_{LCF1} \begin{bmatrix} \Delta e_{q2} \\ \Delta e_{d2} \\ \Delta I_{Loadq2} \\ \Delta I_{Loadd2} \\ \Delta I_{Lineq} \\ \Delta I_{Lined} \end{bmatrix} \quad (4.36)$$

Where,

$$A_{LCF2} = A_{LCF1} \quad (4.37)$$

$$B_{LCF2} = \begin{bmatrix} 1/L_f & 0 & 0 & 0 & 0 & 0 \\ 0 & 1/L_f & 0 & 0 & 0 & 0 \\ 0 & 0 & -1/C_f & 0 & 1/C_f & 0 \\ 0 & 0 & 0 & -1/C_f & 0 & 1/C_f \end{bmatrix} \quad (4.38)$$

$$C_{LCF1} = C_{LCF2} \quad (4.39)$$

$$D_{LCF1} = D_{LCF2} \quad (4.40)$$

- Local load current:

$$\begin{bmatrix} \Delta I_{Loadqi} \\ \Delta I_{Loaddi} \end{bmatrix} = A_{Loadi} \begin{bmatrix} \Delta I_{Loadqi} \\ \Delta I_{Loaddi} \end{bmatrix} + B_{Loadi} \begin{bmatrix} \Delta V_{oqi} \\ \Delta V_{odi} \end{bmatrix} \quad (4.41)$$

$$\begin{bmatrix} \Delta I_{Loadqi} \\ \Delta I_{Loaddi} \end{bmatrix} = C_{Loadi} \begin{bmatrix} \Delta I_{Loadqi} \\ \Delta I_{Loaddi} \end{bmatrix} + D_{Loadi} \begin{bmatrix} \Delta V_{oqi} \\ \Delta V_{odi} \end{bmatrix} \quad (4.42)$$

Where,

$$A_{Loadi} = \begin{bmatrix} -R_{Loadi}/L_{Loadi} & \omega_o \\ -\omega_o & -R_{Loadi}/L_{Loadi} \end{bmatrix} \quad (4.43)$$

$$B_{Loadi} = \begin{bmatrix} 1/L_{Loadi} & 0 \\ 0 & 1/L_{Loadi} \end{bmatrix} \quad (4.44)$$

$$C_{Loadi} = \begin{bmatrix} 1 & 0 \\ 0 & 1 \end{bmatrix} \quad (4.45)$$

$$D_{Loadi} = \begin{bmatrix} 0 & 0 \\ 0 & 0 \end{bmatrix} \quad (4.46)$$

Where, “i” is for the i<sup>th</sup> inverter.

- Line impedance current:

$$\begin{bmatrix} \Delta \dot{I}_{Lineq} \\ \Delta \dot{I}_{Lined} \end{bmatrix} = A_{Line} \begin{bmatrix} \Delta I_{Lineq} \\ \Delta I_{Lined} \end{bmatrix} + B_{Line} \begin{bmatrix} \Delta V_{oq1} \\ \Delta V_{od1} \\ \Delta V_{oq2} \\ \Delta V_{od2} \end{bmatrix} \quad (4.47)$$

$$\begin{bmatrix} \Delta I_{Lineq} \\ \Delta I_{Lined} \end{bmatrix} = C_{Line} \begin{bmatrix} \Delta I_{Lineq} \\ \Delta I_{Lined} \end{bmatrix} + D_{Line} \begin{bmatrix} \Delta V_{oq1} \\ \Delta V_{od1} \\ \Delta V_{oq2} \\ \Delta V_{od2} \end{bmatrix} \quad (4.48)$$

Where,

$$A_{Line} = \begin{bmatrix} -R_g/L_g & \omega_o \\ -\omega_o & -R_g/L_g \end{bmatrix} \quad (4.49)$$

$$B_{Line} = \begin{bmatrix} 1/L_g & 0 & -1/L_g & 0 \\ 0 & 1/L_g & 0 & -1/L_g \end{bmatrix} \quad (4.50)$$

$$C_{Line} = \begin{bmatrix} 1 & 0 \\ 0 & 1 \end{bmatrix} \quad (4.51)$$

$$D_{Line} = \begin{bmatrix} 0 & 0 & 0 & 0 \\ 0 & 0 & 0 & 0 \end{bmatrix} \quad (4.52)$$

The system is completely linearized. However, one needs to do one more step to get the whole system in one state-space matrix ( $A_{inv}$ ). There are 14 states for Inverter #1 (including local load current), 15 states for Inverter #2 and two states for the feeder (as the following equation shows). From Eq. 4.2-4.37 and Eq. 3.47-52, one can derive the small-signal state-space matrix of the complete system. Note that the matrix ( $A_{inv}$ ) is always an nxn matrix (31-by-31 in this case) unless some eigenvalues could not be calculated. These later are used to analyse the stability and dynamic behaviour of the system.

$$\begin{bmatrix}
 \Delta \dot{P}_{Inv1} \\
 \Delta \dot{Q}_{Inv1} \\
 \Delta \ddot{\varphi}_{q1} \\
 \Delta \ddot{\varphi}_{q1} \\
 \Delta \dot{\varphi}_{q1} \\
 \Delta \ddot{\varphi}_{d1} \\
 \Delta \ddot{\varphi}_{d1} \\
 \Delta \dot{\varphi}_{d1} \\
 \Delta \dot{I}_{Lq1} \\
 \Delta \dot{I}_{Ld1} \\
 \Delta \dot{V}_{oq1} \\
 \Delta \dot{V}_{od1} \\
 \Delta \dot{I}_{Loadq1} \\
 \Delta \dot{I}_{Loadd1} \\
 \Delta \delta \\
 \Delta \dot{P}_{Inv2} \\
 \Delta \dot{Q}_{Inv2} \\
 \Delta \ddot{\varphi}_{q2} \\
 \Delta \ddot{\varphi}_{q2} \\
 \Delta \dot{\varphi}_{q2} \\
 \Delta \ddot{\varphi}_{d2} \\
 \Delta \ddot{\varphi}_{d2} \\
 \Delta \dot{\varphi}_{d2} \\
 \Delta \dot{I}_{Lq2} \\
 \Delta \dot{I}_{Ld2} \\
 \Delta \dot{V}_{oq2} \\
 \Delta \dot{V}_{od2} \\
 \Delta \dot{I}_{Loadq2} \\
 \Delta \dot{I}_{Loadd2} \\
 \Delta \dot{I}_{Lineq} \\
 \Delta \dot{I}_{Lined}
 \end{bmatrix}
 = A_{inv}
 \begin{bmatrix}
 \Delta P_{Inv1} \\
 \Delta Q_{Inv1} \\
 \Delta \ddot{\varphi}_{q1} \\
 \Delta \dot{\varphi}_{q1} \\
 \Delta \varphi_{q1} \\
 \Delta \ddot{\varphi}_{d1} \\
 \Delta \dot{\varphi}_{d1} \\
 \Delta \varphi_{d1} \\
 \Delta I_{Lq1} \\
 \Delta I_{Ld1} \\
 \Delta V_{oq1} \\
 \Delta V_{od1} \\
 \Delta I_{Loadq1} \\
 \Delta I_{Loadd1} \\
 \Delta \delta \\
 \Delta P_{Inv2} \\
 \Delta Q_{Inv2} \\
 \Delta \ddot{\varphi}_{q2} \\
 \Delta \dot{\varphi}_{q2} \\
 \Delta \varphi_{q2} \\
 \Delta \ddot{\varphi}_{d2} \\
 \Delta \dot{\varphi}_{d2} \\
 \Delta \varphi_{d2} \\
 \Delta I_{Lq2} \\
 \Delta I_{Ld2} \\
 \Delta V_{oq2} \\
 \Delta V_{od2} \\
 \Delta I_{Loadq2} \\
 \Delta I_{Loadd2} \\
 \Delta I_{Lineq} \\
 \Delta I_{Lined}
 \end{bmatrix}
 \quad (4.53)$$

Where,





The components of the matrix “ $A_{inv}$ ” are as follows.

$$A_1 = -\omega_c \qquad A_2 = 1.5\omega_c(I_{Loadq1o} + I_{Lineqo})$$

$$A_3 = 1.5\omega_c(I_{Loadd1o} + I_{Linedo}) \qquad A_4 = 1.5\omega_c V_{oq1o}$$

$$A_5 = (3/2)\omega_c V_{od1o} \qquad A_6 = -n_{q1}$$

$$A_7 = -2/T_p \qquad A_8 = -1/T_p^2$$

$$A_9 = K_{pi}\tau/T_p^2/L_f \qquad A_{10} = 2K_{pi}/T_p^2/L_f$$

$$A_{11} = K_{pi}/\tau T_p^2/L_f \qquad A_{12} = -R_f/L_f$$

$$A_{13} = -1/L_f \qquad A_{14} = 1/C_f$$

$$A_{15} = 1/L_{Load1} \qquad A_{16} = -R_{Load1}/L_{Load1}$$

$$A_{17} = 1.5\omega_c(I_{Loadq1o} - I_{Lineqo}) \qquad A_{18} = 1.5\omega_c(I_{Loadd1o} - I_{Linedo})$$

$$A_{19} = 1.5\omega_c V_{oq2o} \qquad A_{20} = 1.5\omega_c V_{od2o}$$

$$A_{21} = -V_{qref2o}\sin\delta_{2o} - V_{dref2o}\cos\delta_{2o} \qquad A_{22} = -n_{q2}\cos\delta_{2o}$$

$$A_{23} = V_{qref2o}\cos\delta_{2o} - V_{dref2o}\sin\delta_{2o} \qquad A_{24} = -n_{q2}\sin\delta_{2o}$$

$$A_{25} = 1/L_{Load2} \qquad A_{26} = -R_{Load2}/L_{Load2}$$

$$A_{27} = 1/L_g \qquad A_{28} = -R_g/L_g$$

$$A_{29} = \omega_o \qquad A_{30} = -m_{p1}$$

$$A_{31} = -m_{p2}$$

The eigenvalues of the matrix ( $A_{inv}$ ) have been calculated by Matlab. As mentioned in Chapter 3, the initial values have been gotten from Simulink/Matlab simulation of the average model (dq model) of the system shown in Fig. 4.2. The results of the latter will be verified in the next section. The .m file of Matlab which contains the small-signal state-space model of the complete system is given in the Appendix-C.

As in chapter 3, the reduced system small-signal model has been derived in order to verify the statement in [12] regarding the neglect of the high frequency poles' elements in case of two parallel inverters. Based on Eq. 4.40 and 4.41, the simplified system model is given by Eq. 4.42. The characteristic equation of the latter is a 7<sup>th</sup> order function since  $A_{rinv}$  is a 7x7 matrix, and its roots have been calculated by Matlab and compared to the roots of the complete system mode, as shown in the following section.

$$\Delta V_{oq1} = \Delta V_{qref1} ; \Delta V_{od1} = \Delta V_{dref1} \quad (4.55)$$

$$\Delta V_{oq2} = \Delta V_{qref2} ; \Delta V_{od2} = \Delta V_{dref2} \quad (4.56)$$

$$\begin{bmatrix} \Delta \dot{P}_{Inv1} \\ \Delta \dot{Q}_{Inv1} \\ \Delta \dot{\delta} \\ \Delta \dot{P}_{Inv2} \\ \Delta \dot{Q}_{Inv2} \\ \Delta \dot{I}_{Lineq} \\ \Delta \dot{I}_{Lined} \end{bmatrix} = A_{rinv} \begin{bmatrix} \Delta P_{Inv1} \\ \Delta Q_{Inv1} \\ \Delta \delta \\ \Delta P_{Inv2} \\ \Delta Q_{Inv2} \\ \Delta I_{Lineq} \\ \Delta I_{Lined} \end{bmatrix} \quad (4.57)$$

Where,

$$A_{rinv} = \begin{bmatrix} A_{r1} & A_{r2} & 0 & 0 & 0 & A_{r3} & A_{r4} \\ 0 & A_{r5} & 0 & 0 & 0 & A_{r4} & -A_{r3} \\ A_{r6} & 0 & 0 & A_{r7} & 0 & 0 & 0 \\ 0 & 0 & A_{r8} & A_{r1} & A_{r9} & A_{r10} & A_{r11} \\ 0 & 0 & A_{r12} & 0 & A_{r13} & A_{r11} & -A_{r10} \\ 0 & A_{r14} & A_{r15} & 0 & A_{r16} & A_{r17} & A_{r18} \\ 0 & 0 & A_{r19} & 0 & A_{r20} & -A_{r18} & A_{r17} \end{bmatrix} \quad (4.58)$$

The components of the matrix  $A_{rinv}$  are given by the followings;

$$\begin{aligned}
 A_{r1} &= -\omega_c & A_{r2} &= -1.5\omega_c I_{Lineqo} n_{q1} \\
 A_{r3} &= 1.5\omega_c V_{oq1o} & A_{r4} &= 1.5\omega_c V_{od1o} \\
 A_{r5} &= -\omega_c - 1.5\omega_c I_{Linedo} n_{q1} & A_{r6} &= m_{p1} \\
 A_{r7} &= -m_{p2} & A_{r8} &= -1.5\omega_c (I_{Lineqo} (-V_{qref2o} \sin(\delta_o) - V_{dref2o} \cos(\delta_o)) + I_{Linedo} (V_{qref2o} \cos(\delta_o) - V_{dref2o} \sin(\delta_o))) \\
 A_{r10} &= -1.5\omega_c V_{oq2o} & A_{r9} &= 1.5\omega_c n_{q2} (I_{Lineqo} \cos(\delta_o) + I_{Linedo} \sin(\delta_o)) \\
 A_{r11} &= -1.5\omega_c V_{od2o} & A_{r12} &= 1.5\omega_c (I_{Linedo} (-V_{qref2o} \sin(\delta_o) - V_{dref2o} \cos(\delta_o)) - I_{Lineqo} (V_{qref2o} \cos(\delta_o) - V_{dref2o} \sin(\delta_o))) \\
 A_{r14} &= -n_{q1}/L_g & A_{r13} &= -\omega_c + 1.5\omega_c n_{q2} (I_{Lineqo} \sin(\delta_o) - I_{Linedo} \cos(\delta_o)) \\
 A_{r16} &= n_{q2} \cos(\delta_o)/L_g & A_{r15} &= -(-V_{qref2o} \sin(\delta_o) - V_{dref2o} \cos(\delta_o))/L_g \\
 A_{r17} &= -R_g/L_g & A_{r18} &= \omega_o \\
 A_{r20} &= n_{q2} \sin(\delta_o)/L_g & A_{r19} &= -(V_{qref2o} \cos(\delta_o) - V_{dref2o} \sin(\delta_o))/L_g
 \end{aligned}$$

The .m file of Matlab which contains the small-signal state-space model of the reduced system is given in the Appendix-D.

### 4.3 Schematics of the simulation file

Based on Fig. 4.1 and 4.2, the schematics of Simulink/Matlab simulation files of the complete system and the average model are shown in Fig. 4.4 and 4.5, respectively.

Note that in order to make the simulations run fast, the three-phase inverters, in Fig. 4.4, are represented by two three-phase controllable AC voltage sources. The switching harmonics in this case are neglected but this is not a problem since the main interest is the investigation of the stability of the

system and the behavior of the active and reactive power flows, which are not influenced by the harmonics.

The dq model shown in Fig. 4.5 has three main blocks (inverter #1, inverter #2 and the line impedance). Where, each block contains its appropriate mathematical model derived in the previous chapter.

In order to verify the mathematical model of the system, a comparison between the results (the output active power of the two inverters) obtained after running a simulation, using the same parameters, of the Simulink/Matlab real simulation file shown in Fig. 4.4 and the dq model shown in Fig. 4.5, which has been also ran on Simulink/Matlab.

The curves shown in Fig 4.6 and 4.7 describe the transient and the steady-state responses of the inverter's output active and reactive power respectively when a step in the inverter #2's local load of +7.5kW occurred at 0.2s. Note that the initial local loads of Inverter #1 and inverter #2 are 5kW and 2.5kW, respectively. The system parameters in these simulations are given in Table 4.1 but  $f_{nL1}$  is equal to 62Hz.

As one can see in Fig 4.6, the two inverters share the load variation with respect to their ratings as the total power supplied by Inverter #1 is twice that of Inverter #2. Since the load change has occurred at the inverter #2 side, the latter has to take over the big part of the transient. That is why  $P_{inv2}$  has a shorter rising time. The inaccuracy of the steady-state values is due to the small  $X_g/R_g$  ratio used in that simulation which generates a coupling between P and Q after the load step.

Finally, the dq average system model (Fig 4.5) gives similar results as the simulation file of the system (Fig. 4.4); hence the modeling that has been done is correct.

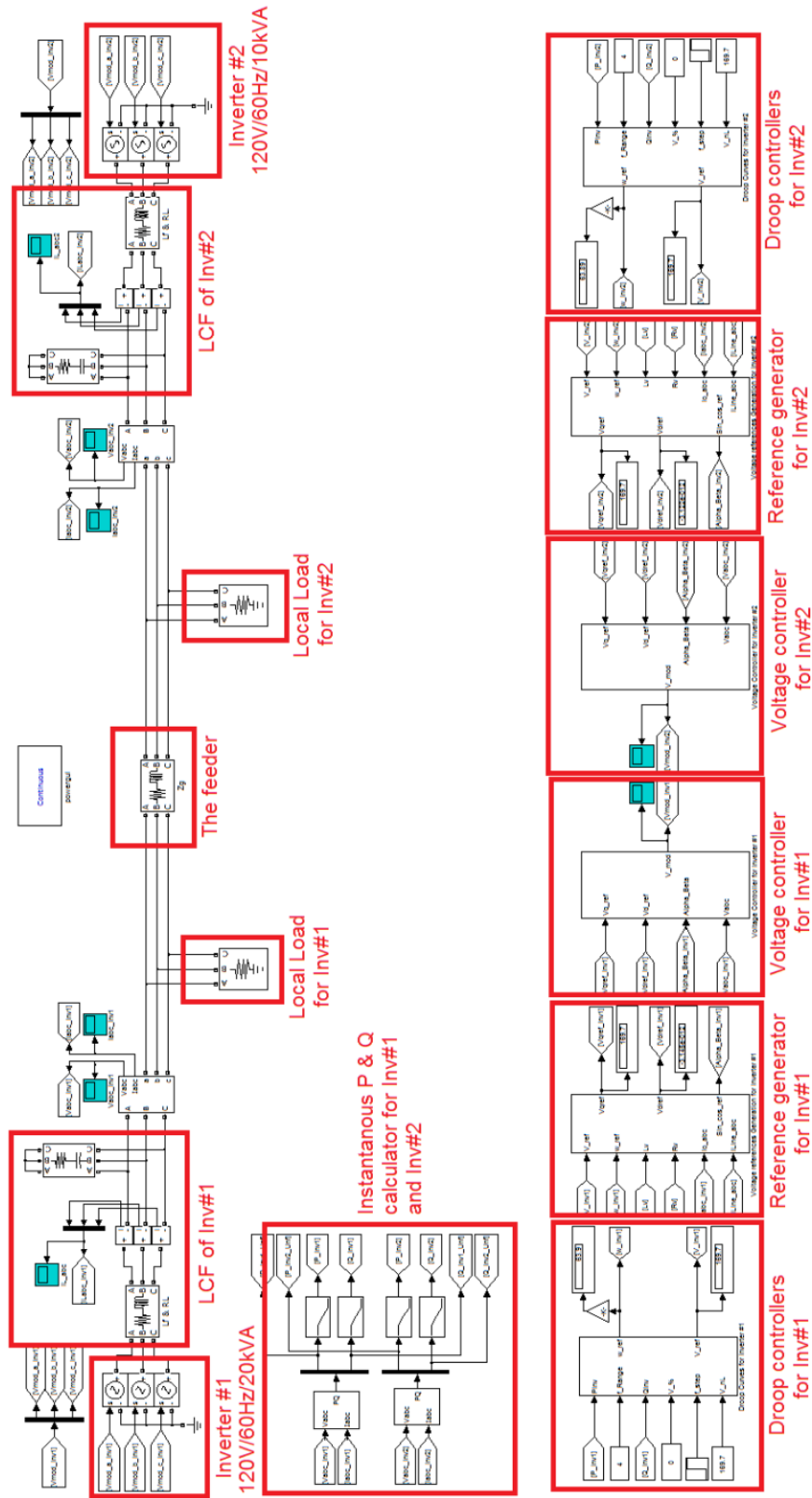


Figure 4.4: The system's Simulink/Matlab simulation file scheme

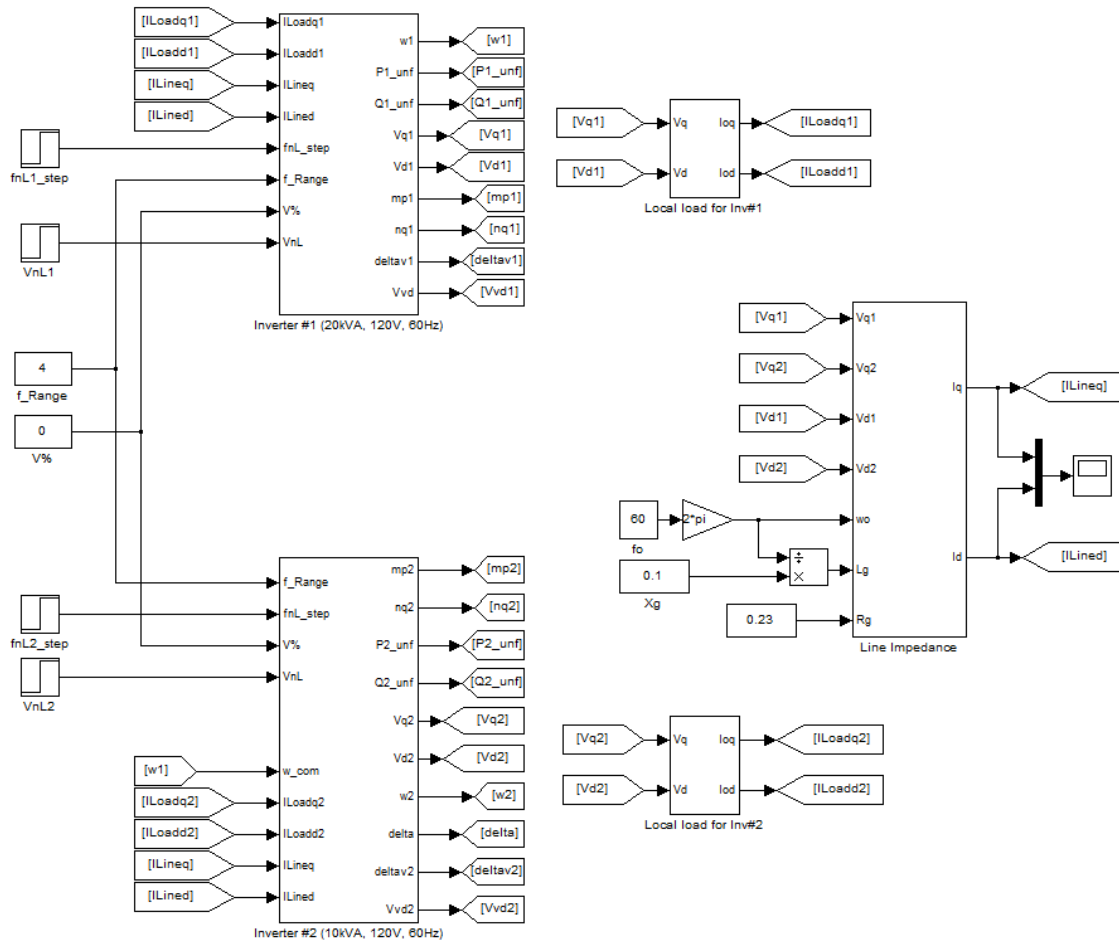


Figure 4.5: The system's dq model in Simulink/Matlab

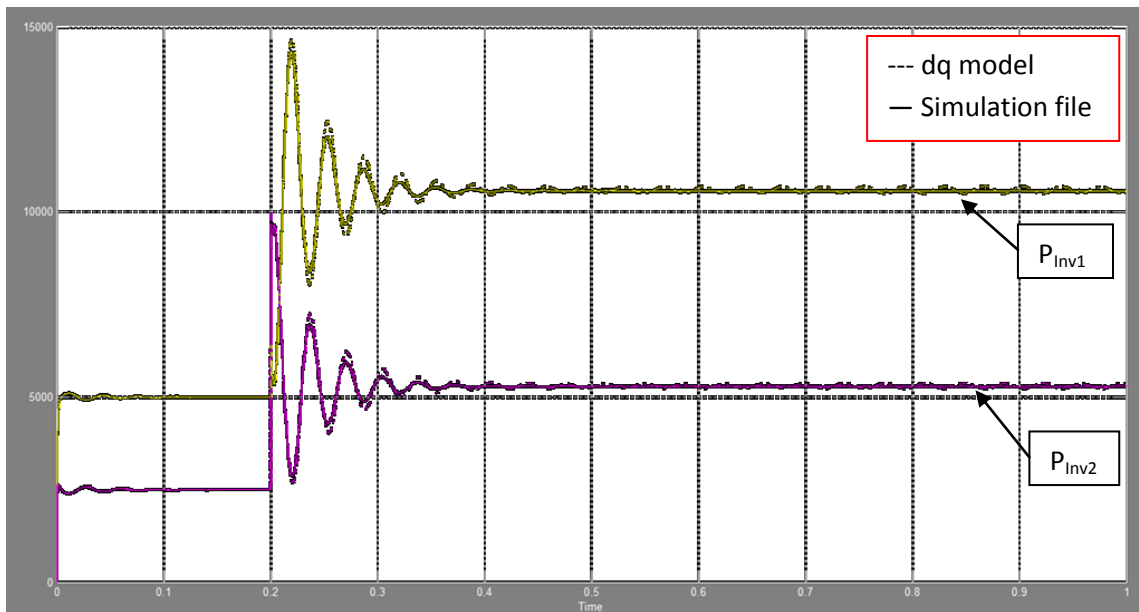


Figure 4.6: Inverters' output active power (W) vs. Time (s)

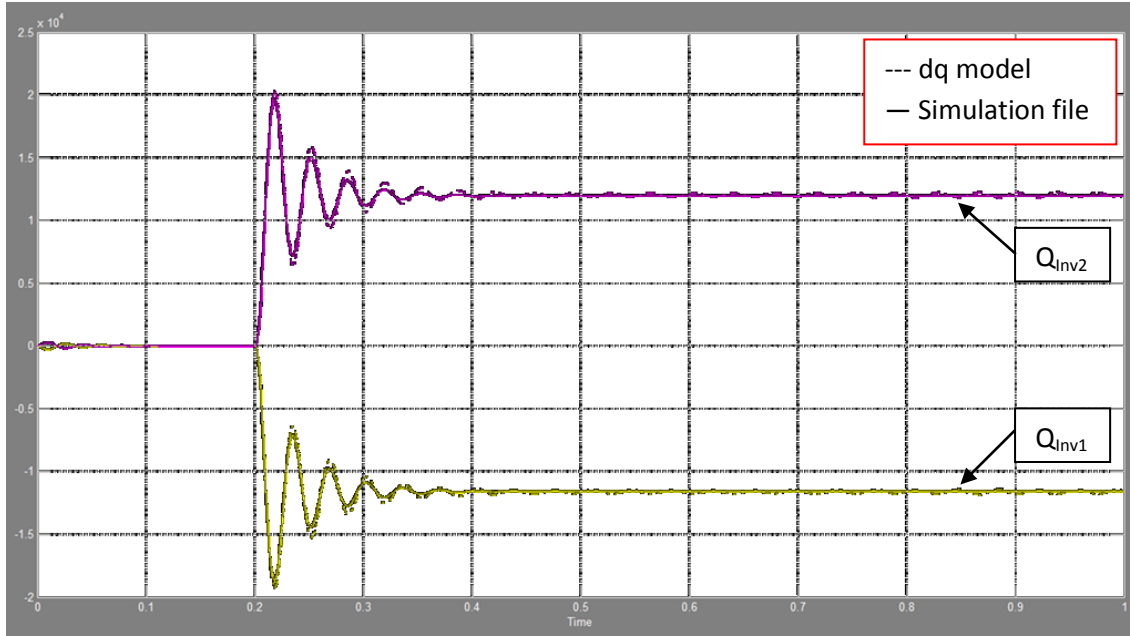


Figure 4.7: Inverters' output reactive power (VAr) vs. Time (s)

#### 4.4 Root locus of the system to various parameters

The location of the roots of Eq. 4.38 and 4.42 are shown in Fig. 4.8 and 4.9 respectively. The system parameters are given in Table 4.1. The only variation occurred in the no-load frequency of inverter #1 of +3Hz in order to generate a line active power flow of 5kW, from inverter #1 to inverter #2. Note that the local load power demand is null for both inverters.

As one can see in Fig. 4.9, only low-frequency poles are presented since the voltage controller and the LC filter have been disregarded in the model. In Fig 4.8, all poles are shown and grouped in three clusters. As in Chapter 3 (Fig. 3.13), the poles in cluster #2 are mainly influenced by the LC filter, the cluster #3 contains poles which are directly influenced by the voltage controller, and in cluster #1 (as in Fig. 4.9) there are the low-frequency poles that are mainly dictated by the droop controllers and the output impedance including the feeder and the LC filter.



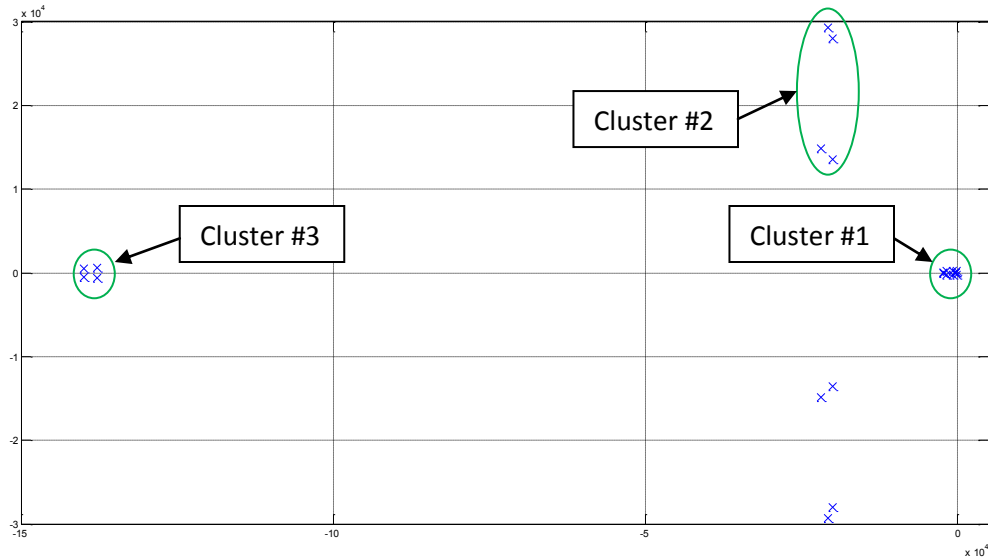


Figure 4.8: Location of the roots of the complete system small-signal model

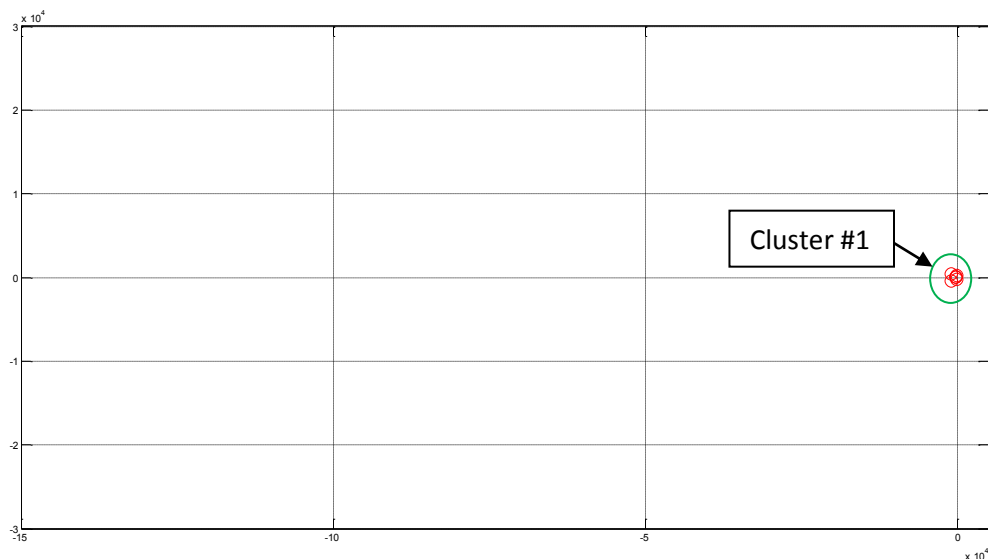


Figure 4.9: Location of the roots of the reduced system small-signal model

In order to compare the location of the roots of the complete and the reduced system small-signal models given by Eq. 4.38 and 4.42 respectively, Fig. 4.10 shows a zoom on cluster #1 of Fig. 4.8 and 4.9. The dominant poles of the two models are similar but the intermediate complex poles which are around  $-800 \pm j300$  are significantly different due to the difference of the output impedance in the two models. Those intermediate poles are significantly influenced by the LC filter components, explaining the reason

why the same poles have different values in the complete and the reduced system models. Recall that the LC filter has been neglected in the latter.

Table 4.1: system parameters

Parameter	Value	Unit
$V_r$	120/208	$V_{rms}$
$f_r$	60	Hz
$m_{p1}$	1.257m	rad/s/W
$m_{p2}$	2.513m	rad/s/W
$n_{q1}$ & $n_{q2}$	0	V/VAr
$\Delta f$	4	Hz
$f_{nL1}$	65	Hz
$f_{nL2}$	62	Hz
$X_g$	0.1	$\Omega$
$R_g$	0.23	$\Omega$
$f_c$ (LPF cut-off frequency)	30	Hz

Where,  $V_r$  and  $f_r$  are the rated voltage amplitude and the rated frequency respectively.

The roots of the reduced system model move the same way as the complete system model when some parameters are varied (see Fig. 4.12). However, it doesn't give accurate values of the system low-frequency poles which make the droop controller and virtual impedance control loop design inaccurate.

Note that in Fig. 4.10, the real pole of the reduced system model represents three poles with exactly the same values which make sense since  $A_{rinv}$  is a 7x7 matrix, hence seven poles must be shown.

In order to verify the effect of the LC filter's components on the system dynamics or low-frequency poles, some variations have been done in  $L_f$  and  $C_f$  while the LC filter's cut-off frequency ( $f_{LCF}$ ) is fixed at 2 kHz as designed in Chapter 2. In Fig. 4.11, one can see the displacement of the system low-frequency poles while  $L_f$  is increased. As deduced in Chapter 3, the intermediate complex poles in Fig. 4.11 are very sensitive to the LCF components' variation. However, the dominant poles are practically unchanged.

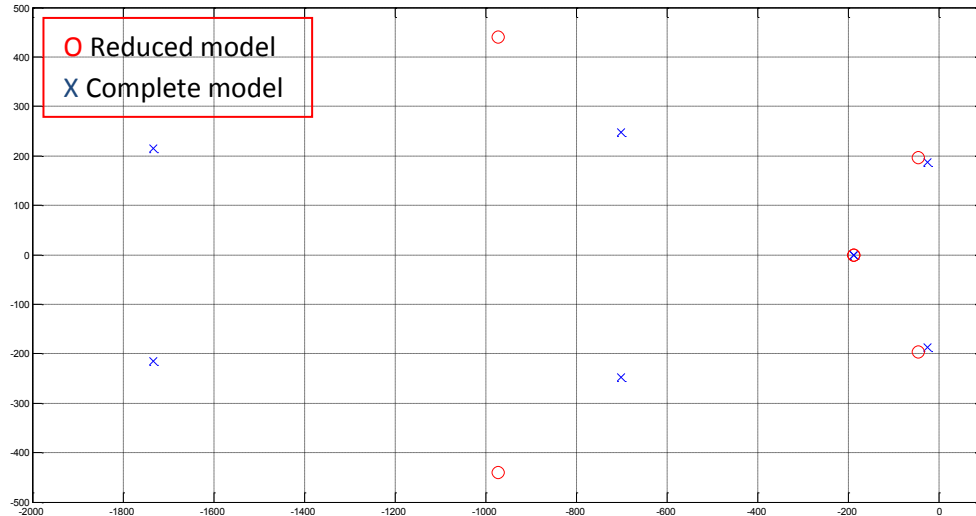


Figure 4.10: Low frequency poles of the complete and reduced system's small-signal models

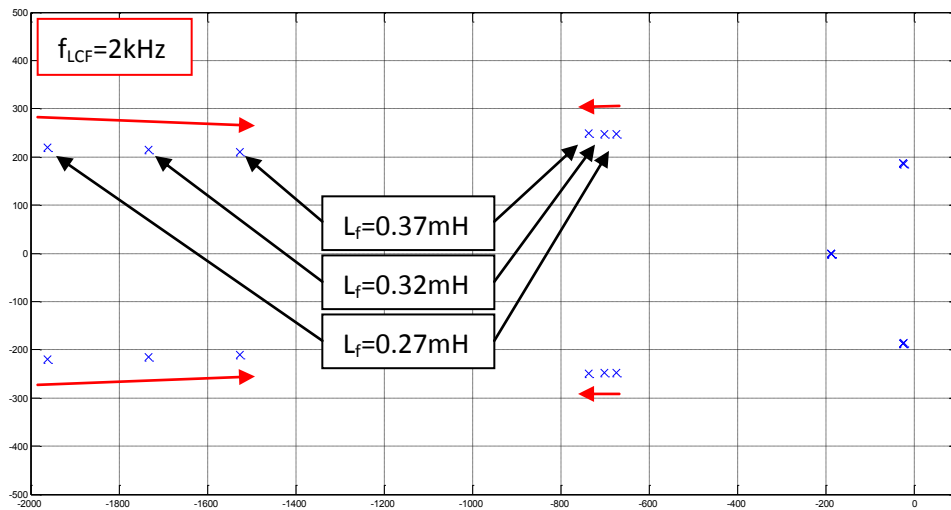


Figure 4.11: Low frequency poles of the complete system model when increasing  $L_f$  while  $f_{LCF}$  is fixed at 2kHz

The most important poles which indicate how a system behaves during transients are the dominant poles. Since the latter are mostly unaffected by the LCF, as shown in Fig. 4.11, the reduced system model can be used in the frequency domain studies of the system. Therefore, only Eq. 4.42 is used for further system dynamics' studies.

As mentioned previously, the dominant poles are mainly influenced by three elements: The droop controllers' gains, the line impedance and the LPF. In order to see the influence of those elements on

the system dynamics, a root locus has been obtained showing the poles displacement when those elements' parameters are varied. Setting all the system's parameters according to Table 4.1, Fig. 4.12 shows the root locus of the reduced system model when  $\Delta f$  (of both inverters) is varied from 1Hz to 14Hz. Note that the initial values have been obtained after a step of +3Hz in  $f_{nL1}$  when  $\Delta f$  is set to 4Hz in order to draw 5kW from inverter #1 to inverter #2, then proper eigenvalues are obtained for different values of  $\Delta f$ . The root locus of the complete system model is shown also in Fig. 4.12 just for comparison. It is shown that indeed both system models' poles move similarly when increasing the active power droop controller gains. However, as Fig. 4.12 shows, the reduced system becomes unstable when  $\Delta f$  is above 9Hz whereas the complete system becomes unstable when  $\Delta f$  is above 6Hz. However, since the value of  $\Delta f$  will be kept small, either system model can be used.

As deduced in Chapter 3, the system tends to instability when increasing the active power droop controller gains ( $m_{p1}$  &  $m_{p2}$ ).

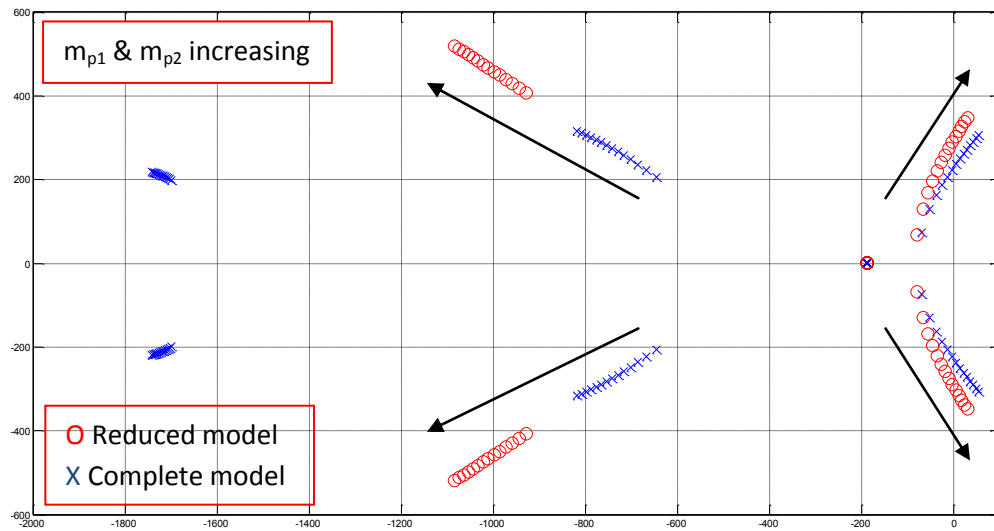


Figure 4.12: Roots of the reduced and the complete system models when  $m_{p1}$  &  $m_{p2}$  are increased

To study the effect of the reactive power droop gains ( $n_{q1}$  &  $n_{q2}$ ) on the system behavior, the system parameters are set as Table 4.2 shows. By increasing  $\Delta V\%$  from 0% to 1.5% for both inverters, the reduced system becomes unstable when  $\Delta V\%$  is above 0.9% as seen in Fig. 4.13.

Note that the initial values have been obtained after a step of  $+\Delta V$  occurred in  $V_{nL1}$  to draw some reactive power from inverter #1 toward inverter #2 through the feeder, then proper eigenvalues are obtained for different values of  $\Delta V\%$ .

The system behavior is very sensitive to the reactive droop controller gain's variation due to the actual  $X_g/R_g$  ratio. The bigger the latter is the bigger is the value of  $\Delta V$  that could be implemented.

Table 4.2: system parameters when  $n_{q1}$  &  $n_{q2}$  are increased

Parameter	Value	Unit
$V_r$	120/208	$V_{rms}$
$f_r$	60	Hz
$m_{p1}$	1.257m	rad/s/W
$m_{p2}$	2.513m	rad/s/W
$\Delta f$	4	Hz
$f_{nL1}$ & $f_{nL2}$	62	Hz
$V_{nL1}$	$169.7+\Delta V$	V
$V_{nL2}$	169.7	V
$X_g$	0.1	$\Omega$
$R_g$	0.23	$\Omega$
$f_c$ (LPF cut-off frequency)	30	Hz

Fig. 4.14 shows the system's root locus when increasing the  $X_g/R_g$  ratio from 0.1 to 15 while the resistive component of the line impedance ( $R_g$ ) is fixed at  $0.23\Omega$ . Like what has been obtained in chapter 3, the system never becomes unstable when the  $X_g/R_g$  ratio is increased.

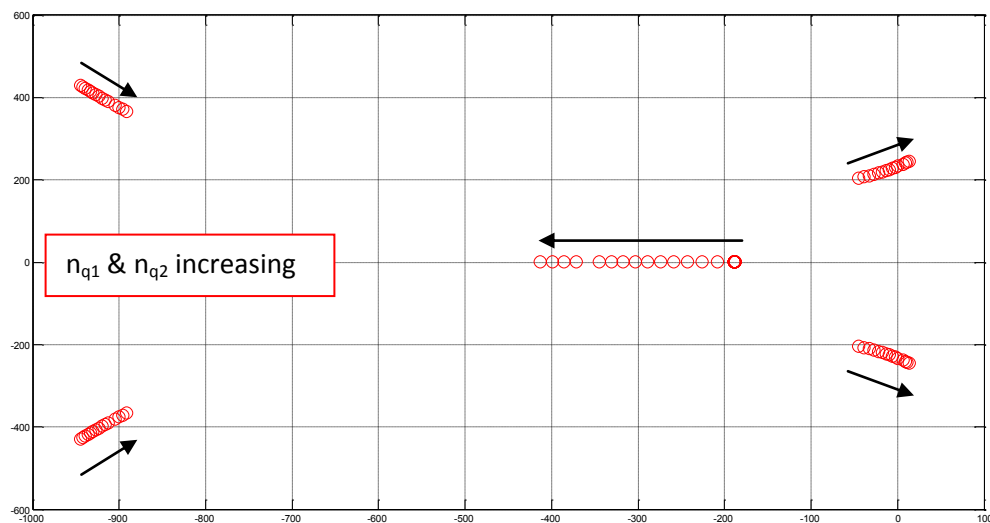


Figure 4.13: Roots of the reduced system model when  $n_{q1}$  &  $n_{q2}$  are increased

For large values of  $X_g/R_g$ , the system is dominated by two poles since they are both close to the imaginary axes. The time domain results will be shown in the next section.

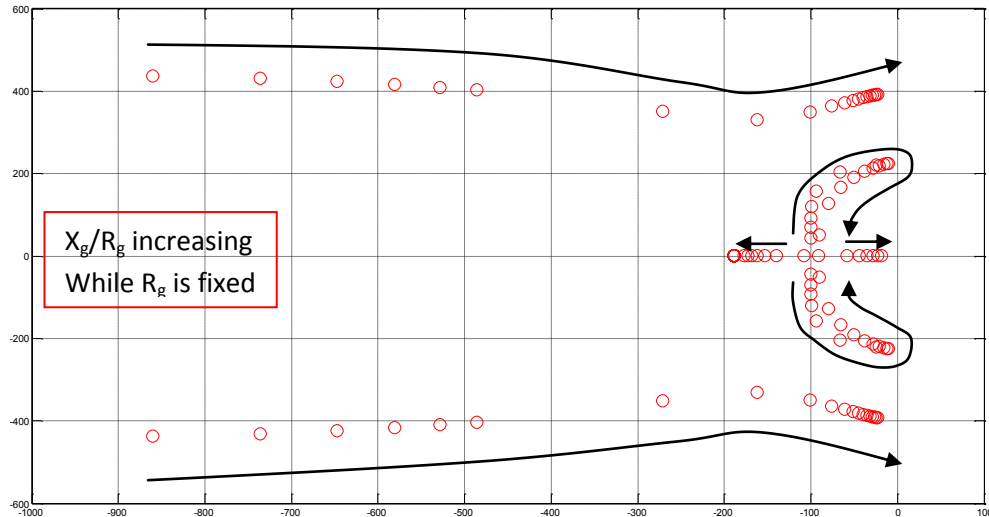


Figure 4.14: Roots of the reduced system model when  $X_g/R_g$  is increased while  $R_g$  is fixed at  $0.23\Omega$

Fig. 4.15 shows the system root locus when decreasing the  $X_g/R_g$  from 1 to 0.14 while  $X_g$  is fixed at  $0.1\Omega$ . The system becomes more stable when the ratio  $X_g/R_g$  is decreasing and it becomes unstable when  $R_g$  is smaller than  $0.15\Omega$ .

From Fig. 4.14 and 4.15, the increasing of the ratio  $X_g/R_g$  turns the system stable since the P vs. f and Q vs. V droop control has been adopted. However,  $R_g$  must be higher than a certain value to make the dominant pole at the left side of the imaginary axis.

The effect of the LPF on the system dynamics is the same as in the previous chapter. The increasing of  $f_c$  leads the system to become more stable as Fig. 4.16 shows. The system parameter of this frequency domain simulations are given in Table 4.2. However,  $f_c$  has been varied from 1Hz to 60Hz.

The LPF is a very important element which can solve many dynamics issues as demonstrated in chapter 3. For example, it can be used to damp the system's transients when a large value of  $\Delta V$  is required. However, the  $f_c$  values range is very limited.

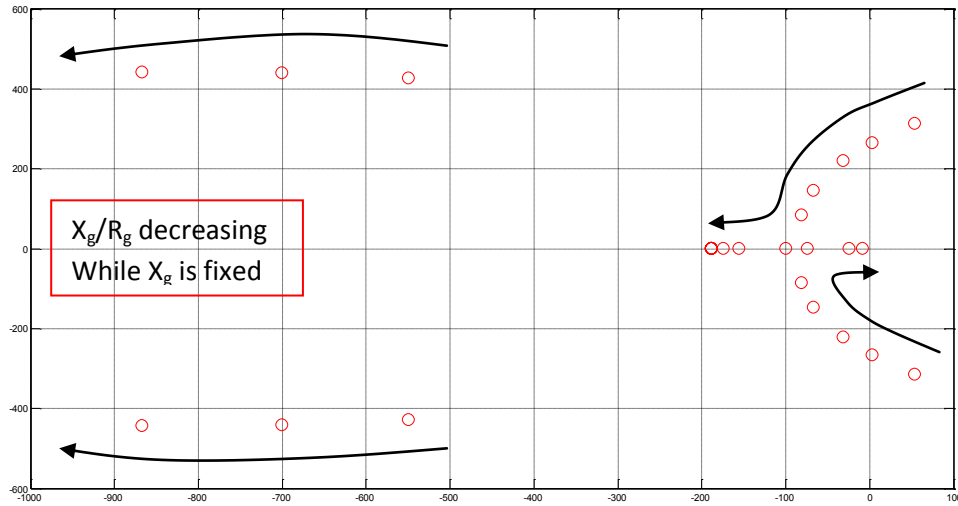


Figure 4.15: Root locus of the reduced system model when  $X_g/R_g$  is decreased while  $X_g$  is fixed at  $0.1\Omega$

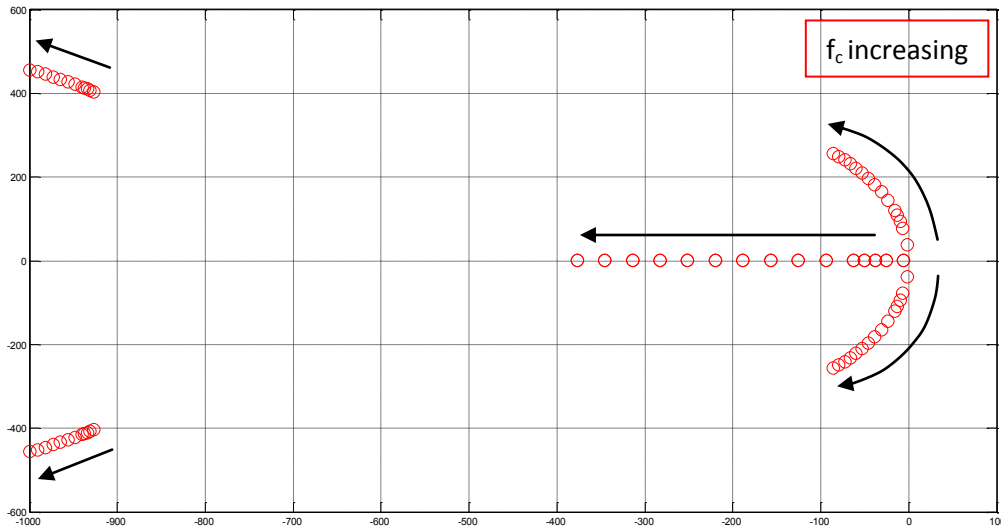


Figure 4.16: Root locus of the reduced system model when  $f_c$  is increased

In the next section, time domain simulations are done in order to verify the frequency domain analysis.

## 4.5 Performance verification

In the previous section, a frequency domain modeling and analysis have been done showing how the system behaves dynamically under some specific parameter variations. In this section, the previous modeling is verified by time domain simulations using Simulink/Matlab. Note that since the inverters share their local loads, the system should be tested under worst cases of load variations. Because the

local loads have been neglected in the reduced system modeling, the complete system model, given by Eq. 4.38, is used in this section for root locus verifications. Then, variations in no-load frequency are done to verify the system performance while controlling the state-of-charge of the batteries in the DC buses of the inverters.

#### 4.5.1 Response of the system to load variations

Setting the system parameters as given by Table 4.3, Fig. 4.17 shows the inverters' output active power. The simulation steps are given by Table 4.4.

Table 4.3: system parameters for load variation condition

Parameter	Value	Unit
$V_r$	120/208	$V_{rms}$
$f_r$	60	Hz
$m_{p1}$	1.257m	rad/s/W
$m_{p2}$	2.513m	rad/s/W
$n_{q1}$ & $n_{q2}$	0	V/VAr
$\Delta f$	4	Hz
$f_{nL1}$ & $f_{nL2}$	62	Hz
$V_{nL1}$ & $V_{nL2}$	169.7	V
$X_g$	0.1	$\Omega$
$R_g$	0.23	$\Omega$
$f_c$ (LPF cut-off frequency)	30	Hz

Table 4.4: Simulation steps for load variation test

Time (s)	$P_{Load1}$ (W)	$P_{Load2}$ (W)
0	20	10
0.1	20	10k

Where,  $P_{Loadi}$  is the local load power demand of the  $i^{th}$  inverter.

The purpose for this simulation is to verify how the system behaves dynamically under a large load step condition. Fig. 4.18 shows the low-frequency poles of the complete system model under the same condition. The system is actually stable but its transient response could be more damped. This could be done theoretically by one or all of the following points;



- Decreasing the active power droop gain ( $m_p$ )
- Increasing the resistive part of the line impedance ( $R_g$ )
- Increasing the LPF's cut-off frequency ( $f_c$ )

Fig. 4.19 shows a simulation result when the system's parameters are as in Table 4.3 but with a smaller value of the active droop gains ( $m_{p1}$  and  $m_{p2}$ ) by setting  $\Delta f$  at 2Hz. The decreasing of the active droop gains makes the system's transient response less oscillatory. This is confirmed by the root locus of the system shown in Fig. 4.20 for two values of  $\Delta f$  (4Hz and 2Hz). The dominant poles move to the left when decreasing  $\Delta f$ .

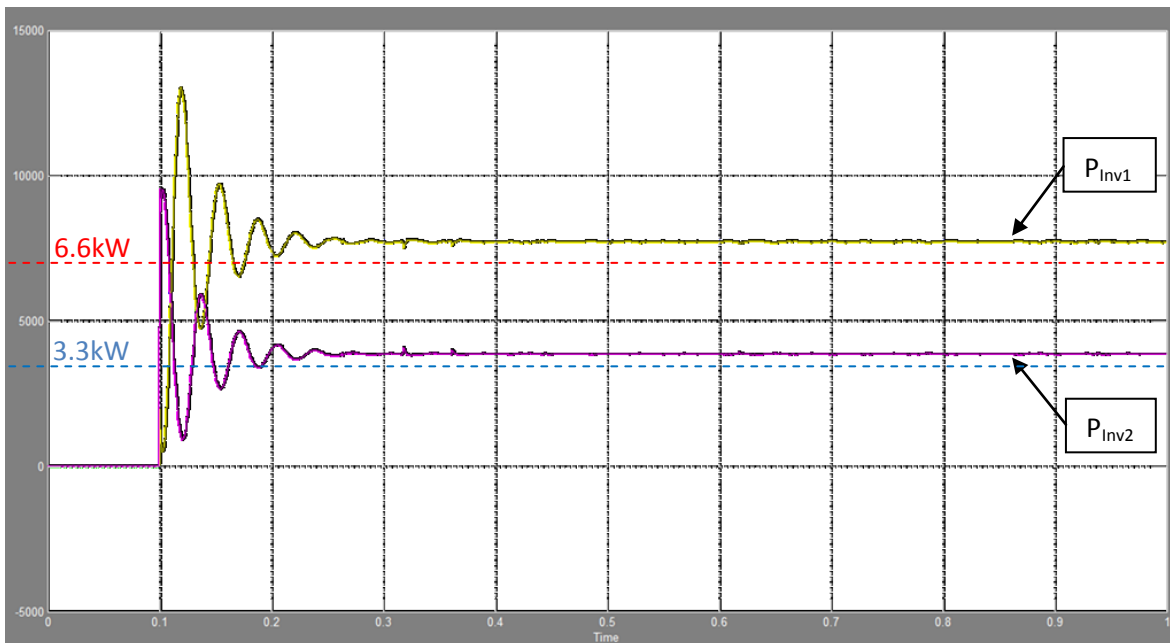


Figure 4.17: Inverters' output active power when large load step occurred (W) vs. Time (s)

After getting the system's parameters to default (Table 4.3), a time domain simulation has been done with the same steps described in Table 4.4 but with larger value of  $R_g$ . Setting the latter at  $0.3\Omega$ , instead of  $0.23\Omega$ , the system dynamic has been more damped as Fig. 4.21 shows. This is verified by the frequency domain results shown in Fig. 4.22. The dominant poles move to the left when the resistive part of the feeder is increased.

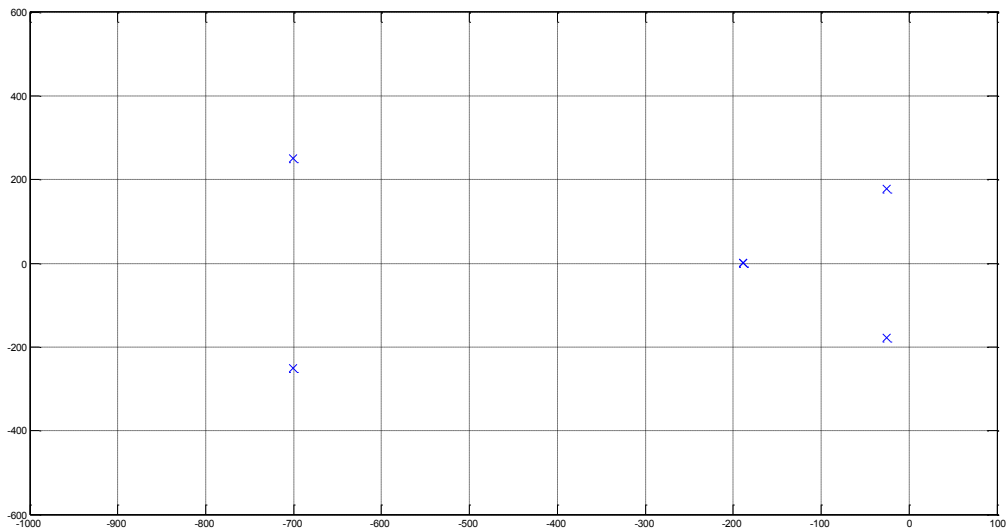


Figure 4.18: Dominant pole of the complete system model for large load variation condition

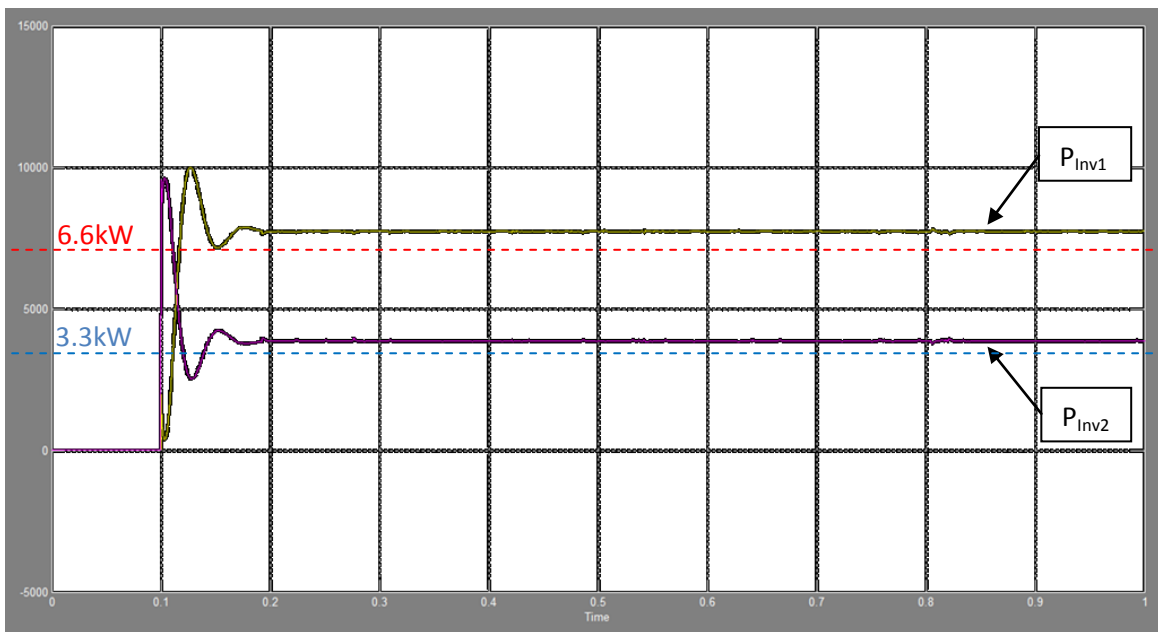


Figure 4.19: Inverters' output active power when large load step occurred when  $\Delta f=2\text{Hz}$  (W) vs. Time (s)

By increasing  $R_g$  and keeping the same value of  $X_g$ , the ratio  $X_g/R_g$  has been decreased generating a larger steady-state error (see Fig. 4.21) with respect to results obtained in Fig. 4.17 or 4.19, where  $R_g$  was set at  $0.23\Omega$ . This confirms that the ratio  $X_g/R_g$  is the most important element for the accuracy of the steady-state value. Fig. 4.23 shows simulation results with zero steady-state error after setting  $X_g$  five

times bigger than  $R_g$ . Unfortunately, the line impedance components are not controllable and usually unknown. Hence another approach should be considered in order to enhance simultaneously the system's transient and steady-state responses.

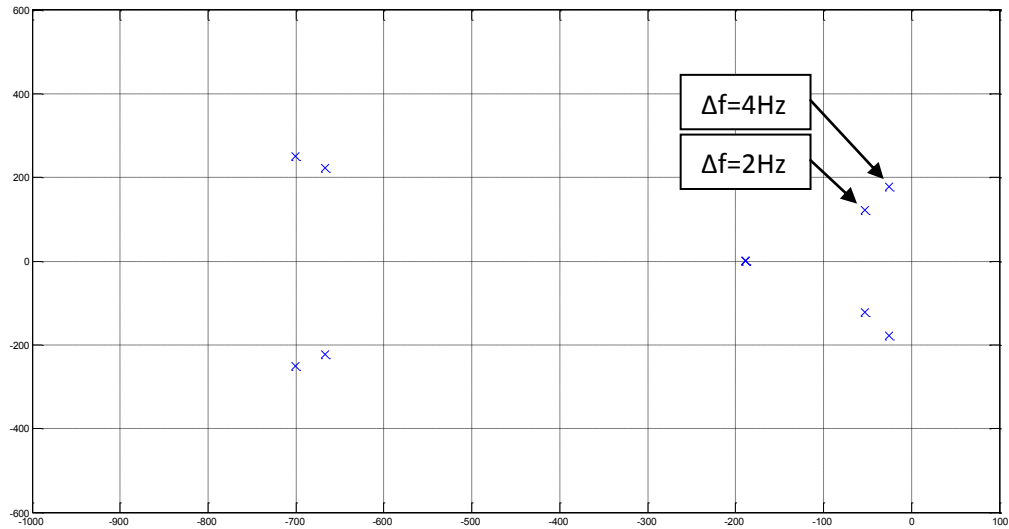


Figure 4.20: Dominant pole of the complete system model when  $\Delta f$  is decreased (W) vs. time (s)

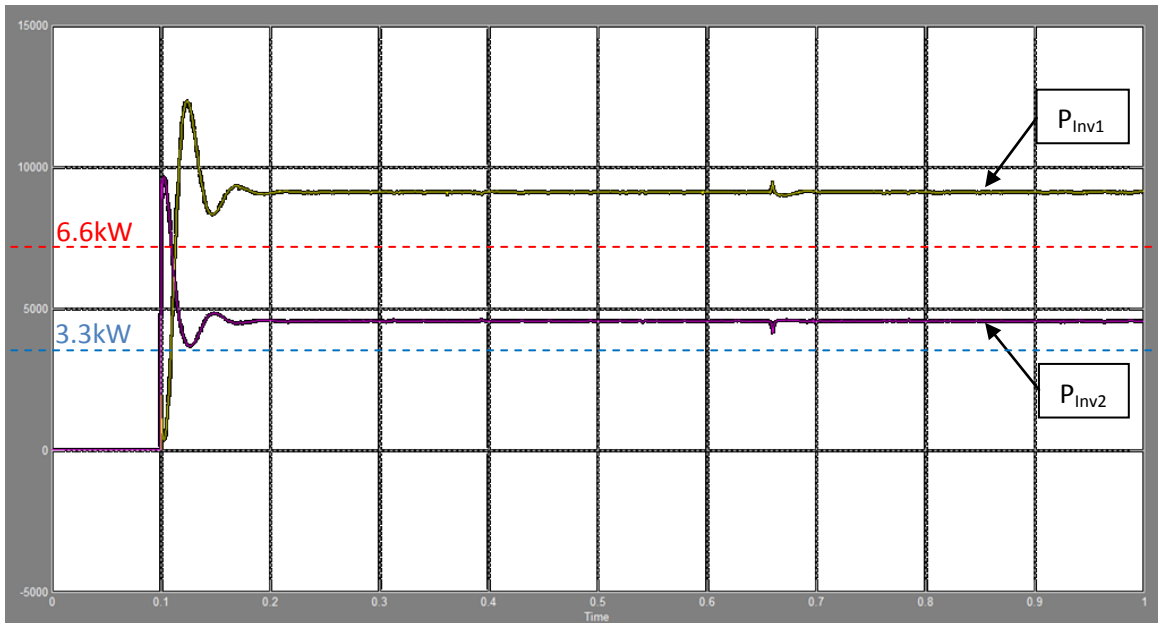


Figure 4.21: Inverters' output active power when large load step occurred when  $R_g=0.3\Omega$  (W) vs. Time (s)

Now setting the system parameters as in Table 4.3 but with larger LPF's cut-off frequency ( $f_c=60\text{Hz}$ ), Fig. 4.24 and 4.25 show the time domain and frequency domain results respectively. The increasing of  $f_c$  makes the system's transient less oscillatory.

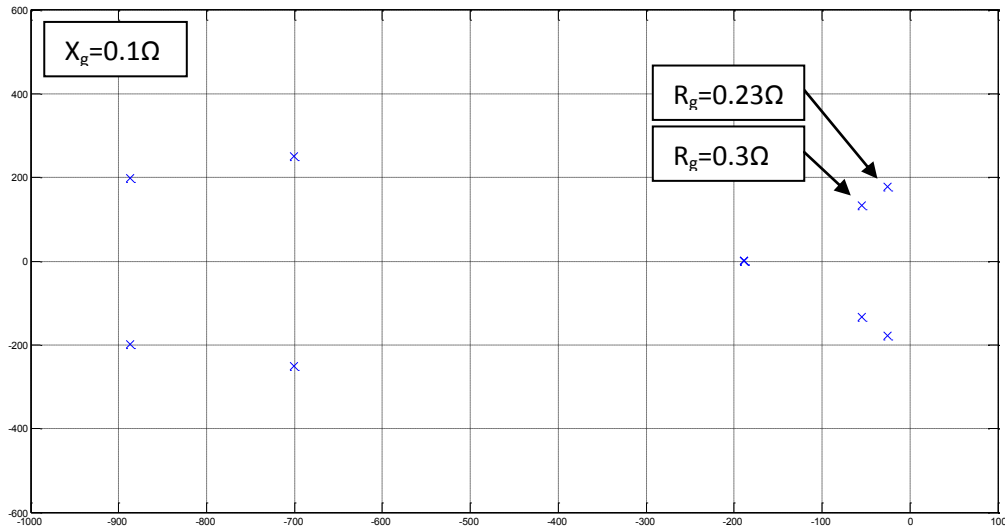


Figure 4.22: Dominant pole of the complete system model when  $R_g$  is increased (W) vs. time (s)

After doing the previous simulations, one can conclude that in such a system, three parameters influence significantly the transient responses ( $\Delta f$ ,  $R_g$  and  $f_c$ ), and only one parameter ( $X_g/R_g$  ratio) influence the steady state response. However, two of those parameters are controllable ( $\Delta f$  and  $f_c$ ) but limited by some constraints, and the others are non-controllable ( $R_g$  and  $X_g/R_g$  ratio).

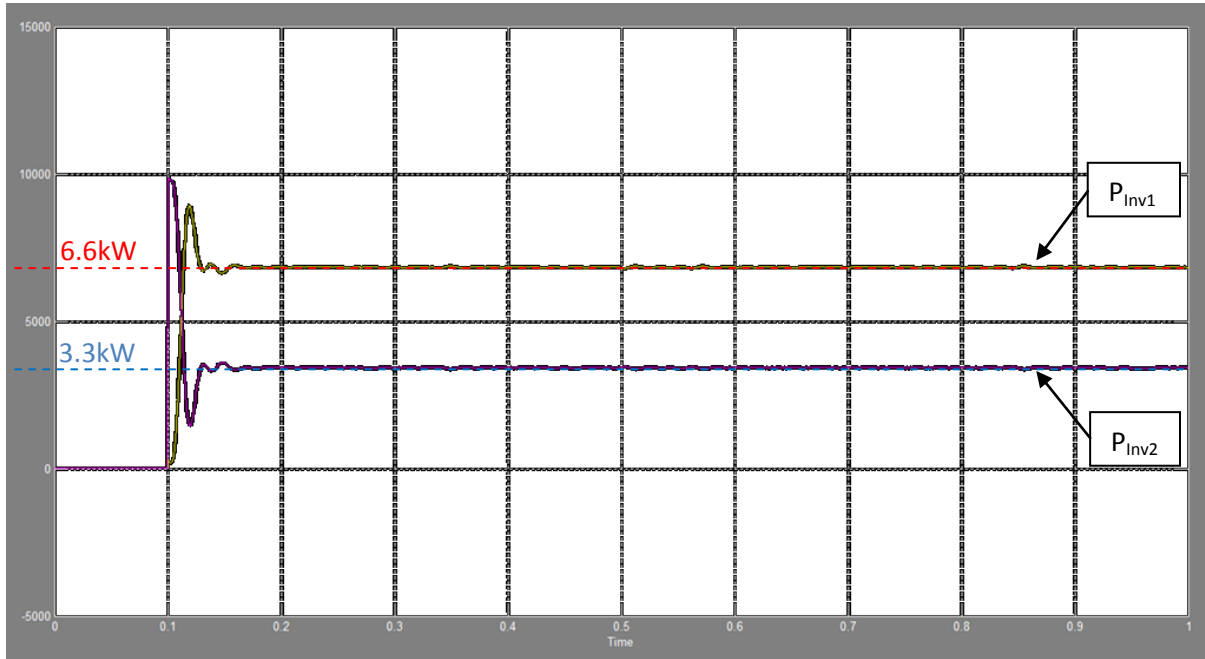


Figure 4.23: Inverters' output active power when large load step occurred while  $X_q/R_g=5$  and  $R_g=0.3\Omega$  (W) vs. Time (s)

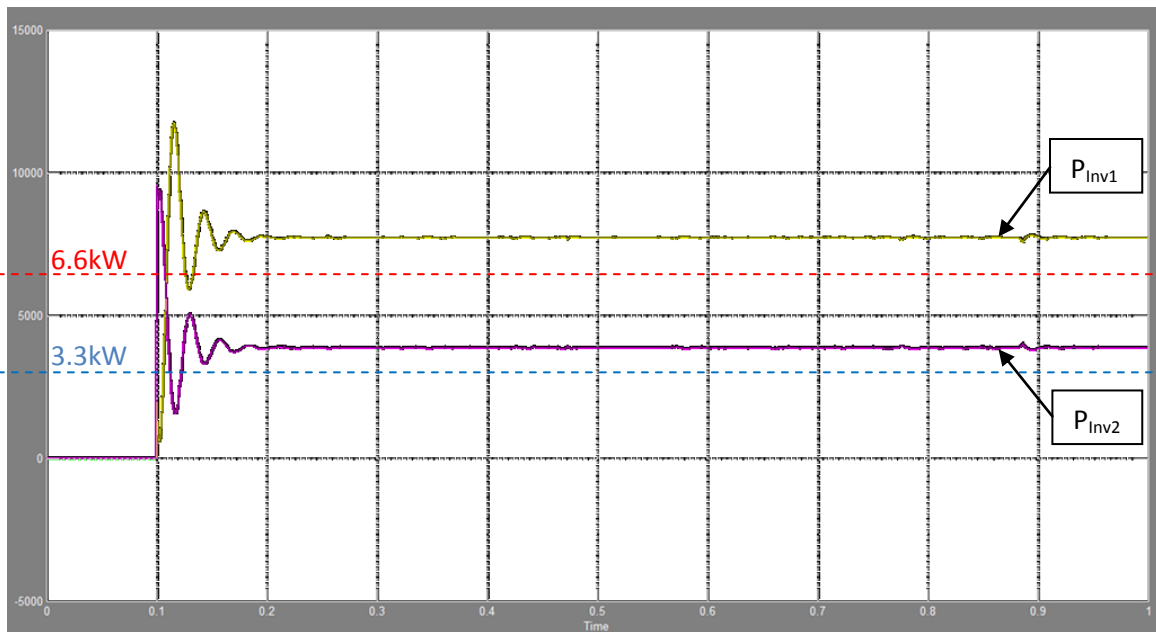


Figure 4.24: Inverters' output active power when large load step occurred when  $f_c=60\text{Hz}$  (W) vs. Time (s)

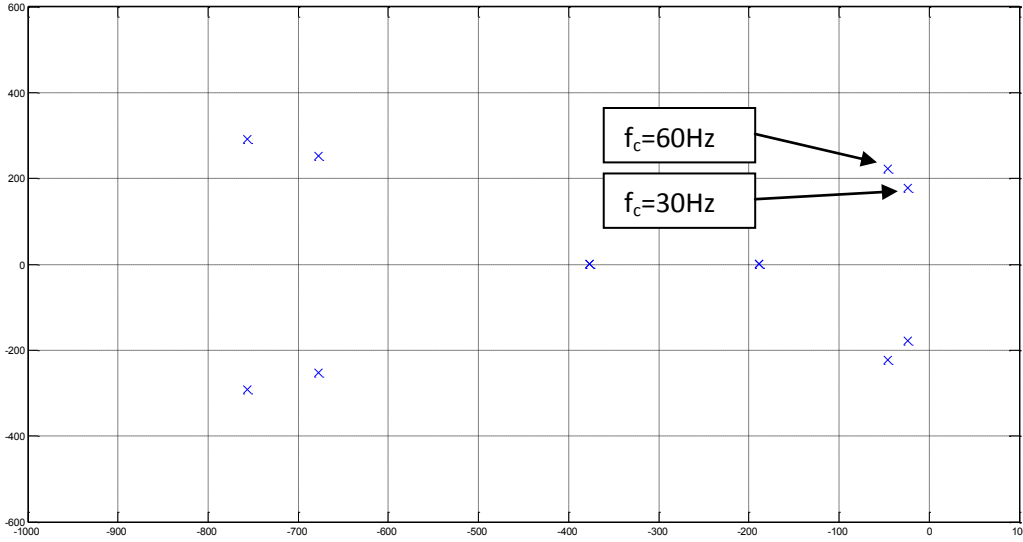


Figure 4.25: Dominant pole of the complete system model when  $f_c$  is increased (W) vs. time (s)

### 4.5.2 Response of the system due to reference (power) signal variations

In a mini-grid, DGs share loads depending on their ratings and energy availability in their DC sides. Therefore, controlling the state-of-charge of the batteries bank is necessary in such application. This could be achieved by controlling the output power by varying the no-load frequency ( $f_{nL}$ ). In this section, time domain simulations have been done in order to verify the system behavior when  $f_{nL}$  is varied. Setting the system’s parameters as in Table 4.3, Table 4.5 gives the simulation steps when the no-load frequency of the inverter #2 ( $f_{nL2}$ ) has been decreased assuming that its battery bank has been discharged and it is time to be charged.

The  $f_{nL2}$  variation is given by Eq. 4.44, where  $P_{o2}^*$  is the inverter #2 output active power reference.

$$\Delta f_{nL2} = \frac{3}{2} m_{p2} (P_{Inv2}^* - P_{Inv2}) \tag{4.59}$$

In case where inverter #2’s battery bank needs 5kW to be charged,  $f_{nL2}$  should be decreased by 4.5Hz.

Table 4.5: Simulation steps for  $f_{nL}$  variation condition

Time (s)	$P_{Load1}$ (kW)	$P_{Load2}$ (kW)	$f_{nL1}$ (Hz)	$f_{nL2}$ (Hz)
0	2.5	5	62	62
0.5	2.5	5	62	57.5
1	2.5	5	62	62

Fig. 4.26 shows the simulation results. Again the system parameters in Table 4.3 do not allow getting good transient and steady-state responses when the conventional droop control has been implemented. The same effects of the influencing parameters on the system behavior have been gotten when  $f_{nL}$  is varied. Fig. 4.27 shows a simulation result when the ratio  $X_g/R_g$  has been increased to 5 and  $R_g$  to  $0.3\Omega$ . Accordingly, the system's transient and steady-state responses have been enhanced.

In hybrid mini-grids where PEIDGs could operate in parallel with *gensets*, the latter are usually considered as the main source of energy and their droop characteristics are generally fixed. Therefore, PEIDGs should adopt the same droop characteristics in order to share loads with parallel gensets. In other words, P vs. f and Q vs. V droop control approaches have to be implemented in the inverters. Moreover, each DG in the mini-grid should provide energy with respect to its ratings, and since gensets are characterized by fixed P vs. f droop slopes other DGs have to respect this constraint. In that case,  $\Delta f$  could not be varied in order to damp the system's transients.

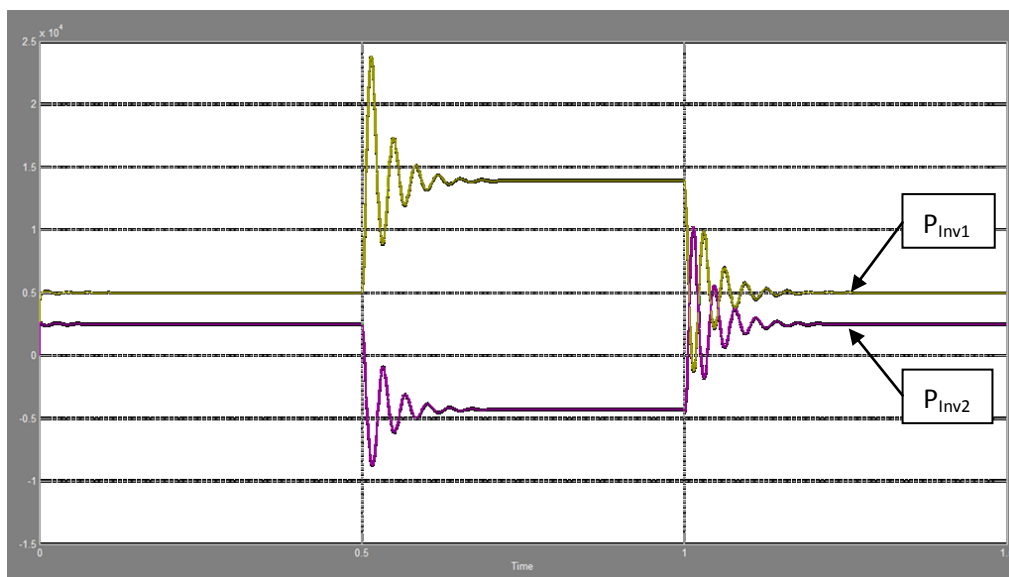


Figure 4.26: output active power when  $f_{nL1}$  is varied (W) vs. Time (s)

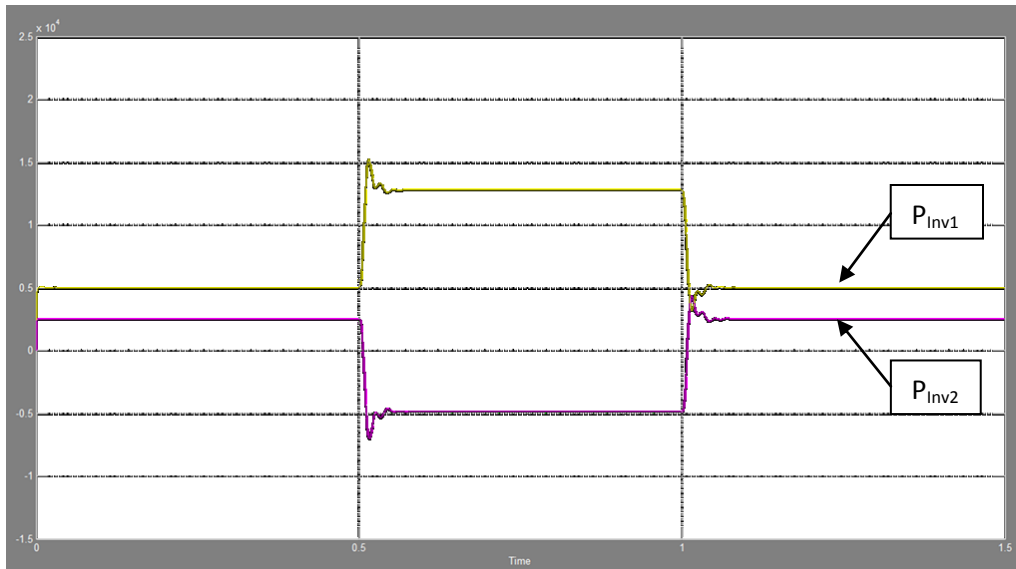


Figure 4.27: Inverters' output active power when  $f_{nL1}$  is varied while  $X_q/R_g=5$  and  $R_g=0.3\Omega$  (W) vs. Time (s)

As mentioned in chapter 3 regarding the value of the LPF cut-off frequency ( $f_c$ ) that should be selected, the latter has to be small in order to avoid conflicts between the outer loop (Droop controllers) and the inner loop (Voltage controller). Moreover, the LPF in this case suppresses harmonics caused by voltage distortions in the AC bus; hence  $f_c$  should be small enough allowing good operation of droop controllers.

Finally, using conventional droop controllers in LV networks does not provide an efficient and reliable solution to share loads as expected among DGs. However, many papers have come up with some solutions regarding the enhancement of the transient response by modifying the conventional droop controllers (e.g. Eq. 3.79 and 3.80) since the latter do not provide any degrees of freedom. In other words, the system's dominant poles could not be moved to the left when conventional droop control is used. The most common technique for mitigating this problem is the "virtual impedance" loop which is studied in the next section.



## 4.6 Virtual impedance loop

### 4.6.1 Virtual impedance loop implementation

In Mini-grids where line impedances' amplitudes and angles are usually small, voltage source Inverters which are droop controlled using P vs. f approach may not behave properly as concluded previously. Therefore, the virtual impedance loop consists on adding virtually an impedance in series with the real line impedance as Fig. 4.28 shows. The virtual impedance creates a "voltage drop" without generating real active and/or reactive power losses. According to many papers (e.g. [17] and [18]), Fig. 4.29 shows how the virtual impedance control loop should be implemented in the case where local loads are directly connected to the Inverters. The virtual voltage drop is calculated using the inverters' output current. Hence, in this case, the virtual impedance is expected to be added between the LC filter and the local load. This allows varying the inverters' output impedance virtually.

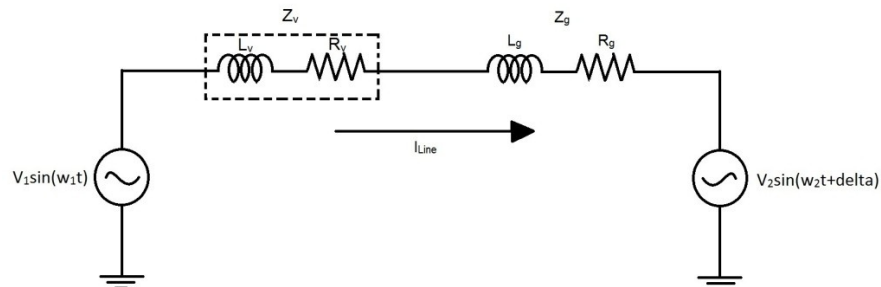


Figure 4.28: virtual impedance in series with the real line impedance

Where,  $Z_v$  is the virtual impedance,  $R_v$  is the resistive part of the virtual impedance,  $L_v$  is the inductive part of the virtual impedance.

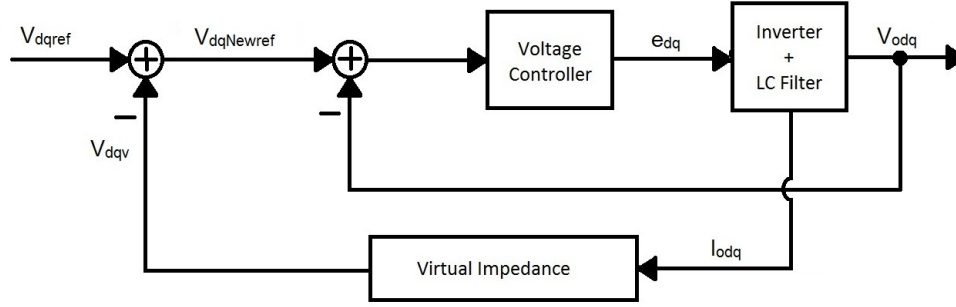


Figure 4.29: Virtual impedance loop

Where,  $V_{dqNewref}$  is the new voltage reference,  $V_{dqref}$  is the voltage reference obtained from the droop curves,  $V_{dqv}$  is the voltage drop across the virtual impedance and  $I_{odq}$  is the output current.

From Fig. 4.29, the new voltage reference is calculated by the following equation;

$$\overrightarrow{V_{dqNewref}} = \overrightarrow{V_{dqref}} - \overrightarrow{V_{dqv}} \quad (4.60)$$

Developing Eq. 4.45, one can get the followings;

$$\overrightarrow{V_{dqNewref}} = \overrightarrow{V_{dqref}} - \overrightarrow{Z_v I_{odq}} \quad (4.61)$$

Then,

$$V_{qNewref} + jV_{dNewref} = V_{qref} + jV_{dref} - [(R_v + j\omega_o L_v) \times (I_{oq} + jI_{od})] \quad (4.62)$$

Hence, one can get;

$$V_{qNewref} = V_{qref} - (R_v I_{oq} - \omega_o L_v I_{od}) \quad (4.63)$$

And,

$$V_{dNewref} = V_{dref} - (\omega_o L_v I_{oq} + R_v I_{od}) \quad (4.64)$$

Finally, from Eq. 4.48 and 4.49, the virtual voltage drop across the virtual impedance is given by;

$$V_{qv} = R_v I_{oq} - \omega_o L_v I_{od} \quad (4.65)$$

And,

$$V_{dv} = \omega_o L_v I_{oq} + R_v I_{od} \quad (4.66)$$

From Eq. 4.50 and 4.51, the implementation of the virtual impedance loop is shown in Fig. 4.30.

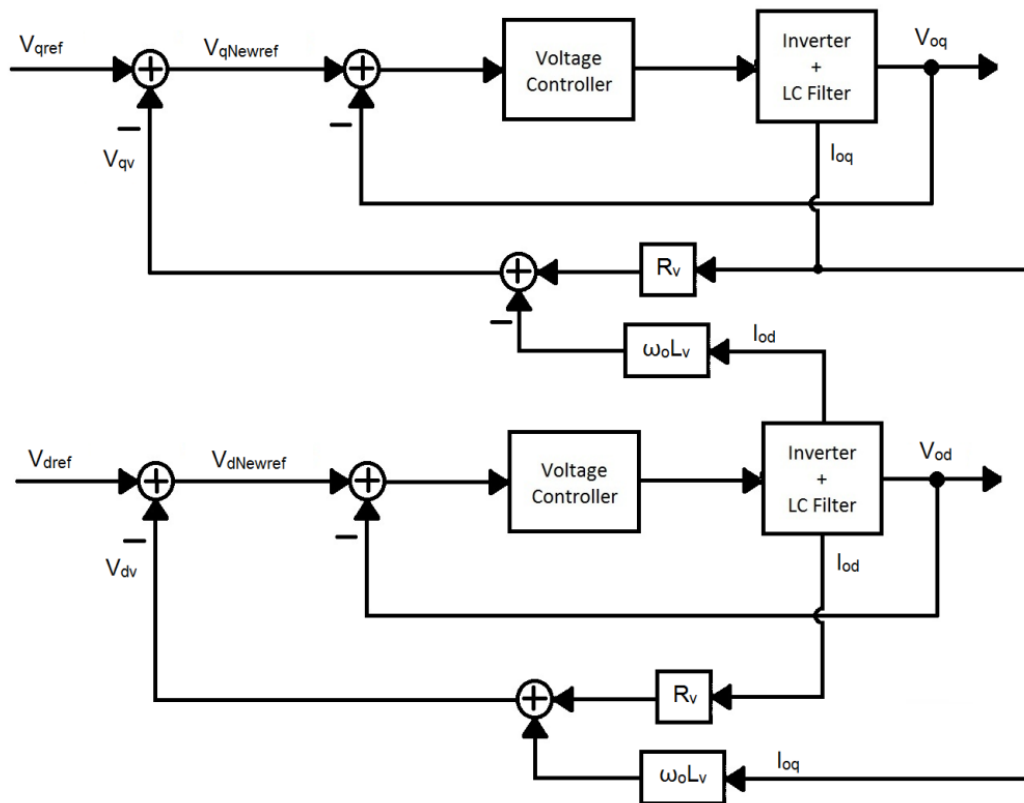


Figure 4.30: Virtual impedance loop implementation

After implementing the virtual impedance in the dq model shown in Fig. 4.2, the blocks “Inv#1” and “Inv#2” contain what Fig. 4.31 illustrates.

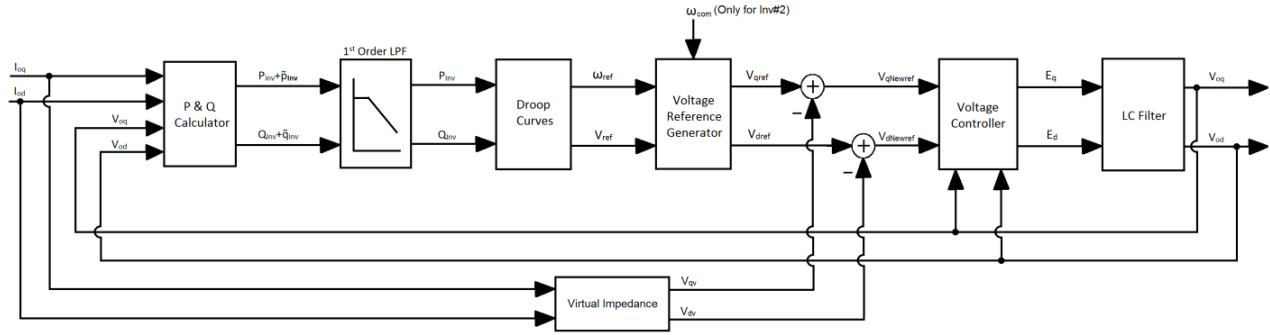


Figure 4.31: Bloc diagram of the dq model of the inverters including the virtual impedance loop

Note that the virtual impedance block contains the Eq. 4.50 and 4.51. Since the Inverter #1 has been considered as the reference,  $\omega_{com}$  in Fig. 4.31 represents the operating frequency of inverter #1 and used to calculate the angle delta for inverter #2.

#### 4.6.2 The system small-signal model including the virtual impedance loop

Based on the small-signal model of the complete system derived previously, the only modification that should be done is at the voltage reference equations (Eq. 4.3 and 4.9). After including the virtual impedance components, the small-signal model of the new voltage references for inverter #1 and inverter #2 are given by Eq. 4.52 and 4.55 respectively.

$$\begin{bmatrix} \Delta\omega_1 \\ \Delta V_{qNewref1} \\ \Delta V_{dNewref1} \end{bmatrix} = C_{PQv1} \begin{bmatrix} \Delta P_{Inv1} \\ \Delta Q_{Inv1} \end{bmatrix} + D_{PQv1} \begin{bmatrix} \Delta V_{oq1} \\ \Delta V_{od1} \\ \Delta I_{Loadq1} \\ \Delta I_{Loadd1} \\ \Delta I_{Lineq} \\ \Delta I_{Lined} \end{bmatrix} \quad (4.67)$$

Where,

$$C_{PQv1} = \begin{bmatrix} -mp_1 & 0 \\ 0 & -nq_1 \\ 0 & 0 \end{bmatrix} \quad (4.68)$$

$$D_{PQv1} = \begin{bmatrix} 0 & 0 & -R_{v1} & \omega_o L_{v1} & -R_{v1} & \omega_o L_{v1} \\ 0 & 0 & -\omega_o L_{v1} & -R_{v1} & -\omega_o L_{v1} & -R_{v1} \end{bmatrix} \quad (4.69)$$

$$\begin{bmatrix} \Delta V_{qNewref2com} \\ \Delta V_{dNewref2com} \end{bmatrix} = C_{PQv2} \begin{bmatrix} \Delta \delta \\ \Delta P_{Inv2} \\ \Delta Q_{Inv2} \end{bmatrix} + D_{PQv2} \begin{bmatrix} \Delta \omega_1 \\ \Delta V_{oq2} \\ \Delta V_{od2} \\ \Delta I_{Loadq2} \\ \Delta I_{Loadd2} \\ \Delta I_{Lineq2} \\ \Delta I_{Lined2} \end{bmatrix} \quad (4.70)$$

Where,

$$C_{PQv2} = \begin{bmatrix} -V_{qref2o} \sin \delta_o - V_{dref2o} \cos \delta_o & 0 & -nq_2 \cos \delta_o \\ V_{qref2o} \cos \delta_o - V_{dref2o} \sin \delta_o & 0 & -nq_2 \sin \delta_o \end{bmatrix} \quad (4.71)$$

$$D_{PQv2} = \begin{bmatrix} 0 & 0 & 0 & -R_{v2} & \omega_o L_{v2} & R_{v2} & -\omega_o L_{v2} \\ 0 & 0 & 0 & -\omega_o L_{v2} & -R_{v2} & \omega_o L_{v2} & R_{v2} \end{bmatrix} \quad (4.72)$$

Where,  $R_{vi}$  and  $L_{vi}$  are the virtual impedance components for the  $i^{\text{th}}$  inverter.

Therefore, four lines in Eq. 4.39 have to be updated to include the virtual voltage drops. The matrix “ $A_{inv}$ ” components (for Inverter #1);  $A_{3,13}$ ,  $A_{3,14}$ ,  $A_{3,30}$ ,  $A_{3,31}$ ,  $A_{6,13}$ ,  $A_{6,14}$ ,  $A_{6,30}$  and  $A_{6,31}$  (in Eq. 4.39) which are null become  $-R_{v1}$ ,  $\omega_o L_{v1}$ ,  $-R_{v1}$ ,  $\omega_o L_{v1}$ ,  $-\omega_o L_{v1}$ ,  $-R_{v1}$ ,  $-\omega_o L_{v1}$  and  $-R_{v1}$  respectively. The matrix “ $A_{inv}$ ” components (for Inverter #2);  $A_{20,28}$ ,  $A_{20,29}$ ,  $A_{20,30}$ ,  $A_{20,31}$ ,  $A_{23,28}$ ,  $A_{23,29}$ ,  $A_{23,30}$  and  $A_{23,31}$  (in Eq. 4.39) become  $-R_{v2}$ ,  $\omega_o L_{v2}$ ,  $R_{v2}$ ,  $-\omega_o L_{v2}$ ,  $-\omega_o L_{v2}$ ,  $-R_{v2}$ ,  $\omega_o L_{v2}$  and  $R_{v2}$  respectively. The .m file of Matlab containing the small-signal model of the complete system including the virtual impedance loop is given in the Appendix-E.

The small-signal model of the reduced system model could be derived starting from the following equations;

$$\Delta V_{oq1} = \Delta V_{qNewref1} ; \Delta V_{od1} = \Delta V_{dNewref1} \quad (4.73)$$

And,

$$\Delta V_{oq2} = \Delta V_{qNewref2com} ; \Delta V_{od2} = \Delta V_{dNewref2com} \quad (4.74)$$

Then, after including the virtual impedance loop, the matrix given by Eq. 4.43 becomes as the following.

$$A_{rvinv} = \begin{bmatrix} A_{rv1} & A_{rv2} & 0 & 0 & 0 & A_{rv3} & A_{rv4} \\ 0 & A_{rv5} & 0 & 0 & 0 & A_{rv6} & A_{rv7} \\ A_{rv8} & 0 & 0 & A_{rv9} & 0 & 0 & 0 \\ 0 & 0 & A_{rv10} & A_{rv11} & A_{rv11} & A_{rv12} & A_{rv13} \\ 0 & 0 & A_{rv14} & 0 & A_{rv15} & A_{rv16} & A_{rv17} \\ 0 & A_{rv18} & A_{rv19} & 0 & A_{rv20} & A_{rv21} & A_{rv22} \\ 0 & 0 & A_{rv23} & 0 & A_{rv24} & -A_{rv22} & A_{rv21} \end{bmatrix} \quad (4.75)$$

Where,

$$A_{rv1}=A_{r1}$$

$$A_{rv2}=A_{r2}$$

$$A_{rv3}=A_{r3}$$

$$A_{rv4}=A_{r4}$$

$$A_{rv5}=A_{r5}$$

$$A_{rv6}=1.5*\omega_c*(-I_{Lineqo}*\omega_o*L_{v1}-I_{Linedo}*R_{v1}+V_{d1o})$$

$$A_{rv7}=1.5*\omega_c*(-I_{Lineqo}*R_{v1}+I_{Linedo}*\omega_o*L_{v1}-V_{q1o})$$

$$A_{rv8}=A_{r6}$$

$$A_{rv9}=A_{r7}$$

$$A_{rv10}=A_{r8}$$

$$A_{rv11}=A_{r9}$$

$$A_{rv12}=1.5*\omega_c*(-I_{Lineqo}*R_{v2}-I_{Linedo}*\omega_o*L_{v2}-V_{q2o})$$

$$A_{rv13}=1.5*\omega_c*(I_{Lineqo}*\omega_o*L_{v2}-I_{Linedo}*R_{v2}-V_{d2o})$$

$$A_{rv14}=A_{r12}$$

$$A_{rv15}=A_{r13}$$

$$A_{rv16}=1.5*\omega_c*(-I_{Lineqo}*\omega_o*L_{v2}+I_{Linedo}*R_{v2}-V_{d2o});$$

$$A_{rv17}=1.5*\omega_c*(-I_{Lineqo}*R_{v2}-I_{Linedo}*\omega_o*L_{v2}+V_{q2o})$$

$$A_{rv18}=A_{r14}$$

$$A_{rv19}=A_{r15}$$

$$A_{rv20}=A_{r16}$$

$$A_{rv21}=-\frac{(R_g+R_{v1}+R_{v2})}{L_g}$$

$$A_{rv22}=\frac{(\omega_o*L_g+\omega_o*L_{v1}+\omega_o*L_{v2})}{L_g}$$

$$A_{rv23}=A_{r19}$$

$$A_{rv24}=A_{r20}$$

Where,  $R_{v1}$  and  $R_{v2}$  are the resistive components of the virtual impedance of inverter #1 and inverter #2 respectively, and  $L_{v1}$  and  $L_{v2}$  are the inductive components of the virtual impedance of inverter #1 and inverter #2 respectively. Note the .m file of Matlab containing the small-signal model of the reduced system including the virtual impedance loop is given in the Appendix-F.

In order to compare the small-signal model of the complete and reduced system, the dominant poles have been shown in Fig. 4.32 of both system models. Setting the system's parameters as in Table 4.3, the frequency domain results are gotten when the virtual impedance components have been increased proportionally ( $R_{vi}=K_v$  and  $X_{vi}=K_v$ , where  $K_v$  varies from 0 to 1).

As one can see in Fig. 4.32, the dominant poles of the reduced and the complete model move similarly when the virtual impedance ( $VI$ ) is increased. The latter makes the system's transient less oscillatory since the dominant pole moves to the left and been damped. This is verified by time domain simulations in the next section.

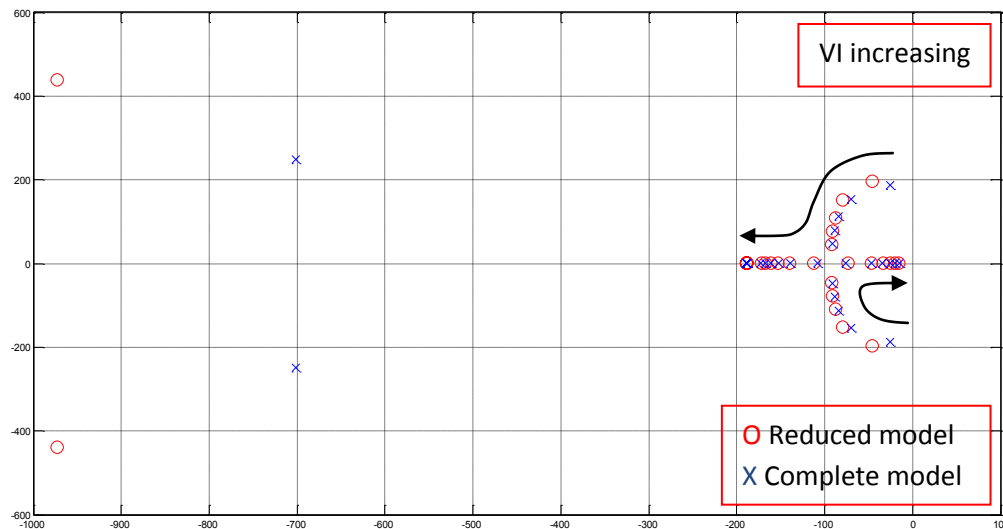


Figure 4.32: Dominant poles of the reduced and the complete system models when the virtual impedance is increased

The matrix ( $A_{rinv}$ ) components'  $A_{rv21}$  and  $A_{rv22}$  in Eq. 4.60 which are used to calculate the line impedance current reveal a very important aspect of the VI. Since the local loads have been neglected in the

reduced system model, the virtual impedance has been considered to be in series with the real line impedance. That is why one can see the VI resistive and inductive components of both inverters are added to the real line impedance resistive and inductive components in  $A_{rv21}$  and  $A_{rv22}$  respectively. Therefore, in order to see the effect of the VI on the system with respect to the effect of the real impedance,  $R_v$  and  $L_v$  have been varied the same way as in Fig. 4.14 and 4.15. In other words,  $R_g$  and  $X_g$  are fixed but  $R_v$  and  $L_v$  are varied such a way to get the same  $X_g/R_g$  ratios in Fig. 4.14 and 4.15. The total  $X_g/R_g$  ratio including the VI is given by Eq. 4.61.

$$\frac{X_{gT}}{R_{gT}} = \frac{X_g + X_{v1} + X_{v2}}{R_g + R_{v1} + R_{v2}} \quad (4.76)$$

Fig. 4.33 shows the position of the dominant poles of the reduced system model when the ratio  $X_g/R_g$  and the ratio  $X_{gT}/R_{gT}$  are increased from 0.1 to 15 while  $R_g$  is fixed to  $0.23\Omega$ . Note that the ratio  $X_{gT}/R_{gT}$  is increased only by increasing  $X_{v1}$  and  $X_{v2}$  while  $R_{v1}$  and  $R_{v2}$  are null, and  $X_g$  and  $R_g$  are fixed at  $0.1\Omega$  and  $0.23\Omega$  respectively.

The dominant poles of the reduced system model in both cases move similarly. However, the virtual impedance has a different effect on the intermediate pole as the real impedance has. This is a good thing because the increasing of  $X_v$  does not generate oscillations caused by the movement of the intermediate pole toward the instability region.

For the frequency domain results shown in Fig 4.15 when the ratio  $X_g/R_g$  is decreased while  $X_g$  is fixed to  $0.1\Omega$ , in Fig. 4.34, the same variations have been done in the ratio  $X_{gT}/R_{gT}$  by increasing  $R_{v1}$  and  $R_{v2}$  while  $X_{v1}$  and  $X_{v2}$  are null. Fig. 4.34 shows that the dominant poles move exactly the same way as in Fig. 4.15 when the ratio  $X_{gT}/R_{gT}$  is decreased by increasing  $R_v$ .



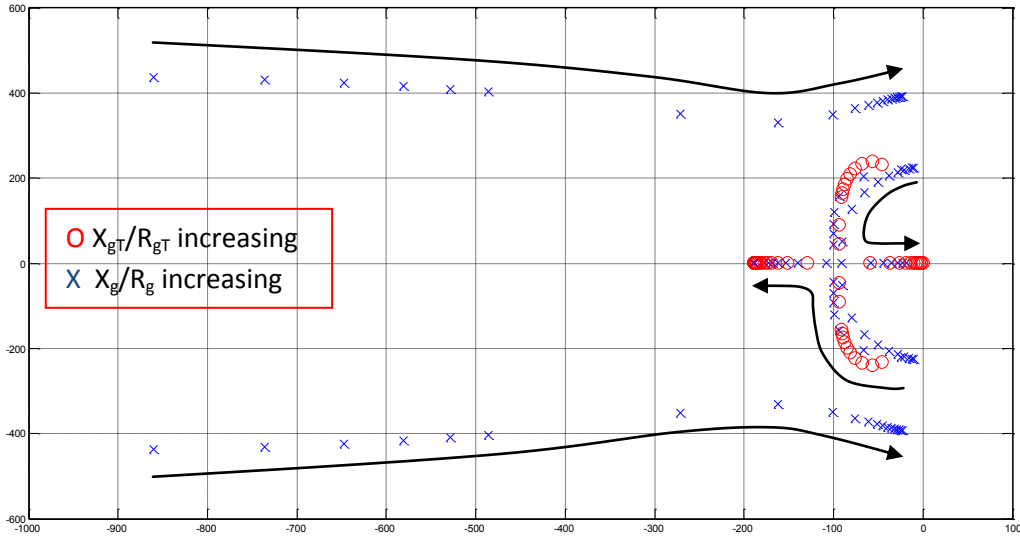


Figure 4.33: The dominant pole of the reduced system model when the  $X_{gT}/R_{gT}$  is increased by increasing  $L_v$

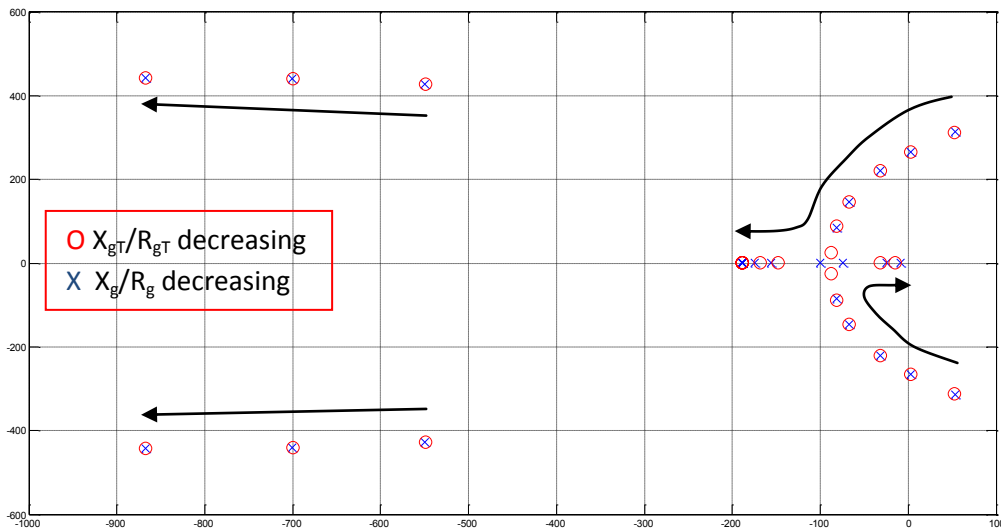


Figure 4.34: The dominant pole of the reduced system model when the  $X_{gT}/R_{gT}$  is decreased by increasing  $R_v$

The results shown in Fig. 4.33 and 4.34 confirm that the VI is a very good solution to the oscillatory system's transients that could be generated due to the line impedance characteristic. However, the virtual impedance loop implementation shown in Fig 4.30 generates a voltage drop in the voltage references which makes the inverters' output voltage decreases. In other words, the actual VI implementation affects the inverters' voltage regulation. This is verified in the next section.

### 4.6.3 Performance verification of the system including the virtual impedance loop

#### 4.6.3.1 Load variation

Time domain simulations have been done in order to verify the impact of the VI on the system dynamics and steady-state values. The simulations steps in this section are given by Table 4.6. Note that the systems' parameters are given by Table 4.3. However, the VI components of both inverters have been varied. In order to get the same voltage drop, the VI of inverter #2 should be twice larger than the VI of inverter #1 since the latter provides twice as large output current as inverter #2 provides. Otherwise, reactive power will be drawn through the feeder due to different values of inverters' local loads.

Table 4.6: Simulation steps when VI loop is included

Time (s)	$P_{Load1}$ (kW)	$P_{Load2}$ (kW)
0	5	2.5
0.5	5	10

Fig. 4.35 and 4.36 show the inverters' output active and coupling reactive power respectively with different values of  $R_v$  while  $X_v$  is null to see the effect of a purely resistive virtual impedance on the system behavior. As one can see in Fig. 4.35, the system dynamic has been damped by the resistive VI as confirmed in Fig. 4.38. However, the voltage drop caused by the latter affects the steady-state response even when there is no power drawn through the feeder as it is seen in Fig. 4.35 and 4.37.

The impact of the purely inductive VI is verified by time domain and frequency domain simulations as shown in Fig. 4.39 and 4.42 respectively. From Fig. 4.39 and 4.41, one sees that the purely inductive VI enhances the system's transient response but it affects also the inverters' voltage regulation. (See Fig. 4.41). However, the purely inductive VI affects the system's steady-state response less than the purely resistive VI (See Fig 4.35 and 4.39).

From Fig. 4.36 and 4.40, one sees that the implementation of purely resistive or purely inductive VI makes the reactive power, generated due to the line impedance characteristics, decrease. This means that the VI does not influence the system's steady-state as the real line impedance does when the latter has to be highly inductive to get accurate steady-state values due to the elimination of the coupling effects between P and Q.

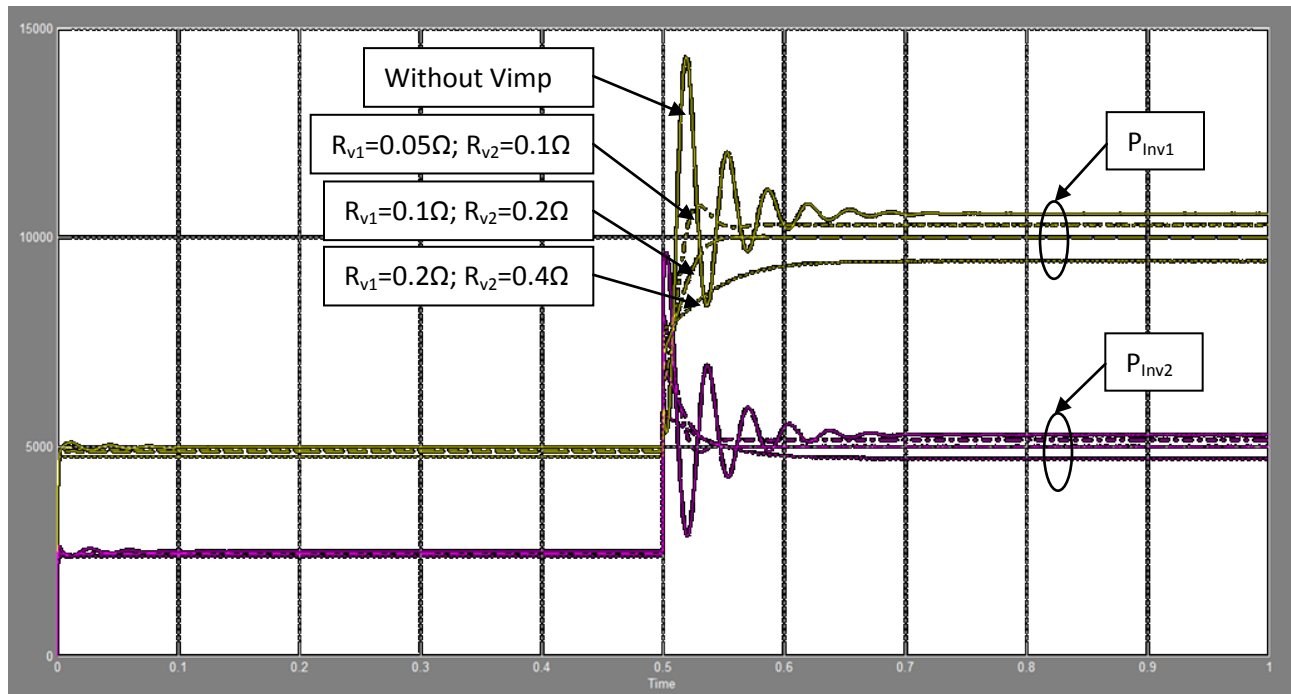


Figure 4.35: Inverters' output active power when  $R_v$  is increased while  $X_v$  is null (W) vs. Time (s)

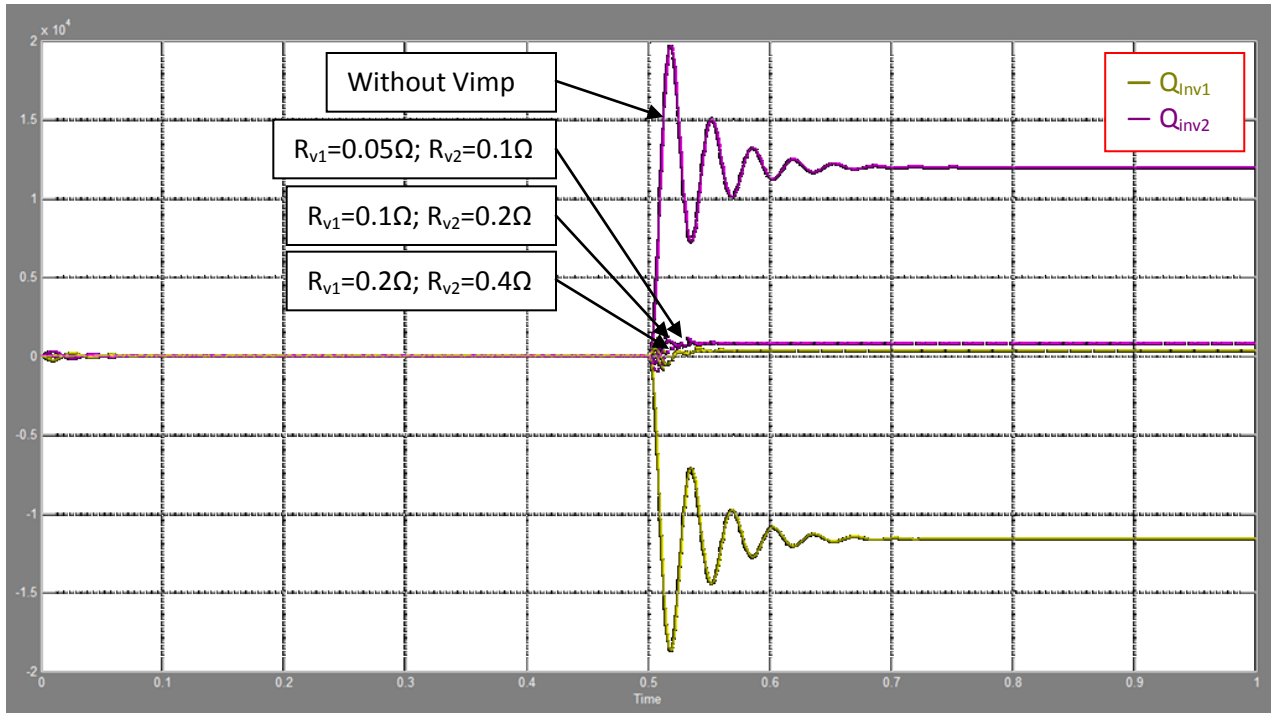


Figure 4.36: Inverters' output reactive power when  $R_v$  is increased while  $X_v$  is null (VAR) vs. Time (s)

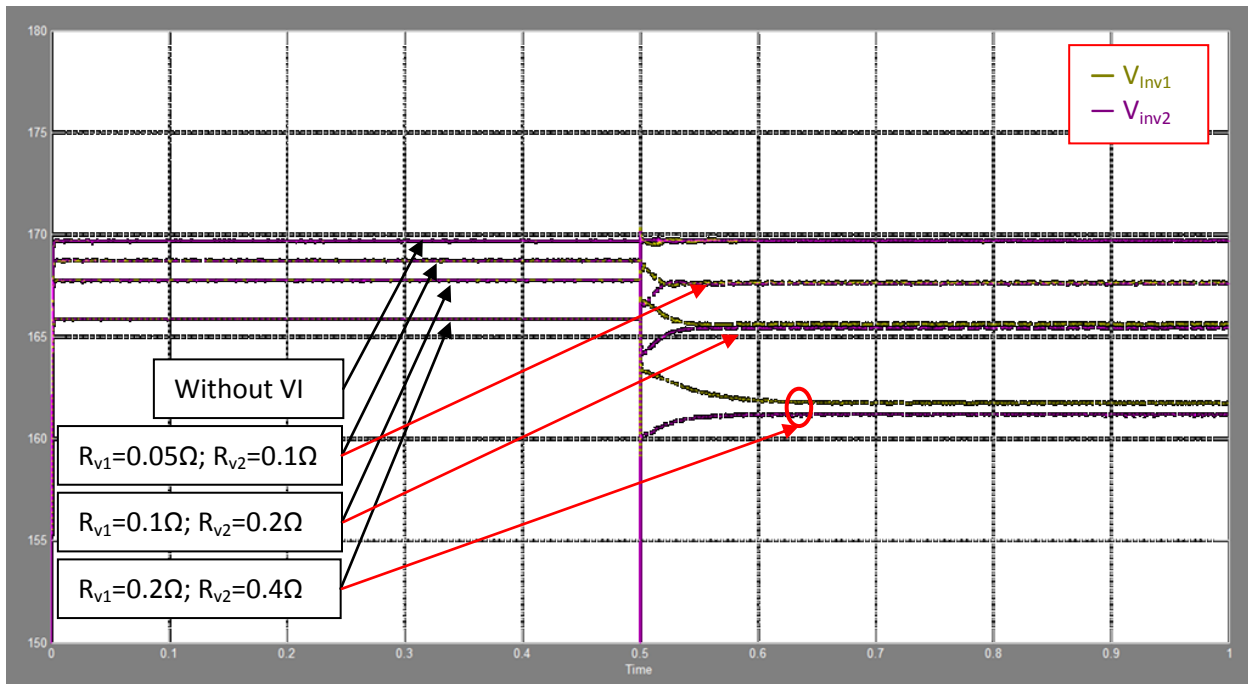


Figure 4.37: Inverters' output peak voltage amplitudes when  $R_v$  is increased while  $X_v$  is null (V) vs. Time (s)

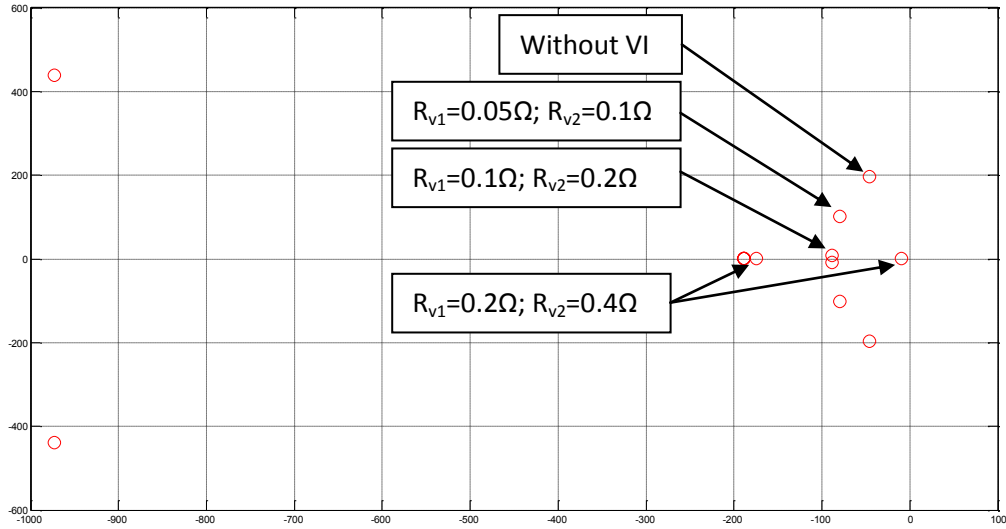


Figure 4.38: Dominant pole of the reduced system model when purely resistive VI is increased

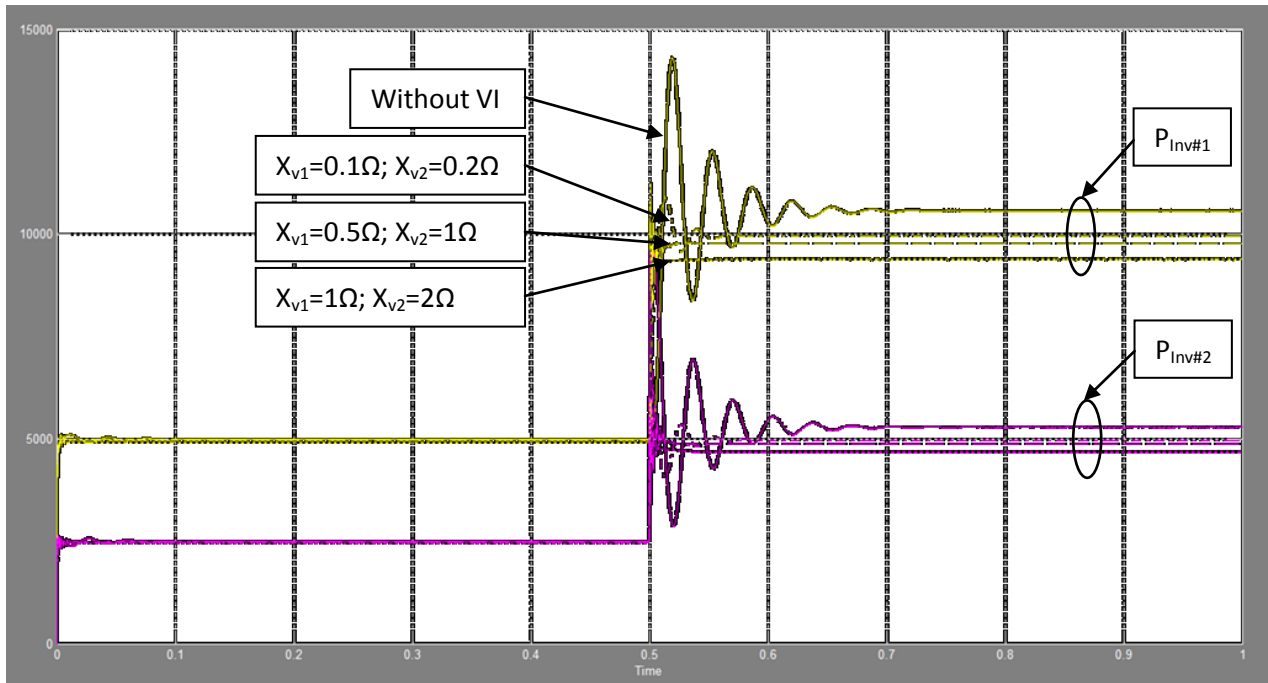


Figure 4.39: Inverters' output active power when  $X_v$  is increased while  $R_v$  is null (W) vs. Time (s)

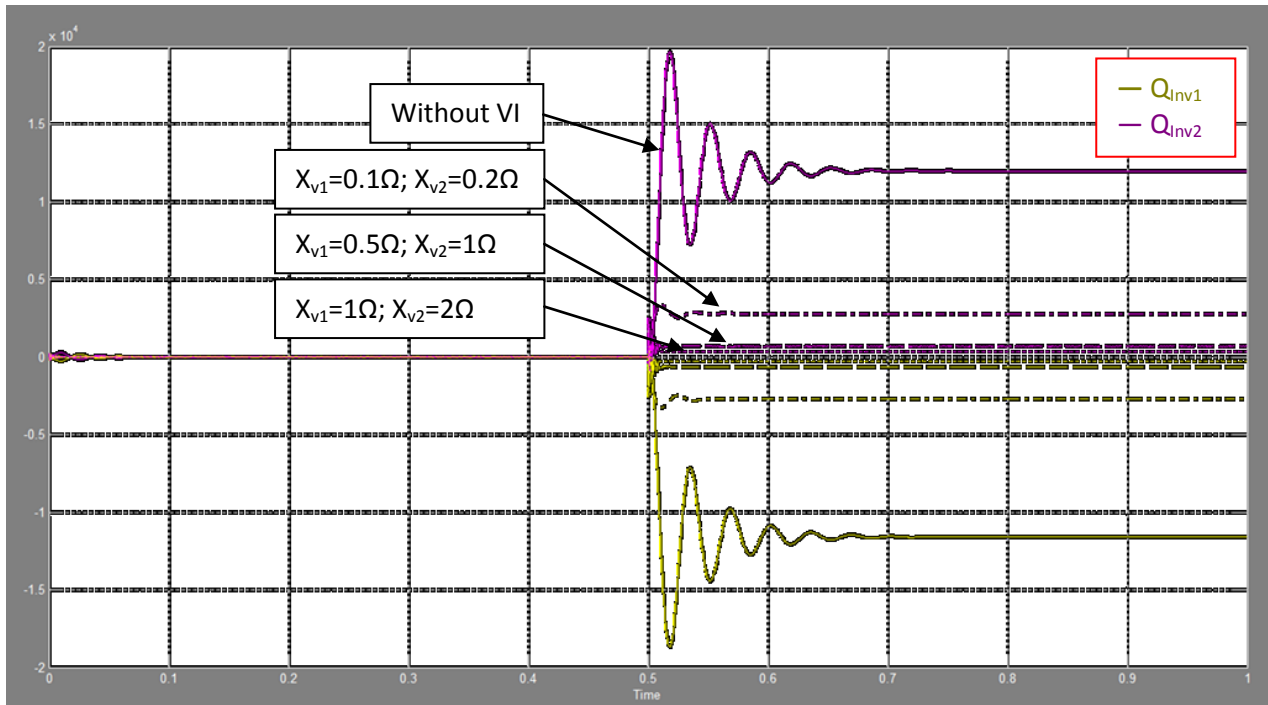


Figure 4.40: Inverters' output reactive power when  $X_v$  is increased while  $R_v$  is null (VAR) vs. Time (s)

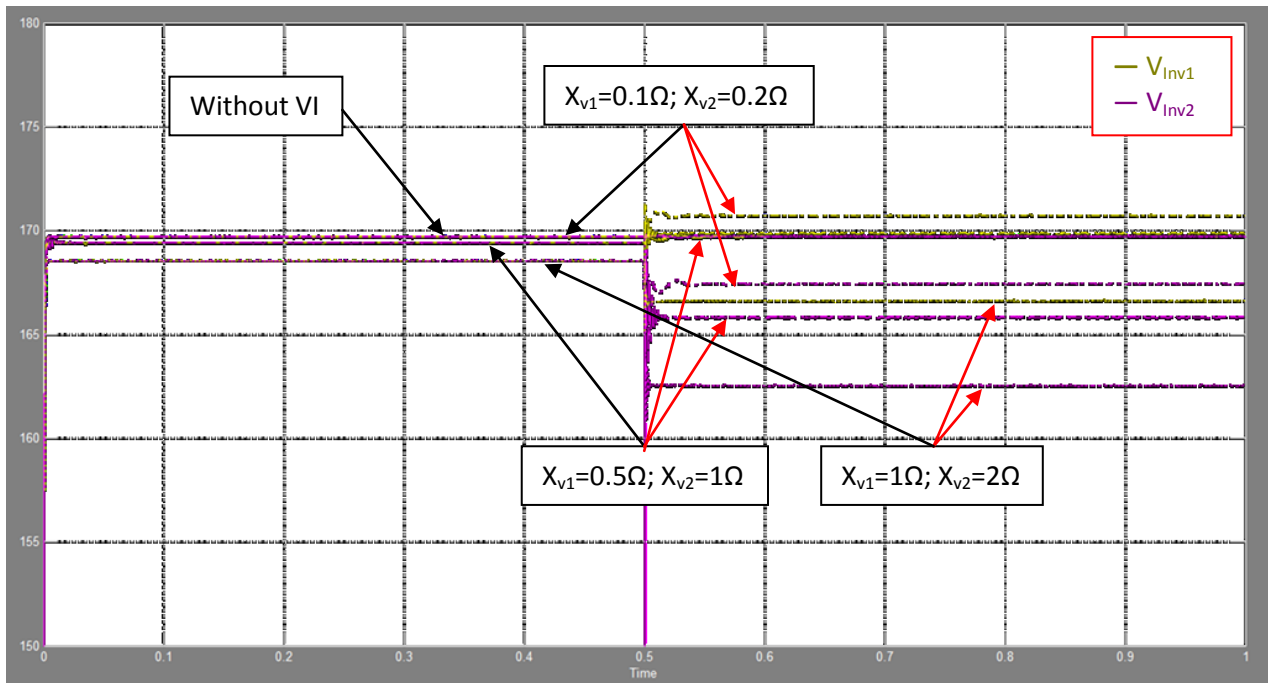


Figure 4.41: Inverters' output peak voltage amplitudes when  $X_{v1}$  is increased while  $R_{v1}$  is null (V) vs. Time (s)

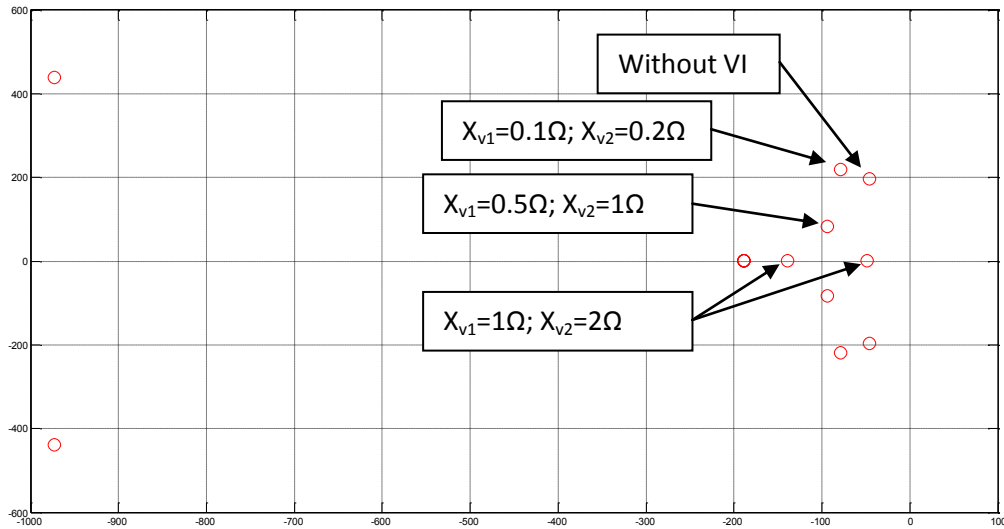


Figure 4.42: Dominant pole of the reduced system model when purely inductive VI is increased

Finally, one can conclude that both resistive and inductive VIs can generate good system transient and steady-state responses if designed properly. However, this could not be done if the line impedance is unknown [17].

There is another important aspect about the VI; the increasing of the VI makes the system more accurate in terms of reactive power sharing [7] [19]. This is because larger VI allows implementing larger reactive power droop gain  $n_q$ , hence the Q sharing is improved [19]. However P sharing will be deteriorated due to the large voltage drop generated by the large VI.

#### 4.6.3.2 Power signal variation

As studied previously, the increasing of the  $n_q$  leads the system to instability. As shown in Fig. 4.13, the reduced system becomes unstable when  $\Delta V\%$  is above 0.9% (above 0.4% for the detailed system). This small value of  $\Delta V\%$  generates inaccurate Q sharing. In order to verify that, some time domain simulations have been done to see the effect of the VI on the value of  $n_q$  that could be implemented, and of the latter on the steady-state value. During the simulations, the local loads have been removed, and a step in the  $V_{nL1}$  of  $2.5\Delta V$  occurs at 0.1s in order to generate a reactive power of

6kVAr drawn from the inverter #1 to the inverter #2. Setting the system's parameters as given by Table 4.3, Fig. 4.43 shows the inverters' output reactive power with different values of  $n_q$  or  $\Delta V\%$ . Note that a resistive VI has been used with  $R_{v1}=0.1\Omega$  and  $R_{v2}=0.2\Omega$  since these are the best values for a resistive VI as Fig. 4.35 shows.

From the results shown in Fig. 4.43, the VI allows implementing larger values of  $n_q$  while making the system stable. Moreover, the increasing of  $n_q$  makes the system's steady-state response more accurate but the transient response becomes more oscillatory. This reinforces the hypothesis that the virtual impedance has to be large and designed depending on the feeder characteristics [7] [19].

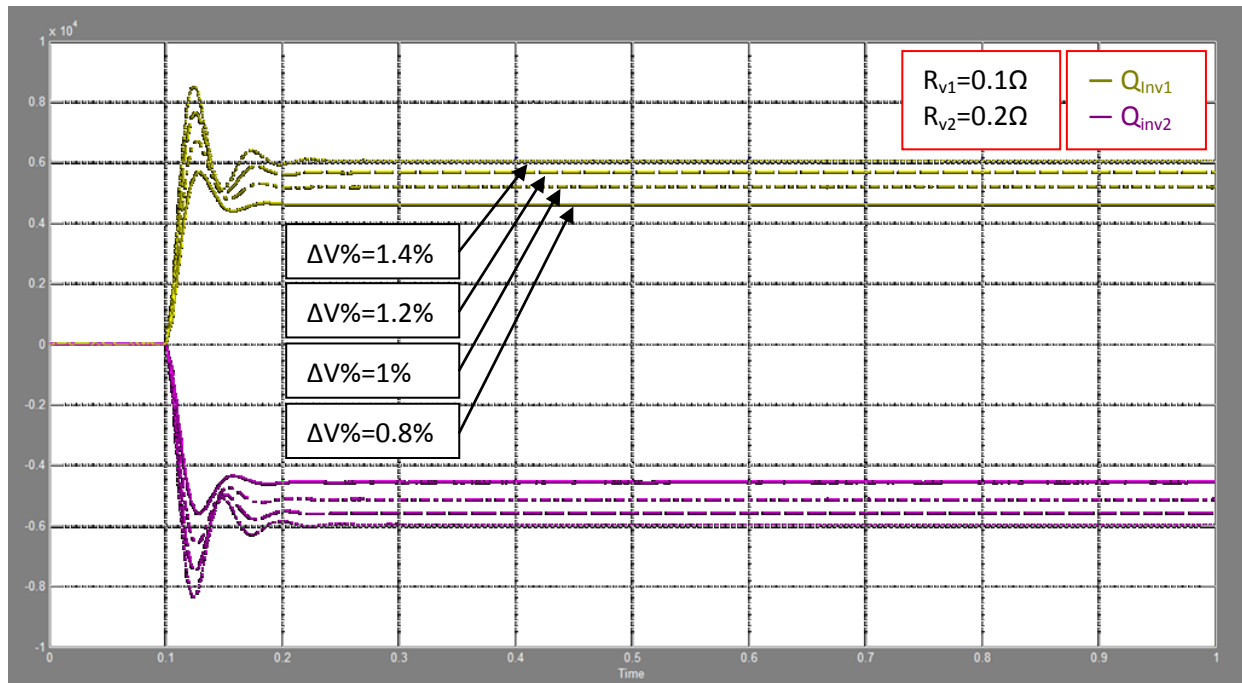


Figure 4.43: Inverters' output reactive power including VI and when  $n_q$  is increased (VAr) vs. Time (s)

In the next section, a VI loop implementation that allows the system's transients enhancement, large values of  $n_q$  implementation, keeping good voltage regulation and no need of line impedance knowledge is proposed.



## 4.7 Proposed virtual impedance loop

It is well known that the idea behind the conventional “Virtual Impedance loop,” analysed in the previous section, is to add virtually in series an impedance to the real line impedance (see Fig. 4.28), without generating real power losses, to improve the system dynamics in case where feeders’ characteristics generates oscillatory responses. Therefore, the conventional VI is implemented in such a way to generate a voltage drop in the inverters’ output voltage in order to mimic the internal impedance influence to the system. From Eq. 4.48 and 4.49 and Fig. 4.30, the new voltage references ( $V_{qNewref}$  and  $V_{dNewref}$ ) not only make the inverters’ output voltage magnitudes decrease but also change their phase angles. This “virtual angle” which is added by the  $V_{imp}$  is what exactly one needs to get from the VI loop to lead the system into stability regions.

In other words, the voltage reference’s d and q components are calculated by the “voltage reference generator” block using  $\omega$  and  $V$  from the droop curves. However, when the conventional virtual impedance is implemented, it generates an additional angle to the voltage reference in order to modify the phase angle of the output voltage as illustrated in Fig. 4.44.

In order to verify that, Fig. 4.45 shows different phase angles between the inverters’ output voltages obtained when  $R_v$  is increased. Note that the angle in Fig. 4.45 has been calculated using Eq. 4.1. The system parameters are listed in Table 4.3.

As one can see in Fig. 4.45, the phase angle between the inverters’ output voltage increases with  $R_v$ . Therefore, the VI influences the voltage magnitude and phase angle.

From Fig 4.44, one can calculate the virtual angle ( $\theta_v$ ) added by the VI and which is between  $V_{dqNewref}$  and  $V_{dqref}$ . Eq. 4.62 describes the relation between  $V_{dqNewref}$  and  $V_{dqref}$ .

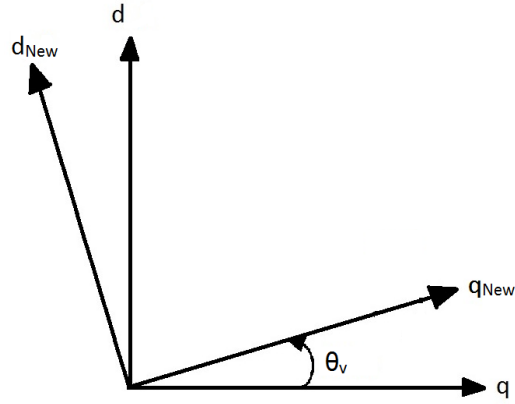


Figure 4.44: Virtual angle

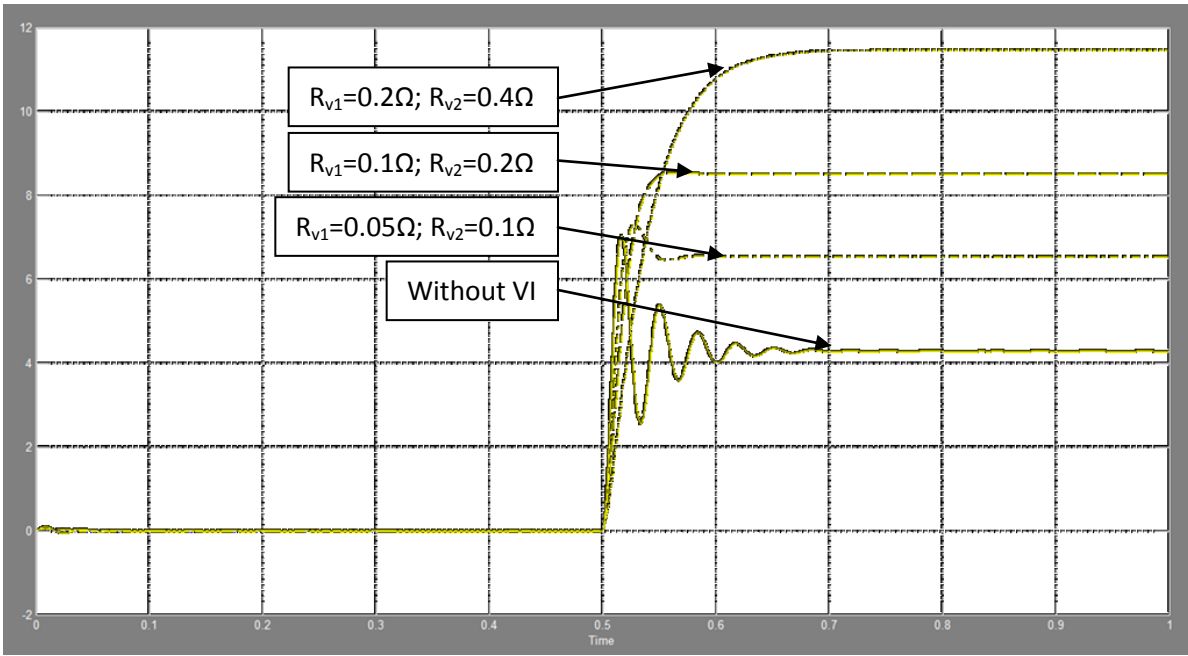


Figure 4.45: Phase angles between the inverters' output voltages when  $R_v$  is increased (Degree) vs. Time (s)

$$\begin{bmatrix} V_{qNewref} \\ V_{dNewref} \end{bmatrix} = \begin{bmatrix} \cos(\theta_v) & \sin(\theta_v) \\ -\sin(\theta_v) & \cos(\theta_v) \end{bmatrix} \cdot \begin{bmatrix} V_{qref} \\ V_{dref} \end{bmatrix} \quad (4.77)$$

After developing Eq. 4.62,  $\theta_v$  can be calculated using the following equation.

$$\theta_v = \text{asin} \left( \frac{V_{dref} - V_{dNewref}}{V_{qref} + V_{dref}} \right) \quad (4.78)$$

Where,  $V_{qref}$  is a constant 169.7V,  $V_{dref}$  is null and  $V_{dref}-V_{dNewref}$  is the voltage drop across the VI in d channel. Hence, Eq. 4.63 becomes as follows. From Eq. 4.51, the angle  $\theta_v$  is function of the output current and the VI components.

$$\theta_v = \text{asin}\left(\frac{V_{dv}}{169.7}\right) \quad (4.79)$$

#### 4.7.1 Proposed virtual impedance implementation

From Eq. 4.51 and 4.64, the proposed VI is implemented in the system's dq model as Fig. 4.46 shows. The "voltage reference generator" block calculates the voltage references in dq using the angle  $\delta-\theta_v$ .

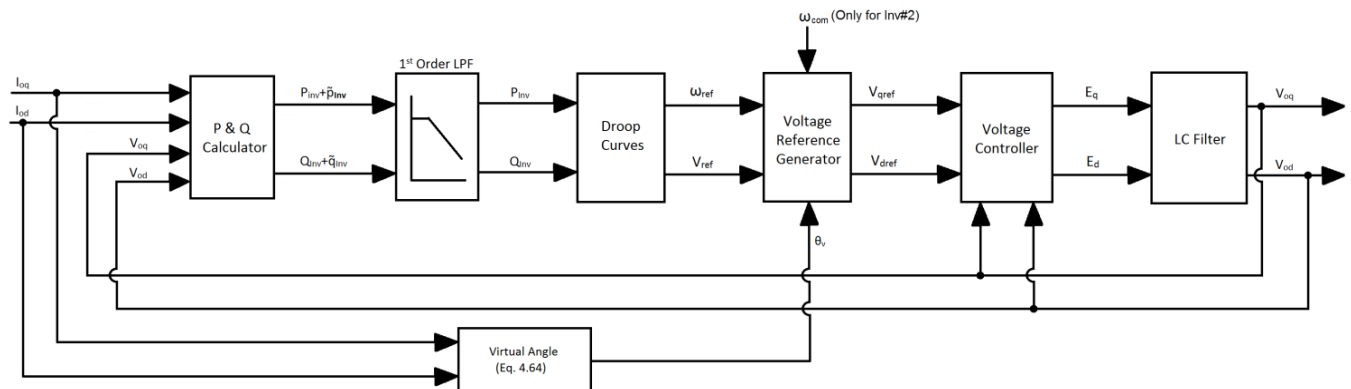


Figure 4.46: Proposed virtual impedance implementation

The "Voltage Reference Generator" block contains what the next figure shows. Note that the angle  $\delta$  in Eq. 3.31 is replaced by  $\delta-\theta_v$  in Fig. 4.47. Remember that in the dq model of the system,  $\delta$  is null for the inverter #1 hence its  $V_{dqNewref}$  are calculated using  $-\theta_v$ .

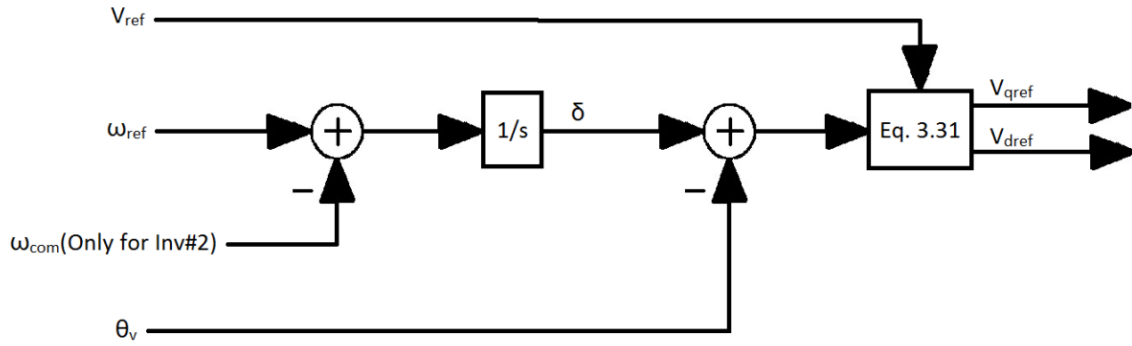


Figure 4.47: Voltage reference generator bloc

#### 4.7.2 Small-signal model including the proposed virtual impedance

The small-signal modeling of the system including the new VI implementation which is based on phase shifts starts by linearizing the Eq. 4.64. This allows the calculation of the small-signal of the new voltage reference in dq coordinates. The small-signal of  $\theta_v$  is given by Eq. 4.65.

$$\Delta\theta_v = \frac{1}{169.7 \sqrt{169.7^2 - V_{dvo}^2}} \Delta V_{dv} \quad (4.80)$$

From Eq. 4.51, the small signal of the voltage drop across the VI in the d channel is given by the following;

$$\Delta V_{dv} = \omega_o L_v \Delta I_{oq} + R_v \Delta I_{od} \quad (4.81)$$

Hence, Eq. 4.65 becomes as follows.

$$\Delta\theta_v = \frac{\omega_o L_v}{169.7 \sqrt{169.7^2 - V_{dvo}^2}} \Delta I_{oq} + \frac{R_v}{169.7 \sqrt{169.7^2 - V_{dvo}^2}} \Delta I_{od} \quad (4.82)$$

Based on Eq. 3.19, the new voltage reference in dq for the inverters is given by;

$$\begin{bmatrix} \Delta V_{qref1v} \\ \Delta V_{dref1v} \end{bmatrix} = \begin{bmatrix} -n_{q1} \cos(-\theta_{v1o}) \\ -n_{q1} \sin(-\theta_{v1o}) \end{bmatrix} [\Delta Q_1] - \begin{bmatrix} -V_{qref1o} \sin(-\theta_{v1o}) - V_{dref1o} \cos(-\theta_{v1o}) \\ V_{qref1o} \cos(-\theta_{v1o}) - V_{dref1o} \sin(-\theta_{v1o}) \end{bmatrix} [\Delta\theta_{v1}] \quad (4.83)$$

And,

$$\begin{aligned}
 \begin{bmatrix} \Delta V_{qref2v} \\ \Delta V_{dref2v} \end{bmatrix} &= \begin{bmatrix} -n_{q2} \cos(\delta_o - \theta_{v2o}) \\ -n_{q2} \sin(\delta_o - \theta_{v2o}) \end{bmatrix} [\Delta Q_2] \\
 &+ \begin{bmatrix} -V_{qref1o} \sin(\delta_o - \theta_{v2o}) - V_{dref1o} \cos(\delta_o - \theta_{v2o}) \\ V_{qref1o} \cos(\delta_o - \theta_{v2o}) - V_{dref1o} \sin(\delta_o - \theta_{v2o}) \end{bmatrix} [\Delta \delta - \Delta \theta_{v2}] \quad (4.84)
 \end{aligned}$$

Where,  $\Delta V_{dqref1v}$  is the voltage reference based on the phase shift  $\theta_{v1}$  of the inverter #1, and  $\Delta V_{dqref2v}$  is the voltage reference based on  $\delta$  (Eq. 4.1) and  $\theta_{v2}$  of the inverter #2.

Finally from Eq. 4.67, 4.68 and 4.69 and following the same modeling steps in section 4.2, the system's small-signal model can be derived. Setting the system's parameters as listed in Table 4.3, Fig. 4.48 and 4.49 show the position of the dominant poles of the detailed system with the proposed VI compared with that of the detailed system with the conventional VI when purely resistive and purely inductive VI in increased respectively. Note that  $R_{v2}$  and  $L_{v2}$  chosen for this frequency domain comparison are still twice bigger than  $R_{v1}$  and  $L_{v1}$  respectively. The  $R_{v1}$  has been varied from  $0.02\Omega$  to  $0.3\Omega$  and from  $1\Omega$  to  $100\Omega$  for the system with the conventional VI and for the system with the proposed VI respectively. For the purely inductive VI,  $X_{v1}$  has been varied from  $0.1\Omega$  to  $2\Omega$  and from  $1\Omega$  to  $100\Omega$  for the system with the conventional VI and for the system with the proposed VI respectively. Unlike the system with the proposed VI, the one with the conventional VI is very sensitive to the VI variations.

As one can see in Fig. 4.48 and 4.49, the proposed VI influences the system dynamics similarly as the conventional VI does. In other words, both systems with the conventional and with the proposed VI loops make the dominant poles move to the left side.

In the next section, time domain simulations are done to verify the impact of the proposed VI on the system's dynamic and steady-state responses.

Note that the .m file of Matlab which contains the small-signal state-space model of the detailed system including the proposed VI loop is given in the Appendix-G.

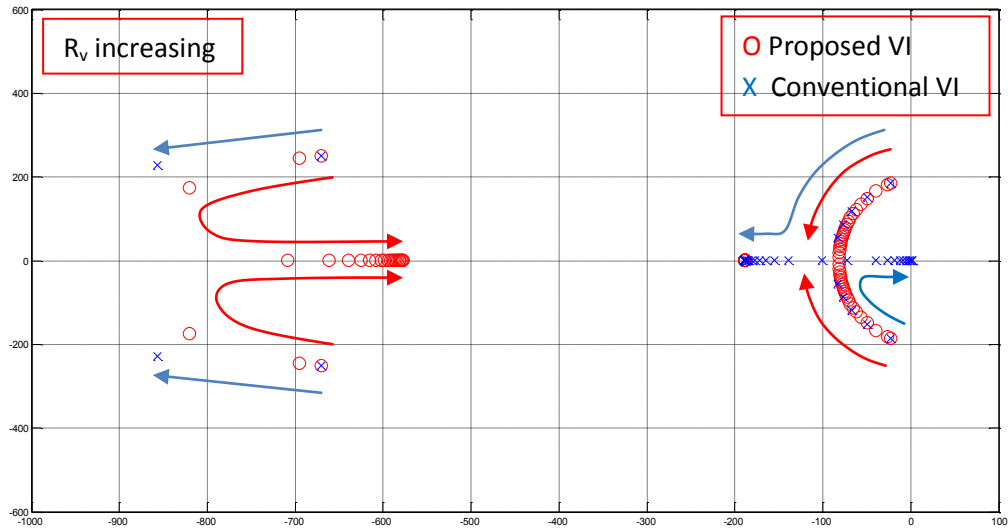


Figure 4.48: Dominant poles of the systems detailed model with conventional and proposed VI when  $R_v$  is increased

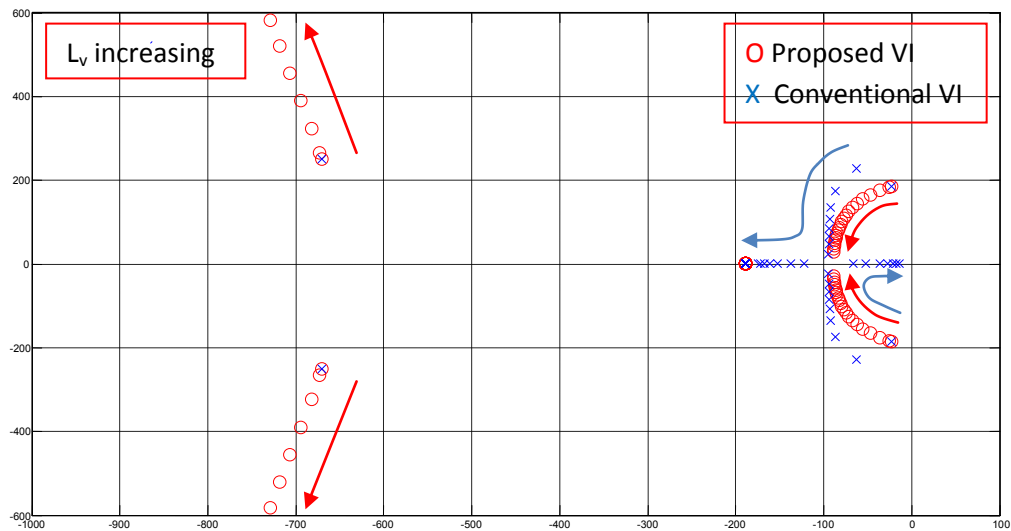


Figure 4.49: Dominant poles of the systems detailed model with conventional and proposed VI when  $L_v$  is increased

### 4.7.3 Performance verification of the system including the proposed virtual impedance loop

#### 4.7.3.1 Load variation test

Using the same simulation steps and system parameters as in section 4.6.3.1, Fig. 4.50 and 4.51 show the inverters' output active power and coupling reactive power respectively when purely resistive VI ( $R_v$ ) is increased.

From Fig. 4.50 and 4.51, the proposed VI loop damps the system transients (See Fig. 4.52) while using large values of  $R_v$ . Moreover, it does not influence the steady-state value since it does not affect the voltage regulation (see Fig. 4.53).

Regarding the purely inductive VI, Fig. 4.54 and 4.55 show the inverters' output active power and coupling reactive power respectively when  $L_v$  is increased. As one can see in those figures, the proposed VI when using only  $L_v$  also damps the system's transient response (See Fig. 4.56) and does not affect the voltage regulation (See fig. 4.57).

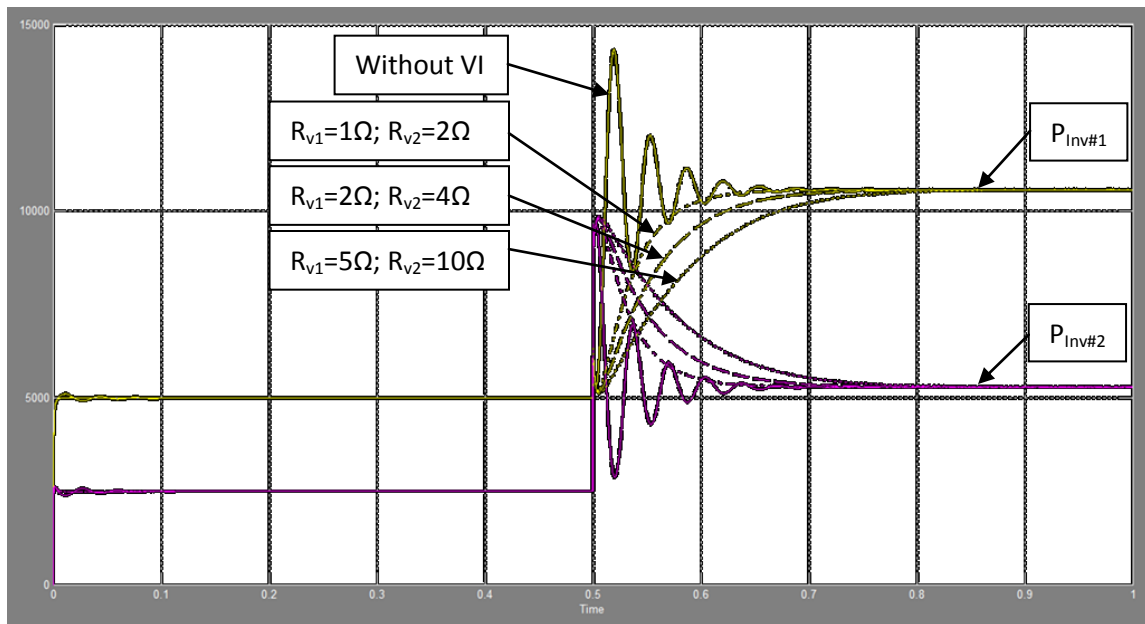


Figure 4.50: Inverters' output active power when  $R_v$  in the proposed VI is increasing (W) vs. Time (s)

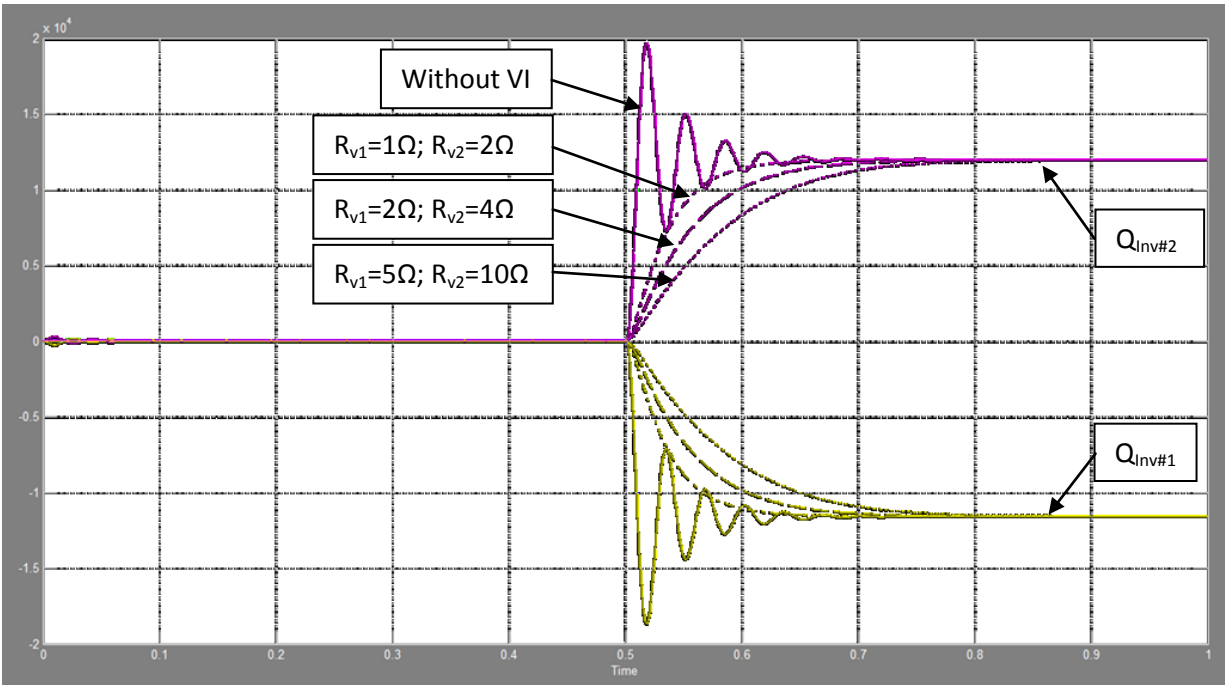


Figure 4.51: Inverters' output reactive power when  $R_v$  in the proposed VI is increasing (VAr) vs. Time (s)

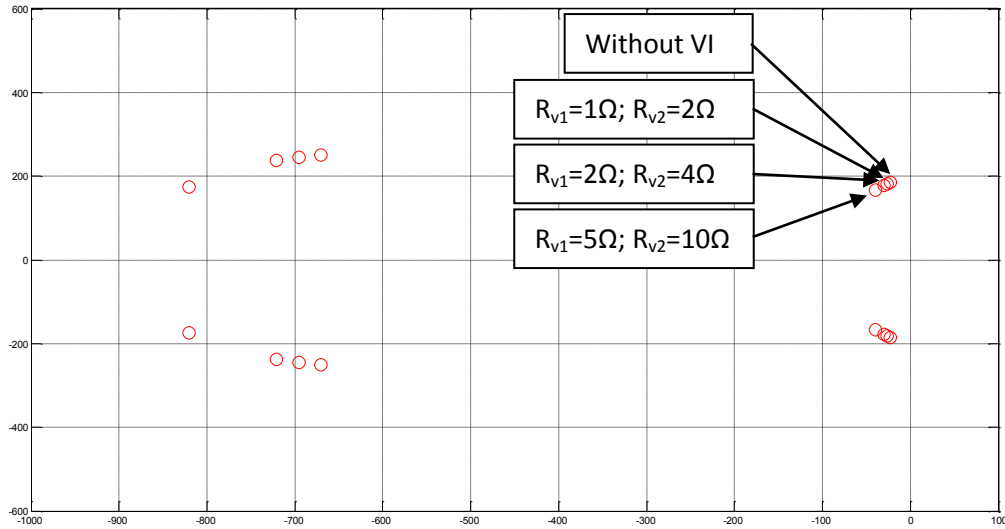


Figure 4.52: Dominant pole of the detailed system including the proposed VI for different values of  $R_v$



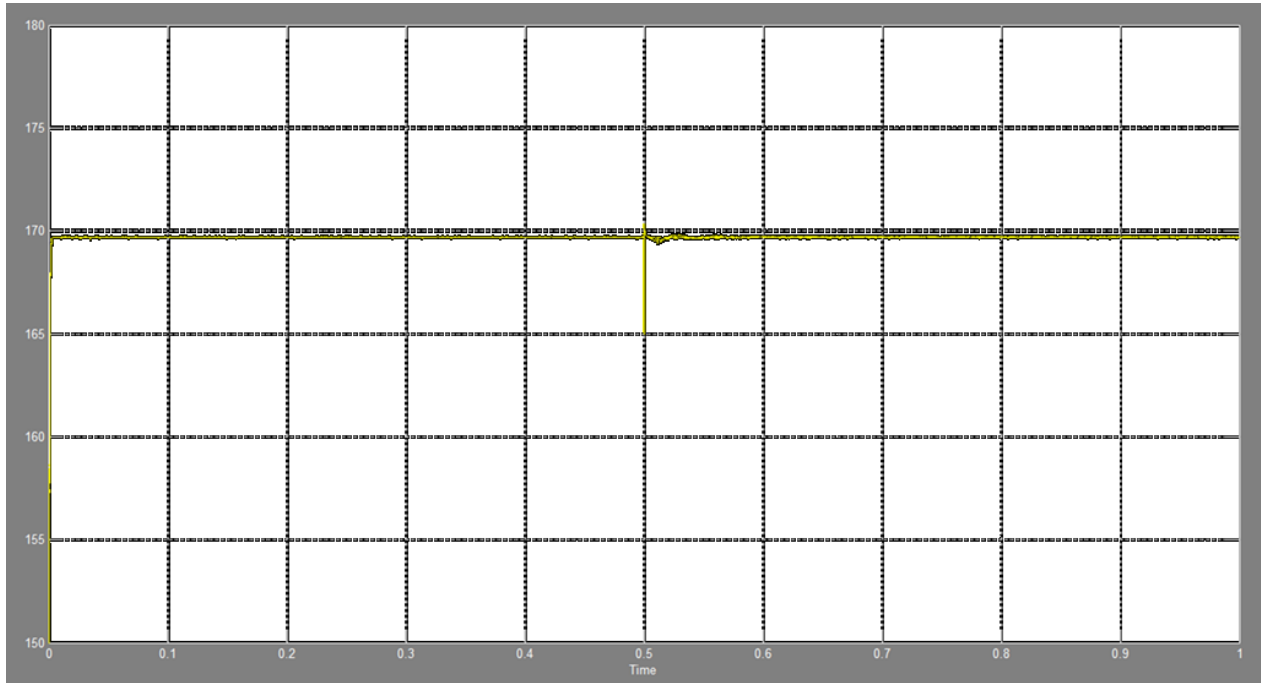


Figure 4.53: Inverters' output peak voltage magnitudes for different values of  $R_v$  (V) vs. Time (s)

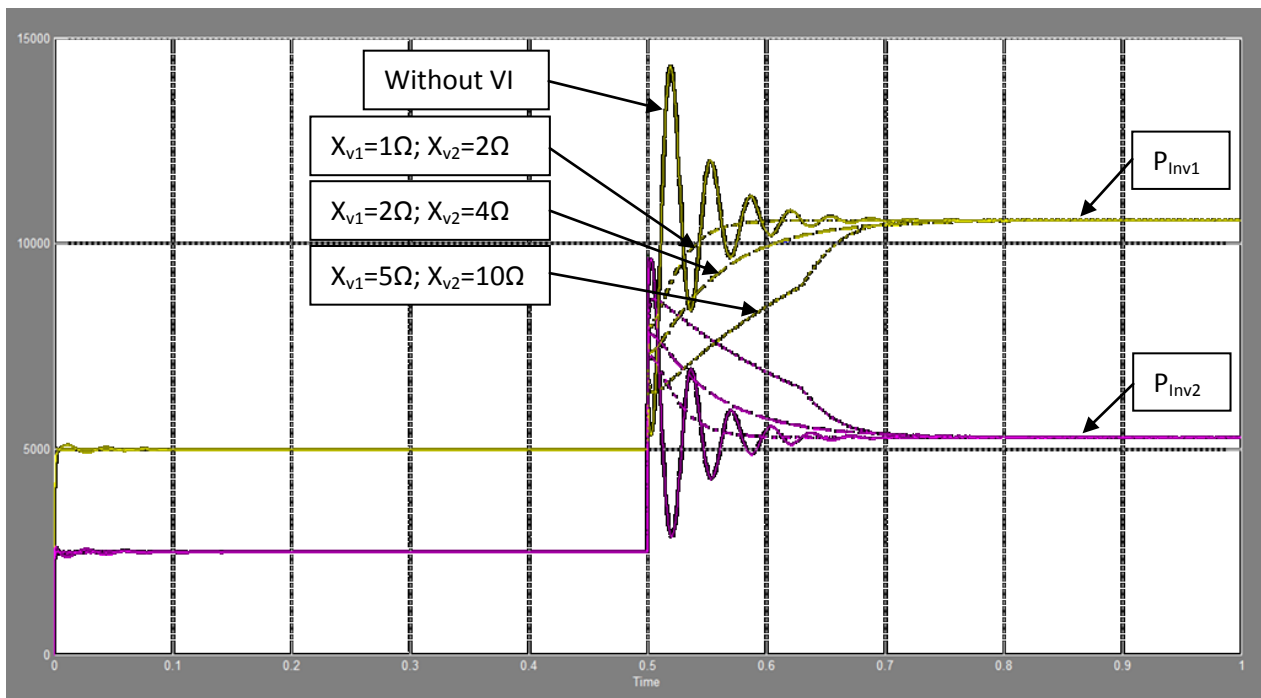


Figure 4.54: Inverters' output active power when  $L_v$  in the proposed VI is increasing (W) vs. Time (s)

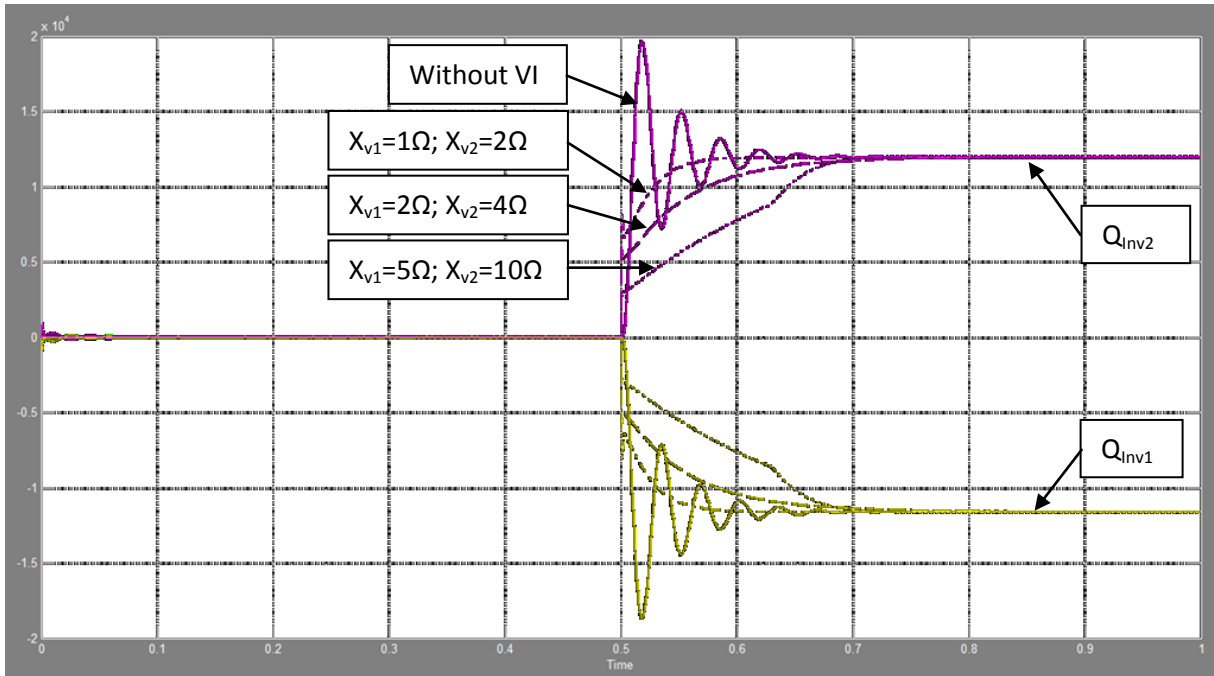


Figure 4.55: Inverters' output reactive power when  $L_v$  in the proposed VI is increasing (VAr) vs. Time (s)

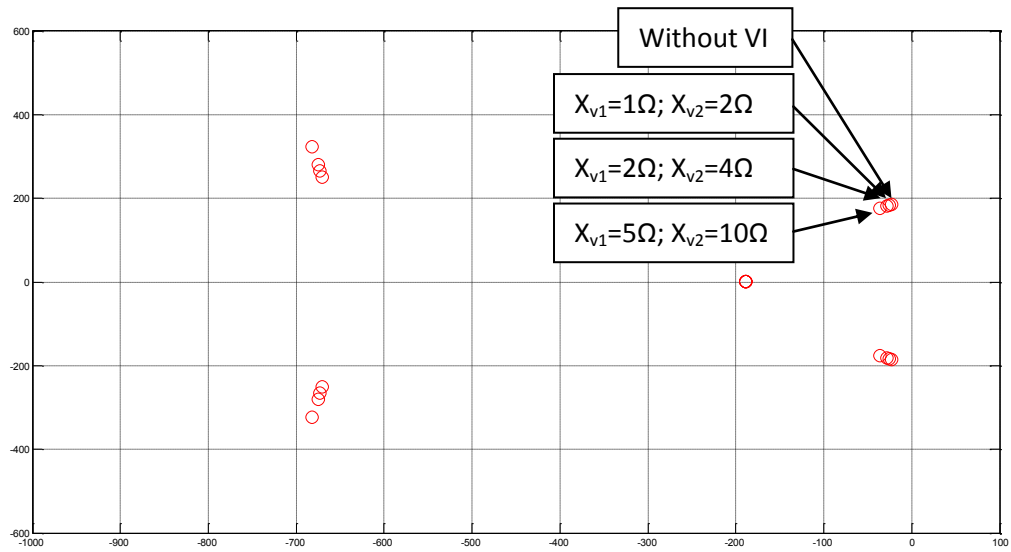


Figure 4.56: Dominant pole of the detailed system including the proposed VI for different values of  $L_v$

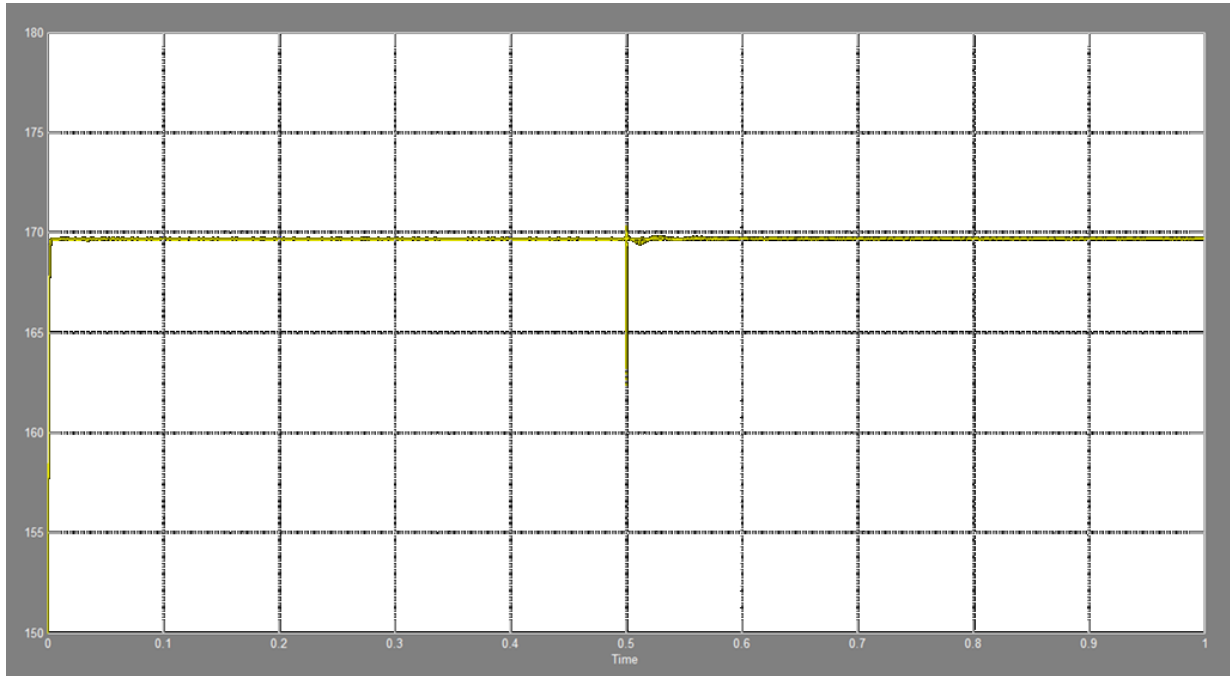


Figure 4.57: Inverters' output peak voltage magnitudes for different values of  $L_v$  (V) vs. Time (s)

Comparing the results obtained in this section, the resistive proposed VI generates better dynamics than the inductive proposed VI.

#### 4.7.3.2 Power signal variation test

It has been proven previously that the conventional VI allows implementing larger values of  $n_q$  and consequently enhancing the reactive power sharing. In this section, the same verification is done for the proposed VI.

Setting the system's parameters as listed in Table 4.3, Fig. 4.58 shows the inverters' output reactive power, with different values of  $n_q$ , generated after a step in  $V_{nL1}$  which occurs at 0.1s. The amount of the step is  $+2.5\Delta V$  in order to draw 6kVAR from inverter #1 to inverter #2.

As mentioned before, the increasing of  $n_q$  generates better Q sharing. However, large values of  $n_q$  make the system response more oscillatory. From the results obtained in Fig. 4.58, the proposed VI allows implementing larger values of  $n_q$  generating accurate Q sharing.

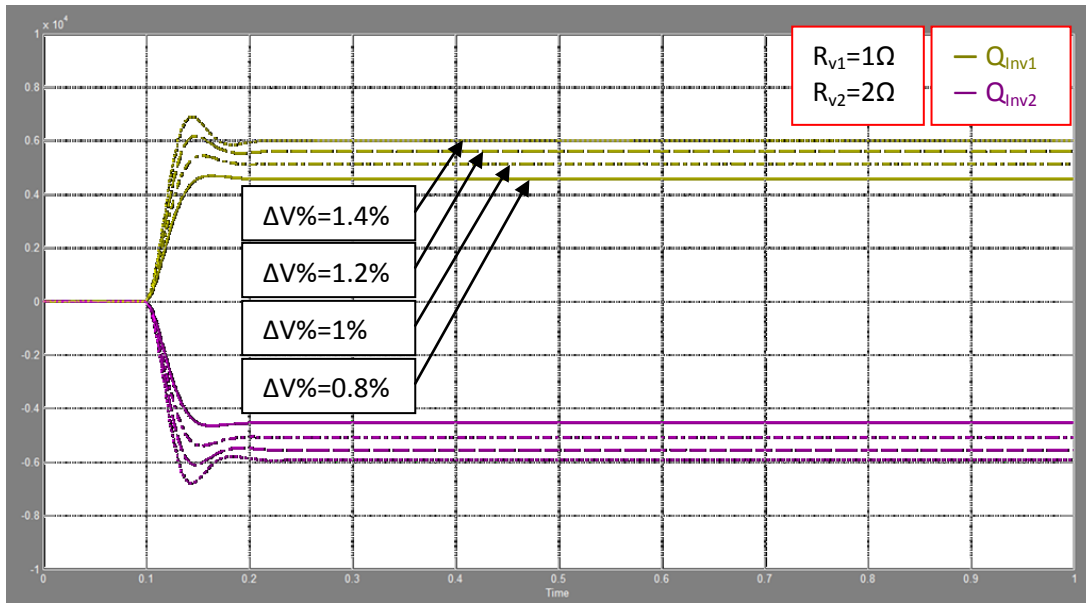


Figure 4.58: Inverters' output reactive power including proposed VI and when  $n_q$  is increased (VAr) vs. Time (s)

For  $f_{nL}$  variation, same simulation as in section 4.5.2 has been done. Fig. 4.59 shows the inverters' output active power when the proposed VI is used.  $f_{nL2}$  is decreased by 4.5Hz at 0.5s, in order to charge the inverter #2's battery bank (in the DC bus) with a power of 5kW, then it is returned to its initial value (62Hz) at 1s.

The steady-state responses when using the proposed VI are still inaccurate due to the real line impedance characteristics. The proposed virtual impedance has no influence on the steady-state values but it has a very good impact on the system's transients. The proposed VI allows implementing larger values of  $R_v$  and  $L_v$  generating smoother and well damped transients.

There is another important characteristic of the proposed virtual impedance. From Fig. 4.48 and 4.49, the proposed VI components could be very large yet the system never becomes unstable. By increasing VI, the dominant poles for large value of VI become real (e.g. when  $R_{v1}$  is above 35Ω) hence the system's settling time becomes fixed when it reaches its maximum values. This characteristic of the proposed VI; allowing the implementation of very large values of  $R_v$  and  $L_v$ , makes this technique less dependent on

the real line impedance characteristics than the conventional VI technique. To verify this, Fig. 4.60 shows simulations' results when using very large values of  $R_v$ .

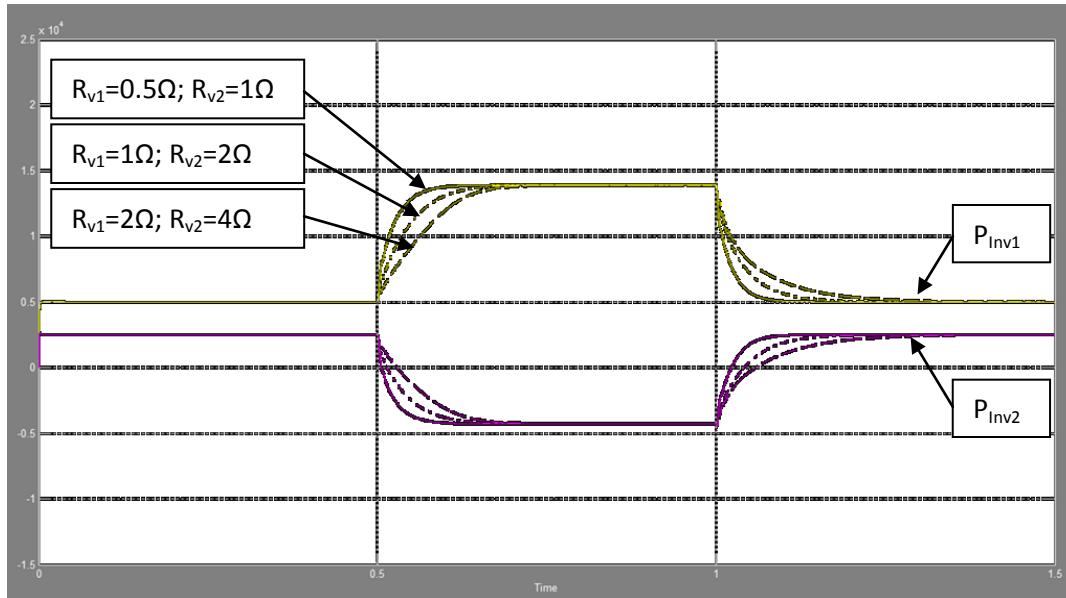


Figure 4.59: Inverters' output active power while using purely resistive proposed VI when a step occurred in  $f_{nl2}$  (W) vs. Time (s)

The system's parameters are listed in Table 4.3, and the simulations' steps are described in Table 4.6.

The very large range of  $R_v$  that could be implemented in the proposed VI makes the system's transients less sensitive by the real line impedance characteristics or at least the proposed VI ensures good transients for a large range of line impedance amplitudes and angles. To verify this, some simulations have been done using different values of  $R_g$  and  $X_g$  when implementing a large purely resistive proposed VI ( $R_{v1}=5\Omega$  and  $R_{v2}=5\Omega$ ).

Fig. 4.61 and 4.62, shows the simulations' results when the ratio  $X_g/R_g$  is fixed and variable respectively. The simulation steps are listed in Table 4.7 where a very large step occurs in the inverter #2's local load. Note that the values of  $R_g$  and  $X_g$  in these tests have been chosen arbitrarily but the line impedance is still resistive. As one can see from Fig. 4.61 and 4.62, the proposed VI is robust to the line impedance components variations. This allows the enhancement of the system's transients for a wide range of

feeders' characteristics. Moreover, the VI components of the inverter #2 do not have to be twice as large as the VI components of the inverter #1 since the AC voltage amplitude is not affected, unlike in the case when conventional VI is used, making the implementation of the VI less complicated where many DGs are connected in parallel.

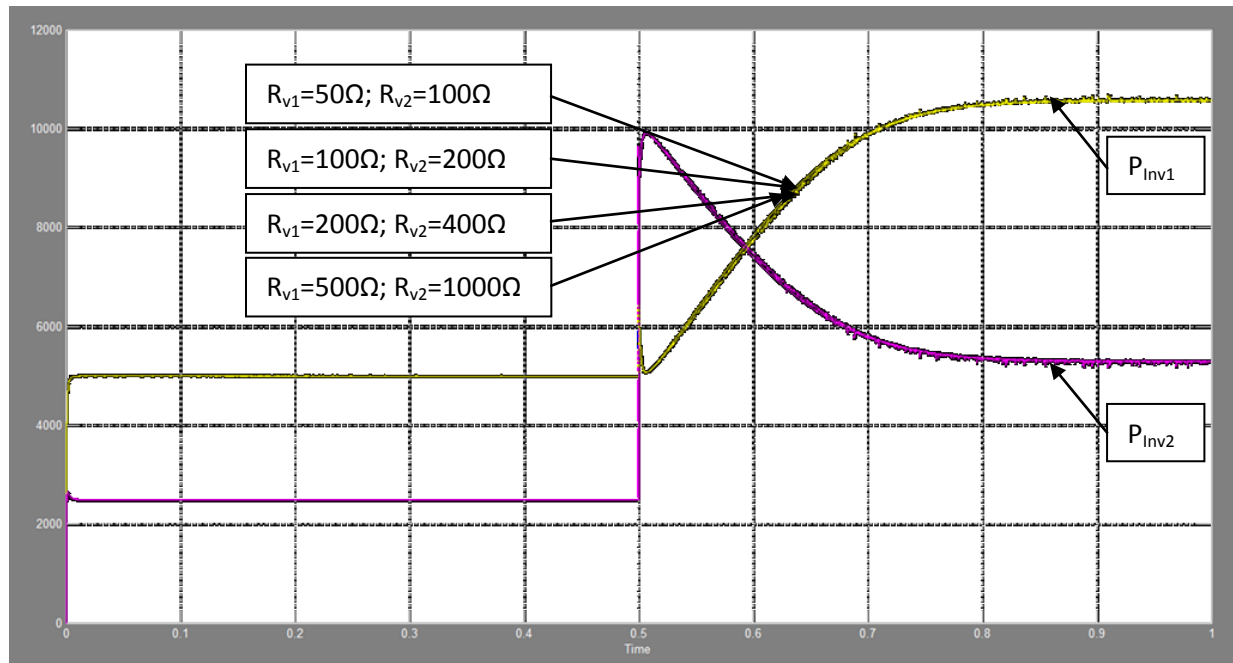


Figure 4.60: Inverters' output active power when  $R_v$  in the proposed VI is very large (W) vs. Time (s)

In Fig. 4.61, the values of  $R_g$  and  $X_g$  have been varied from 4 times smaller than the  $R_g$  and  $X_g$  in Table 4.3 to 1.5 times larger. As one can see, the system still has good dynamics when the proposed VI is used. However, in Fig. 4.62, only  $R_g$  is varied from 5 times smaller than the  $R_g$  in Table 4.3 to  $0.23\Omega$ . This is because, as discussed above,  $R_g$  is the most influencing element of the line impedance on the system's dynamics. From the results shown in fig. 4.62, the proposed VI ensures good dynamics even for very small values of  $R_g$ . In the other hand, the conventional VI needs to be designed for each value of the feeder's components. Moreover, the conventional VI design depends also on the inverters' ratings since the voltage drop caused is a function of the inverters' output currents.

Therefore, the proposed VI is more robust than the conventional virtual impedance in terms of systems' transients' enhancement and could be considered as a technique that allows the inverters plug-and-play into a mini-grid for at least a wide range of feeders.

Note, the different values of steady-state responses in fig. 4.61 and 4.62 are caused by the different values of  $R_g$  and  $L_g$ . Therefore, the P & Q coupling needs to be eliminated or reduced by another control technique when the proposed VI is used.

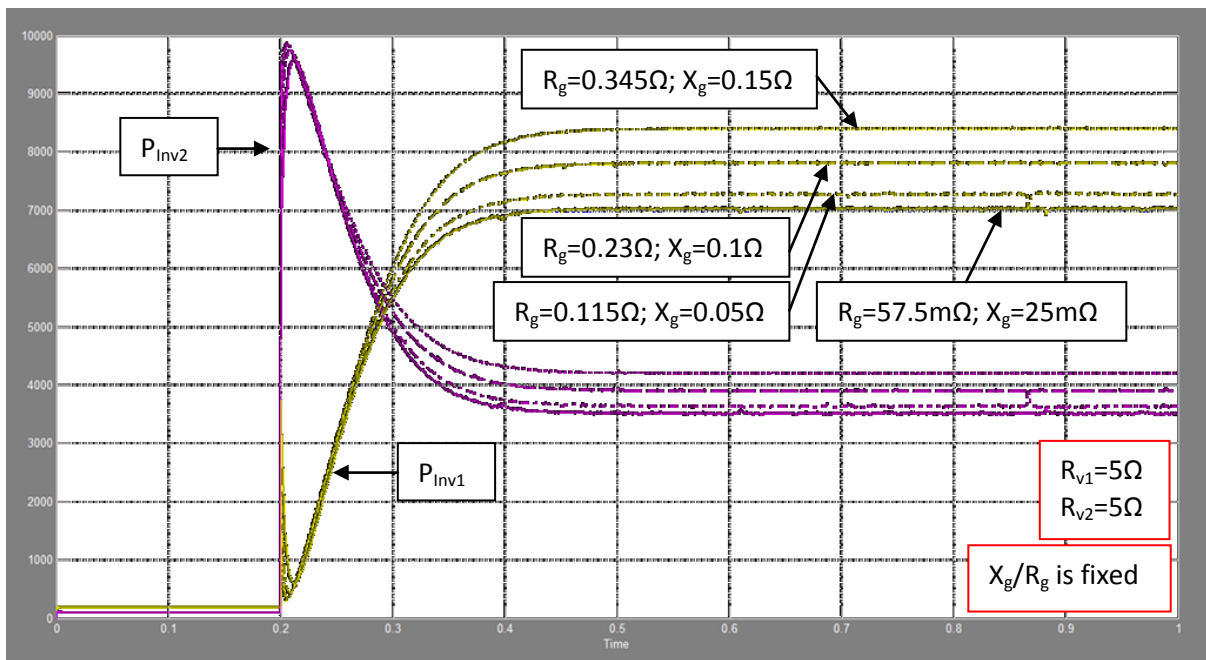


Figure 4.61: Inverters' output active power when  $R_v$  in the proposed VI is very large and  $X_g/R_g$  is fixed (W) vs. Time (s)

Table 4.7: Simulations' steps when  $R_v$  is large

Time (s)	$P_{Load1}$ (kW)	$P_{Load2}$ (kW)
0	0.2	0.1
0.2	0.2	10

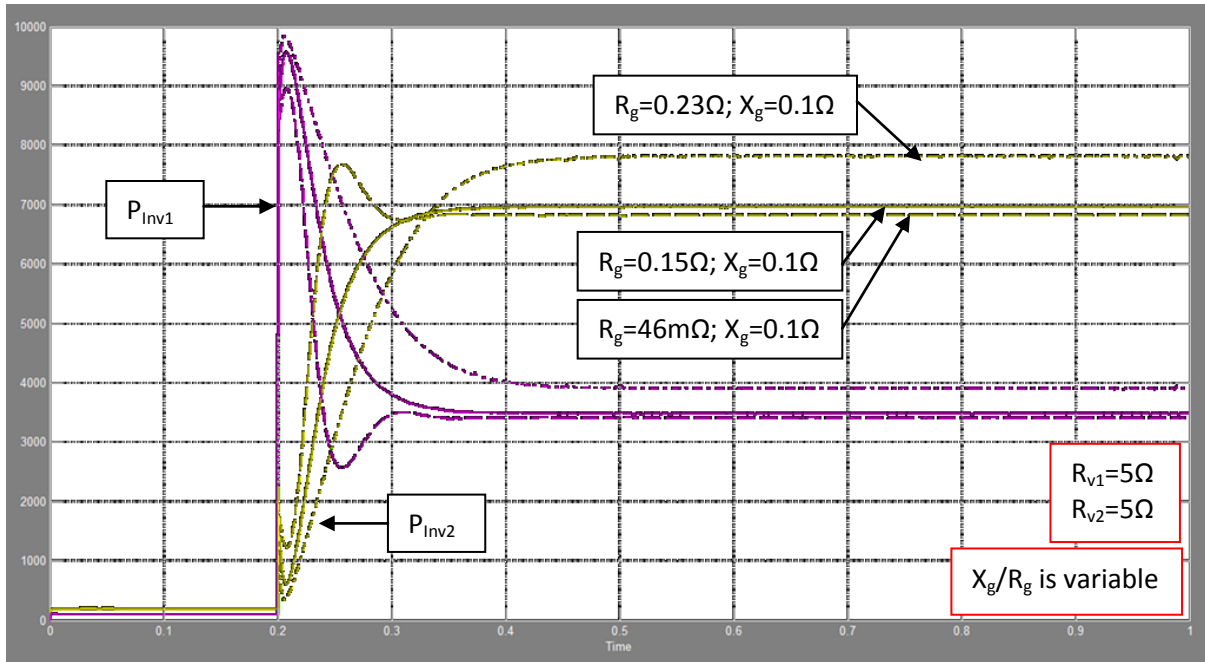


Figure 4.62: Inverters' output active power when  $R_v$  in the proposed VI is very large and  $X_g/R_g$  is variable (W) vs. Time (s)

## 4.8 Conclusions

In this chapter, an in-depth analysis have been done about a simple mini-grid, composed by of two three-phase voltage source inverters, two local loads and a resistive feeder. After deriving the small-signal model of the system, the most influencing parameters have been identified. As found out in Chapter 3, the parameters that affect directly the system's dynamics are still the same. Therefore, the dominant poles of the system move to the left due to the following actions;

- A decrease in the P vs. f droop gain ( $m_p$ )
- A decrease in the Q vs. V droop gain ( $n_q$ )
- An increase in the inductive component of the line impedance ( $X_g$ )
- An increase in the resistive component of the line impedance ( $R_g$ )
- An increase in the LPF's cut-off frequency ( $f_c$ )



To verify the points above, time domain simulations have been done by Simulink/Matlab showing the same results obtained in the frequency domain. Moreover, it has been shown that the  $X_g/R_g$  ratio also affects the system's steady-state responses. The increasing of  $X_g/R_g$  ratio generates smaller coupling between P and Q. However, in LV networks the feeders are usually resistive which generates very bad P and Q sharing when using the conventional droop control.

Due to some constraints, some of the influencing parameters could not be varied, to enhance the system's behavior, and others are uncontrollable. Therefore, the conventional droop control needs to be improved in order to get a good system's transient and steady-state responses. Note that only the enhancement of the dynamic responses has been discussed in this chapter.

Because the line impedance is uncontrollable, the virtual impedance loop is the most common approach used to enhance the system's dynamics. The idea behind this technique consists on adding virtually an inductive impedance in series to the line impedance, mimicking the influence of an internal impedance to enhance the system's dynamics. However, the conventional virtual impedance implementation affects the AC voltage amplitude causing bad voltage regulation. Moreover, the conventional VI components need to be designed depending on some parameters: The real line impedance, the inverter's ratings (because the voltage drop across the VI is a function of the inverter's output current) and the Q vs. V droop gain ( $n_q$ ) (because the VI has to be large when  $n_q$  is large in order to maintain acceptable dynamics).

After studying and analyzing the conventional VI loop, a proposed VI loop has been presented showing its benefits to the system behavior. The idea behind the new VI loop is based on damping the system's transients by adding a phase angle to the inverters' output voltage. After deriving small-signal models of the same system, but with the different VI loop, it has been found that the new VI loop influences the system's dynamics similarly as the conventional VI loop. However, by time domain simulations, the

proposed VI has shown better robustness to the line impedance variations and better voltage regulation to the output active power variations.

# Chapter 5 - Parallel operation of three-phase voltage source inverter with Genset

## 5.1 Introduction

This chapter focuses on the operation of one droop controlled voltage source inverter in parallel with a diesel engine generator set (*Genset*) in an autonomous micro-grid. As shown in Fig. 5.1, the inverter and the Genset present a local load at their terminals and they are connected by means of a tie-line. The main issue to be studied in this chapter is the transient response of the system at load and power signals variations. The system verifications are done only by means of time domain simulations on Matlab/Simulink.

## 5.2 Problematic description

As mentioned previously, the inverter's droop controller should be designed depending on the characteristics of the Genset in order to get a stable system and the expected power sharing. The diesel generators are equipped by an element called the speed governor which controls the torque applied to the generator shaft [20]. Consequently, the speed governor controls the rotational speed (RPM) of the synchronous generator, hence the output voltage frequency. In general, Genset controls use the principle of droop to maintain stability otherwise the Genset's speed regulation in multi-Genset systems would be unstable [21]. Therefore, a parallel inverter to a Genset should be controlled similarly in order to ensure good transients and good power sharing. In other words, the P vs. f droop approach should be implemented in the inverter using the same droop percentage as in the Genset (See Fig 5.2) in order to share load variations proportionally to their capacities or rated values.

Note that the same inverter including the voltage controller and the LC filter designed in Chapter 2 are used in this system.

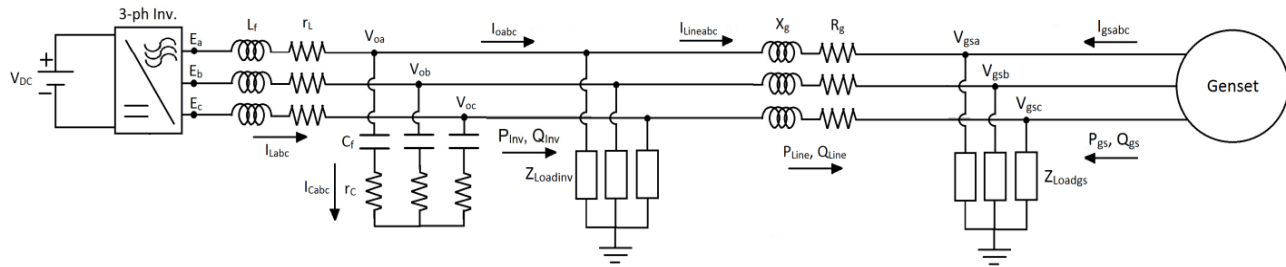


Figure 5.1: Three-phase Voltage Source Inverter connected in parallel with a Genset via a feeder

The following table lists the system ratings.

Table 5.1: Genset and Inverter ratings

AC voltage source	Output Voltage (Vrms)	Full-load Frequency (Hz)	Maximum Power kVA	Droop (%)
Genset	230/400	50	30	3
Inverter	230/400	50	10	3

Fig. 5.2 illustrates the droop governor speed curve and the inverter frequency droop curve. The governor decreases the rotor speed by 3% of the reference speed over the full range of the governor output. Therefore, the inverter needs to get the same droop controller, in %, in order to share load proportionally to its ratings. Since the Genset is three times powerful as the inverter, the frequency droop gains of the inverter ( $m_{pinv}$ ) has to be three times bigger than the frequency droop gain of the Genset ( $m_{pgs}$ ).

The main characteristic difference between the inverter and the Genset is that the latter is very slow in terms of frequency response with respect to the inverter. Fig. 5.3 shows the frequency response of the two sources under heavy load variations when operating separately. A full load step occurs at  $t=5s$  generating a frequency deviation from 51.5Hz (no-load frequency) to 50Hz, then at  $t=10s$  the full-loads are disconnected making the operating frequencies settle at 51.5Hz.

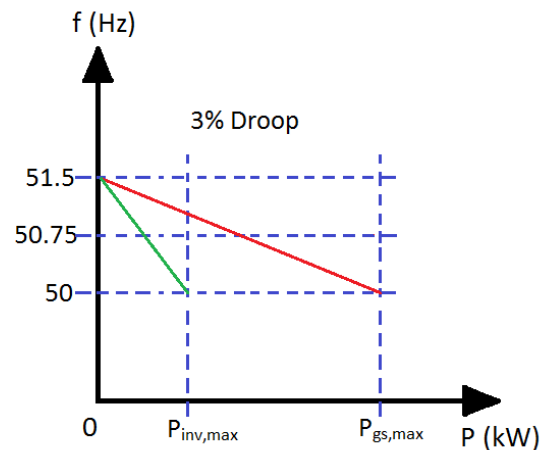


Figure 5.2: P vs. f droop curves

As one can see in Fig. 5.3, the frequency response of the inverter is almost instantaneous as compared to the frequency response of the Genset which has a settling time of 2s. In case where the two sources are connected in parallel through a feeder as shown in Fig. 5.1, that big difference in frequency response speed could generate a large overshoot in the inverter's output power even if a load step occurs at the Genset's side. Letting the inverter taking most of the dynamics could be harmful. Fig. 5.4 shows the output active power of the inverter and the Genset when a full load step occurs at the Genset's side. As one can see there, from the average value of the output power of the two elements, the inverter takes most of the load variation since it reacts much quicker than the Genset. The bigger the difference in power ratings between the Genset and the inverter, the bigger the overshoot that appears in the inverter's output power could be. Moreover, if there were two inverters of the same size and speed, they would be sharing equally the load variations in either side only if the tie-lines which connect them to the Genset are the same. Otherwise, the inverter with smaller tie-line would take bigger load variations. Note that the overshoot percentage in Fig 5.4 appearing in the inverter's active power is equal to 135% of the steady-state value.

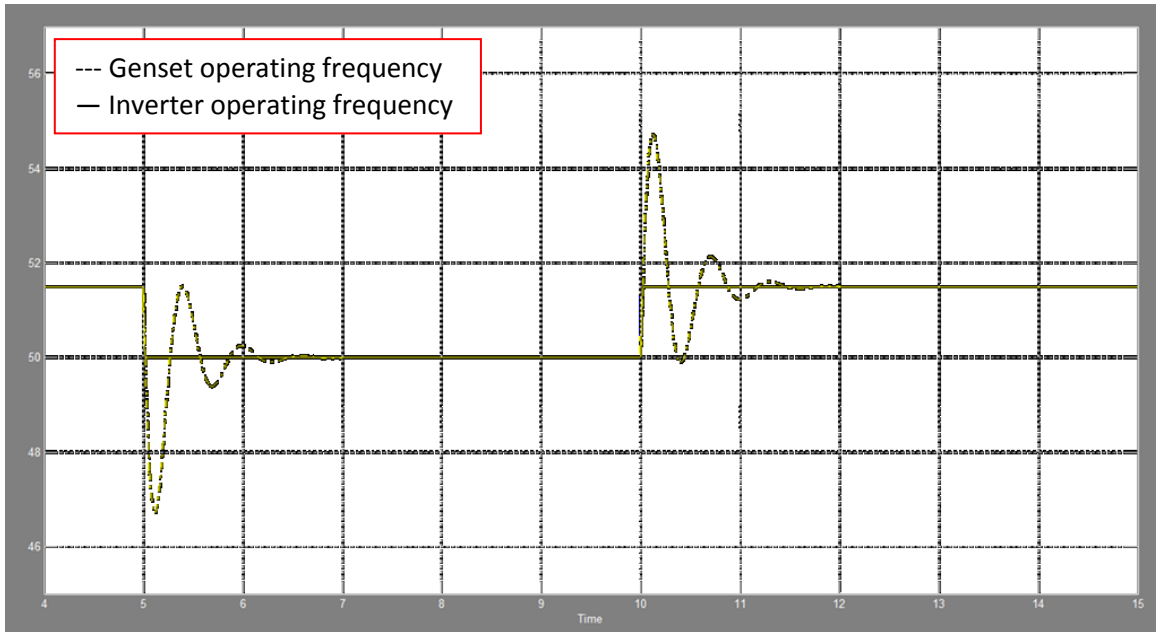


Figure 5.3: Frequency responses of the inverter and the Genset under heavy load variations (Hz) vs. Time (s)

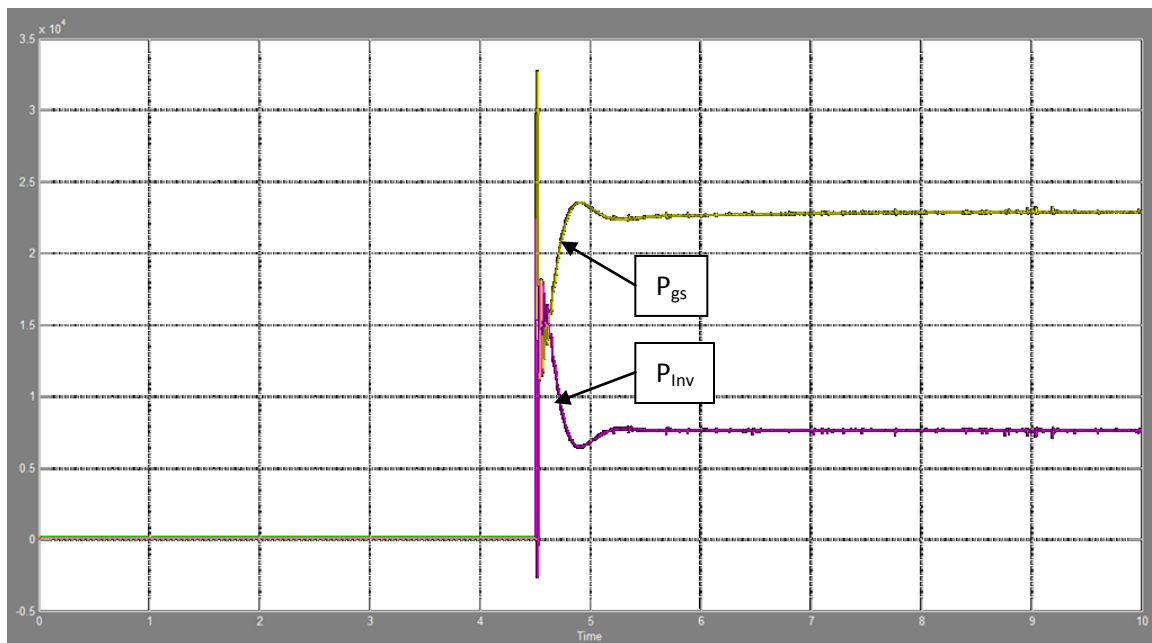


Figure 5.4: Inverter and Genset's output active power (W) vs. Time (s)

Note that the results shown in Fig. 5.3 and 5.4 have been obtained from simulations ran on Matlab/Simulink of the system. The simulation file is described in the following sections. In the next section a proposed solution that allows decreasing the overshoot of the inverter's transients is presented.

### 5.3 Proposed solution: Settling time variation

The proposed solution to the discussed problem in the previous section consists in slowing down the inverter's speed response by adding a new control loop. The purpose of the latter is to add, proportionally to the inverter's output power, a negative angle to the output voltage phase angle of the inverter in order to force the angle ( $\delta$ ), generated physically between the two sources, to increase slowly. For better understanding, one can assume two ideal drooped AC voltage sources connected in parallel through a purely inductive feeder as shown in Fig. 5.5. Note that only the active power dynamics is studied in this chapter.

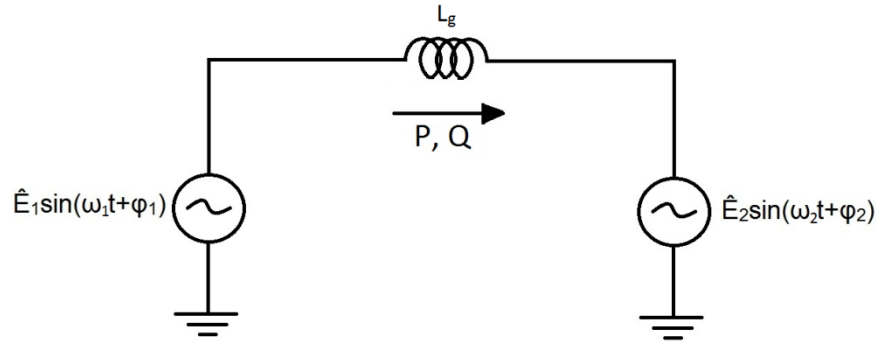


Figure 5.5: Parallel AC voltage sources via a purely inductive feeder

For quick reference, the equations obtained in Chapter 3 concerning this case are rewritten below.

$$P = \frac{E_1 E_2}{X_g} \sin(\varphi_1 - \varphi_2) \quad (5.1)$$

$$Q = \frac{E_1 E_2}{X_g} \cos(\varphi_1 - \varphi_2) - \frac{E_2^2}{X_g} \quad (5.2)$$

Where,  $X_g$  is the reactance of the feeder ( $\omega L_g$ ). The phase angle ( $\delta$ ) generated due to drooping the operating frequency of AC source #1, which is based on its output active power, is given as follows.

$$\delta = \varphi_1 - \varphi_2 = \int (\omega_1 - \omega_2) dt \quad (5.3)$$

And, the  $P$  vs.  $\omega$  droop curve is given by;

$$\omega_{ref} = \omega_{nL} - m_p P \quad (5.4)$$

From Eq. 5.1-5.4, the closed loop block diagram of the large-signal model showing the output active power of the AC source #1 ( $P_1$ ) using the conventional droop control is shown in Fig. 5.6 [22].

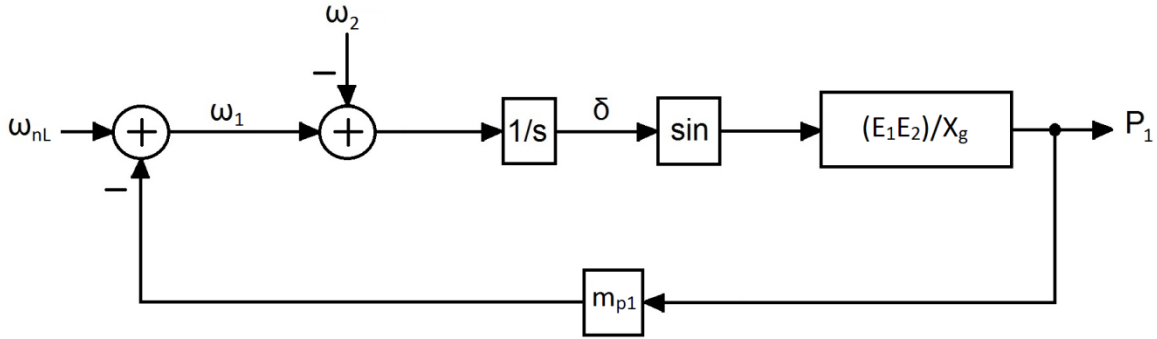


Figure 5.6: The closed loop bloc diagram of the large-signal of  $P_1$  when conventional droop control is used

In order to study the dynamic response of  $P_1$ , a small-signal model should be derived. After linearizing Eq. 5.1-5.4, the closed loop block diagram of the small-signal model of  $P_1$  is shown in Fig 5.7.

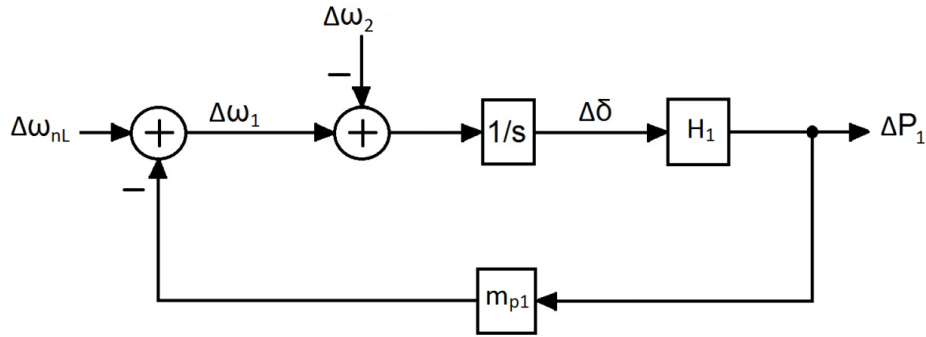


Figure 5.7: The closed loop bloc diagram of the small-signal of  $P_1$  when conventional droop control is used

Where,  $H_1$  is given by the following equation.

$$H_1 = \frac{E_{1o}E_{2o}}{X_g} \cos(\delta_o) \quad (5.5)$$

$E_{1o}$ ,  $E_{2o}$  and  $\delta_o$  are the initial values. From Fig. 5.7, one can derive the closed loop transfer function of the small-signal of  $P_1$  as shown in Eq. 5.6.



$$\Delta P_1(s) = \frac{H_1}{s + m_{p1}H_1} \Delta\omega_{nL}(s) - \frac{H_1}{s + m_{p1}H_1} \Delta\omega_2(s) \quad (5.6)$$

From Eq. 5.6, the only pole that dictates the dynamics is given by the following equation.

$$\rho = -m_{p1}H_1 \quad (5.7)$$

Since the frequency droop gains ( $m_p$ ) have been already fixed by the Genset droop characteristic and the Inverter's ratings, it is impossible to improve the system's dynamic by changing the operating frequency range; hence one needs to add another parameter to achieve that goal without affecting the steady-state response.

In [22], the author has come up with a solution of controlling the speed response of a drooped AC voltage source by using P vs.  $\delta$  instead of P vs. f droop control approach. The modified droop control of [22] consists in measuring the angular frequency at the point of common coupling (PCC), then using it as a feedback signal to compute the output voltage angle of AC source 1. Then, this angle is multiplied by a constant ( $K_{p1}$ ) allowing the variation of the speed of response of its active power. This approach provides one degree of freedom in terms of improving the dynamic response of the system as Eq. 5.8 shows. Note that the small-signal representation of the active power was obtained from Eq. 24 in [22].

$$\Delta P_1(s) = \frac{K_{p1}H_1}{s + K_{p1}m_{p1}H_1} \Delta\omega_{nL}(s) - \frac{K_{p1}H_1}{s + K_{p1}m_{p1}H_1} \Delta\omega_2(s) \quad (5.8)$$

From Eq. 5.8, the dominant pole of the system, given by Eq. 5.9, now is dictated by the multiplication term  $K_{p1}m_{p1}$ .

$$\rho = -K_{p1}m_{p1}H_1 \quad (5.9)$$

The approach of [22] provides good results in terms of controlling the system speed response. However, the measurement of the angular frequency at the common coupling point is not practical. Therefore, a

new control loop has been designed in this Chapter allowing the variation of the system speed response using only a local measurement.

From Eq. 5.1, the phase angle between the two AC voltage sources is given by the following.

$$\delta = \text{asin} \left( \frac{PX_g}{E_1 E_2} \right) \quad (5.10)$$

The proposed control loop is shown in Fig. 5.8. The idea behind this control approach is to increase the rise time and the settling time of the physically generated phase angle ( $\delta$ ) by adding to the latter a negative angle ( $-\delta_d$ ). The constant ( $K_d$ ) serves to increase  $\delta_d$  in order to decrease the system's speed of response, as shown later on.

The large-signal representation of  $P_1$  including the proposed control loop could be simplified as Fig. 5.9 shows. Then, the small-signal representation of  $P_1$  is illustrated in Fig. 5.10. Therefore, from that figure, the closed loop small-signal transfer function of  $P_1$  including the proposed control loop is given by Eq. 5.12. Note that the element  $G_1$  in Fig. 5.10 and Eq. 5.12 is given by Eq. 5.11.

The dominant pole of Eq. 5.12 is given by Eq. 5.13. As one can see, the system's transient response including the proposed control loop can be damped by increasing constant  $K_d$ . In other words, the larger  $K_d$ , the farther the dominant pole will be from the instability region. To verify this, time domain simulations have been done of the system shown in Fig. 5.5. The two ideal AC voltage sources have been assumed to be equal in ratings (10kVA). The system parameters for the simulations are listed in Table 5.2. Note that the new control loop implementation is described in detail in the next section. The simulation results of the system using different values of  $K_d$  are shown in Fig. 5.11. The latter shows the output active power of the two ideal sources when a step of +1.5Hz occurs in the no-load frequency signal at  $t=0.2s$ , in order to produce an active power of 5kW flowing through the feeder.

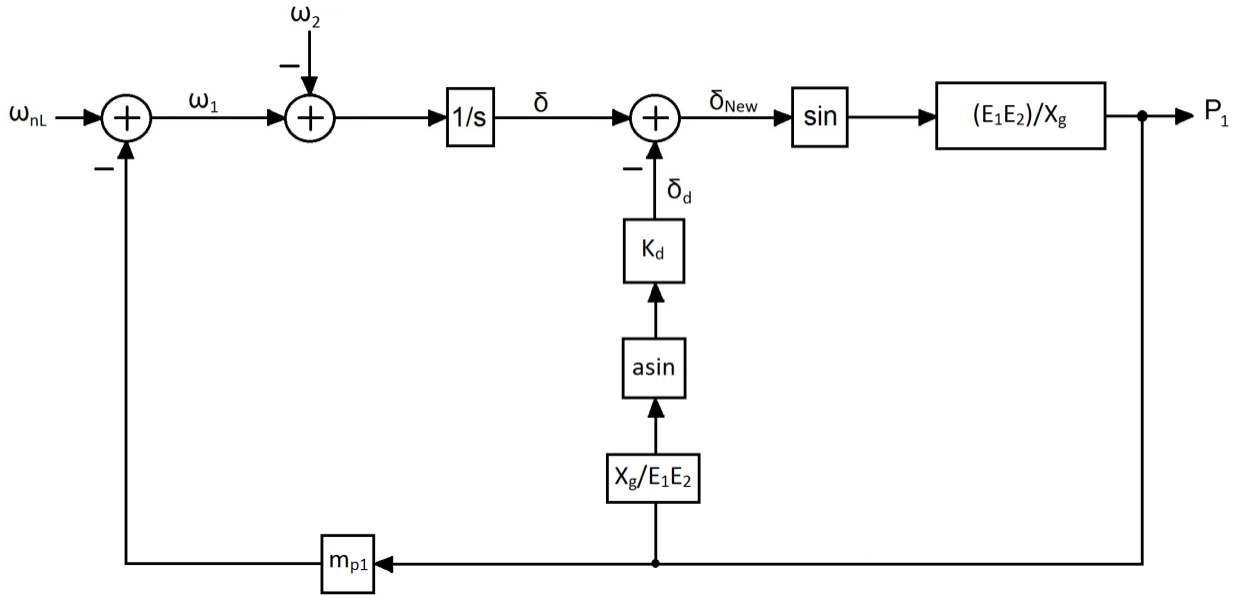


Figure 5.8: Large-signal representation of  $P_1$  including the proposed control loop

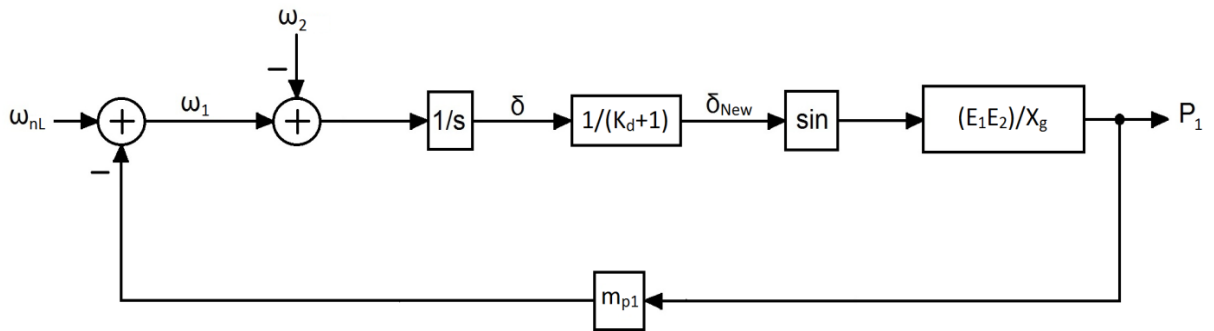


Figure 5.9: Large-signal representation of  $P_1$  including the simplified proposed control loop

$$G_1 = \frac{E_{1o} E_{2o}}{X_g} \cos\left(\frac{\delta_o}{K_d + 1}\right) \tag{5.11}$$

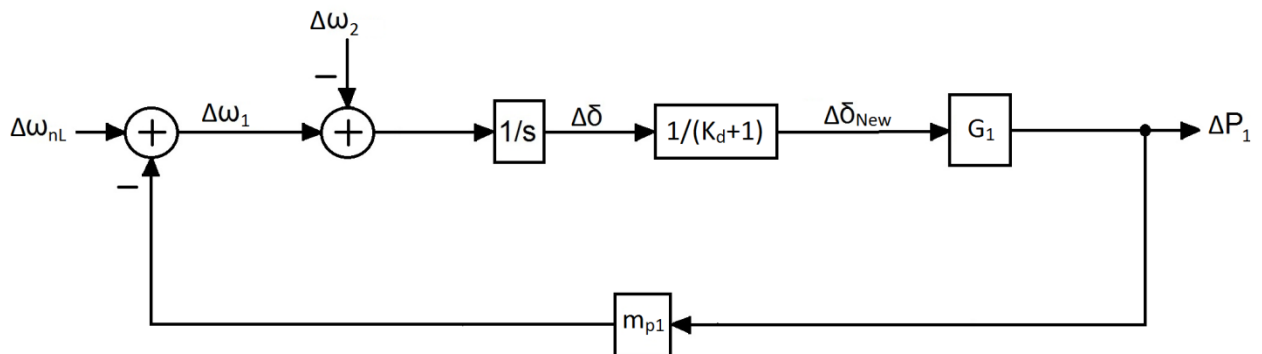


Figure 5.10: Small-signal representation of  $P_1$  including the simplified proposed control loop

$$\Delta P_1(s) = \frac{(K_d + 1)G_1}{s + m_{p1}(K_d + 1)G_1} \Delta \omega_{nL}(s) - \frac{(K_d + 1)G_1}{s + m_{p1}(K_d + 1)G_1} \Delta \omega_2(s) \quad (5.12)$$

$$\rho = -m_{p1}(K_d + 1)G_1 \quad (5.13)$$

Table 5.2: System parameters in Fig. 5.5

Parameter	Value	Unit
$V_r$	230	$V_{rms}$
$f_r$	50	Hz
$m_p$	0.9425m	rad/s/W
$n_q$	0	V/VAr
$\Delta f$	1.5	Hz
$f_{nL}$	51.5	Hz
$X_g$	3	$\Omega$

As one can see in Fig. 5.11, the increasing of  $K_d$  of the proposed control loop makes the system speed response slower, yet the steady-state response is not affected. Using Matlab, the system information given by table 5.3 confirms the previous statement. Therefore, the settling time and the rise time increase with  $K_d$ . Note that the settling time and the rising time given in Table 5.3 have been calculated within  $\pm 2\%$  error band and 10-90% of the steady-state value respectively.

In the next section, the proposed control loop is implemented in the three-phase voltage source inverter. Then, simulations are done to see the benefits of the new control loop on the overall system behavior when operating in parallel with the Genset.

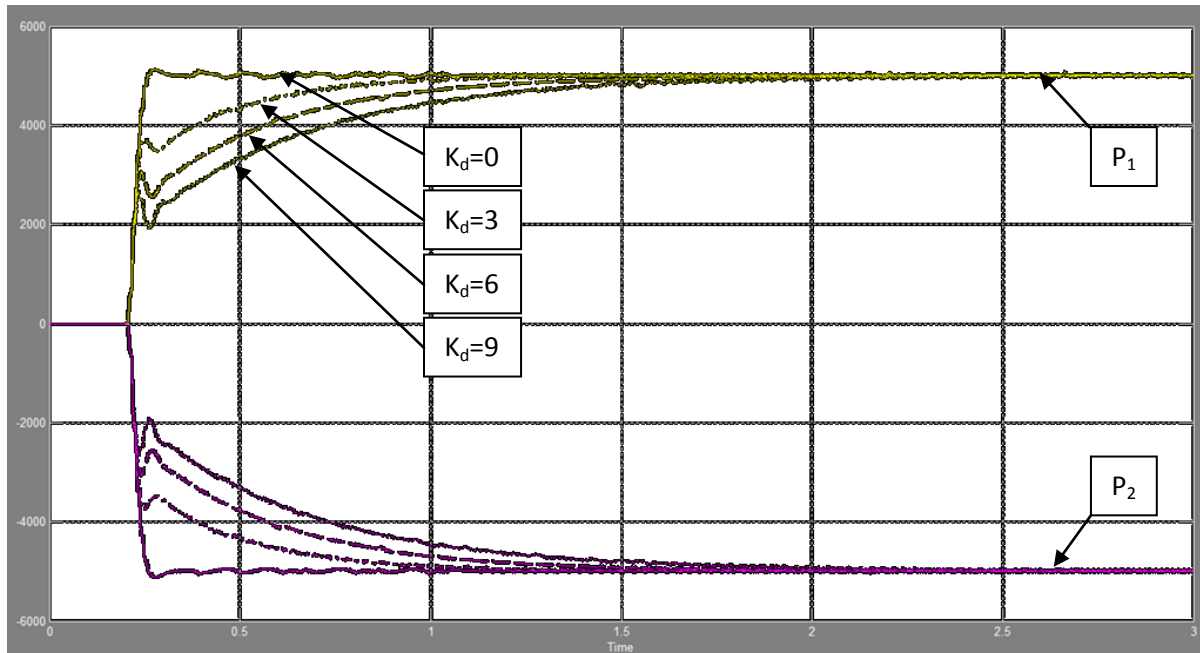


Figure 5.11: Line active power when  $K_d$  is increased (W) vs. Time (s)

Table 5.3: Step-info of the system when  $K_d$  is increased

$K_d$	Rise Time (s)	Settling Time (s)
0	0.0520	0.0919
3	0.3587	0.773
6	0.6051	1.1746
9	0.8283	1.5456

## 5.4 The proposed settling time control loop implementation in the three-phase inverter

As in the previous Chapter, the proposed settling time control loop implementation in the three-phase voltage source inverter using dq control technique is similar to the one used for the proposed virtual impedance loop. In order to vary the inverter's output voltage phase angle, the voltage reference of dq channels needs to be computed using the phase angle ( $\delta_d$ ). Note that, the inverter's operating frequency is still provided by the P vs. f droop controller. Fig. 5.12 shows the whole system simulation file in Matlab/Simulink.

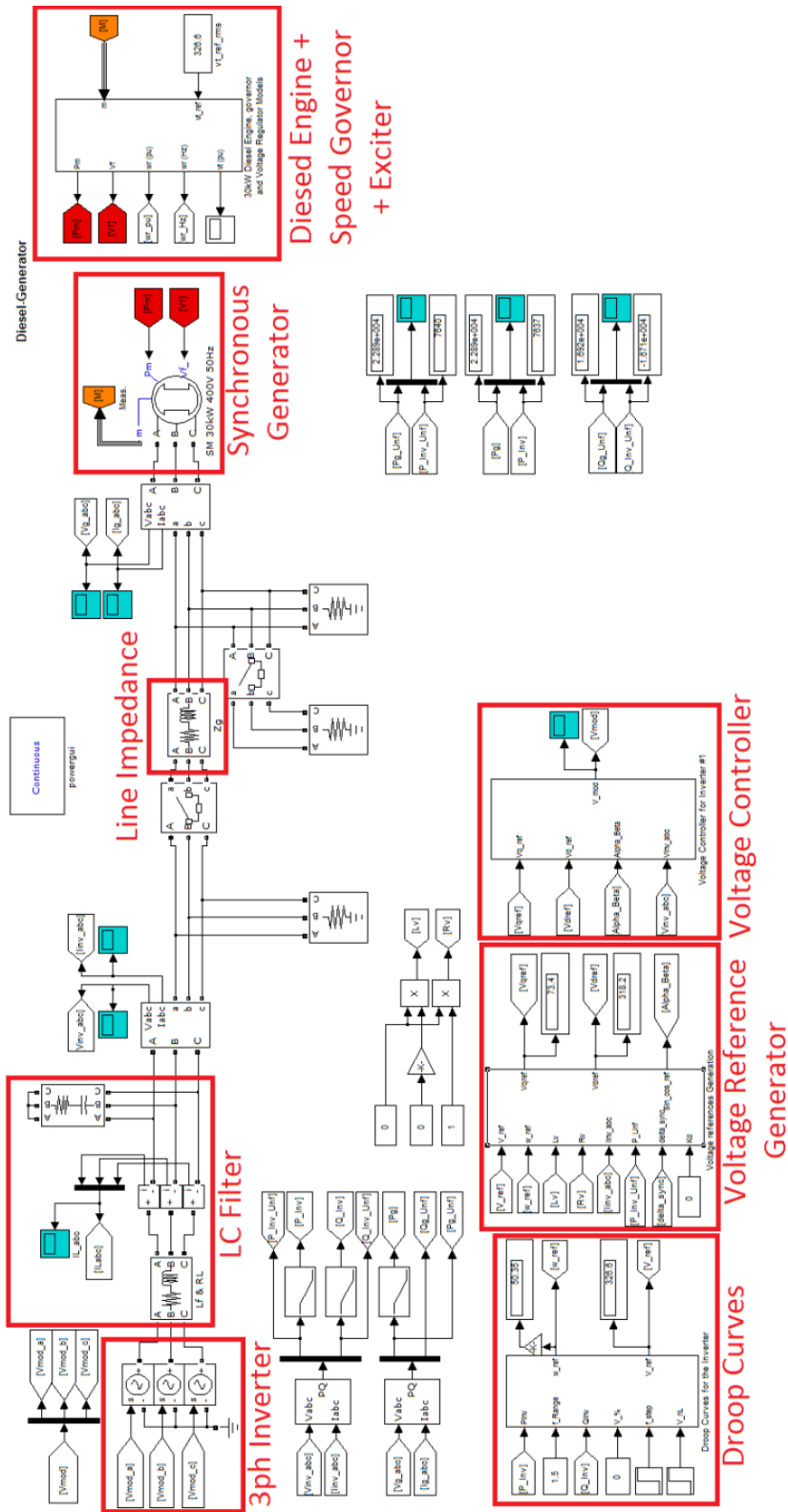


Figure 5.12: Matlab/Simulink simulation file of the inverter, Genset, local loads and the feeder

The “voltage reference generator” block contains what Fig. 5.13 illustrates. The LPF is used to slow down the variation of  $\delta_d$  because the new control loop is in parallel to the conventional droop control loop, hence the latter should be quicker than the newly added control loop. The bandwidth of that LPF ( $f_{cd}$ ) is set to 1Hz.

The purpose for which the proposed virtual impedance loop is included is discussed in the next section.

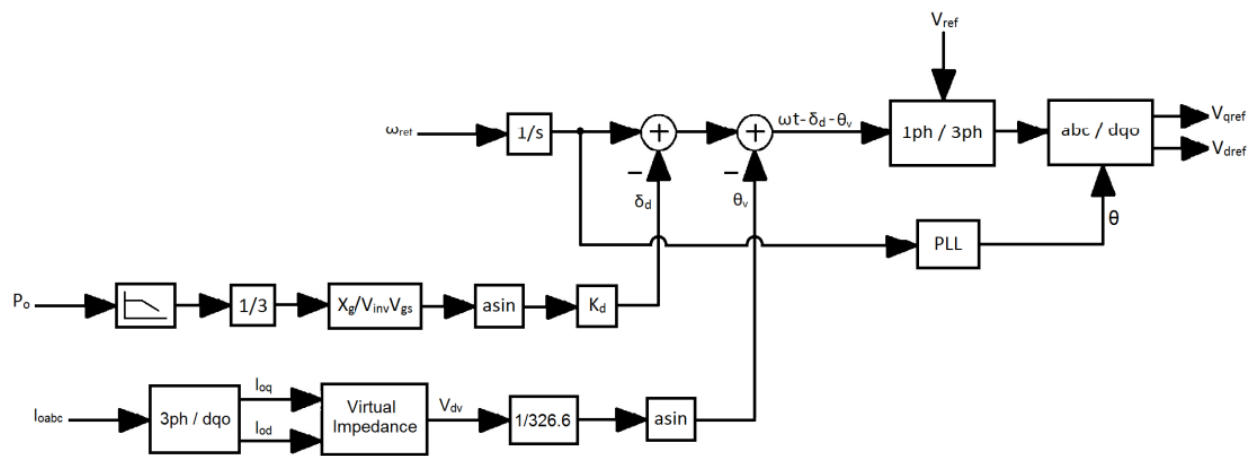


Figure 5.13: Voltage reference generator including the proposed control loop and the proposed VI loop

The diesel engine model, the speed governor, and the terminal voltage exciter are grouped in one block as shown in Fig. 5.12. Their details are illustrated in Fig. 5.14 ad 5.15. The speed governor and the terminal voltage controllers are of the PID and PI types, respectively [23]. Since the PID based speed governor model does not allow frequency droop, the angular frequency reference is calculated using droop equation which is a function of the filtered electrical output power.

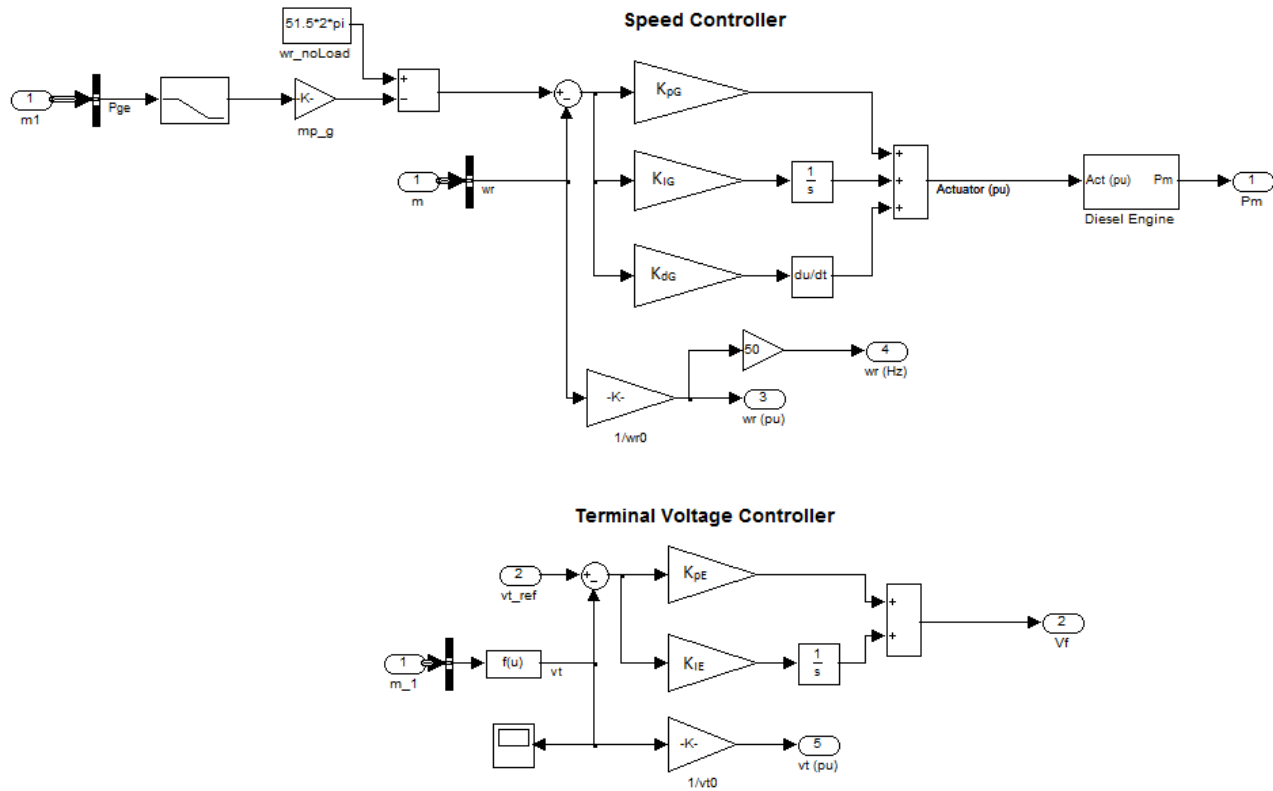


Figure 5.14: The Diesel Engine and the Terminal Voltage Exciter models of the Genset [23]

The “Diesel Engine” block in Fig. 5.14 is shown in detail in Fig. 5.15.

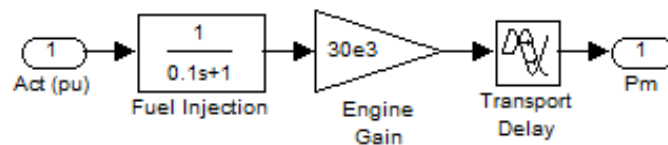


Figure 5.15: Diesel Engine Model

## 5.5 Performance verification of the system including the proposed control loop

Time domain simulations have been done of the system shown in Fig. 5.12 for different values of  $K_d$ . The system parameters are listed in Table 5.4.



Table 5.4: System parameters

Parameter	Value	Unit
$V_r$	230/400	$V_{rms}$
$f_{fL}$	50	Hz
$m_{p_{inv}}$	0.9245m	rad/s/W
$n_{q_{inv}}$	0	V/VAr
$\Delta f$	1.5	Hz
$f_{nL\_inv}$ & $f_{nL\_gs}$	51.5	Hz
$X_g$	0.1	$\Omega$
$R_g$	0.23	$\Omega$
$f_c$	30	Hz
$f_{cd}$	1	Hz

Where,  $f_{fL}$  is the full-load frequency,  $m_{p_{inv}}$  and  $n_{q_{inv}}$  are the inverter's frequency and voltage droop gains,  $f_{nL\_inv}$  and  $f_{nL\_gs}$  are the no-load frequency of the inverter and the genset, and  $f_{cd}$  is the cut-off frequency of the LPF used in the new control loop. Note that, the same line impedance used in the previous chapters is used in this study.

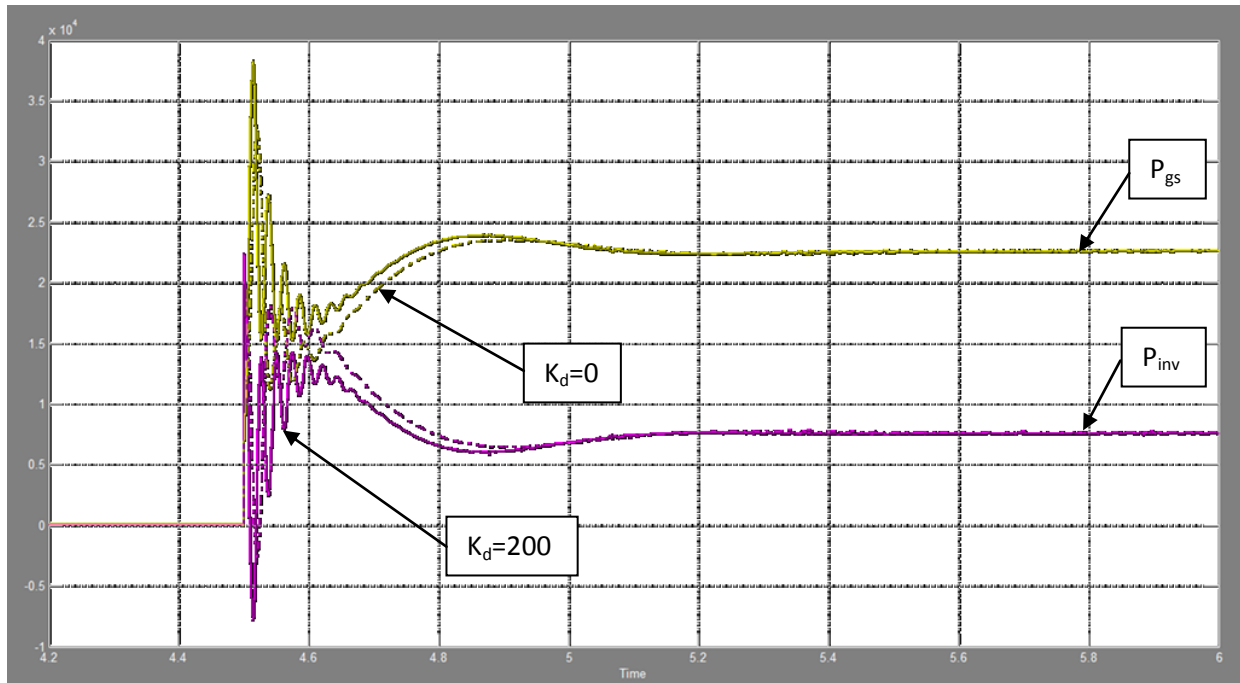
### 5.5.1 Load variation test

Before connecting the Genset to the inverter, the latter needs to be synchronized with the Genset in order to avoid large transient currents. In these simulations, the synchronization has been done in a very basic manner. The inverter's output voltage phase angle has been varied manually until it equals the one of the Genset, then a switch is closed to connect the two sources. Table 5.5 describes the simulations steps.

The synchronization is done at  $t=4s$  due to the low speed response of the Genset. Then, a large load step of +29.85kW occurs at the Genset's side at  $t=4.5s$ . The increasing of  $K_d$  decreases the overshoot but it seems that it makes the system dominated by two poles which generate oscillations with higher frequency as shown in Fig. 5.16. Therefore, the proposed virtual impedance loop, discussed in Section 4.7, has been used to suppress those oscillations.

Table 5.5: Simulations steps for load variation test

Time (s)	Sources connected	$P_{inv}$ (kW)	$P_{gs}$ (kW)
0	No	0.05	0.15
4	Yes	0.05	0.15
4.5	Yes	0.05	30

Figure 5.16: Inverter and Genset's output active power for different  $K_d$  without the proposed VI (W) vs. Time (s)

As one can see in Fig. 5.17, the proposed VI loop improves the system dynamic by eliminating the high frequency oscillations caused by the new control loop. Fig. 5.18 shows the simulation results when using different values of  $K_d$  while the resistive virtual impedance ( $R_v$ ) is fixed at  $2\Omega$ . The system transient response is well improved by the two proposed control loops.

One can conclude that by decreasing the inverter's speed response and making it as close as possible to the speed response of the Genset, the whole system dynamics is improved reducing the large overshoot and the oscillations. The overshoot percentage is equal to 83% when  $K_d=100$ , 62% when  $K_d=200$  and 36% when  $K_d=400$ .

Note that the system become unstable when  $K_d$  is larger than 500.

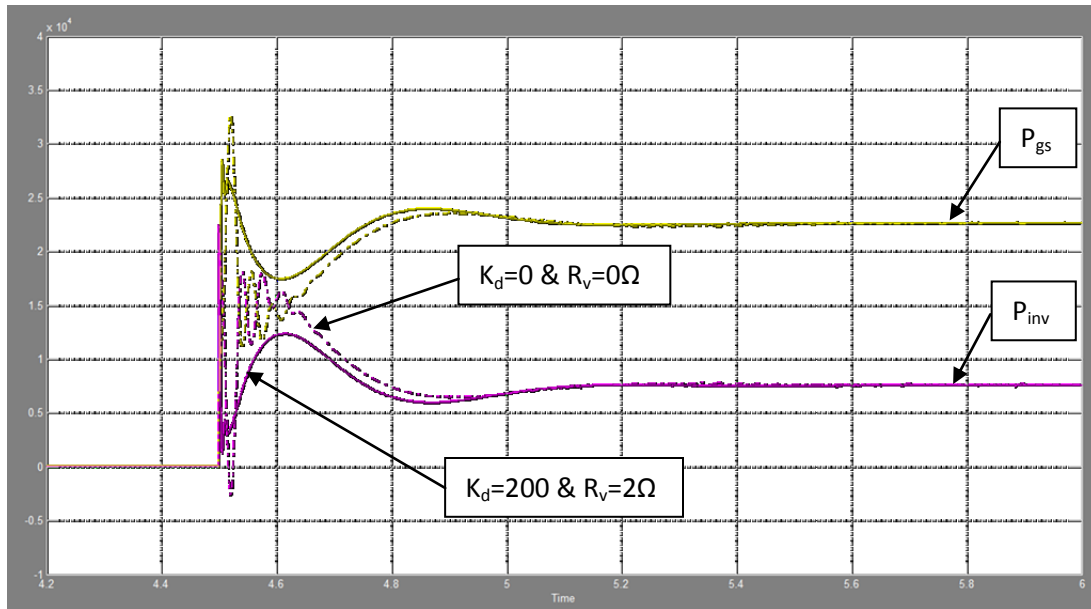


Figure 5.17: Inverter and Genset's output active power for different  $K_d$  (W) vs. Time (s)

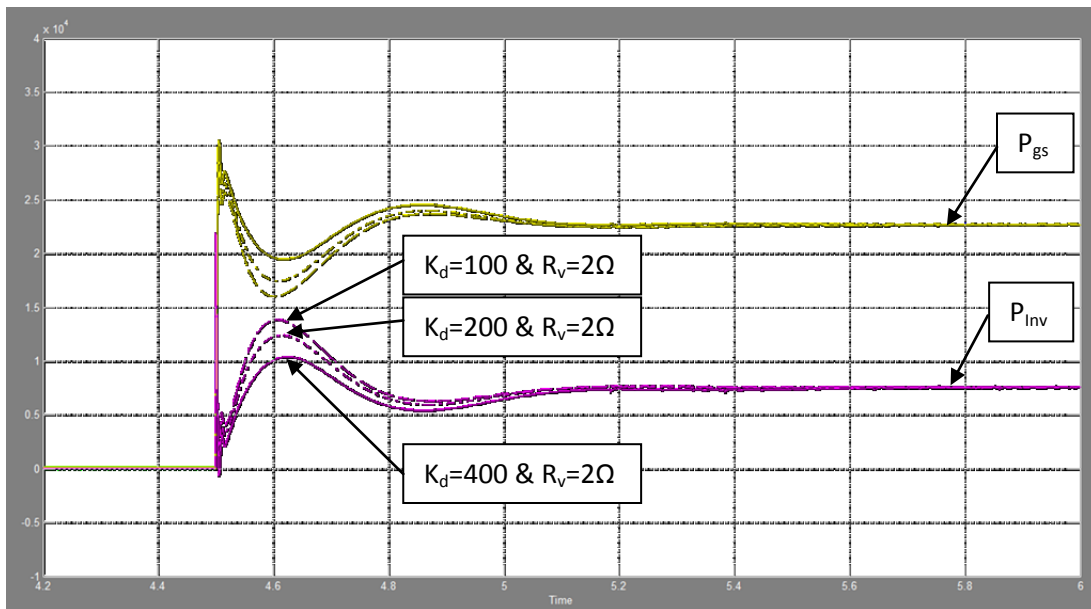


Figure 5.18: Inverter and Genset's output active power when  $K_d$  is increased and  $R_v=2\Omega$ , (W) vs. Time (s)

### 5.5.2 Power signal variation test

In this section, the effect of the no-load frequency variation on the system performance is verified when the new control loop is implemented. Setting the system parameters as listed in Table 5.4, Fig.

5.19 shows the inverter and the Genset output active power for different values of  $K_d$ . Note that the proposed virtual impedance is still activated. The simulation steps are given in Table 5.6.

Table 5.6: Simulations steps for power signal variation test

Time (s)	Sources connected	The inverter no-load frequency ( $f_{nL\_inv}$ ) (Hz)	$P_{inv}$ (kW)	$P_{gs}$ (kW)
0	No	51.5	0.05	0.15
4	Yes	51.5	0.05	0.15
4.5	Yes	51.5	0.05	20
6	Yes	49.5	0.05	20

The simulation results shown in Fig. 5.19 prove that the system behaves properly under various perturbations. However, the system becomes unstable after the variation of  $f_{nL\_inv}$  when  $K_d$  is equal to 400. This can be resolved by decreasing the cut-off frequency ( $f_{cd}$ ) of the LPF to 0.05Hz. Therefore, it is well recommended to derive the small-signal model of the system in order to study the latter in frequency domain and to see the influence of all the slow elements on the system dynamics.

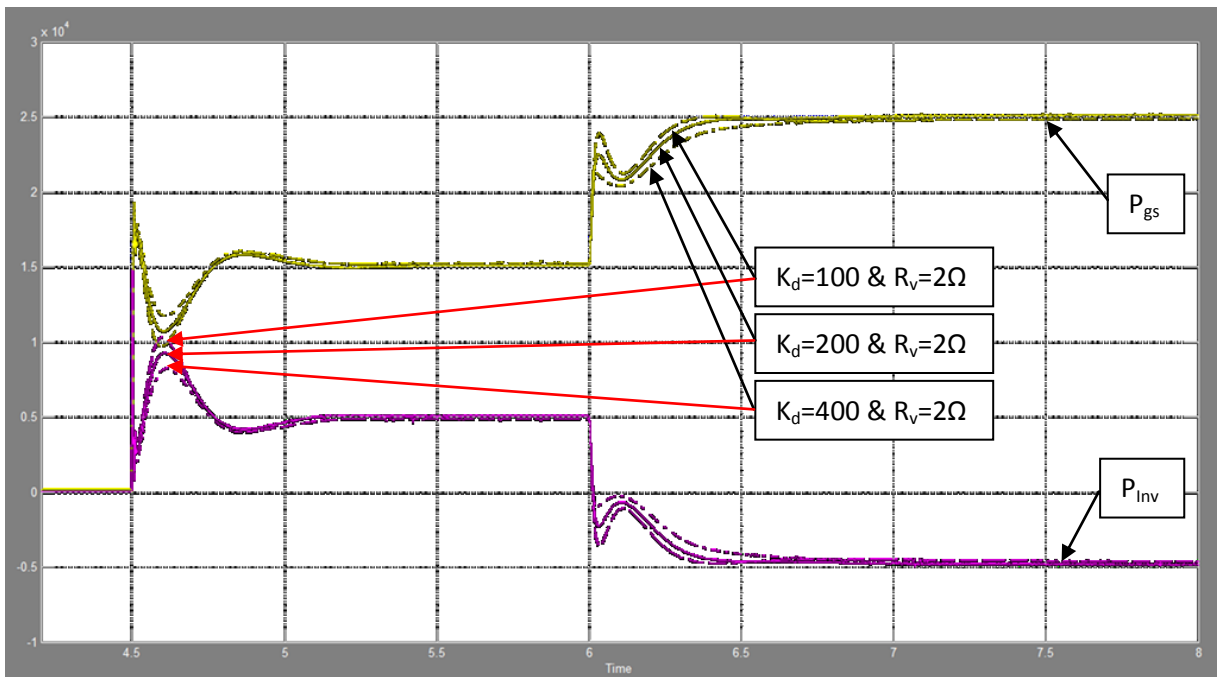


Figure 5.19: and Genset's output active power when  $K_d$  is increased and  $R_v=2\Omega$  (W) vs. Time (s)

## 5.6 Conclusion

In this chapter, the parallel operation of a three-phase voltage source inverter with a Genset has been studied. It has been shown that since both AC voltage sources have different frequency speed response, the system dynamics after load variations could contain large oscillations and large overshoots. In this case since the inverter is much quicker than the Genset, it takes most of the sudden load variations even if these occur in the Genset's side of the tie-line. This could generate an overload and possible result in the shut down of the inverter.

A proposed solution has been presented which consists on slowing down the inverter's speed response by controlling its output voltage phase angle. Unlike in [22], the implementation of the proposed control loop allows the elimination of the communication links.

The system performance including the new control loop has been verified by mean of time domain simulations on Matlab/Simulink. It has been shown that the system's transient response is improved. The overshoot decreases when the new added phase angle is increased. The proposed virtual impedance loop has been activated in the system allowing the elimination of the high frequency oscillations generated due the increasing of  $K_d$ .

Finally, the system dynamics improvement of such applications using the parallel loop which is based on phase shifts is very promising. However, the system used in this chapter needs additional studies based on frequency domain in order to extract the most influencing parameters on its dynamics. This should allow a more robust control design.

# Chapter 6 - Conclusions and future work

## 6.1 Conclusions

In this thesis, detailed studies have been done on the dynamic response of a three-phase voltage source inverter (VSI) when operating in parallel with various ac voltage sources (Stiff grid, Inverter and Genset). The main contributions and conclusions of this thesis are as follows:

- A three-phase VSI with an output LC filter, for attenuating the switching harmonics, and a closed loop voltage control scheme, for regulating the output voltage magnitude and frequency, has been designed. A simple PI type-3 controller using the dq (vector) control approach has been used. It has been shown by means of time domain simulations in Simulink that the inverter performs very well under various conditions including: Heavy balanced and linear load variations and voltage and frequency references variations.
- Small-signal models of two systems, based on their average dq model, have been developed. The first system consists of a droop controlled three-phase VSI, with a local load, connected in parallel to a stiff grid through a tie-line. The second system consists of two parallel droop controlled VSIs, with their local loads, connected through a tie-line. It has been shown for both systems that the fast elements (Voltage controller and LC filter) can be neglected in the modeling and analysis since they have negligible influence on the system's dominant poles. Therefore, reduced small-signal models have been derived confirming the previous statement. After varying the most influencing elements of the systems' behavior, which are the droop controllers' gains, the line impedance and the LPF of the active and reactive power calculator, it has been shown that both systems tend toward stability when decreasing  $m_p$  and  $n_q$ , (droop

factors) and when increasing  $X_g$  and  $R_g$  (components of the tie line) and  $f_c$  (of the power calculator). This has been verified by means of time domain simulations in Simulink. Regarding the systems' steady-state response, the main element which affects the accuracy of the power sharing between inverters is the ratio  $X_g/R_g$ . The larger the latter is, the smaller the steady-state error will be.

- The conventional virtual impedance (VI) control loop has been designed and implemented in the system, which is composed of two droop controlled VSI, since the line impedance characteristics of the system generates high oscillatory dynamic responses for both inverters. It has been shown in the thesis that the conventional VI provides a good solution to the dynamic issue. However, its design is difficult because it depends on the inverter's ratings and the line impedance. Moreover, it affects the inverters' output voltage amplitudes because of the way it is implemented. Therefore, a new VI control loop has been proposed, which is based on the variation of the inverters' output voltage phase angle. It has been shown, by means of frequency domain analysis (root locus) and time domain simulations that the new VI loop is more performing than the conventional one, it allows better voltage regulation, and it ensures good transients for a large range of line impedance values.
- Regarding the system where the droop controlled VSI shares local loads with a Genset through a tie-line, no frequency domain analysis (root locus) has been conducted. It has been investigated only by means of simulations in Simulink. In this system, the studies focused on the dynamic response issue since both ac voltage sources behave differently in terms of speed response. Because the inverter is much quicker than the Genset, large overshoot can be generated in the inverter's output active power even if the load variations occur at the Genset side of the tie-line. In order to avoid overloading the inverter, a new control loop has been conceived. This latter allows varying the inverter's settling time by a factor of " $K_d$ " to make its speed response as close

as possible to the one of the Genset. This technique consists of adding a negative angle to the inverter's output voltage phase angle in order to curb the angle  $\delta$  generated physically between the two sources. Moreover, this settling time variation technique uses only local measurement, unlike previous attempts, making its implementation simple. It has been shown, using a simplified small-signal model of two ideal ac voltage sources, that this new control loop creates an additional degree of freedom to the system dynamics improvement. The system performance verification has been done by means of time domain simulations in Simulink, which showed that the overshoot appearing in the inverter output active power decreases by increasing  $K_d$ . Although this generated at first high frequency oscillations in inverter's dynamics, the use of the new (proposed) VI loop allowed the mitigation of the oscillations, resulting in an overall well damped and smooth response for the entire system.

## 6.2 Future work

The following topics are suggested for a future work.

- The three-phase three-leg VSI should be capable to regulate its output voltage under unbalanced and no-linear loads conditions when the Genset is off. For this, a new voltage control loop should be designed.
- The small-signal model of the system in chapter 5 needs to be developed for a better understanding of the parameters influencing its dynamic behavior under variable perturbations. This will lead to a better analysis of the new control loop benefits and limits on the system.
- Modeling and analysing bigger systems which regroup the three ac voltage sources (the two inverters and the Genset) for additional studies.



## Appendix A

```
%-----%
% The small-signal state-space modulation of a system composed
% by one droop-controlled three-phase voltage source inverter with LC
% filter, a local load and one feeder operating in parallel with a stiff Grid
% The initial values have been calculated for a local load of the inverter
% 5kW, then a no-load frequency step of  $\Delta f/4$  occurred in the power droop
% controller of the inverter generating a line power of 2.5kW
%-----%

% Voltage Controller coefficients (PI type-3):
    t=1.8294e-4;
    Tp=3.8460e-6;
    Kpi=1.1508;
% LC Filter components:
    Rf=0.5;
    Lf=0.32e-3;
    Cf=20e-6;
% 1st Order Low-Pass Filter cut-off frequency:
    wc=2*pi*30;
% Inverters characteristics:
    Pinv_max=10e3;           %rating active power
    Qinv_max=5e3;           %rating reactive power
    Pload=5e3;              %initial local load power demand
    Pg=2.5e3;               %initial active power drawn
through the feeder
% Active Power Droop Controller:
    w_Range=2*pi*4;         % frequency range
    w_r=2*pi*60;           % rating frequency
    w_step=w_Range/4;      % no-load frequency step
    w_nl=w_r+(w_Range/2)+w_step; % no-load frequency
    w_fl=w_r-(w_Range/2)+w_step; % full-load frequency
    mp=(w_nl-w_fl)/Pinv_max; % P vs. f droop gain
% Reactive Power Droop Controller:
    V_pCent=0;              %deltaV in percent
    V_r=169.7;              %rating voltage amplitude
    V_range=V_r*V_pCent/100; %deltaV in V
    nq=V_range/Qinv_max;    %Q vs. V droop gain
% Operating frequency:
    wo=w_nl-mp*(Pload+Pg);
% Line Impedance components:
    Rg=0.23;
    Lg=0.1/wo;
% Initial value of the angle delta for Pg=2.5kW:
    deltao=0.03547;
% Local Inductive Load for the Inverter (Pload=5kW, Qload=0Var):
    Rload=8.64;
    Lload=1e-10;
% Initial Values of output current and voltage of the Inverter
(Po=Pload+Pg=7.5kW):
    Voqo=169.596;
```

```

Vodo=5.939;
Vqrefo=169.7;
Vdrefo=0;
ILoadqo=19.6291;
ILoaddo=0.6874;
% Initial values of line current (Pg=2.5kW):
Iqgo=-9.0655;
Igdo=-21.886;
% Amg matrix components:
A1=1.5*wc*(ILoadqo-Iggo);
A2=1.5*wc*(ILoaddo-Igdo);
A3=1.5*wc*Voqo;
A4=1.5*wc*Vodo;
A5=-A3;
A6=-A4;
A7=-A2;
A8=A1;
A9=A4;
A10=-A3;
A11=-A9;
A12=-A10;
A13=-Vqrefo*sin(deltao)-Vdrefo*cos(deltao);
A14=-nq*cos(deltao);
A15=Vqrefo*cos(deltao)-Vdrefo*sin(deltao);
A16=-nq*sin(deltao);
A17=(Kpi*t)/(Tp^2)/Lf;
A18=(2*Kpi)/(Tp^2)/Lf;
A19=Kpi/(t*Tp^2)/Lf;

% The Matrix Amg:
Amg=[ 0  -mp  0  0  0  0  0  0  0  0  0
      0  0  0  0  0  0  0  0  0  0  0
; ...
      0  -wc  0  0  0  0  0  0  0  0  0
      A1  A2  A3  A4  A5  A6
; ...
      0  0  -wc  0  0  0  0  0  0  0  0
      A7  A8  A9  A10  A11  A12
; ...
      A13  0  A14  -2/Tp  -1/Tp^2  0  0  0  0  0  0
      -1  0  0  0  0  0  0  0  0  0  0
; ...
      0  0  0  1  0  0  0  0  0  0  0
      0  0  0  0  0  0  0  0  0  0  0
; ...
      0  0  0  0  1  0  0  0  0  0  0
      0  0  0  0  0  1  0  0  0  0  0
; ...
      A15  0  A16  0  0  0  0  -2/Tp  -1/Tp^2  0  0
      0  -1  0  0  0  0  0  0  0  0  0
; ...
      0  0  0  0  0  0  0  1  0  0  0
      0  0  0  0  0  0  0  0  1  0  0
; ...
      0  0  0  0  0  0  0  0  1  0  0
      0  0  0  0  0  0  0  0  0  1  0
; ...

```

```

      0  0  0      A17      A18      A19  0      0      0      -Rf/Lf
wo    -1/Lf  0      0      0      0      0      0      0      0
; ...
-Rf/Lf  0  0  0      0      0      0      A17      A18      A19  -wo
      0      -1/Lf      0      0      0      0      0      0
; ...
      0  0  0      0      0      0      0      0      0      1/Cf
0      0      wo      -1/Cf      0      0      0      1/Cf      0
; ...
1/Cf  -wo      0      0      0      0      -1/Cf      0      0      1/Cf
; ...
      0  0  0      0      0      0      0      0      0      0
0      1/Lload  0      -Rload/Lload  wo      0      0
; ...
      0  0  0      0      0      0      0      0      0      0
0      0      1/Lload  -wo      -Rload/Lload  0      0
; ...
      0  0  0      0      0      0      0      0      0      0
0      -1/Lg   0      0      0      0      0      -Rg/Lg   wo
; ...
      0  0  0      0      0      0      0      0      0      0
0      0      -1/Lg   0      0      0      0      0      -wo   -
Rg/Lg ];

```

```
% Eigen vectors calculation:
```

```

    d=eig(Amg);
    plot(d,'x','MarkerSize',12); grid; xLim([-2e3, 0.1e3]); yLim([-0.5e3,
0.5e3]); %xLim([-15e4, 5e3]); yLim([-30e3, 30e3]); %xLim([-0.5e3, 0.3e3]);
yLim([-0.4e3, 0.4e3]);

```

## Appendix B

```
%-----%
% The small-signal state-space modulation of the reduced system composed
% by one droop-controlled three-phase voltage source inverter (without the
% voltage controller, LC filter and local load) operating in parallel with
% a stiff Grid through a feeder.
% The initial values have been calculated for a local load of the inverter
% 5kW, then a no-load frequency step of  $\Delta f/4$  occurred in the power droop
% controller of the inverter generating a line power of 2.5kW
%-----%

% 1st Order Low-Pass Filter cut-off frequency:
    wc=2*pi*30;
% Inverters characteristics:
    Pinv_max=10e3;
    Qinvs_max=5e3;
% Active Power Droop Controller:
    w_Range=2*pi*4;           % frequency range
    mp=w_Range/Pinv_max;     % inverter's active power droop
slope
% Reactive Power Droop Controller:
    V_pCent=0;
    V_r=169.7;
    V_range=V_r*V_pCent/100;
    nq=V_range/Qinvs_max;
% Operating frequency:
    wo=2*pi*60;
% Line Impedance components:
    Rg=0.23;
    Lg=0.1/wo;
% Initial value of the angle delta for Pg=2.5kW:
    deltao=0.03547;
% Initial Values of output current and voltage of the Inverter where
Po=Pload+Pg:
    Voqo=169.596;
    Vodo=5.939;
    Vqrefo=169.7;
    Vdrefo=0;
% Initial values of line current (Pg=2.5kW):
    Igqo=-9.0655;
    Igdo=-21.886;
% Amg matrix components:
    Ar1=-mp;
    Ar2=1.5*wc*(-Igqo*(-Vqrefo*sin(deltao)-Vdrefo*cos(deltao))-
    Igdo*(Vqrefo*cos(deltao)-Vdrefo*sin(deltao)));
    Ar3=-wc;
    Ar4=-1.5*wc*nq*(-Igqo*cos(deltao)-Igdo*sin(deltao));
    Ar5=-1.5*wc*Voqo;
    Ar6=-1.5*wc*Vodo;
    Ar7=1.5*wc*(Igdo*(-Vqrefo*sin(deltao)-Vdrefo*cos(deltao))-
    Igqo*(Vqrefo*cos(deltao)-Vdrefo*sin(deltao)));
    Ar8=-wc+1.5*wc*nq*(-Igdo*cos(deltao)+Igqo*sin(deltao));
```

```

Ar9=-(-Vqrefo*sin(deltao)-Vdrefo*cos(deltao))/Lg;
Ar10=nq*cos(deltao)/Lg;
Ar11=-Rg/Lg;
Ar12=wo;
Ar13=- (Vqrefo*cos(deltao)-Vdrefo*sin(deltao))/Lg;
Ar14=nq*sin(deltao)/Lg;

% The Matrix "Armrg" of the reduced system:
Armrg=[ 0      Ar1    0      0      0      ; ...
        Ar2    Ar3    Ar4    Ar5    Ar6    ; ...
        Ar7    0      Ar8    Ar6    -Ar5   ; ...
        Ar9    0      Ar10   Ar11   Ar12   ; ...
        Ar13   0      Ar14   -Ar12  Ar11  ];

% Coefficients of the characteristic euqation of Amg
(s^5+alpha*s^4+beta*s^3+gamma*s^2+omega*s+zeta=0):
alpha=-Ar3-Ar8-2*Ar11;
beta=Ar11^2+Ar12^2-Ar1*Ar2+Ar3*Ar8+2*Ar3*Ar11-
Ar6*Ar10+Ar5*Ar14+2*Ar8*Ar11;
gamma=-Ar3*Ar11^2-Ar3*Ar12^2-Ar8*Ar11^2-Ar8*Ar12^2+Ar1*Ar2*Ar8-
Ar1*Ar4*Ar7-Ar1*Ar5*Ar9+2*Ar1*Ar2*Ar11+Ar3*Ar6*Ar10-Ar1*Ar6*Ar13-
Ar3*Ar5*Ar14-2*Ar3*Ar8*Ar11-Ar5*Ar10*Ar12+Ar6*Ar10*Ar11-Ar5*Ar11*Ar14-
Ar6*Ar12*Ar14;
lambda=-Ar1*Ar2*Ar11^2-Ar1*Ar2*Ar12^2+Ar3*Ar8*Ar11^2+Ar3*Ar8*Ar12^2-
Ar1*Ar4*Ar6*Ar9+Ar1*Ar5*Ar8*Ar9+Ar1*Ar2*Ar6*Ar10-Ar1*Ar2*Ar5*Ar14-
2*Ar1*Ar2*Ar8*Ar11+Ar1*Ar4*Ar5*Ar13+2*Ar1*Ar4*Ar7*Ar11-
Ar1*Ar5*Ar7*Ar10+Ar1*Ar5*Ar9*Ar11-
Ar1*Ar6*Ar7*Ar14+Ar1*Ar6*Ar8*Ar13+Ar1*Ar6*Ar9*Ar12+Ar3*Ar5*Ar10*Ar12-
Ar3*Ar6*Ar10*Ar11-
Ar1*Ar5*Ar12*Ar13+Ar1*Ar6*Ar11*Ar13+Ar3*Ar5*Ar11*Ar14+Ar3*Ar6*Ar12*Ar14;
zeta=Ar1*Ar2*Ar8*Ar11^2+Ar1*Ar2*Ar8*Ar12^2-Ar1*Ar4*Ar7*Ar11^2-
Ar1*Ar4*Ar7*Ar12^2-Ar1*Ar5^2*Ar9*Ar14-
Ar1*Ar6^2*Ar9*Ar14+Ar1*Ar5^2*Ar10*Ar13+Ar1*Ar6^2*Ar10*Ar13-
Ar1*Ar4*Ar5*Ar9*Ar12+Ar1*Ar4*Ar6*Ar9*Ar11-Ar1*Ar5*Ar8*Ar9*Ar11-
Ar1*Ar6*Ar8*Ar9*Ar12+Ar1*Ar2*Ar5*Ar10*Ar12-
Ar1*Ar2*Ar6*Ar10*Ar11+Ar1*Ar2*Ar5*Ar11*Ar14-
Ar1*Ar4*Ar5*Ar11*Ar13+Ar1*Ar5*Ar7*Ar10*Ar11+Ar1*Ar2*Ar6*Ar12*Ar14-
Ar1*Ar4*Ar6*Ar12*Ar13+Ar1*Ar6*Ar7*Ar10*Ar12-
Ar1*Ar5*Ar7*Ar12*Ar14+Ar1*Ar5*Ar8*Ar12*Ar13+Ar1*Ar6*Ar7*Ar11*Ar14-
Ar1*Ar6*Ar8*Ar11*Ar13;

% Roots of the characteristic equation of Amg:
dreq=roots([1 alpha beta gamma lambda zeta]);

% Eigen vectors calculation:
dr=eig(Armrg);

plot(dreq,'or','MarkerSize',12); grid; xLim([-1e3, 0.1e3]); yLim([-
0.6e3, 0.6e3]); %xLim([-0.5e3, 0.3e3]); yLim([-0.4e3, 0.4e3]); %hold;
plot(drnrlcq,'o');

```

## Appendix C

```
%-----%
% The small-signal state-space model of a small mini-grid composed
% by two droop-controlled three-phase voltage source inverters with LC
% filters, two local loads and one feeder. The initial values have been
% calculated for local loads of inverter #1 and #2 of 5kW and 2.5kW
% respectively, then a load step of +7.5kW occurred on the side of
% inverter #2. Hence, the line power is equal to 5kW.
%-----%

% Voltage Controller coefficients (PI type-3):
    t=1.8294e-4;
    Tp=3.8460e-6;
    Kpi=1.1508;
% LC Filter components:
    rL=0.5;
    Lf=0.32e-3;
    Cf=20e-6;
% 1st Order Filter cut-off frequency:
    wc=2*pi*30;
% Inverters characteristics:
    Pmax1=20e3; % Active power rating of inverter #1
    Qmax1=12e3; % Reactive power rating of inverter #1
    Pmax2=10e3; % Active power rating of inverter #2
    Pload1o=5e3; % Initial active power demand of inverter
#1 local load
    PLineo=5e3; % Initial active power passing through
the feeder
% Active Power Droop Slopes:
    w_range=2*pi*4; % Angular frequency range
    w_r=2*pi*60; % Rating angular frequency
    w_nl=w_r+(w_range/2); % no-Load angular frequency
    mp1=w_range/Pmax1; % Inverter #1 active power droop slope
    mp2=2*mp1; % Inverter #2 active power droop slope
% Reactive Power Droop Slopes:
    V_pCent=0; % deltaV in %
    nq1=(V_pCent/100)*169.7/Qmax1; % Inverter #1 reactive power droop slope
    nq2=2*nq1; % Inverter #2 reactive power droop slope
% Initial Operating frequency:
    wo=w_nl-mp1*(Pload1o+PLineo); % Initial operating angular frequency
% Line Impedance components:
    Rg=0.23;
    Lg=0.1/wo;
% Initial value of the angle delta PLineo=5kW:
    deltao=-0.074717545;
% Local Inductive Loads for the Inverters (P1o=5kW, P2o=10kW & Q1=Q2=0Var):
    Rload1=8.64;
    Lload1=1e-10; % the reactive power demand is equal to zero
    Rload2=17.28-12.96; % a load step of +7.5kW has occurred at Inv#2 side
    Lload2=Lload1;
% Initial Values of output current and voltage of Inverter #1:
```







```

0      0      0      0      0      0      0      0      0      0      0      0      0      0      0      0      0
0 0    0 0    0 0    0 1    0      0      0      0      0      0      0      0      0      0      0
0      ; ...
0      0      0      0      0      0      0      0      0      0      0      0      0      0      0      0      0
0 0    A9 A10 A11 0 0      0      A12 A29  A13 0      0      0      0      0      0      0
0      ; ...
0      0      0      0      0      0      0      0      0      0      0      0      0      0      0      0      0
0 0    0 0    0 0      A9 A10 A11 -A29 A12 0  A13 0      0      0      0      0      0      0
0      ; ...
0      0      0      0      0      0      0      0      0      0      0      0      0      0      0      0      0
0 0    0 0    0 0      0 0      0      A14 0      0      A29 -A14      0      A14
0      ; ...
0      0      0      0      0      0      0      0      0      0      0      0      0      0      0      0      0
0 0    0 0    0 0      0 0      0      0      A14 -A29 0      0      0      -A14      0      0
A14    ; ...
0      0      0      0      0      0      0      0      0      0      0      0      0      0      0      0      0
0 0    0 0    0 0      0 0      0      0      0      A25 0      A26      A29      0      0
0      ; ...
0      0      0      0      0      0      0      0      0      0      0      0      0      0      0      0      0
0 0    0 0    0 0      0 0      0      0      0      0      0      A25 -A29      A26      0      0
0      ; ...
0      0      0      0      0      0      0      0      0      0      0      0      A27 0      0      0      0
0 0    0 0    0 0      0 0      0      0      0      0      -A27 0      0      0      0      A28
A29    ; ...
0      0      0      0      0      0      0      0      0      0      0      0      0      A27 0      0      0
0 0    0 0    0 0      0 0      0      0      0      0      0      -A27 0      0      0      -A29
A28    ];

```

```
% Eigen vectors calculation:
```

```

d=eig(Ainv);
plot(d, 'x', 'MarkerSize',12); grid; xLim([-1e3, 0.1e3]); yLim([-0.6e3,
0.6e3]); %xLim([-0.5e3, 0.3e3]); yLim([-0.4e3, 0.4e3]);

```

## Appendix D

```
%-----%
% The small-signal state-space model of a small mini-grid composed
% by two droop-controlled three-phase voltage source inverters (without
% voltage controllers, LC filters and local loads) and one feeder.
% The initial values have been calculated after step of +3Hz in the
% no-load frequency signal of inverter #2. Hence, the line power is equal to
% 5kW.
%-----%

% 1st Order Filter cut-off frequency:
    wc=2*pi*30;
% Inverters characteristics:
    Pmax1=20e3;           % Active power rating of inverter #1
    Pmax2=10e3;          % Active power rating of inverter #2
    PLineo=5e3;          % Initial active power passing through
the feeder
% Active Power Droop Slopes:
    w_Range=2*pi*4;      % Angular frequency range
    w_r=2*pi*60;         % Rating angular frequency
    w_step=2*pi*3;       % no-Load angular frequency step
    w_nl=w_r+(w_Range/2)+w_step; % no-Load angular frequency
    mp1=w_Range/Pmax1;   % Inverter #1 active power droop slope
    mp2=2*mp1;           % Inverter #2 active power droop slope
% Reactive Power Droop Slopes:
    V_pCent=0;           % deltaV in %
    nq1=(V_pCent/100)*169.7/Qmax1; % Inverter #1 reactive power droop slope
    nq2=2*nq1;           % Inverter #2 reactive power droop slope
% Initial Operating frequency:
    wo=w_nl-mp1*PLineo;  % Initial operating angular frequency
% Line Impedance components:
    Rg=0.23;
    Lg=0.1/wo;
% Initial value of the angle delta Plineo=5kW:
    deltao=-0.075;
% Initial Values of output current and voltage of Inverter #1 where Po=5.5kW:
    Vq1o=169.7;
    Vd1o=0;
% Initial Values of output current and voltage of Inveter #2 where Po=5.5kW:
    Vq2o=169.2;
    Vd2o=-12.73;
    Vqref2o=169.7;
    Vdref2o=0;
% Initial values of line current (PLineo=500W):
    ILineo=22;
    ILinedo=45.8;
% Amg matrix components:
    Ar1=-wc;
    Ar2=-1.5*wc*ILineo*nq1;
    Ar3=1.5*wc*Vq1o;
    Ar4=1.5*wc*Vd1o;
```

```

Ar5=-wc-1.5*wc*ILinedo*nq1;
Ar6=mp1;
Ar7=-mp2;
Ar8=-1.5*wc*(ILineqo*(-Vqref2o*sin(deltao)-
Vdref2o*cos(deltao))+ILinedo*(Vqref2o*cos(deltao)-Vdref2o*sin(deltao)));
Ar9=1.5*wc*nq2*(ILineqo*cos(deltao)+ILinedo*sin(deltao));
Ar10=-1.5*wc*Vq2o;
Ar11=-1.5*wc*Vd2o;
Ar12=1.5*wc*(ILinedo*(-Vqref2o*sin(deltao)-Vdref2o*cos(deltao))-
ILineqo*(Vqref2o*cos(deltao)-Vdref2o*sin(deltao)));
Ar13=-wc+1.5*wc*nq2*(ILineqo*sin(deltao)-ILinedo*cos(deltao));
Ar14=-nq1/Lg;
Ar15=-(-Vqref2o*sin(deltao)-Vdref2o*cos(deltao))/Lg;
Ar16=nq2*cos(deltao)/Lg;
Ar17=-Rg/Lg;
Ar18=wo;
Ar19=- (Vqref2o*cos(deltao)-Vdref2o*sin(deltao))/Lg;
Ar20=nq2*sin(deltao)/Lg;

% The Mini-Grid Matrix "Arinv" of the reduced system:
Arinv=[ Ar1  Ar2  0  0  0  Ar3  Ar4  ;...
        0  Ar5  0  0  0  Ar4  -Ar3  ;...
        Ar6  0  0  Ar7  0  0  0  ;...
        0  0  Ar8  Ar1  Ar9  Ar10  Ar11  ;...
        0  0  Ar12  0  Ar13  Ar11  -Ar10  ;...
        0  Ar14  Ar15  0  Ar16  Ar17  Ar18  ;...
        0  0  Ar19  0  Ar20  -Ar18  Ar17  ];

% Eigen vectors calculation:
dr=eig(Arinv);
plot(dr,'ro','MarkerSize',12); grid; xLim([-2e3, 0.1e3]); yLim([-0.6e3,
0.6e3]); %xLim([-15e4, 5e3]); yLim([-3e4, 3e4]); % %xLim([-0.5e3, 0.3e3]);
yLim([-0.4e3, 0.4e3]);
%plot(d, 'x', 'MarkerSize',12); grid; xLim([-2e3, 0.1e3]); yLim([-0.5e3,
0.5e3]); hold; plot(dr, 'or', 'MarkerSize',12);

```

## Appendix E

```
-----%
% The small-signal state-space model of a small mini-grid composed
% by two droop-controlled three-phase voltage source inverters with LC
% filters, two local loads and one feeder. The initial values have been
% calculated for local loads of inverter #1 and #2 of 5kW and 2.5kW
% respectively, then a load step of +7.5kW occurred on the side of
% inverter #2. Hence, the line power is equal to 5kW. Note the conventional
% virtual impedance is implemented with Rv1=0.1ohm and Xv1=0.1ohm.
-----%

% Voltage Controller coefficients (PI type-3):
    t=1.8294e-4;
    Tp=3.8460e-6;
    Kpi=1.1508;
% LC Filter components:
    rL=0.5;
    Lf=0.32e-3;
    Cf=20e-6;
% 1st Order Filter cut-off frequency:
    wc=2*pi*30;
% Inverters characteristics:
    Pmax1=20e3; % Active power rating of inverter #1
    Qmax1=12e3; % Reactive power rating of inverter #1
    Pmax2=10e3; % Active power rating of inverter #2
    Pload1=5e3; % Initial active power demand of inverter
#1 local load
    PLineo=5e3; % Initial active power passing through
the feeder
% Active Power Droop Slopes:
    w_Range=2*pi*4; % Angular frequency range
    w_r=2*pi*60; % Rating angular frequency
    w_nl=w_r+(w_Range/2); % no-Load angular frequency
    mp1=w_Range/Pmax1; % Inverter #1 active power droop slope
    mp2=2*mp1; % Inverter #2 active power droop slope
% Reactive Power Droop Slopes:
    V_pCent=0; % deltaV in %
    nq1=(V_pCent/100)*169.7/Qmax1; % Inverter #1 reactive power droop slope
    nq2=2*nq1; % Inverter #2 reactive power droop slope
% Initial Operating frequency:
    wo=w_nl-mp1*(Pload1+PLineo); % Initial operating angular frequency
% Line Impedance components:
    Rg=0.23;
    Lg=0.1/wo;
% Virtual Impedance Components of inverter #1:
    Kv=0.1;
    Rv1=Kv*1;
    Lv1=Kv*1/wo;
% Virtual Impedance Components of inverter #2:
    Rv2=Rv1*2;
    Lv2=Lv1*2;
```

```

% Initial value of the angle delta Plineo=5kW:
    deltao=-0.074717545;
% Local Inductive Loads for the Inverters (P1o=5kW, P2o=10kW & Q1=Q2=0Var):
    Rload1=8.64;
    Lload1=1e-10;           % the reactive power demand is equal to zero
    Rload2=17.28-12.96;    % a load step of +7.5kW has occurred at Inv#2 side
    Lload2=Lload1;
% Initial Values of output current and voltage of Inverter #1:
    Vq1o=169.7;
    Vd1o=0;
    ILoadq1o=19.6409;
    ILoadd1o=0;
% Initial Values of output current and voltage of Inveter #2:
    Vq2o=169.2;
    Vd2o=-12.73;
    Vqref2o=169.7;
    Vdref2o=0;
    ILoadq2o=39.1727;
    ILoadd2o=-2.93;
% Initial values of line current (PLineo=5kW):
    ILineqo=22;
    ILinedo=45.8;
% Acvinv matrix components:
    A1=-wc;
    A2=1.5*wc*(ILoadq1o+ILineqo);
    A3=1.5*wc*(ILoadd1o+ILinedo);
    A4=1.5*wc*Vq1o;
    A5=1.5*wc*Vd1o;
    A6=-nq1;
    A7=-2/Tp;
    A8=-1/(Tp^2);
    A9=(Kpi*t)/(Tp^2)/Lf;
    A10=(2*Kpi)/(Tp^2)/Lf;
    A11=Kpi/(t*Tp^2)/Lf;
    A12=-rL/Lf;
    A13=-1/Lf;
    A14=1/Cf;
    A15=1/Lload1;
    A16=-Rload1/Lload1;
    A17=1.5*wc*(ILoadq1o-ILineqo);
    A18=1.5*wc*(ILoadd1o-ILinedo);
    A19=1.5*wc*Vq2o;
    A20=1.5*wc*Vd2o;
    A21=-Vqref2o*sin(deltao)-Vdref2o*cos(deltao);
    A22=-nq2*cos(deltao);
    A23=Vqref2o*cos(deltao)-Vdref2o*sin(deltao);
    A24=-nq2*sin(deltao);
    A25=1/Lload2;
    A26=-Rload2/Lload2;
    A27=1/Lg;
    A28=-Rg/Lg;
    A29=wo;
    A30=-mp1;
    A31=-mp2;

% The Mini-Grid Matrix "Acvinv" of the complete system including the
conventional virtual impedance loop:

```

```

Acvinv=[ A1  0  0  0  0  0  0  0  0  0  0  0  A2  A3  A4  A5
0  0  0  0  0  0  0  0  0  0  0  0  0  0  0  A4
A5      ; ...
          0  A1  0  0  0  0  0  0  0  0  0  0  -A3  A2  A5  -A4
0  0  0  0  0  0  0  0  0  0  0  0  0  0  0  A5
-A4     ; ...
          0  A6  A7  A8  0  0  0  0  0  0  0  0  -1  0  -Rv1  wo*Lv1
wo*Lv1 ; ...
          0  0  1  0  0  0  0  0  0  0  0  0  0  0  0  0
0  0  0  0  0  0  0  0  0  0  0  0  0  0  0  0
0      ; ...
          0  0  0  1  0  0  0  0  0  0  0  0  0  0  0  0
0  0  0  0  0  0  0  0  0  0  0  0  0  0  0  0
0      ; ...
          0  0  0  0  0  0  A7  A8  0  0  0  0  0  -1  -wo*Lv1  -Rv1
-Rv1   ; ...
          0  0  0  0  0  0  1  0  0  0  0  0  0  0  0  0
0  0  0  0  0  0  0  0  0  0  0  0  0  0  0  0
0      ; ...
          0  0  0  0  0  0  0  1  0  0  0  0  0  0  0  0
0  0  0  0  0  0  0  0  0  0  0  0  0  0  0  0
0      ; ...
          0  0  A9  A10  A11  0  0  0  0  A12  A29  A13  0  0  0  0
0  0  0  0  0  0  0  0  0  0  0  0  0  0  0  0
0      ; ...
          0  0  0  0  0  0  A9  A10  A11  -A29  A12  0  A13  0  0  0
0  0  0  0  0  0  0  0  0  0  0  0  0  0  0  0
0      ; ...
          0  0  0  0  0  0  0  0  0  0  A14  0  0  A29  -A14  0
0  0  0  0  0  0  0  0  0  0  0  0  0  0  0  -A14
0      ; ...
          0  0  0  0  0  0  0  0  0  0  0  A14  -A29  0  0  -A14
-A14   ; ...
          0  0  0  0  0  0  0  0  0  0  0  0  A15  0  A16  A29
0  0  0  0  0  0  0  0  0  0  0  0  0  0  0  0
0      ; ...
          0  0  0  0  0  0  0  0  0  0  0  0  0  A15  -A29  A16
0  0  0  0  0  0  0  0  0  0  0  0  0  0  0  0
0      ; ...
          -A30  0  0  0  0  0  0  0  0  0  0  0  0  0  0  0
0  A31  0  0  0  0  0  0  0  0  0  0  0  0  0  0  0
0      ; ...
          0  0  0  0  0  0  0  0  0  0  0  0  0  0  0  0
0  A1  0  0  0  0  0  0  0  0  0  A17  A18  A19  A20  -A19
-A20   ; ...
          0  0  0  0  0  0  0  0  0  0  0  0  0  0  0  0
0  0  A1  0  0  0  0  0  0  0  0  0  -A18  A17  A20  -A19  -A20
A19    ; ...
          0  0  0  0  0  0  0  0  0  0  0  0  0  0  0  0
A21  0  A22  A7  A8  0  0  0  0  0  0  0  -1  0  -Rv2  wo*Lv2  Rv2
-wo*Lv2 ; ...
          0  0  0  0  0  0  0  0  0  0  0  0  0  0  0  0
0  0  0  1  0  0  0  0  0  0  0  0  0  0  0  0
0      ; ...

```

```

0 0 0 0 0 0 0 0 0 0 0 0 0 0 0 0 0
0 0 0 0 1 0 0 0 0 0 0 0 0 0 0 0 0
0 ; ...
0 0 0 0 0 0 0 0 0 0 0 0 0 0 0 0 0
A23 0 A24 0 0 0 A7 A8 0 0 0 0 -1 -wo*Lv2 -Rv2 wo*Lv2
Rv2 ; ...
0 0 0 0 0 0 0 0 0 0 0 0 0 0 0 0 0
0 ; ...
0 0 0 0 0 0 0 0 1 0 0 0 0 0 0 0 0
0 ; ...
0 0 0 0 0 0 0 0 0 0 0 0 0 0 0 0 0
0 ; ...
0 0 0 A9 A10 A11 0 0 0 A12 A29 A13 0 0 0 0 0
0 ; ...
0 0 0 0 0 0 A9 A10 A11 -A29 A12 0 A13 0 0 0 0
0 ; ...
0 0 0 0 0 0 0 0 0 0 A14 0 0 A29 -A14 0 A14
0 ; ...
0 0 0 0 0 0 0 0 0 0 A14 -A29 0 0 -A14 0
A14 ; ...
0 0 0 0 0 0 0 0 0 0 0 0 A25 0 A26 A29 0
0 ; ...
0 0 0 0 0 0 0 0 0 0 0 0 A25 -A29 A26 0
0 ; ...
0 0 0 0 0 0 0 0 0 0 0 0 A27 0 0 0
A29 ; ...
0 0 0 0 0 0 0 0 0 0 0 0 -A27 0 0 0 A28
A28 ];

```

```
% Eigen vectors calculation:
```

```

dcv=eig(Acvinv);
plot(dcv, 'x', 'MarkerSize',12); grid; xLim([-1e3, 0.1e3]); yLim([-0.6e3, 0.6e3]); %xLim([-0.5e3, 0.3e3]); yLim([-0.4e3, 0.4e3]);

```

## Appendix F

```
%-----%
% The small-signal state-space model of a small mini-grid composed
% by two droop-controlled three-phase voltage source inverters (without
% voltage controllers, LC filters and local loads) and one feeder.
% The initial values have been calculated after step of +3Hz in the
% no-load frequency signal of inverter #2. Hence, the line power is equal to
% 5kW.
%Note the conventional virtual impedance is implemented with Rv1=0.1ohm and
%Xv1=0.1ohm.
%-----%

% 1st Order Filter cut-off frequency:
    wc=2*pi*30;
% Inverters caractristics:
    Pmax1=20e3;           % Active power rating of inverter #1
    Pmax2=10e3;          % Active power rating of inverter #2
    PLineo=5e3;          % Initial active power passing through
the feeder
% Acive Power Droop Slopes:
    w_Range=2*pi*4;      % Angular frequency range
    w_r=2*pi*60;         % Rating angular frequency
    w_step=2*pi*3;       % no-Load angular frequency step
    w_nl=w_r+(w_Range/2)+w_step; % no-Load angular frequency
    mp1=w_Range/Pmax1;   % Inverter #1 active power droop slope
    mp2=2*mp1;           % Inverter #2 active power droop slope
% Reactive Power Droop Slopes:
    V_pCent=0;           % deltaV in %
    nq1=(V_pCent/100)*169.7/Qmax1; % Inverter #1 reactive power droop slope
    nq2=2*nq1;           % Inverter #2 reactive power droop slope
% Initial Operating frequency:
    wo=w_nl-mp1*PLineo;  % Initial operating angular frequency
% Line Impedance components:
    Rg=0.23;
    Lg=0.1/wo;
% Virtual Impedance Components of inverter #1:
    Kv=0.1;
    Rv1=Kv*1;
    Lv1=Kv*1/wo;
% Virtual Impedance Components of inverter #2:
    Rv2=Rv1*2;
    Lv2=Lv1*2;
% Initial value of the angle delta Plineo=5kW:
    deltao=-0.075;
% Initial Values of output current and voltage of Inverter #1 where Po=5.5kW:
    Vq1o=169.7;
    Vd1o=0;
% Initial Values of output current and voltage of Inveter #2 where Po=5.5kW:
    Vq2o=169.2;
    Vd2o=-12.73;
    Vqref2o=169.7;
```



```

Vdref2o=0;
% Initial values of line current (PLineo=500W):
  ILineqo=22;
  ILinedo=45.8;
% Arcvinv matrix components:
  Arv1=-wc;
  Arv2=-1.5*wc*ILineqo*nq1;
  Arv3=1.5*wc*(-ILineqo*Rv1-ILinedo*wo*Lv1+Vq1o);
  Arv4=1.5*wc*(ILineqo*wo*Lv1-ILinedo*Rv1+Vd1o);
  Arv5=-wc-1.5*wc*ILinedo*nq1;
  Arv6=1.5*wc*(-ILineqo*wo*Lv1-ILinedo*Rv1+Vd1o);
  Arv7=1.5*wc*(-ILineqo*Rv1+ILinedo*wo*Lv1-Vq1o);
  Arv8=mp1;
  Arv9=-mp2;
  Arv10=-1.5*wc*(ILineqo*(-Vqref2o*sin(deltao)-
Vdref2o*cos(deltao))+ILinedo*(Vqref2o*cos(deltao)-Vdref2o*sin(deltao)));
  Arv11=1.5*wc*nq2*(ILineqo*cos(deltao)+ILinedo*sin(deltao));
  Arv12=1.5*wc*(-ILineqo*Rv2-ILinedo*wo*Lv2-Vq2o);
  Arv13=1.5*wc*(ILineqo*wo*Lv2-ILinedo*Rv2-Vd2o);
  Arv14=1.5*wc*(ILinedo*(-Vqref2o*sin(deltao)-Vdref2o*cos(deltao))-
ILineqo*(Vqref2o*cos(deltao)-Vdref2o*sin(deltao)));
  Arv15=-wc+1.5*wc*nq2*(ILineqo*sin(deltao)-ILinedo*cos(deltao));
  Arv16=1.5*wc*(-ILineqo*wo*Lv2+ILinedo*Rv2-Vd2o);
  Arv17=1.5*wc*(-ILineqo*Rv2-ILinedo*wo*Lv2+Vq2o);
  Arv18=-nq1/Lg;
  Arv19=-(-Vqref2o*sin(deltao)-Vdref2o*cos(deltao))/Lg;
  Arv20=nq2*cos(deltao)/Lg;
  Arv21=- (Rg+Rv1+Rv2) /Lg;
  Arv22=wo*(Lg+Lv1+Lv2) /Lg;
  Arv23=- (Vqref2o*cos(deltao)-Vdref2o*sin(deltao))/Lg;
  Arv24=nq2*sin(deltao)/Lg;

% The Mini-Grid Matrix "Arcvinv" of the reduced system including the virtual
impedance loop:
  Arcvinv=[ Arv1   Arv2   0       0       0       Arv3   Arv4   ;...
            0     Arv5   0       0       0       Arv6   Arv7   ;...
            Arv8   0     0       Arv9   0       0       0     ;...
            0     0     Arv10  Arv11  Arv11  Arv12  Arv13  ;...
            0     0     Arv14  0     Arv15  Arv16  Arv17  ;...
            0     Arv18  Arv19  0     Arv20  Arv21  Arv22  ;...
            0     0     Arv23  0     Arv24  -Arv22  Arv21  ];

% Eigen vectors calculation:
  drcv=eig(Arcvinv);
  plot(drcv,'ro','MarkerSize',12); grid; xLim([-1e3, 0.1e3]); yLim([-
0.6e3, 0.6e3]);

```

## Appendix G

```
%-----%
% The small-signal state-space model of a small mini-grid composed
% by two droop-controlled three-phase voltage source inverters with LC
% filters, two local loads and one feeder. The initial values have been
% calculated for local loads of inverter #1 and #2 of 200W and 100W
% respectively, then a load step of +9.9kW occurred on the side of
% inverter #2. Hence, the line power is equal to 6.6kW. Note the proposed
% virtual impedance is implemented with Rv1=Rv2=5ohm and Xv1=Xv2=0ohm.
%-----%

% Voltage Controller coefficients (PI type-3):
    t=1.8294e-4;
    Tp=3.8460e-6;
    Kpi=1.1508;
% LC Filter components:
    rL=0.5;
    Lf=0.32e-3;
    Cf=20e-6;
% 1st Order Filter cut-off frequency:
    wc=2*pi*30;
% Inverters characteristics:
    Pmax1=20e3; % Active power rating of inverter #1
    Qmax1=12e3; % Reactive power rating of inverter #1
    Pmax2=10e3; % Active power rating of inverter #2
    Pload1=0.2e3; % Initial active power demand of inverter
#1 local load
    PLineo=6.6e3; % Initial active power passing through
the feeder
% Active Power Droop Slopes:
    w_range=2*pi*4; % Angular frequency range
    w_r=2*pi*60; % Rating angular frequency
    w_nl=w_r+(w_range/2); % no-Load angular frequency
    mp1=w_range/Pmax1; % Inverter #1 active power droop slope
    mp2=2*mp1; % Inverter #2 active power droop slope
% Reactive Power Droop Slopes:
    V_pCent=0; % deltaV in %
    nq1=(V_pCent/100)*169.7/Qmax1; % Inverter #1 reactive power droop slope
    nq2=2*nq1; % Inverter #2 reactive power droop slope
% Initial Operating frequency:
    wo=w_nl-mp1*(Pload1+PLineo); % Initial operating angular frequency
% Line Impedance components:
    Rg=0.23;
    Lg=0.1/wo;
% Virtual Impedance Components of inverter #1:
    Kv=5;
    Rv1=Kv*1;
    Lv1=Kv*0/wo;
% Virtual Impedance Components of inverter #2:
    Rv2=Rv1;
    Lv2=Lv1;
```

```

% Initial value of the angle delta Plineo=5kW:
deltao=-1.761;
tetav1o=0.7525;
tetav2o=-0.9089;
% Local Inductive Loads for the Inverters (Pload1o=5kW; Pload2o=2.5kW):
Rload1=216;
Lload1=1e-10;           % the reactive power demand is equal to zero
Rload2=432-427.68;     % a load step of 9.9kW has occurred at Inv#2 side
Lload2=Lload1;
% Initial Values of output current and voltage of Inverter #1:
Vq1o=123.9;
Vd1o=-116;
Vqref1o=169.7;
Vdref1o=0;
ILoadq1o=0.5735;
ILoadd1o=-0.5369;
Vdv1o=116;             % d-channel voltage drop across the virtual
impedance of inverter #1
% Initial Values of output current and voltage of Inveter #2:
Vq2o=111.7;
Vd2o=-127.8;
Vqref2o=169.7;
Vdref2o=0;
ILoadq2o=25.85;
ILoadd2o=-29.58;
Vdv2o=-133.9;        % d-channel voltage drop across the virtual
impedance of inverter #2
% Initial values of line current:
ILineqo=63.41;
ILinedo=23.73;
% Apvinv matrix components:
Apv1=-wc;
Apv2=1.5*wc*(ILoadq1o+ILineqo);
Apv3=1.5*wc*(ILoadd1o+ILinedo);
Apv4=1.5*wc*Vq1o;
Apv5=1.5*wc*Vd1o;
Apv6=-nq1*cos(-tetav1o);
Apv7=-2/Tp;
Apv8=-1/(Tp^2);
Apv9=-wo*Lv1*(-Vqref1o*sin(-tetav1o)-Vdref1o*cos(-
tetav1o))/(Vqref1o*sqrt(Vqref1o^2-Vdv1o^2));
Apv10=-Rv1*(-Vqref1o*sin(-tetav1o)-Vdref1o*cos(-
tetav1o))/(Vqref1o*sqrt(Vqref1o^2-Vdv1o^2));
Apv11=-nq1*sin(-tetav1o);
Apv12=-wo*Lv1*(Vqref1o*cos(-tetav1o)-Vdref1o*sin(-
tetav1o))/(Vqref1o*sqrt(Vqref1o^2-Vdv1o^2));
Apv13=-Rv1*(Vqref1o*cos(-tetav1o)-Vdref1o*sin(-
tetav1o))/(Vqref1o*sqrt(Vqref1o^2-Vdv1o^2));
Apv14=(Kpi*t)/(Tp^2)/Lf;
Apv15=(2*Kpi)/(Tp^2)/Lf;
Apv16=Kpi/(t*Tp^2)/Lf;
Apv17=-rL/Lf;
Apv18=wo;
Apv19=-1/Lf;
Apv20=1/Cf;
Apv21=1/Lload1;
Apv22=-Rload1/Lload1;

```

```

Apv23=mp1;
Apv24=-mp2;
Apv25=1.5*wc*(ILoadq1o-ILineqo);
Apv26=1.5*wc*(ILoadd1o-ILinedo);
Apv27=1.5*wc*Vq2o;
Apv28=1.5*wc*Vd2o;
Apv29=-Vqref2o*sin(deltao-tetav2o)-Vdref2o*cos(deltao-tetav2o);
Apv30=-nq2*cos(deltao-tetav2o);
Apv31=wo*Lv2*(-Vqref2o*sin(deltao-tetav2o)-Vdref2o*cos(deltao-
tetav2o))/(Vqref2o*sqrt(Vqref2o^2-Vdv2o^2));
Apv32=Rv2*(-Vqref2o*sin(deltao-tetav2o)-Vdref2o*cos(deltao-
tetav2o))/(Vqref2o*sqrt(Vqref2o^2-Vdv2o^2));
Apv33=Vqref2o*cos(deltao-tetav2o)-Vdref2o*sin(deltao-tetav2o);
Apv34=-nq2*sin(deltao-tetav2o);
Apv35=wo*Lv2*(Vqref2o*cos(deltao-tetav2o)-Vdref2o*sin(deltao-
tetav2o))/(Vqref2o*sqrt(Vqref2o^2-Vdv2o^2));
Apv36=Rv2*(Vqref2o*cos(deltao-tetav2o)-Vdref2o*sin(deltao-
tetav2o))/(Vqref2o*sqrt(Vqref2o^2-Vdv2o^2));
Apv37=1/Lload2;
Apv38=-Rload2/Lload2;
Apv39=1/Lg;
Apv40=-Rg/Lg;

```

% The Mini-Grid Matrix "Apvinv" of the complete system including the proposed virtual impedance loop:

```

Apvinv=[ Apv1  0  0  0  0  0  0  0  0  0  0  0
0  Apv2  Apv3  Apv4  Apv5  0  0  0  0  0  0  0
0  0  0  0  0  0  0  0  0  0  Apv4
Apv5 ; ...
0  Apv1  0  0  0  0  0  0  0  0  0  0
0  -Apv5  Apv2  Apv5  -Apv4  0  0  0  0  0  0  0
Apv4 ; ...
0  Apv6  Apv7  Apv8  0  0  0  0  0  0  0
0  -1  0  0  0  0  0  0  0  0  0  0
0  0  0  0  0  0  0  0  0  0  Apv9
Apv10 ; ...
0  0  0  1  0  0  0  0  0  0  0  0
0  0  0  0  0  0  0  0  0  0  0  0
0  0  0  0  0  0  0  0  0  0  0  0
0 ; ...
0  0  0  0  1  0  0  0  0  0  0  0
0  0  0  0  0  0  0  0  0  0  0  0
0  0  0  0  0  0  0  0  0  0  0  0
0 ; ...
0  Apv11  0  0  0  0  Apv7  Apv8  0  0  0
0  0  -1  0  0  0  0  0  0  0  0  0
0  0  0  0  0  0  0  0  0  0  Apv12
Apv13 ; ...
0  0  0  0  0  0  0  0  1  0  0  0
0  0  0  0  0  0  0  0  0  0  0  0
0  0  0  0  0  0  0  0  0  0  0  0
0 ; ...
0  0  0  0  0  0  0  0  0  1  0  0
0  0  0  0  0  0  0  0  0  0  0  0
0  0  0  0  0  0  0  0  0  0  0  0
0 ; ...

```

	0	0	Apv14	Apv15	Apv16	0	0	0	0	0	0
Apv17	Apv18	Apv19	0	0	0	0	0	0	0	0	0
0	0	0	0	0	0	0	0	0	0	0	0
0	; ...										
	0	0	0	0	0	0	Apv14	Apv15	Apv16	-	
Apv18	Apv17	0	Apv19	0	0	0	0	0	0	0	0
0	0	0	0	0	0	0	0	0	0	0	0
0	; ...										
	0	0	0	0	0	0	0	0	0	0	0
Apv20	0	0	Apv18	-Apv20	0	0	0	0	0	0	0
0	0	0	0	0	0	0	0	0	0	0	-
Apv20	0	; ...									
	0	0	0	0	0	0	0	0	0	0	0
Apv20	-Apv18	0	0	-Apv20	0	0	0	0	0	0	0
0	0	0	0	0	0	0	0	0	0	0	-
Apv20	; ...										
	0	0	0	0	0	0	0	0	0	0	0
0	Apv21	0	Apv22	Apv18	0	0	0	0	0	0	0
0	0	0	0	0	0	0	0	0	0	0	0
0	; ...										
	0	0	0	0	0	0	0	0	0	0	0
0	0	Apv21	-Apv18	Apv22	0	0	0	0	0	0	0
0	0	0	0	0	0	0	0	0	0	0	0
0	; ...										
	0	0	0	0	0	0	0	0	0	0	0
0	0	Apv23	0	0	0	0	0	0	0	0	0
0	0	0	0	0	0	0	Apv24	0	0	0	0
0	0	0	0	0	0	0	0	0	0	0	0
0	; ...										
	0	0	0	0	0	0	0	0	0	0	0
0	0	0	0	0	0	0	Apv1	0	0	0	0
0	0	0	0	0	0	Apv25	Apv26	Apv27	Apv28	-Apv27	-
Apv28	; ...										
	0	0	0	0	0	0	0	0	0	0	0
0	0	0	0	0	0	0	0	0	0	0	0
0	0	0	0	0	0	-Apv26	Apv25	Apv28	-Apv27	-Apv28	
Apv27	; ...										
	0	0	0	0	0	0	0	0	0	0	0
0	0	0	0	0	0	Apv29	0	Apv30	Apv7	Apv8	0
0	0	0	0	0	-1	0	0	0	0	Apv31	
Apv32	; ...										
	0	0	0	0	0	0	0	0	0	0	0
0	0	0	0	0	0	0	0	0	1	0	0
0	0	0	0	0	0	0	0	0	0	0	
0	; ...										
	0	0	0	0	0	0	0	0	0	0	0
0	0	0	0	0	0	0	0	0	0	0	0
0	0	0	0	0	0	0	0	0	0	1	0
0	; ...										
	0	0	0	0	0	0	0	0	0	0	0
0	0	0	0	0	0	Apv33	0	Apv34	0	0	0
Apv7	Apv8	0	0	0	0	0	-1	0	0	0	Apv35
Apv36	; ...										
	0	0	0	0	0	0	0	0	0	0	0
0	0	0	0	0	0	0	0	0	0	0	0
1	0	0	0	0	0	0	0	0	0	0	
0	; ...										

```

0      0      0      0      0      0      0      0      0      0      0      0      0      0
0      0      0      0      0      0      0      0      0      0      0      0      0      0
0      1      0      0      0      0      0      0      0      0      0      0      0      0
0      ; ...
0      0      0      0      0      0      0      0      0      0      0      0      0      0
Apv16 0      0      0      0      Apv17 Apv18 Apv19 0      0      Apv14 Apv15
0      ; ...
0      0      0      0      0      0      0      0      0      0      0      0      0      0
Apv14 Apv15 Apv16 -Apv18 Apv17 0      Apv19 0      0      0      0      0      0
0      ; ...
0      0      0      0      0      0      0      0      0      0      0      0      0      0
0      0      0      Apv20 0      0      Apv18 -Apv20 0      Apv20
0      ; ...
0      0      0      0      0      0      0      0      0      0      0      0      0      0
0      0      0      0      Apv20 -Apv18 0      0      -Apv20 0
Apv20 ; ...
0      0      0      0      0      0      0      0      0      0      0      0      0      0
0      0      0      0      0      Apv37 0      Apv38 Apv18 0
0      ; ...
0      0      0      0      0      0      0      0      0      0      0      0      0      0
0      0      0      0      0      0      Apv37 -Apv18 Apv38 0
0      ; ...
0      Apv39 0      0      0      0      0      0      0      0      0      0      0      0
0      0      0      0      0      -Apv39 0      0      0      Apv40
Apv18 ; ...
0      0      Apv39 0      0      0      0      0      0      0      0      0      0      0
0      0      0      0      0      0      -Apv39 0      0      -Apv18
Apv40 ];

```

```
% Eigen vectors calculation:
```

```

    dpv=eig(Apvinv);
    plot(dpv, 'x', 'MarkerSize',12); grid; xLim([-1e3, 0.1e3]); yLim([-
0.6e3, 0.6e3]);

```

# Bibliography

- [1] “Hybrid Mini-grids for Rural Electrification: lessons learned”; by *Alliance for Rural Electrification (ARE)*. *Project Report*, pp. 5-6, 2011
- [2] “Integration of Photovoltaic Power Systems in High Penetration Clusters for Distribution Networks and Mini-grids”; by *Farid Katiraei, Konrad Mauch and Lisa Dignard-Bailey*, *International Journal of Distributed Energy Sources*, vol. 3, no. 3, 2007.
- [3] “Per-Phase DQ Control of a Three-Phase Battery Inverter in a Diesel Hybrid Mini-Grid Supplying Single-Phase Loads”; by *Nayeem A. Ninad and Luiz A. C. Lopes*, *IEEE International Conference, March 2011*.
- [4] “Modeling and Dynamic Analysis of a Medium penetration PV-Diesel Mini-Grid System”; by *F. Katiraei, D. Turcotte, A. Swingler and J. Ayoub*. *The 4th European Conference on PV-Hybrid and Mini-Grid*, 2008.
- [5] “Parallel Operation of Generators for Stand-Alone Single-Phase Hybrid Systems, First Implementation of a New Control Technology”; by *A. Engler, C. Hardt, P. Strauss and M. Vandenberg*. *The 17th European Photovoltaic Solar Energy Conference and Exhibition*, 2001.
- [6] “Output Impedance Design of Parallel-Connected UPS Inverters With Wireless Load-Sharing Control”; by *Josep M. Guerrero, Luis García de Vicuña, José Matas, Miguel Castilla, and Jaume Miret*. *IEEE Transactions on*, vol. 52, pp. 1126-1135, 2005.
- [7] “Frequency Regulation and Enhanced Power Sharing in Microgrids Including Modified Droop Coefficients and Virtual Resistances”; by *Mohammad Ali Aghasafari, Luiz A.C. Lopes, and Sheldon Williamson*. *Electrical Power & Energy Conference (EPEC)*, IEEE, 2009.

- [8] "A Voltage and Frequency Droop Control Method for Parallel Inverters"; by *K. De Brabandere, B. Bolsens, J. Van den Keybus, A. Woyte, J. Driesen and R. Belmans*. *Power Electronics, IEEE Transactions on*, vol. 22, pp. 1107-1115, 2007.
- [9] "Small Signal Stability for Single Phase Inverter Connected to Stiff AC System"; by *Coelho E.A.A., Cortizo P.C. and Garcia P.F.D.* *Industrial Applications Conference, 1999. Thirty-Fourth IAS Annual Meeting. Conference Record of the 1999 IEEE*, vol. 4, pp. 2180-2187.
- [10] "Decentralized control for parallel operation of distributed generation inverters using resistive output impedance"; by *Guerrero J.M., Berbel N., Matas J., Sosa J.L., Cruz J. and Alentorn A.* *IEEE Transactions on*, vol. 54, pp. 994-1004, 2007.
- [11] "Microgrid Control"; by Paolo Piagi, Ph.D. dissertation of University of Wisconsin-Madison, 2.2.4, p. 20, 2005.
- [12] "Adaptive Decentralized Droop Controller to Preserve Power Sharing Stability of Paralleled Inverters in Distributed Generation Microgrids"; by *Yasser Abdel-Rady Ibrahim Mohamed and Ehab F. El-Saadany*. *Power Electronics, IEEE Transactions on*, vol. 23, pp. 2806-2816, 2008.
- [13] "Defining Control Strategies for Analysing MicroGrids Islanded Operation"; by *J. A. Peças Lopes, C. L. Moreira and A. G. Madureira*. *Power Tech, IEEE Russia*, 2005.
- [14] "Voltage and Frequency Droop Control in Low Voltage Grids by Distributed Generators with Inverter Front-End"; by *Karel De Brabandere*, Ph.D. dissertation, Dept. Elec. Eng., Leuven Univ. of Technology, 3.1, p. 16, 2006.
- [15] "Voltage and Frequency Control of Inverter Based Weak LV Network Microgrid"; by *Hannu Laaksonen, Pekka Saari and Risto Komulainen*. *Future Power Systems, IEEE International Conference on*, 2005.



- [16] "Modeling, Analysis and Testing of Autonomous Operation of an Inverter-Based Microgrid"; by *Nagaraju Pogaku, Milan Prodanovic and Timothy C. Green*. *Power Electronics, IEEE Transactions on*, vol. 22, pp. 613-625, 2007.
- [17] "Analysis and design of interfacing inverter output virtual impedance in a low voltage microgrid"; by *Jinwei He and Yun Wei Li*. *Energy Conversion Congress and Exposition (ECCE), IEEE*, pp. 2857-2864, 2010.
- [18] "Virtual Impedance Loop for Droop-Controlled Single-Phase Parallel Inverters Using a Second-Order General-Integrator Scheme"; by *José Matas, Miguel Castilla, Luis Garcia de Vicuna, Jaume Miret and Juan Carlos Vasquez*. *Power Electronics, IEEE Transactions on*, vol. 25, pp. 2993-3002, 2010.
- [19] "Enabling High Droop Gain for Improvement of Reactive Power Sharing Accuracy in an Electronically-Interfaced Autonomous Microgrid"; by *Aboutaleb Haddadi, Ali Shojaei, and Benoit Boulet*. *Energy Conversion Congress and Exposition (ECCE), IEEE*, pp. 673-679, 2011.
- [20] "Generator basics applied to field problems"; by *S, David Alley, P.E. ANNA, Inc.*, *The official publication of the International Electrical Testing Association*, summer 1993.
- [21] "Speed droop and power generation"; by *WOODWARD*, *application note 01302*.
- [22] "Autonomous Load Sharing of Voltage Source Converters"; by *Charles K. Sao, and Peter W. Lehn*. *Power Delivery, IEEE Transactions on*, vol. 20, pp. 1009-1016, 2005.
- [23] "Frequency Control Improvement in an Autonomous Power System: An application of Virtual Synchronous Machines"; by *M. Torres and L.A.C. Lopes*. *Power Electronics and ECCE Asia (ICPE & ECCE), IEEE 8<sup>th</sup> International Conference on*, pp. 2188-2195, 2011.